

NASA/TP-1999-209537



Investigation of Vortex Flaps and Other Flow Control Devices on Generic High-Speed Civil Transport Planforms

*Kevin J. Kjerstad, Bryan A. Campbell, Brenda E. Gile, and Guy T. Kemmerly
Langley Research Center, Hampton, Virginia*

December 1999

The NASA STI Program Office . . . in Profile

Since its founding, NASA has been dedicated to the advancement of aeronautics and space science. The NASA Scientific and Technical Information (STI) Program Office plays a key part in helping NASA maintain this important role.

The NASA STI Program Office is operated by Langley Research Center, the lead center for NASA's scientific and technical information. The NASA STI Program Office provides access to the NASA STI Database, the largest collection of aeronautical and space science STI in the world. The Program Office is also NASA's institutional mechanism for disseminating the results of its research and development activities. These results are published by NASA in the NASA STI Report Series, which includes the following report types:

- **TECHNICAL PUBLICATION.** Reports of completed research or a major significant phase of research that present the results of NASA programs and include extensive data or theoretical analysis. Includes compilations of significant scientific and technical data and information deemed to be of continuing reference value. NASA counterpart of peer-reviewed formal professional papers, but having less stringent limitations on manuscript length and extent of graphic presentations.
- **TECHNICAL MEMORANDUM.** Scientific and technical findings that are preliminary or of specialized interest, e.g., quick release reports, working papers, and bibliographies that contain minimal annotation. Does not contain extensive analysis.
- **CONTRACTOR REPORT.** Scientific and technical findings by NASA-sponsored contractors and grantees.

- **CONFERENCE PUBLICATION.** Collected papers from scientific and technical conferences, symposia, seminars, or other meetings sponsored or co-sponsored by NASA.
- **SPECIAL PUBLICATION.** Scientific, technical, or historical information from NASA programs, projects, and missions, often concerned with subjects having substantial public interest.
- **TECHNICAL TRANSLATION.** English-language translations of foreign scientific and technical material pertinent to NASA's mission.

Specialized services that complement the STI Program Office's diverse offerings include creating custom thesauri, building customized databases, organizing and publishing research results . . . even providing videos.

For more information about the NASA STI Program Office, see the following:

- Access the NASA STI Program Home Page at <http://www.sti.nasa.gov>
- Email your question via the Internet to help@sti.nasa.gov
- Fax your question to the NASA STI Help Desk at (301) 621-0134
- Telephone the NASA STI Help Desk at (301) 621-0390
- Write to:
NASA STI Help Desk
NASA Center for Aerospace Information
7121 Standard Drive
Hanover, MD 21076-1320

NASA/TP-1999-209537



Investigation of Vortex Flaps and Other Flow Control Devices on Generic High-Speed Civil Transport Planforms

*Kevin J. Kjerstad, Bryan A. Campbell, Brenda E. Gile, and Guy T. Kemmerly
Langley Research Center, Hampton, Virginia*

National Aeronautics and
Space Administration

Langley Research Center
Hampton, Virginia 23681-2199

December 1999

Available from:

NASA Center for AeroSpace Information (CASI)
7121 Standard Drive
Hanover, MD 21076-1320
(301) 621-0390

National Technical Information Service (NTIS)
5285 Port Royal Road
Springfield, VA 22161-2171
(703) 605-6000

Summary

A parametric cranked delta planform study has been conducted in the Langley 14- by 22-Foot Subsonic Tunnel with the following objectives: (1) to evaluate the vortex flap design methodology for cranked delta wings, (2) to determine the influence of leading-edge sweep and the outboard wing on vortex flap effectiveness, (3) to evaluate novel flow control concepts, and (4) to validate unstructured grid Euler computer code predictions with modeled vortex and trailing-edge flaps.

Two families of cranked delta planforms were investigated. One family had a constant aspect ratio, while the other had a constant nondimensional semispan location of the leading-edge break. Planform inboard leading-edge sweeps of 68° , 71° , and 74° were tested in combination with outboard leading-edge sweeps of 48° and 61° . The planform 68/48 with 68° inboard and 48° outboard leading-edge sweeps was used as the baseline for comparison with other planform families. Vortex flaps for the different planforms were designed by an analytical vortex flap design method.

The results indicate that less than optimal performance was obtained with the analytically designed vortex flaps, and the effectiveness of the vortex flaps was only slightly influenced by the variations in the parametric planforms. The unstructured grid Euler computer code was successfully used to model the configurations with vortex flaps. Also, the vortex trap concept was successfully demonstrated on a cranked delta planform.

Introduction

NASA and the U. S. A. aerospace industry have entered a joint high-speed research (HSR) program to reexamine the feasibility of High-Speed Civil Transports (HSCT). A major focus of this work is to determine the environmental impact of the next generation HSCT and the cost associated with reducing the environmental impact to acceptable levels. The main environmental concerns of the next generation HSCT are ozone depletion in the stratosphere, sonic boom strength, and airport-community noise.

High airport noise levels accompany HSCT configurations because their highly swept, low-aspect-ratio wings, which are required for efficient supersonic flight, are inefficient at subsonic high-lift conditions. During these conditions, the leading-edge flow tends to separate and form a vortex system, which can be useful in producing additional lift. However, the aerodynamic efficiency of the wing is actually reduced because of large increases in drag resulting from the formation of the vortex system and the loss of leading-edge suction. To overcome the

performance deficiency, additional thrust is required for takeoff, which increases source noise levels.

The only commercially flying HSCT, the *Concorde*, produces takeoff noise levels far above conventional subsonic transports and above the current Federal Aviation Regulation (ref. 1) for noise limits. Although the *Concorde* is exempt from the noise restrictions, it has limited access to international airports in the U. S. A. and elsewhere because of concerns about excessive noise. For the next generation HSCT to be economically viable, it must have worldwide access to the air transport market. Therefore, the next generation HSCT must be in compliance with the same airport noise regulations as those for subsonic transports. Significant airport noise reductions will be achieved through advances in engine and acoustic technology. However, additional noise reductions will be required and will likely be obtained through increases in the subsonic high-lift performance of the next generation HSCT. Improvements in the subsonic high-lift performance of an aircraft reduces airport-community noise because less thrust is required for takeoff. Previous research (ref. 2) has shown that substantial noise reductions can be obtained by assuming certain levels of improvements in high-lift performance. However, reference 2 does not address how the performance improvements will be obtained.

One approach that increases the subsonic high-lift performance of a highly swept wing is the use of leading-edge vortex flaps. A correctly designed vortex flap positions the leading-edge vortex system on the forward-facing area of a deflected flap. This creates a low-pressure region over the deflected surface and results in a net thrust component. Although the vortex flap concept has been investigated for a wide range of leading-edge sweeps on delta wings (refs. 3-6), only limited cranked delta wing (ref. 7) data are available for what appears to be the preferred planform of the next generation HSCT. Concern about the influence of the cranked delta wing shape on the design and effectiveness of vortex flaps has resulted in this investigation.

A series of eight flat plate cranked delta planforms with numerically designed vortex flaps has been tested in the Langley 14- by 22-Foot Subsonic Tunnel. The following objectives of this test were: (1) to evaluate the vortex flap design methodology (ref. 8) for cranked delta wings, (2) to determine the influence of planform shape on the effectiveness of vortex flaps, (3) to assess novel flow control concepts, and (4) to evaluate unstructured grid Euler computer code predictions on cranked delta planforms with modeled vortex and trailing-edge flaps.

The cranked delta planforms were divided into two families. One family had a constant aspect ratio, and the other had a constant nondimensional semispan location

of the leading-edge break. (See fig. 1.) Planform inboard leading-edge sweeps of 68°, 71°, and 74° were tested in combination with outboard leading-edge sweeps of 48° and 61°. The planform 68/48 with 68° inboard and 48° outboard leading-edge sweeps was used as the baseline for comparison with other planform families. To isolate the aerodynamic effects of the outboard wing, the planforms were also tested with the segment of the wing outboard of the crank removed. This resulted in a series of very-low-aspect-ratio clipped delta wing planforms.

Additional high-lift and pitch control devices were tested on the baseline planform. Trailing-edge flap end plates were investigated for possible reduction of the tip effects on the very-low-aspect-ratio flaps typically used on HSCT configurations. Outboard leading-edge snags similar to concepts investigated previously by Rao and Johnson (ref. 9) were examined for additional pitch control.

To increase the lifting capability of the aft section of the wing, inboard and outboard vortex trap concepts (fig. 2), also known as locked vortex concepts, were tested. For this concept, an open-ended channel on top of the wing is created by extending the leading- and trailing-edge flaps beyond their respective hinge lines. Spanwise blowing through the channel is normally required to entrain flow into the channel and create the trapped vortex system.

Under certain conditions, the flow separates from the trailing edge of the forward flap and reattaches on the leading edge of the extended trailing-edge flap, which effectively adds camber and thickness to the wing. A complex vortex system is formed in the channel between the two flaps. (See ref. 10.) Previous work on this concept has shown that large increments of lift can be obtained, but very high levels of spanwise blowing through the channel are required. (See refs. 11 and 12.) In this study, work was done to determine if the trapped vortex phenomenon could be reproduced on cranked delta wings and if the dependency on spanwise blowing could be reduced or eliminated.

To aid in the investigation, several of the planforms were pressure instrumented and extensive on- and off-body flow visualizations were obtained. Most of the investigation was conducted at a free-stream dynamic pressure of 70 psf, which corresponds to a Reynolds number of $1.5 \times 10^6 \text{ ft}^{-1}$. The angle of attack was varied between -4° and 20° , while the roll and yaw angles were held constant at 0° .

Symbols

The force, moment, and pressure data were reduced to standard coefficient form. For each planform, the

moment reference center (MRC) was located at the intersection of the upper surface of the flat plate wing, the vertical plane of symmetry, and the model station at 50 percent of the mean aerodynamic chord. Table I lists all the quantities pertinent to data reduction for each of the planforms. The reference areas used to reduce the data with the flaps installed did not include the vortex flap area.

A	wing aspect ratio, $\frac{b^2}{S}$
b	wing span, ft
C_D	drag coefficient, $\frac{\text{Drag}}{q_\infty S}$
$C_{D,i}$	induced-drag coefficient
$C_{D,0}$	drag coefficient at zero lift
ΔC_D	incremental drag coefficient
C_L	lift coefficient, $\frac{\text{Lift}}{q_\infty S}$
ΔC_L	incremental lift coefficient
C_m	pitching-moment coefficient, $\frac{\text{Pitching moment}}{q_\infty S \bar{c}}$
ΔC_m	incremental pitching-moment coefficient
C_p	pressure coefficient, $\frac{p - p_\infty}{q_\infty}$
C_μ	jet momentum coefficient, $\frac{2\dot{m} V_{\text{jet}}}{q_\infty S}$
c_f	distance from TE flap hinge line divided by local chord of TE flap
\bar{c}	mean aerodynamic chord, ft
h	nozzle height above wing upper surface, in.
L/D	lift-drag ratio
$\Delta(L/D)$	incremental lift-drag ratio
M_{jet}	jet Mach number
\dot{m}	mass flow rate per side, slug/sec
p	surface static pressure, psf
p_t	nozzle total pressure, psf
p_∞	free-stream static pressure, psf
q_∞	free-stream dynamic pressure, psf
R	Reynolds number, ft^{-1}
r	outboard panel removed, no spanwise extension
S	reference area, ft^2
s_p	leading-edge suction parameter
$T_{t,\text{jet}}$	jet total temperature, °R
V_{jet}	jet velocity, ft/sec

V_∞	free-stream velocity, ft/sec
X, Y, Z	Cartesian system coordinates
x, y	local coordinates of vortex flaps (table III)
α	angle of attack, deg
δ_{at}	aft trap plate deflection angle, deg
δ_{ft}	forward trap plate deflection angle, deg
δ_{ibf}	inboard trailing-edge flap deflection angle, deg
δ_{obf}	outboard trailing-edge flap deflection angle, deg
δ_{vf}	vortex flap deflection angle, deg
η_w	spanwise distance along wing surface divided by local semispan of wing
η_f	spanwise distance along vortex flap surface divided by local span of vortex flap measured from hinge line to leading edge

Abbreviations:

AR	family with constant aspect ratio
CB	family with constant nondimensional semispan leading-edge break location
LE	leading edge
MRC	moment reference center
OBLE	outboard leading edge
TE	trailing edge
TR	thrust removed

Model Description

Planforms

Eight flat plate cranked delta wing models were tested to investigate the influence of planform shape on the design and effectiveness of leading-edge (LE) vortex flaps. (See fig. 1.) Each model consisted of an inboard wing panel and an outboard wing panel to facilitate planform changes. All the wing panels were constructed from 0.5-in. sheet aluminum with the lower surface beveled 30° normal to all edges. The planforms shared a common ogive forebody and a cylindrical fuselage 4.5 in. in diameter. The fuselage axis of symmetry was located 1.125 in. above the upper surface of the flat wing. Other pertinent model dimensions and details are presented in figure 3. To keep the cost of the models down, stock materials and simple fabrication processes were used. As a result, the quality of the models was significantly lower than normal. Physical dimensions often differed by as much as 0.1 in. from the model design, and some vortex flap deflections varied by several degrees along the hinge line.

The planform models were split into the following two families of varying inboard LE sweep: a family with constant aspect ratio (AR) and a family with a constant nondimensional semispan location of the LE break. For both families of planforms, inboard LE sweeps of 68°, 71°, and 74° were tested. Most planforms were constructed with an outboard LE sweep of 48° and an outboard trailing-edge (TE) sweep of 10°. However, the constant-break (CB) family was tested with an additional outboard wing panel having LE and TE sweeps of 61° and 30°, respectively. The outboard wings in the constant-aspect-ratio family were allowed to grow spanwise and chordwise to maintain the aspect ratio of the LE sweep of planform 68/48, which was chosen to be the baseline in the study.

To isolate the influence of the outboard wing, all planforms were tested with the outboard wing panels removed as indicated by the dashed lines in figures 1 and 3. Small spanwise extensions were added to the constant-aspect-ratio planforms with 71° and 74° of LE sweep to create a family of constant-aspect-ratio clipped delta wings indicated by the dotted lines in figures 1 and 3.

Flaps

LE vortex flaps were designed for each of the five inboard wing panels by Frink's vortex flap design method. (See ref. 8.) The vortex flaps were designed for a configuration lift coefficient $C_L = 0.8$ with the vortex flaps deflected 30° and TE flaps (description to follow) deflected 15°. To maintain a constant C_L , the design α varied slightly for each configuration. (See table II.)

Frink's vortex flap design method uses a vortex lattice analysis (ref. 13) incorporating Polhamus's leading-edge suction analogy (ref. 14) and Lan's vortex action point relationship. (See ref. 15.) From the analysis, predictions of the LE vortex strength and location of the vortex action point (i.e., location of the resultant force vector of the vortex) at multiple spanwise stations are obtained. With this information, the local chord of the flap is increased or decreased to position the resultant force at the user-prescribed chord location (recommended by Frink to be 45 percent of the local chord to produce flow reattachment at the hinge line). A curved leading-edge shape typically results from the design procedure.

All the vortex flaps were designed with the 48° outboard wing panel in place. In the numerical model, the flow on the outboard wing was assumed to be separated from the undeflected sharp leading edge and formed into a crank vortex. Thus, Polhamus's suction analogy was applied in this region to account for the additional lift of the crank vortex.

The planforms with 61° of outboard LE sweep and the clipped delta planforms were tested with the vortex flaps designed with the 48° outboard wing panel in place. This was done to isolate the effects of the outboard wing. Vortex flaps for the AR family clipped delta planforms with the spanwise extensions were created by stretching the corresponding original vortex flaps along the hinge line aft of the maximum chord location. (See fig. 4.) In addition, an inverse tapered vortex flap was tested on planforms CB 74 and CB 74/48 to compare the performance of a numerically designed vortex flap with that of a simpler vortex flap designed with a straight leading edge.

Figure 4 is a sketch of each vortex flap tested and table III lists their coordinates. Table II contains the wetted area and design α of each vortex flap tested; design α was varied slightly between planforms to maintain a constant C_L . The vortex flaps were fabricated from 0.090-in. sheet aluminum with the leading edges left blunt. When the flaps were cut from the aluminum sheet, material extending 0.75 in. inboard of the hinge line was left to create an attachment flange. The flange overlapped the leading edge of the inboard wing instead of being recessed into it. (See fig. 5(a).) This produced a 0.090-in. aft-facing step on the upper surface of the wing after the vortex flaps were installed. Vortex flap deflections were obtained by bending the flaps along the hinge line to the desired deflection angle.

The vortex flaps were tested in combination with inboard and outboard TE flaps. The inboard trailing edge was divided into three equally sized flaps. Outboard, a tapered TE flap extended from a typical location of an outboard engine to the wingtip. Actual dimensions of the flaps are shown in figure 3.

A constant-radius outboard leading-edge (OBLE) flap was also tested with the vortex and TE flaps. (See fig. 5(b).) This flap was constructed by curving a strip of 0.090-in. sheet aluminum into a 1.5-in. arc sector with a 2.0-in. radius. The arc sector begins tangent to the upper surface of the wing and curves normal to the wing leading edge (hinge line). A 0.25-in.-diameter wooden dowel was epoxied to the leading edge of the flap to promote attached flow. Again, a flange was used to mount the OBLE flap in the same manner as the vortex flaps. A photograph of planform 68/48 with vortex and OBLE flaps installed is presented in figure 6(a). The OBLE flaps were also tested with spacers placed between the flap and upper surface of the wing to simulate a crude slotted flap. (See fig. 6(b).)

Additional Flow Control Concepts

The baseline planform 68/48 was used to evaluate some additional high-lift and pitch control devices. An OBLE snag was added to the model for potential pitch control. (See fig. 7(a).) The snag was constructed from a strip of 0.090-in. sheet aluminum that extended 0.8 in. (5 percent of the break chord) upstream of the leading edge and was attached to the planform with use of the same flange system as described previously.

To improve the effectiveness of the TE flaps, end plates were added to the sides of the deflected flaps as shown in figure 7(b). The end plates were created with triangular pieces of cardboard taped over the gaps created by the deflected flaps.

A final concept, the vortex trap or locked vortex concept (fig. 8), was investigated for its high-lift potential. The concept was tested at the following two locations: on the aft sections of the inboard wing as shown in figure 9 and on the outboard wing as shown in figure 10. The inboard vortex trap system was created by deflection of a 4.0-in.-chord flat plate (25 percent of the break chord) from the upper surface of the wing and addition of a 4.0-in. forward extension to the TE flaps. The hinge line of the forward trap plate was located 1.0 in. aft of the LE break and oriented spanwise. Both trap plates spanned the same region of the wing as the inboard TE flaps. A 0.25-in.-diameter dowel was added to the leading edge of the aft trap plate to promote flow reattachment. The spanwise flow required to generate the locked vortex system was produced from a nozzle located in the side of the fuselage between the two trap plates. To recover some of the potential thrust of the spanwise blowing jet, a jet deflector was added to the forward trap plate as shown in figures 8 and 9.

The forward trap plate of the outboard vortex trap system (fig. 10) was created by attachment of an upward-deflected flap plate along the LE. A forward extension was added to the deflected TE flaps to produce the aft trap plate. The chord length of both the forward and aft trap plates were 25 percent of the local wing chord. Again, a 0.25-in.-diameter dowel was added to the leading edge of the aft trap plate, and spanwise blowing from a jet located between the trap plates and in the plane of the wing break was used to increase the flow through the channel.

Pressurized air (50 psi) for the vortex trap system was supplied to each side of the model through a 0.65-in.-inner-diameter stainless steel pipe with 0.6-in.-diameter choke ring at the exit. (See fig. 11.) The air supply lines were mounted nonmetrically to the sting and the

location of the nozzle exits could be moved by a shift in the mounting point.

Pressure Instrumentation

The planforms 68/48, AR 74/48, and CB 74/48 were pressure instrumented on the upper surface with three spanwise rows of ports on the wing panels, two spanwise rows on the vortex flaps, and two chordwise rows on the inboard TE flaps. A sketch and tabulation of the pressure port strip locations are provided in figure 12. Holes were drilled through the wing panels and flaps to create the pressure ports, which were then connected with 0.060-in.-diameter steel tubing to 5-psid electronically scanned pressure transducers inside the fuselage. The steel tubing was routed along the lower surface of each planform and covered with aluminum tape. This procedure undoubtedly increased the drag of the planforms with pressure instrumentation. However, because the tape remained in place during the entire time that a planform was being tested, incremental changes in drag for particular planform configurations (i.e., vortex flaps on-off, etc.) were not caused by the tape. Thus, comparisons between the different planforms based on incremental data should be meaningful.

Note that the strips of pressure ports are located separately for the flaps and main wing (i.e., not necessarily at the same fuselage station). Thus, the pressure data are discontinuous across the strips. Also, the TE flap strips are nondimensionalized by the local flap chord with the origin at the flap hinge line. The strips on the vortex flaps are nondimensionalized by the local span of the vortex flap measured from the hinge line to the leading edge; the strips on the planform are nondimensionalized by the local semispan of the planform with the origin at the plane of symmetry.

Test Conditions and Procedures

The experimental investigation was conducted in the Langley 14- by 22-Foot Subsonic Tunnel configured with a closed test section. (See ref. 16.) The test conditions were limited to variations in tunnel dynamic pressure and angle of attack α . Tunnel dynamic pressure was varied from 10 to 110 psf, which resulted in a Reynolds number range of 0.6×10^6 to $1.8 \times 10^6 \text{ ft}^{-1}$. For most of the LE and TE flap investigation, the dynamic pressure was held at 70 psf, which corresponded to a Reynolds number of $1.5 \times 10^6 \text{ ft}^{-1}$. Throughout the test, angle of attack was varied from -4° to 20° , while the model reference center was maintained at the centerline of the tunnel. The angle of attack was measured with an internally mounted accelerometer.

An internally mounted six-component balance was used to measure the model forces and moments. Longitudinal load capacities and quoted accuracies (0.5 percent of maximum rated load) are presented in table IV.

To ensure a consistent boundary layer state between the planforms, No. 60 carborundum grit was applied to the entire fuselage and the upper surface of the wing. This practice was particularly important because the flow field was vortex dominated with multiple separation and reattachment lines. Although the existence of grit over the entire upper surface will add to the drag of a configuration, comparisons between planforms based on incremental data derived from geometrical changes to the individual planforms (i.e., vortex flaps on-off, etc.) should be valid.

The leading-edge suction parameter s_p was used as an additional figure of merit for evaluation of the effect of planform shape on the performance of vortex flaps. The definition and usefulness of this parameter are discussed in detail in references 17 and 18. For this application, the theoretical upper limit of s_p was computed with the assumption of an elliptically loaded wing with induced-drag coefficient $C_{D,i} = C_L^2/\pi A$. The equation used to define s_p is given by

$$s_p = 100 \left[\frac{(C_D - C_{D,0}) - C_L \tan \alpha'}{C_{D,i} - C_L \tan \alpha'} \right]$$

where

$$\alpha' = \frac{C_L}{\partial C_L / \partial \alpha}$$

During the investigation of the vortex trap system, the free-stream dynamic pressure was typically set at 10 psf to obtain a sufficient momentum ratio of the jet. The spanwise blowing nozzles were maintained at choked conditions to ensure the ability to quantify their flow properties. Prior to the test, total pressure probes upstream of the nozzle exits were calibrated to the total pressure at the exits to establish the choked condition. The mass flow rate was measured by a turbine flow meter located outside of the test section where jet total temperature $T_{t,\text{jet}}$ was also measured. From $T_{t,\text{jet}}$, jet velocity V_{jet} was computed with the assumption that the flow was adiabatic with jet Mach number $M_{\text{jet}} = 1.0$.

Throughout the wind tunnel investigation, flow visualization techniques were used to assist in the analysis. Surface flow visualization was obtained with the use of motor oil mixed with a fluorescent dye and illuminated with ultraviolet light. To increase the effectiveness of the

fluorescent dye, the surfaces of the models were painted flat white to reflect the ultraviolet light back into the fluorescent oil without creating additional glare. Off-body flow visualization was obtained by injection of a cloud of vaporized propylene glycol into the flow upstream of the contraction section. A laser light sheet illuminated the vapor and created a two-dimensional vapor screen.

Discussion of Results

Leading-Edge Flaps

Basic observations. A summary of the test configurations and conditions is presented in table V. The column labeled "Appendix figures" indicates whether pressure or surface flow visualization data were obtained for that condition and, if so, in what figures of the appendix the data are presented. The pressure data presented in the appendix contain plots for a limited number of angles in an angle-of-attack sweep. Typically, the surface flow visualization data presented are for a single α .

The effect of dynamic pressure on the longitudinal aerodynamics of the cranked delta planforms with flaps deflected is typified in figure 13. Over the small range of dynamic pressures and corresponding Reynolds numbers, the data show a slight variation with dynamic pressure; however, the variation is not much larger than the spread of repeat data. The weak influence of dynamic pressure or Reynolds number is expected because the flow field is dominated by LE separation and vortical flow.

Figure 14(a) presents the effect of grit application on the entire upper surface of the model as described in the model description. The effect on the forces and moments is not much more than the differences of repeat data. The surface pressure distributions, with or without grit (typified in fig. 14(b)), follow the same trends.

Figure 15 is representative of the surface flow features and pressure distributions obtained on the cranked delta models with vortex flaps (other planforms are presented in the appendix). On the inboard portion of the wing, the primary reattachment line is clearly shown in figure 15(a). The change in direction of the surface flow lines just outboard of the wing LE break indicates the presence of a crank vortex. Also, the secondary separation lines on the vortex flap and on the outer wing panel are easily discernible. Closer examination of the outer panel reveals the reattachment line of the secondary crank vortex. From these observations and the off-body flow visualization, a detailed understanding of the complex vortex system can be developed, and a sketch of the probable system is presented in figure 16. As shown in figure 16, the primary and crank vortices are two distinct,

corotating vortices over the wing at moderate α 's ($\alpha \approx 10^\circ$). Downstream of the wing, the two vortices merge. As α increases, the location at which the vortices merge moves upstream, and at the higher α 's ($\alpha \geq 16^\circ$) only one vortex can be seen in the off-body flow visualization.

Design of vortex flaps. The surface flow visualization and pressure distributions at $\alpha = 10^\circ$ in figure 15 represents the vortex flap design condition for the planform AR 74/48. A properly optimized vortex flap positions the entire load induced by the primary vortex on the deflected flap and forces flow reattachment at the hinge line. (See ref. 8.) This should produce the most efficient pressure distribution for drag reduction. Clearly in this case, the primary vortex reattachment line is a considerable distance inboard of the vortex flap hinge line. (See fig. 15(a).) As indicated by the suction peaks in the pressure distributions of strips 3 and 4, the induced load is not being carried entirely by the vortex flap. The experimental results suggest this flap design is less than optimal, and a much longer flap chord is required to obtain the greatest drag reduction.

These results are typical of all the vortex flaps tested in this investigation. At the design condition (see the section entitled "Flaps"), the primary reattachment line was always inboard of the vortex flap hinge line, which was indicative of a less than optimal vortex flap design. Another investigation used Frink's vortex flap design method on cranked delta planforms with far better results. (See ref. 7.)

The main difference between the two applications of the design method was in the configuration of the outboard wing. In reference 7, the vortex flap design had attached flow LE flaps on the outboard wing, and these flaps were appropriately modeled in the numerical design of the vortex flaps. In this investigation, the vortex flaps were designed without any LE device on the outboard wing. The sharp, undeflected leading edge of the outboard wing promoted the formation of a crank vortex system. This reduced the probability of having dramatically different outboard flow fields (i.e., different levels of attached flow if outboard LE flaps were used) between the various planforms tested. Maintenance of a consistent outboard wing flow field across the planforms was necessary to eliminate misleading conclusions about the influence of planform shape on the effectiveness of vortex flaps.

In the numerical design of the vortex flaps in this investigation, the flow on the outboard wing was assumed to be dominated by a crank vortex, and Polhamus's leading-edge suction analogy was applied to this region to get vortex load estimates from the vortex

lattice model. The application of the suction analogy accounts for the additional lift of the crank vortex by the addition of an increment directly to the computed attached flow C_L . However, neither the suction analogy nor the vortex lattice computer code, which is based on the assumption of attached flow over the entire lifting surface, can account for changes in the LE upwash due to the existence of the crank vortex system. The changes in the LE upwash, which were not accounted for in the numerical model but which occurred physically, are possibly the main reason for the less than optimal vortex flap designs. The change in upwash created by the crank vortex probably increases the local α along the vortex flap, which will increase the size of the LE vortex and the optimal vortex flap. Even though the vortex flaps in the present investigation did not perform as desired at the design condition, they were all designed on a common design logic basis that should not mask the planform effects.

Planform effects on vortex flaps. The effects of planform variation on the longitudinal aerodynamics of the clipped delta planforms (fig. 1) in the cruise configuration are shown in figure 17. Because the variation in the planform parameters was not very large, trends in the data resulting from the planform effects are not easily discernible. The C_L and drag coefficient C_D data appear to show an influence of both LE sweep and aspect ratio. The pitching-moment coefficient C_m data (fig. 17(b)) for the CB family shows a definite influence of LE sweep or aspect ratio. Because the C_m data for the AR family are essentially independent of planform, the observed trend in the CB data is probably an effect of the changing aspect ratio. Although there are variations in the L/D data, no understandable trends are apparent.

Figure 18 presents the cruise data for the cranked delta planforms. Note that no cruise data were obtained for the planform AR 71/48. At least for the CB family, the C_L and C_D data seem to be influenced by LE sweep or aspect ratio. Isolation of the effect is not possible because of the lack of a discernible trend in the AR family. Both families of planforms show a strong dependency on LE sweep in the C_m data.

Planform influences on TE flap effectiveness are presented in figure 19 for the clipped delta planforms. To make the trends in the data more apparent, increments were computed by subtraction of the cruise data from the deflected flap data for each planform. However, only slight differences in the computed increments occur between the different planforms. The only obvious trend is a decrease in flap effectiveness with an increase in LE sweep in the CB family of clipped delta planforms. The effectiveness of TE flaps on the cranked delta planforms is illustrated in figure 20. Again, the differences between

the planforms are small, and because data for the planform AR 71/48 were not obtained, no conclusions can be drawn from the trends.

The planform effects on the longitudinal aerodynamics of the cranked delta planforms at the vortex flap design condition are shown in figure 21, and plots for the clipped delta planforms at the same condition are included for completeness in figure 22.

Trends in the data resulting from the planform effects are not easily discernible. In this case, increments were computed by subtraction of data without the vortex flaps from data with the vortex flaps for each planform. (See figs. 23 and 24.) Note that the use of increments to determine the planform effects on the vortex flaps has the additional benefit of removing the baseline trends in the data. For example, an increase in the aspect ratio of a wing will increase its lift curve slope. However, this method of computing increments will remove the baseline trend, and the final results will indicate whether the increase in aspect ratio has an additional influence on the effectiveness of vortex flaps. The purpose of this investigation was to obtain this type of information.

Figure 23 presents the resulting increments for the clipped delta planforms. The plots of incremental lift coefficient ΔC_L suggest an influence of LE sweep on the amount of lift lost at up to $\alpha = 10^\circ$ for the CB family. Because the same trend is not apparent in the AR data, this could be an aspect ratio effect. The ΔC_L data for the cranked planforms are presented in figure 24(a). The data appear to group according to LE sweep between $\alpha = 2^\circ$ and 6° . As in the clipped delta data, the absence of trends at higher α 's is likely due to differences between the planforms in the onset of TE flap separation and the angle of attack at which the action point of the LE vortex moves off the vortex flap and onto the main wing. Movement of the vortex action point onto the wing is indicated by ΔC_L becoming less negative with increasing angle of attack (for planform 68/48 this occurs just above $\alpha = 12^\circ$). For unknown reasons, the data from the planforms AR 74/48 and CB 74/48 do not display a break in ΔC_L , although the primary vortex is known to move onto the main wing at higher angles of attack.

The incremental drag coefficient ΔC_D data appear to be grouped along family lines for both the clipped and cranked delta planforms with the 68° LE sweep planforms residing in the CB family. (See figs. 23(a) and 24(a).) This grouping is particularly evident in the clipped delta planforms where there is no outboard wing panel to obscure the results. The clipped delta planforms also show an influence of LE sweep at high α 's. Because both families of clipped delta planforms appear influenced by LE sweep, aspect ratio is not a likely influence.

Why the 68° LE sweep planform tends to group with the CB family and consistently shows a larger incremental difference than the other two members of the AR family is not clear. If this were an influence of LE break location, then more variation between the other AR planforms would be expected because of their different non-dimensional LE break locations. The planform 68/48 does have a slightly lower aspect ratio than the other members of its AR family. (See table I.) However, this does not explain why there is not more variation in the CB family as a result of the relatively large aspect-ratio differences and why the same phenomenon is observed in the clipped delta data where the aspect ratio of the AR family has been held constant.

A more decisive parameter to consider for determination of the influence of the planform on the design and effectiveness of vortex flaps is the lift-drag ratio L/D . This design parameter is typically maximized for best takeoff performance and noise reduction. As shown in figures 23(b) and 24(b), L/D for all the test planforms was increased with the vortex flaps deployed above $\alpha = 2^\circ$. The most prominent trend in the incremental lift-drag ratio $\Delta(L/D)$ data is the grouping into the respective families of planforms above $\alpha = 10^\circ$. Again, planforms 68 and 68/48 group with the CB family. The AR and CB families of cranked delta planforms display a dependency on LE sweep for $\alpha < 10^\circ$.

As shown in figure 23(b), an influence of LE sweep on the incremental pitching-moment coefficient ΔC_m for the clipped delta planforms above $\alpha = 8^\circ$ seems to exist. The ΔC_m increases with an increase in LE sweep, which is the opposite trend typically found for uncambered delta wings. (See fig. 17.) The data for the CB family of cranked delta planforms (fig. 24(b)) also show an influence of LE sweep at higher α 's.

Figure 25 shows the longitudinal aerodynamics of the planforms in the CB family and planforms having a different outboard wing panel. The alternate wing panel changes the outboard LE sweep from 48° to 61° and the outboard TE sweep from 10° to 30°. Generally, the change in the outboard wing shape results in a loss of lift and an increase in drag and pitching moment.

The influence that the alternate outboard wing panel has on the effectiveness of the vortex flaps is illustrated in figure 26. As before, the increments are obtained by subtraction of data without the vortex flaps from data with the vortex flaps for each planform. The planforms with higher outboard sweep tend to produce less drag reduction with deployment of the vortex flaps. However, losses in lift associated with vortex flaps are not as great for the higher outboard sweep planforms. Surprisingly, these two effects result in a slight improvement in L/D

for the planforms with higher outboard sweep. (See fig. 26(b).)

The surface pressure distributions (fig. 27) indicate that the flow on the vortex flap and forward section of the wing is not affected much by changes to the outboard wing. In fact, only the pressure distribution of strip 5 appears to be significantly altered, but the comparison here is limited because the 61° outboard wing panel was not pressure instrumented.

Effect of OBLE flaps. Planform influences on the longitudinal aerodynamics of the cranked delta wings with OBLE flaps are presented in figure 28. The lift, drag, and L/D data of the CB family show a dependency on LE sweep or, more likely, aspect ratio. In the constant-AR family, the most distinct trend is the decrease in pitching moment with an increase in inboard LE sweep. Figure 29 presents the increments obtained by subtraction of the vortex flap data without the OBLE flaps from the data with OBLE flaps. With the data plotted in this form, the baseline trends are subtracted out, and the CB data no longer exhibit the dependency on aspect ratio as observed in figure 28. The most significant effect produced by the addition of the OBLE flaps is the decrease in drag (fig. 29(a)), which is indicative of the leading-edge suction produced by the OBLE flaps. The increased LE suction produces dramatic increases in L/D . (See fig. 29(b).) Why ΔC_L data for the planform 68/48 vary as much as they do and are not more consistent with the other planforms is unclear.

Comparison of the OBLE flaps on and off data clearly shows that the OBLE flaps greatly improve the performance of the planforms. Figure 30 presents such a comparison for the planform 68/48. For α 's between 0° and 16°, substantial drag reduction results with the OBLE flaps on, which dramatically improves the L/D ratio. As shown in the pressure plots of figure 31, the flow over the forward section of the wing is virtually unaffected by the addition of the OBLE flaps. The main effect that the OBLE flaps have on the wing pressure distribution is replacement of the large suction peak created by the coalescing of the primary and crank vortex with two smaller suction peaks over the outboard wing (strip 5). The most inboard suction peak is the footprint of the primary vortex, while, the outboard suction peak is the footprint of a vortex forming from flow separating at the hinge line of the OBLE flaps. The hinge line separation is evident in the surface flow visualization presented in figure 32. (See surface flow visualization of other cranked delta planforms in the appendix for greater clarity.) As seen in the comparison of surface flow visualization (fig. 32), the flow lines of the primary vortex on the OBLE flap configuration no longer change direction at the outer panel prior to flowing into the secondary

separation line. This indicates that the LE crank vortex has been eliminated and accounts for part of the drag reduction obtained with the OBLE flaps in place. However, most of the drag reduction can be attributed to the LE suction produced by the highly curved OBLE flaps. The surface flow visualization clearly indicates attached flow on the forward-facing, thrust-producing, OBLE flap.

Because the flow over the OBLE flaps separates at the hinge line, the full benefit in aerodynamic performance was not realized. To extend attached flow aft of the hinge line, the OBLE flaps were crudely modified to resemble slotted flaps. The resulting force data show no sign of improvement. (See fig. 31.) However, the flow visualization presented in figure 32(c) indicates significant streamwise flow patterns and suggests a potential for improved performance with a cleaner installation and slot optimization.

In figure 33, the leading-edge suction parameter is presented in summary with the aerodynamic performance improvements obtained with the vortex and outboard LE flaps deployed on the cranked delta planforms. Without exception, the addition of the vortex flaps and the OBLE flaps produces substantial improvement in s_p . Note that data for the planform AR 71/48 are not presented because the cruise data for this planform were not obtained.

Variations to vortex flaps. Several vortex flap deflections were tested on the 68° LE sweep clipped and cranked delta planforms. (See fig. 34.) Because the resultant force of a vortex flap acts normal to its surface, an increase in δ_{vf} rotates the resultant force away from the lift plane and toward the thrust plane. Thus, as shown in figure 34, ΔC_L and ΔC_D become more negative with an increase in the vortex flap deflection angle δ_{vf} . The ΔC_m also decreases because of the loss of lift ahead of the moment reference center. As δ_{vf} is increased, the angle of attack relative to the LE of the vortex flap is reduced. This delays the movement of the primary vortex onto the main wing and increases the α for maximum vortex flap effectiveness.

Figure 35 shows the effect of vortex flap design on the longitudinal aerodynamics of the planform CB 74/48. Up to $\alpha = 12^\circ$, the data of the straight LE inverse-tapered flap are surprisingly similar to the highly curved, numerically designed flap. Even above $\alpha = 12^\circ$, the LD data are nearly identical. From a system design and manufacturing point of view, the results are encouraging. The straight LE flap should be much easier to incorporate into the aircraft, and it should be less expensive to manufacture.

Other Flow Control and High-Lift Devices

Flap end plates and LE snags. For the typical HSCT planform, the middle segment of the inboard TE is left undeflected to provide space for an inboard engine. Two very-low-aspect-ratio TE flaps, one on each side of the engine location, are produced by the TE segmentation. To reduce the tip effects on these very-low-aspect-ratio flaps and thereby improve their effectiveness, the TE flaps on the planform 68/48 had end plates attached. The middle flap of the three inboard flaps was left undeflected, and the other two flaps were deflected 15° . Vertical end plates were attached to the side of the flaps to close the gaps created by the flap deflections. As shown in figure 36 the end plates had essentially no effect on the measured forces and moment. The results of the flap end plates suggest the ineffectiveness of the TE flaps is due more to the lack of camber in the flaps than to their low-aspect ratio.

Likewise, the OBLE snags that were investigated for their potential pitch control benefits were ineffective. (See fig. 37.) The normal philosophy for use of an LE snag is to create a strong LE vortex over the wing that will produce considerable pitching moment. In this case, a strong cranked vortex already exists over the outboard wing, and the snag only slightly repositioned it.

Inboard vortex trap system. The flow field over the aft section of the inboard wing has very low momentum, which results in a wing area that is not being used efficiently to generate lift. (See fig. 14.) However, this region of the wing is a good location for lift augmentation through the use of a vortex trap system. The region is large enough to accommodate the components of the trap system, and the area represents a considerable percentage of the planform. Thus, an increase in the amount of lift carried in this region will significantly add to the total lift of the aircraft.

Figure 38 shows vapor screen flow visualization of such a system with and without spanwise blowing. Clearly, the flow separating from the forward trap plate does not reattach on the extended TE flap without the spanwise blowing. However, with sufficient spanwise blowing, flow entrainment into the jet turns the streamlines of the flow above the channel. The flow becomes aligned with the extended TE flap and reattaches to it. The net result is a large increase in the local camber and the lift increment shown in figure 39. Unfortunately, the increase in lift comes at the cost of a considerable reduction in LD when compared with the planform without the trap.

Also shown in figure 39 is the extremely large installation penalty in C_L for jet momentum coefficient

$C_{\mu} = 0.0$, which must be overcome by the vortex trap system before any benefit is obtained. The large amount of spanwise blowing required to overcome the installation penalty produces a favorable α shift in the lift curve even without the trap system installed. The increase in lift for the case of jet alone is due to the creation of a low-pressure region over the wing induced by the jet flow. There is also an effective increase in wing camber due to the free-stream flow maneuvering over the jet flow. At lower α 's, the drag at a given lift does not change between blowing on and off. For $C_L > 0.6$, the jet flow actually has a favorable effect on C_D . The spanwise blowing jet is probably reducing the extent of separated flow on the outboard wing.

Because the mass flow required by the spanwise blowing jet would have to be supplied by the aircraft engines, a jet deflector was added to the outboard end of the forward trap plate to recover some of the thrust lost by blowing spanwise. The deflector turned the spanwise jet flow downstream into the thrust direction. As seen in figure 39, the drag polar is shifted by about 600 drag counts, which means 40 percent of the possible thrust can be recovered ($C_{\mu} = 0.15$). Actually, only about 30 percent of the possible thrust is recovered because some of the drag reduction is an induced effect discussed later. These results are encouraging because the crudeness of the test trap system leaves many opportunities for further reduction of installation penalties and improvement in thrust recovery.

The induced effect of the jet deflectors on drag becomes apparent by examination of thrust-removed (TR) data. These data were obtained by subtraction of the static axial force with blowing on from the axial-force data with the tunnel and blowing on. Even with the thrust removed, C_D and L/D still show a large improvement with the jet deflectors installed when compared with the data without the jet deflectors installed. (See fig. 39.) In fact, the induced drag reduction accounts for at least one-third of the apparent thrust recovered throughout the test α range. Surface flow visualization of the trap system with and without the jet deflector installed (fig. 40) clearly illustrates why the favorable induced effect of the jet deflector exists. Without the jet deflector installed, flow entrainment into the spanwise flowing jet is so strong that most of the flow over the outboard wing aft of the jet is flowing upstream. With the jet deflector in place, the entire flow field on the outboard wing is now flowing downstream. Furthermore, flow entrainment into the deflected jet is sufficiently strong to eliminate the hinge line separation observed previously on the OBLE flap. (See fig. 32.)

Addition of the jet deflector also modifies the behavior of the lift curve. (See fig. 39.) At lower α 's, the lift is

reduced, but its behavior is more linear. As α increases, the effectiveness of the vortex trap system appears to be increased with the jet deflectors in place. The jet deflectors reduce the rate at which the flow can pass through the channel and extend the trapped vortex phenomenon to higher α 's.

Figure 41 shows the influence of C_{μ} on the effectiveness of the inboard vortex trap system. As expected, an increase in C_{μ} increases the trap effectiveness. In fact, the increase is nearly linear with C_{μ} . For this system, a $C_{\mu} = 0.075$ is required just to overcome the installation penalties in lift noted previously. Because the data in figure 41 do not have the thrust removed (note that the jet deflectors are in place), the large decreases in drag obtained with increase in C_{μ} are a thrust effect.

The vortex trap system was tested at two different sets of trap plate deflection angles to examine the influence of deflection on vortex trap effectiveness. At the higher deflection case, the wing camber is increased and so is the lift. (See fig. 42.) However, L/D is essentially unchanged. The installation penalty is significantly less in both lift and drag for the lower deflection case. Also for the low-deflection case, drag actually increases with blowing on. The drag increase, which is caused by destruction of the flow over the outboard wing with the spanwise flowing jet, is possibly greater than the drag reduction obtained from improvement of the flow over the aft inboard trap plate. Note that the nozzle height was adjusted with changes in the plate deflection angles to maintain the same ratio to the forward trap plate height of 60 percent. Also, all the data presented in figure 42 are without the jet deflector.

The influence of nozzle height is presented in figure 43. Only small differences in the data are observed for the two test heights. However, it appears the optimal nozzle height may be sensitive to α .

Outboard vortex trap system. The large amount of spanwise flow on the outer panel presented an opportunity to create the trapped vortex phenomenon with less spanwise blowing. Despite much effort, a working vortex trap system with flow reattachment on the TE trap plate was never developed. The large taper ratio of the outboard wing panel is probably the reason why the trapped vortex phenomenon failed to develop. As the local chord of the outboard wing decreases, the cross-sectional area of the channel created by the trap plates decreases, and there is not enough space for the vortex system to remain trapped between the plates. Flow visualization supports this hypothesis and clearly shows that much of the flow between the trap plates was spilling over the aft trap plate as the wing chord decreased.

Figure 44 shows the buildup of the outboard vortex trap system. Even though flow visualization indicated that the trapped vortex phenomenon never developed, a lift increase was obtained with the vortex trap system in place and spanwise blowing. However, the same lift increase was obtained with only spanwise blowing over the wing with the OBLE flap on and TE flaps deflected. The considerable increase in drag with the vortex trap system in place is partly due to replacement of the OBLE flap (which has been shown to produce significant LE suction) with the forward trap plate, which resembles a spoiler deflected into the free-stream flow. Further drag increases can also be attributed to the greater amounts of separated flow on the higher deflected TE flaps ($\delta_{ibf} = 30$).

Numerical Investigation—Unstructured Euler Computer Code Grids

An unstructured grid Euler flow solver was used to model several of the clipped and cranked delta planforms with vortex flaps deployed and TE flaps deflected. A recently developed time-implicit version (ref. 19) of the Euler solver (USM3D) described in reference 20 was used. The solver is a cell-centered, finite-volume, upwind method utilizing flux-difference splitting.

The unstructured grid Euler flow solver was of particular interest because its unique capabilities were ideally suited for analysis of the type of configurations and flow features found in this investigation. Discretization of the flow field with an unstructured grid provided the capability to model the complex geometry of multiple deflected surfaces with relative ease. Solution of the Euler equations instead of the more complicated Navier-Stokes equations required far less resources and, yet, provided the capability to simulate the dominant flow characteristics of LE flow separation and the formation of LE vortices. However, the strength and extent of the LE vortices may not be correctly predicted because of the lack of viscous effects in the Euler equations. Likewise, viscous flow features such as secondary vortices from secondary separations or hinge line separation cannot be predicted by the Euler equations.

The unstructured grids were created with the interactive tetrahedral grid generator (VGRID) developed by Parikh et al. (See ref. 21.) Improvements by Pirzadeh (ref. 22) to incorporate a structured background grid into the advancing-front methodology of VGRID greatly increased the robustness of the computer code. Another unique feature added by Pirzadeh was the capability to directionally cluster points in the grid with user-prescribed point and line sources. As a result of these improvements, high-quality unstructured Euler grids

about the various planforms with multiple deflected surfaces could be routinely produced in a day.

Although many different configurations were analyzed, only results from the planform 68/48 with $\delta_{vf} = 30^\circ$, inboard TE flap deflection angle $\delta_{ibf} = 15^\circ$, and outboard TE flap deflection angle $\delta_{obf} = 15^\circ$ will be presented in this report to demonstrate the utility of the method and to illustrate the problems encountered. Two grids, one fine and one coarse, were created for this configuration. The fine grid was composed of 660482 tetrahedra created from 119459 nodes with 26620 boundary cells. The far field was extended five mean-chord lengths away from the model in all directions. Figure 45 shows the fine grid triangulation on the surface and the plane of symmetry for the planform 68/48 with the previously stated deflections. The coarse grid for this configuration consisted of 404259 tetrahedra, 74150 nodes, and 20742 boundary cells. Typical solutions on the fine grid required 120 megawords of memory and 6 hr of processing time on a Cray Y-MP.

Figure 46 shows the comparison between the computational data from the two grids and the experimental data. Note that a 0.0069 increment has been added to the computed drag as an estimate of the skin friction drag determined from flow over a flat plate. (See ref. 23.) The fine-grid solutions more accurately predict the experimental results. The benefit from further grid refinement was not investigated because of memory limitations of the computer. Between $\alpha = 6^\circ$ and 10° , the agreement between computational and experimental data is reasonably good for all components. Outside of this limited α range, the computational results vary greatly from the experimental data or do not exist at all. Two definite problems with the computational results are the inability to obtain converged solutions above $\alpha = 11^\circ$ on either of the grids and the inability to predict the effect of decreasing α below 6° .

However, close examination of the flow field data provides clear explanations for the discrepancy in the force correlations and indicates that the Euler method (USM3D) is actually providing an excellent prediction of the dominant flow features. Figure 47 shows computed off-body pressure coefficient C_p contours at several fuselage stations. The C_p contours clearly show the presence of a vortex located over the vortex flap and the outboard wing. The formation of a crank vortex is predicted by USM3D, but it merges with the primary vortex farther upstream than shown in the off-body flow visualization.

As seen in the comparison of surface flow field patterns (fig. 48), the location of the reattachment line of the primary vortex is accurately predicted by USM3D all the way to the TE even though the primary and crank vortex combined prematurely in the numerical simulation.

Because the secondary flow region between the wing LE and the secondary separation line is created by viscous effects, its presence is not expected to be predicted by the Euler computer code. The oil-flow lines indicate, both experimentally and numerically, a large amount of spanwise flow on the outboard wing induced by the primary vortex. The combination of this spanwise flow and the segmented TE flap deflections produces an aft-facing step in the surface flow field. In the numerical simulation, artificial dissipation causes the upper surface flow to separate at the geometric discontinuity and form a region in the flow which resembles a separation bubble. Throughout the remainder of this report, this region in the computed flow field will be referred to as an inviscid separation region. (See fig. 48.) Although not shown here, the inviscid separation region increases in size with an increase in α . The interaction between the inviscid separation region and the primary vortex, located directly above it, is theorized to become unstable, and converged solutions cannot be obtained above $\alpha = 11^\circ$.

As seen in figure 49(a), USM3D correctly predicts the footprint of the primary vortex on the main wing (strips 3, 4, and 5) at $\alpha = 10^\circ$. The good correlation in the onset location of the vortex pressure rise further demonstrates the ability of USM3D to predict the reattachment line of the primary vortex. This is an essential attribute of a vortex-dominated flow that must be captured for design purposes.

At strip 1, the increase in suction caused by the primary vortex is predicted by USM3D, but experimentally, its location is shifted inboard because of the secondary flow region. The nearly constant level of suction seen in strips 1 and 2 between the LE of the vortex flap and the primary vortex is not predicted by the Euler computer code because this secondary flow region is a product of viscous effects.

The pressure distributions on the TE flaps correlate reasonably well for the two α 's presented (fig. 49), but USM3D overpredicts the pressure recovery approaching the trailing edge of the flaps. In both the experimental and computational data, the TE flap pressures are virtually independent of α because the oncoming flow has aligned with the flat surface wing prior to reaching the flaps.

At $\alpha = -2^\circ$ (fig. 49(b)), the C_p correlation along all the other strips is very good. The only noticeable difference between the data is on strip 5 where there is a small suction peak not predicted by USM3D. More importantly, the difference between the computational and experimental upper surface C_p distributions cannot possibly account for the large variation in the force data at this α . So, the errors in the predicted forces may be due to pressure differences on the lower surface. No lower

surface pressure data were obtained during the experimental investigation. However, careful examination of the computed lower surface pressure distribution indicated a possible problem. The inviscid expansion around the discontinuous corner of the TE bevel influenced the flow field much farther upstream than anticipated.

To assess the effect of the TE bevel on the predicted flow, the cruise configuration of the planform 68/48 was run at $\alpha = 0^\circ$ with the normal 30° TE bevel and the blunt TE. Expanded views of the two TE models are presented in figure 50(a). The resulting lower surface pressure contours are shown in figure 50(b). For a flat plate at $\alpha = 0^\circ$, C_p should be zero across most of the plate, which is true for the blunt TE model. However, the beveled TE model has an extensive negative C_p region.

Changes in the pressure distribution of the upper surface (fig. 50(c)) were limited to the TE region. The pressure recovery on the upper surface is greater for the beveled TE model, and this may be one reason why the differences between experimental and computational pressures increase near the TE for the deflected TE flap case. (See fig. 49.) Because the effects of the TE bevel on the upper surface appear to be limited to the TE, the flow field results discussed previously are thought to be indicative of the USM3D capability and are not just fortuitous.

The negative pressures on the lower surface integrate into a considerable loss of lift. However, the negative pressures are not physical because the boundary layer will smooth out the surface discontinuity at the TE bevel and eliminate the large expansion. For this reason, the force and moment data of the blunt TE model agree much better with the experimental data of the cruise configuration at $\alpha = 0^\circ$. (See table in fig. 50(b).) Undoubtedly, the TE bevel influences the solution regardless of the flap deflection angles because of the flow alignment effect discussed previously. So, the inviscid modeling of the flow around the TE bevel is possibly the primary cause of the poor force and moment correlation at the low α 's seen in figure 46.

These results are not indicative of a shortcoming in USM3D or unstructured grid methods, but rather in the Euler equations. Other researchers (ref. 24) have shown similar effects when the TE bevel of a flat plate is modeled in an Euler analysis using structured grids. The problem could probably be eliminated by artificially rounding the discontinuity at the TE bevel or by modifying the boundary condition until the force data matched at a chosen α . However, that was not done because the intent of the Euler analysis was to determine the usefulness of USM3D in modeling configurations that have multiple deflected surfaces and are dominated by vortical flow. The results presented clearly demonstrate this

capability and suggest USM3D would be an excellent analysis tool for the design of vortex flaps.

Conclusions

A parametric planform study has been conducted in the Langley 14- by 22-Foot Subsonic Tunnel to evaluate the influence of leading-edge sweep and the outboard wing panel of cranked delta wings on the effectiveness of vortex flaps. The test results were also used to evaluate a vortex flap design methodology for cranked delta planforms and to assess the capability of an unstructured grid Euler computer code to model configurations with leading-edge vortex flaps and trailing-edge flaps. In addition, the baseline planform was used to evaluate novel flow control concepts for future High-Speed Civil Transports. The most significant results are summarized as follows:

1. The vortex flaps designed with Frink's vortex flap design methodology did not perform as desired. At the design condition for every configuration tested, the primary vortex reattachment line was inboard of the vortex flap hinge line instead of along the hinge line as prescribed in the design methodology. The less than optimal designs were the result of the numerical model not accounting for the induced effects on the overall flow field of the crank vortex.
2. The influences of leading-edge sweep and the outboard wing panel on the effectiveness of the vortex flaps are very small across the range of test parameters. However, the vortex flap data show a slight dependency on LE sweep with the data grouped along the planform families at higher angles of attack α . For undetermined reasons the baseline planform 68/48 tends to follow the trends of the family with the constant nondimensional semispan leading-edge break location.
3. Addition of the outboard leading-edge flap greatly improves the aerodynamic performance of the configuration even though hinge line separation occurs. The constant radius of the outboard leading-edge flap accelerates the flow around the forward-facing flap surface, which produces a substantial amount of thrust.
4. Except at the highest test α 's, a straight LE inverse-tapered vortex flap nearly duplicates the results of the numerically designed vortex flap.
5. Neither the TE flap end plates nor the outboard LE snags produces any discernible effect on the force and moment data.
6. The vortex trap phenomenon is successfully produced over the aft inboard portion of the wing. However, very high blowing rates in the spanwise direction are required to overcome the installation penalties. Some of the potential thrust of the spanwise blowing jet is recovered by adding a flow deflector to turn the spanwise jet flow downstream.
7. The vortex trap system on the outboard wing panel is ineffective. The results indicate that the tapered outboard wing panel limited the development of the trapped vortex system.
8. The unstructured grid Euler computer code, USM3D, provides an excellent prediction of dominant upper surface flow features on cranked delta wing planforms with vortex and trailing-edge flaps as indicated by the outstanding correlation in the pressure data and surface flow visualization.
9. As discussed in the previous section, the force and moments predicted by USM3D do not agree well with the experimental data across much of the α range investigated, but the reasons for the differences are well understood. At low α 's, the predicted flow overexpands around the discontinuous corner of the TE bevel, which results in poor force and moment correlation. Above $\alpha = 11^\circ$, computational results could not be obtained. The interaction between the inviscid flow separation region, which is produced by spanwise flow over the undeflected portion of the TE, and the primary vortex probably drives the solution unstable.

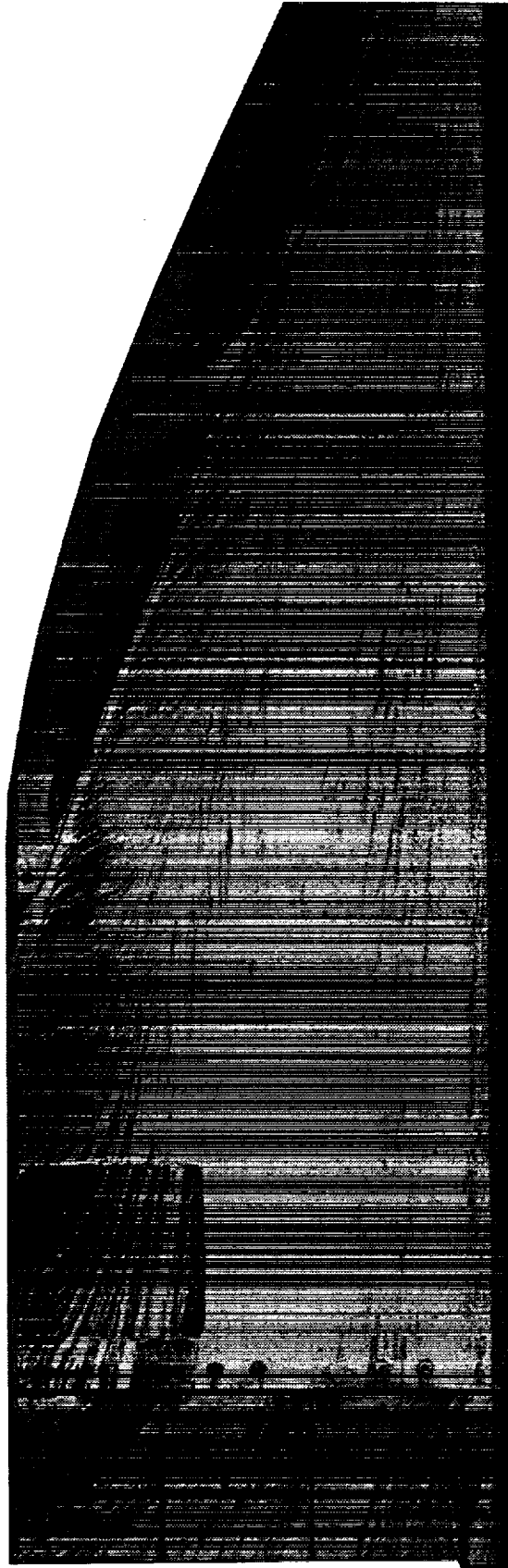
NASA Langley Research Center
Hampton, VA 23681-0001
September 15, 1995

Appendix

Surface Oil Flow Visualization and Surface Pressure Distributions

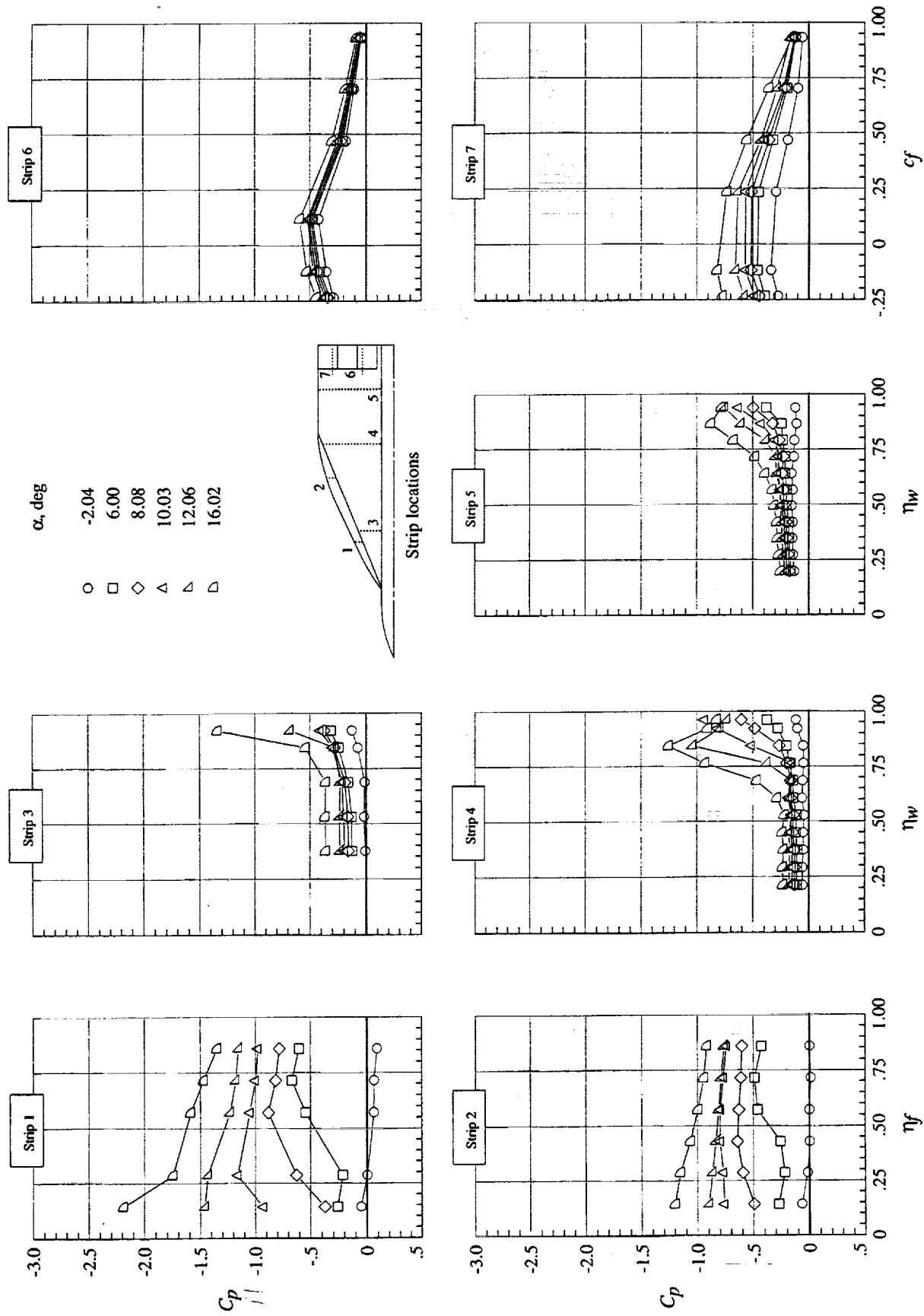
Figures A1–A19 present some of the surface flow visualization and pressure data obtained during the wind tunnel investigation. The surface flow visualization was

obtained by coating the surface of the model with a mixture of motor oil and fluorescent dye. Ultraviolet strobe lights were used to stimulate the fluorescence. For the conditions tested, 40W motor oil produced the best results. Surface oil flow visualization data are presented for each of the test planforms (table V), but only at $\alpha = 10^\circ$. Similarly, surface pressure data for each planform are included for selected α 's. Refer to figure 12 for pressure port locations.



(a) Upper surface flow visualization at $\alpha = 10^\circ$.

Figure A1. Planform 68; $q_\infty = 70$ psf; $\delta_{vf} = 30^\circ$; and $\delta_{pbf} = 15^\circ$.



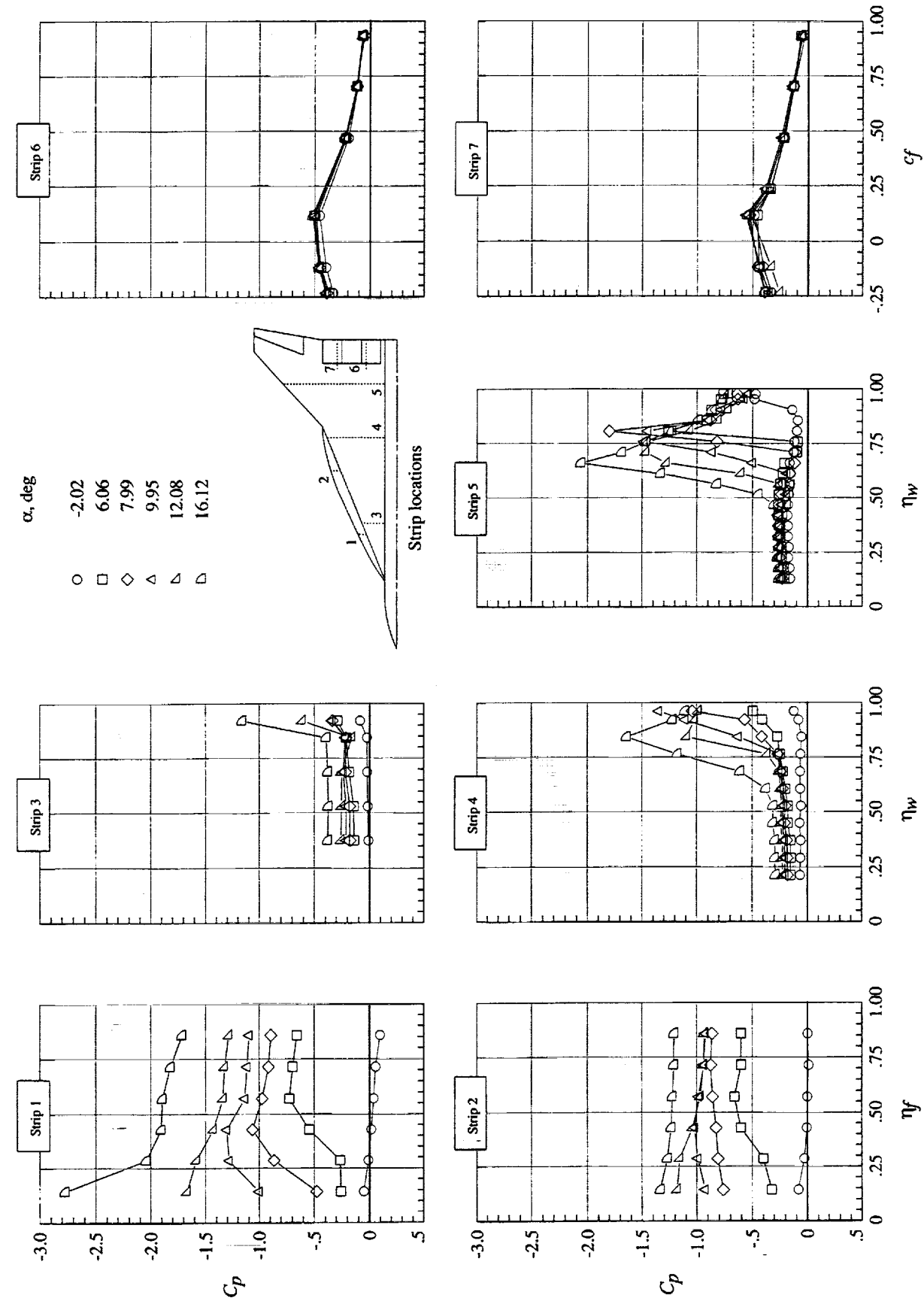
(b) Pressure distributions at various α 's.

Figure A1. Concluded.



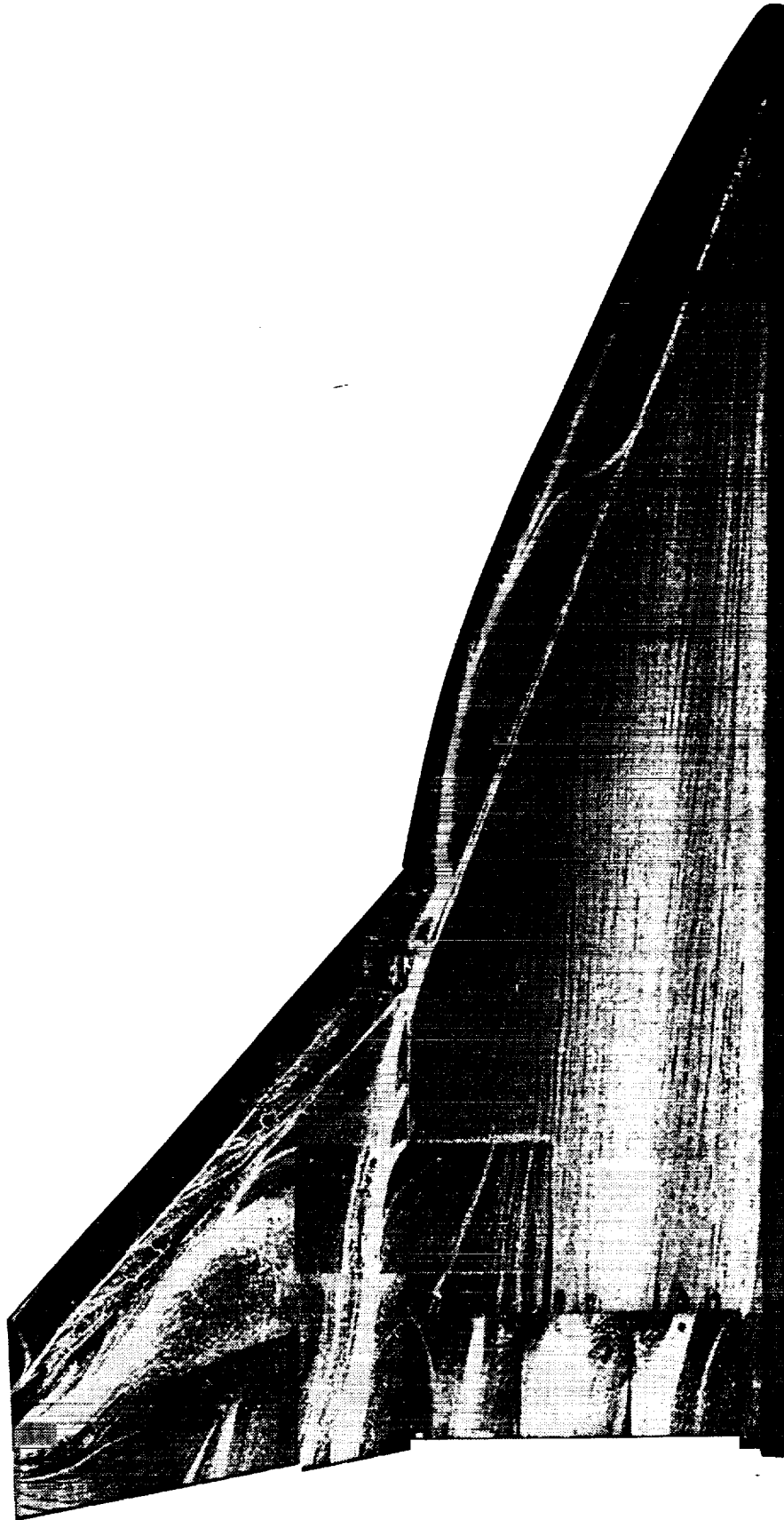
(a) Upper surface flow visualization at $\alpha = 10^\circ$.

Figure A2. Planform 68/48; $q_\infty = 70$ psf; $\delta_{vf} = 30^\circ$; $\delta_{hbf} = 15^\circ$; $\delta_{obf} = 15^\circ$; and OBLE flaps off.



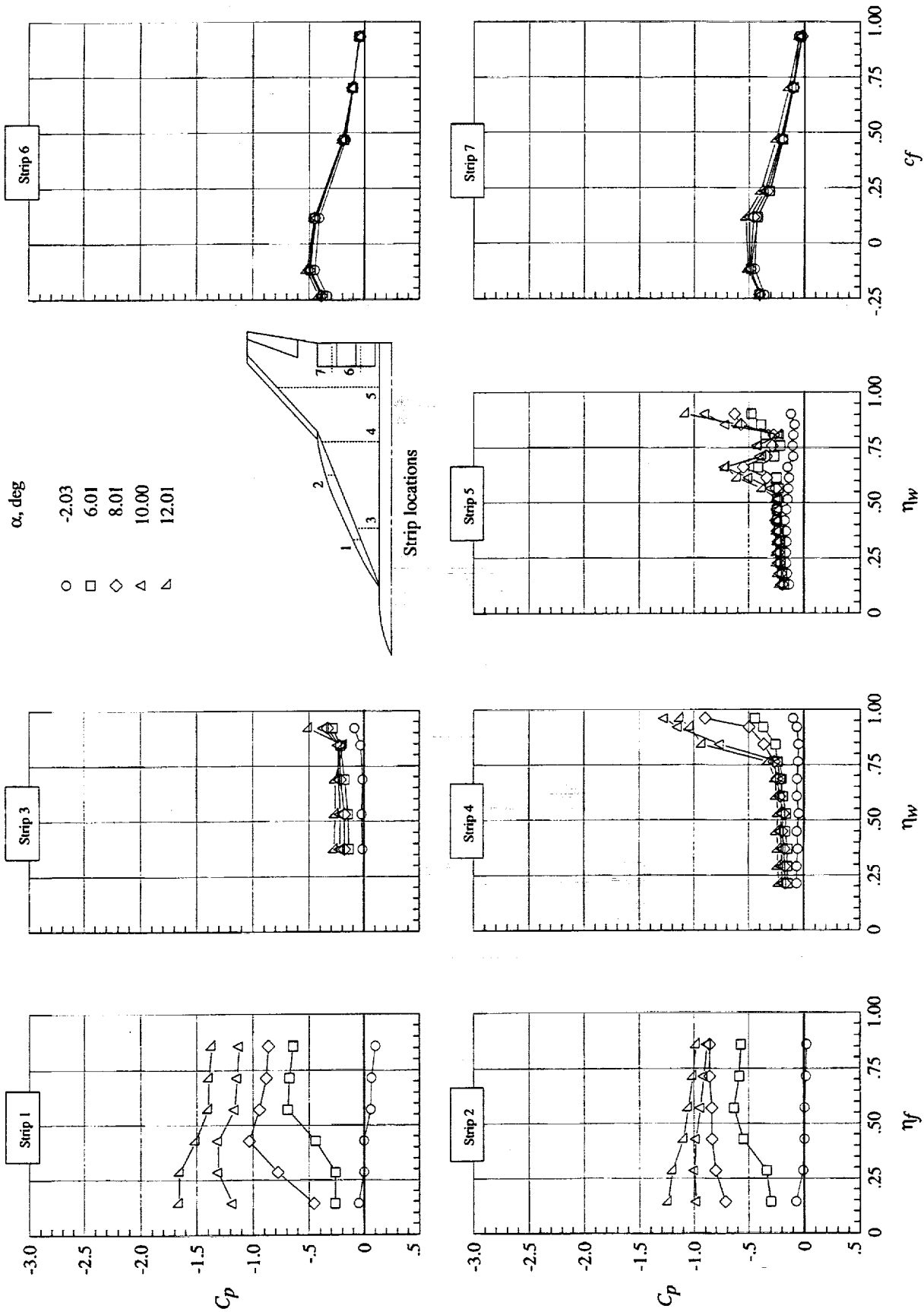
(b) Pressure distributions at various α 's.

Figure A2. Concluded.



(a) Upper surface flow visualization at $\alpha = 10^\circ$.

Figure A3. Planform 68/48; $q_\infty = 70$ psf; $\delta_{vf} = 30^\circ$; $\delta_{hf} = 15^\circ$; $\delta_{obf} = 15^\circ$; and OBLE flaps on.



(b) Pressure distributions at various α 's.

Figure A.3. Concluded.

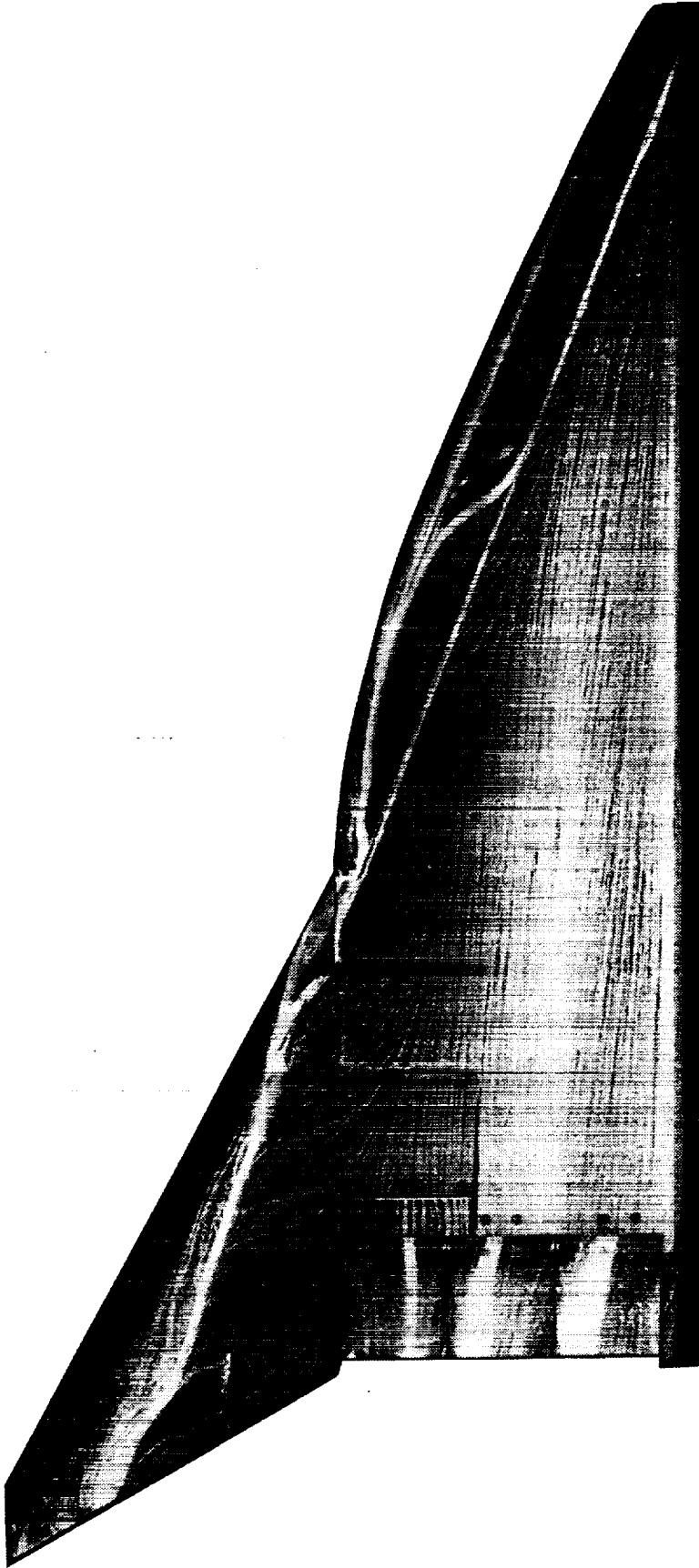


Figure A4. Planform 68/61 upper surface flow visualization. $q_\infty = 70$ psf; $\alpha = 10^\circ$; $\delta_{vf} = 30^\circ$; $\delta_{jpf} = 15^\circ$; $\delta_{obf} = 15^\circ$; and OBLE flaps off.

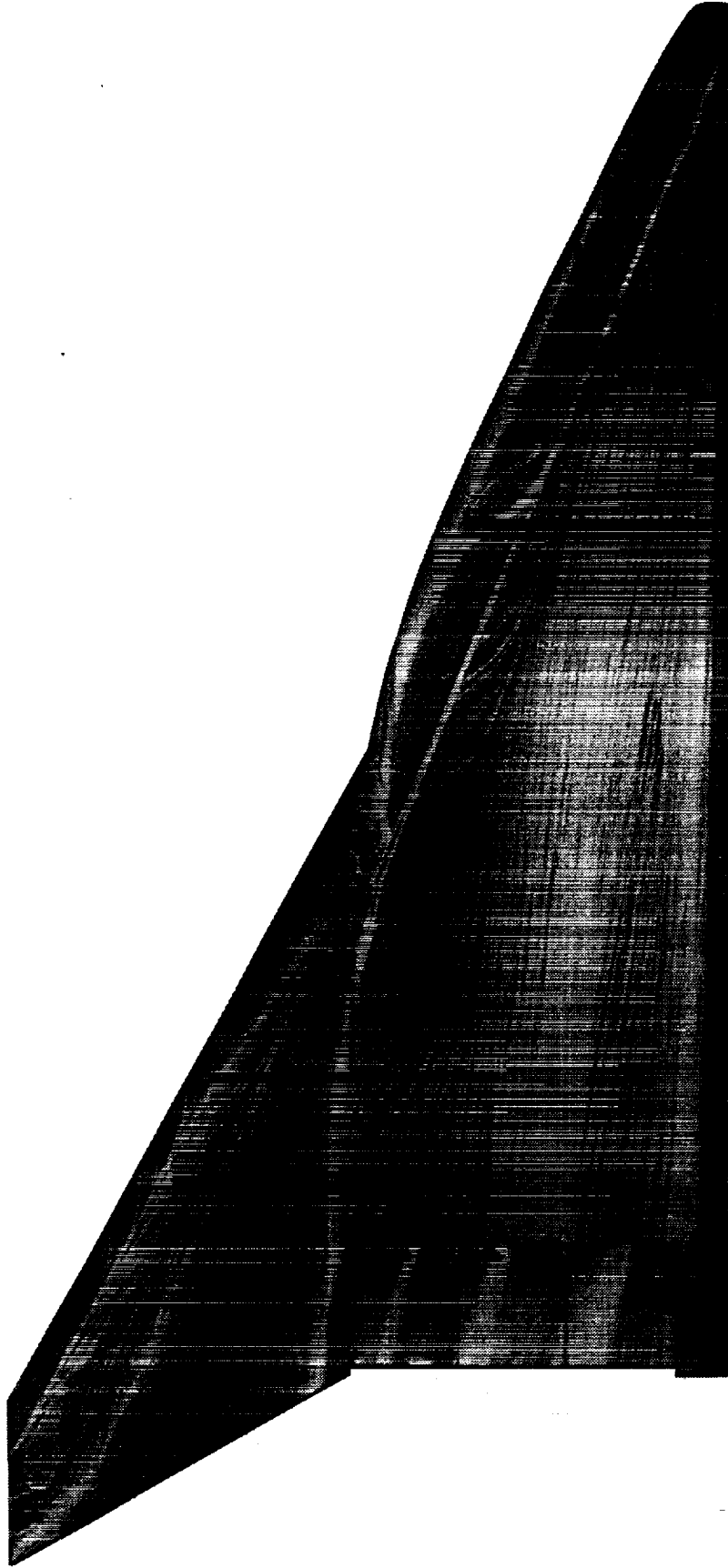


Figure A5. Planform 68/61 upper surface flow visualization. $q_\infty = 70$ psf; $\alpha = 10^\circ$; $\delta_{vf} = 30^\circ$; $\delta_{bf} = 15^\circ$; $\delta_{obf} = 15^\circ$; and OBLE flaps on.

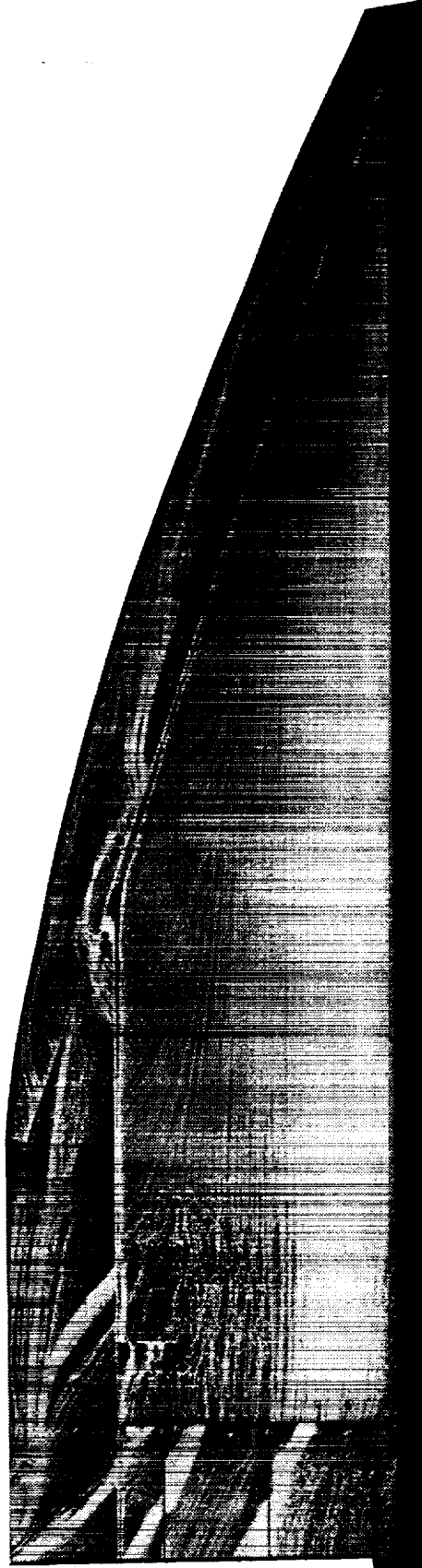


Figure A6. Planform AR 71 upper surface flow visualization. $q_\infty = 70$ psf; $\alpha = 10^\circ$; $\delta_{vt} = 30^\circ$; and $\delta_{ipf} = 15^\circ$.

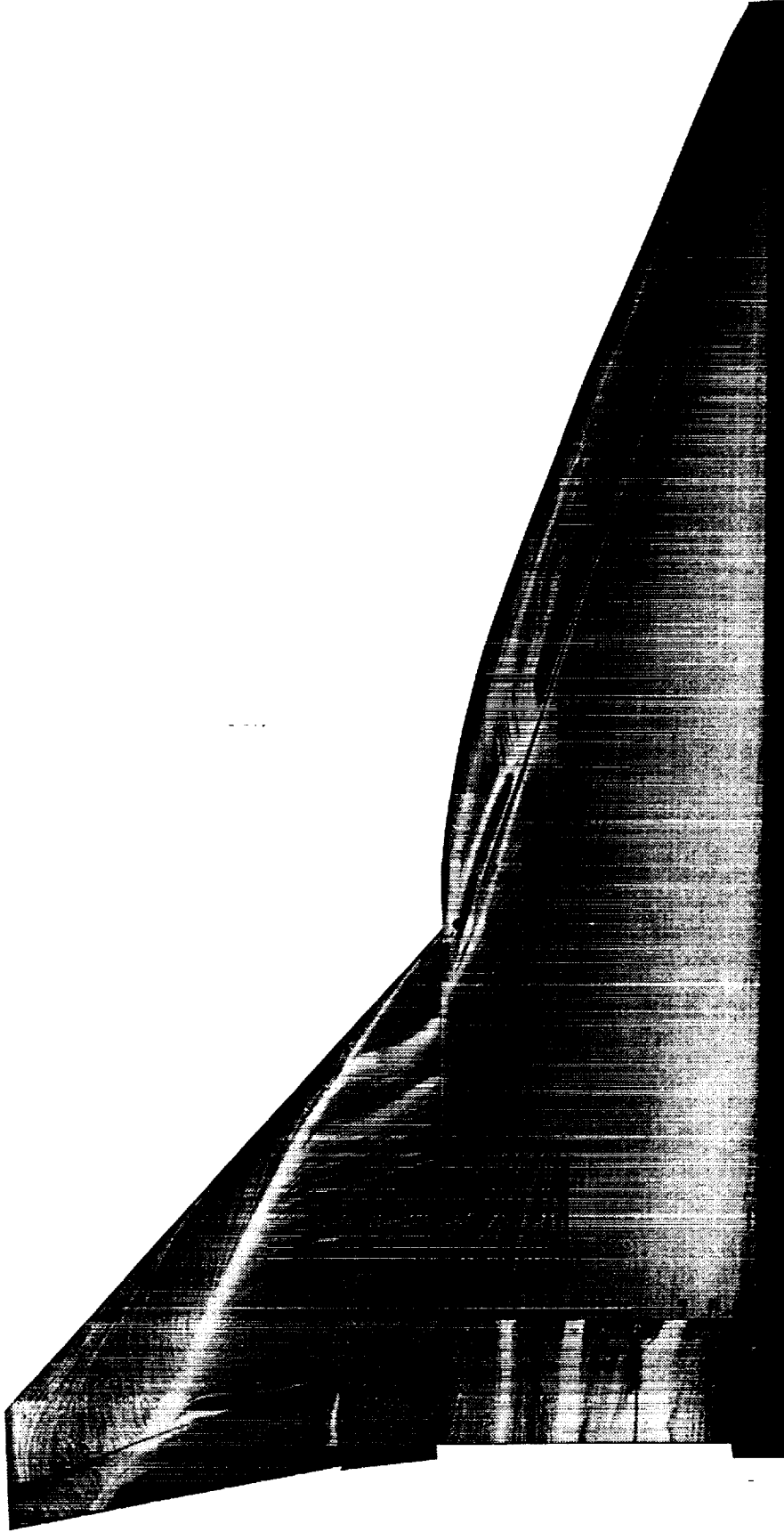


Figure A7. Planform AR 71/48 upper surface flow visualization. $q_\infty = 70$ psf; $\alpha = 10^\circ$; $\delta_{vf} = 30^\circ$; $\delta_{ibf} = 15^\circ$; $\delta_{obf} = 15^\circ$; and OBLE flaps off.

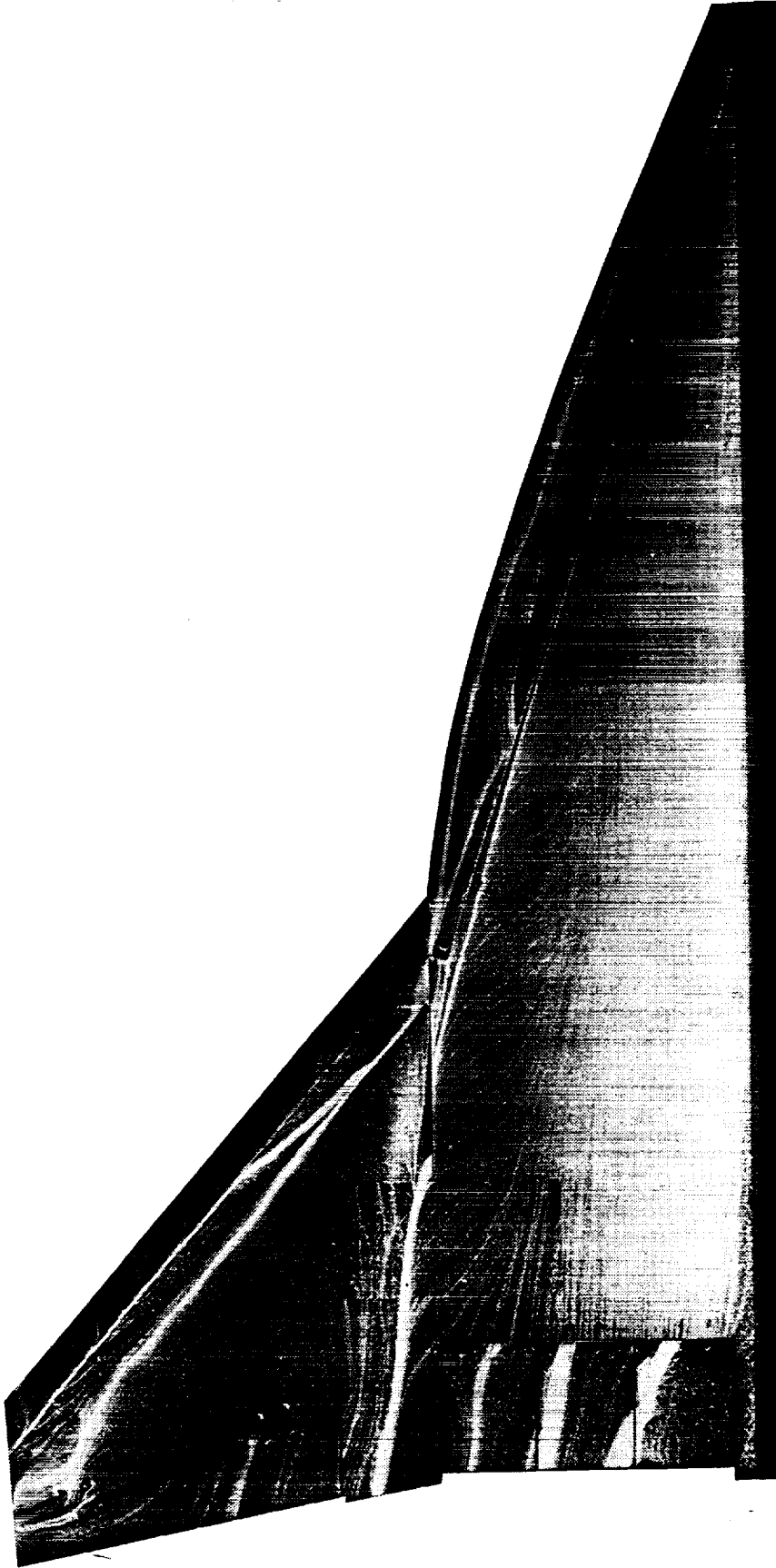


Figure A8. Planform AR 71/48 upper surface flow visualization. $q_\infty = 70$ psf; $\alpha = 10^\circ$; $\delta_{yf} = 30^\circ$; $\delta_{tbf} = 15^\circ$; $\delta_{obf} = 15^\circ$; and OBLE flaps on.

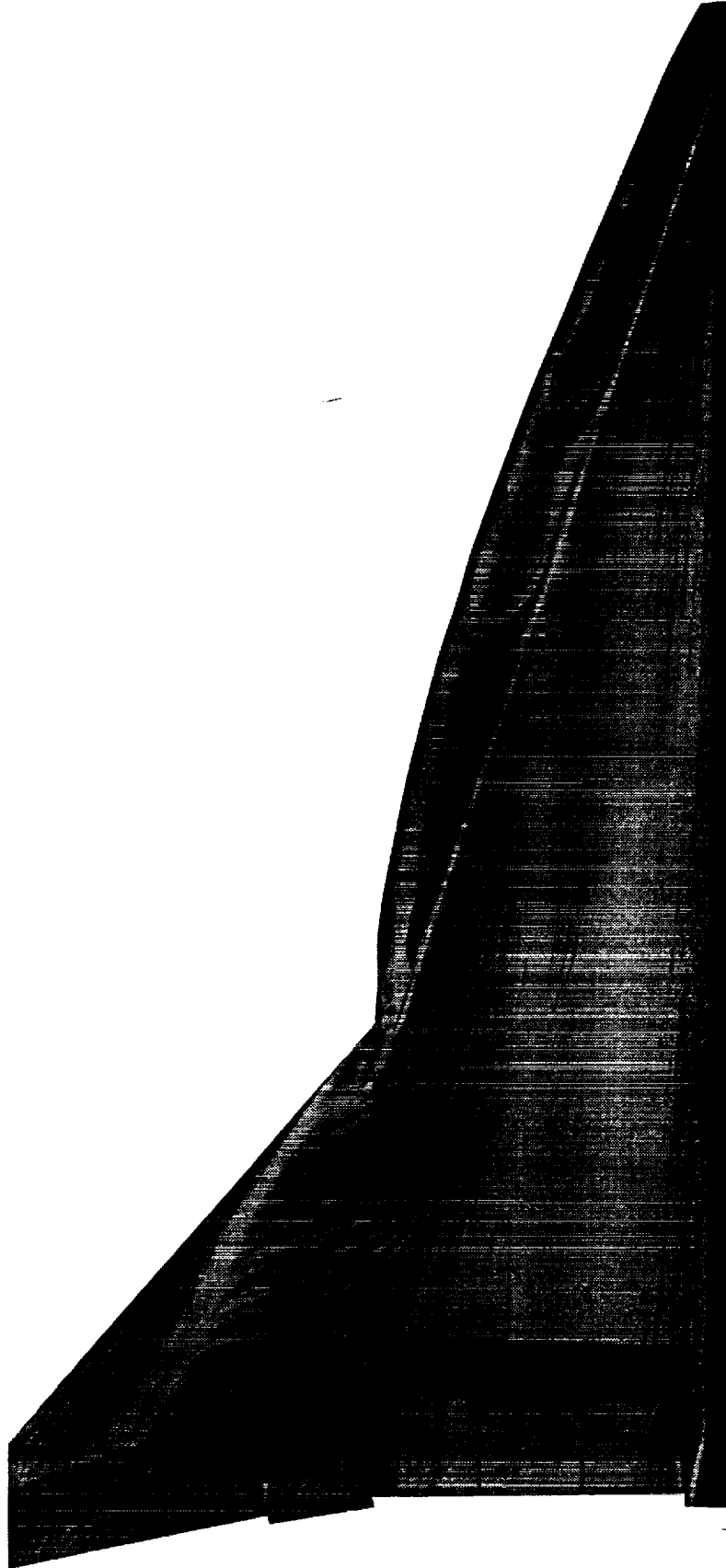


Figure A9. Planform CB 71/48 upper surface flow visualization. $q_{\infty} = 70$ psf; $\alpha = 10^\circ$; $\delta_{vf} = 30^\circ$; $\delta_{ibf} = 15^\circ$; $\delta_{obf} = 15^\circ$; and OBLE flaps off.

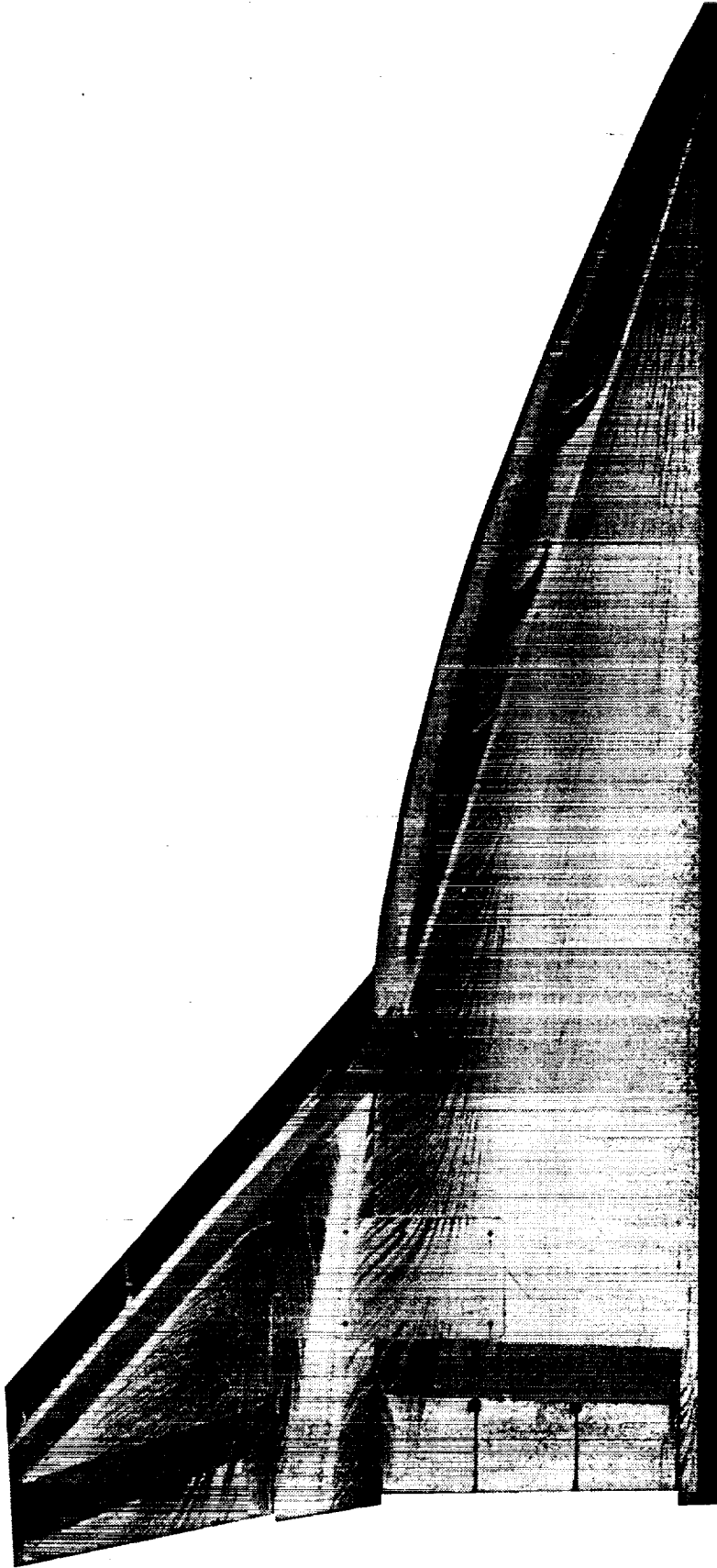


Figure A10. Planform CB 71/48 upper surface flow visualization. $q_{\infty} = 70$ psf; $\alpha = 10^\circ$; $\delta_{vf} = 30^\circ$; $\delta_{ibf} = 15^\circ$; $\delta_{obf} = 15^\circ$; and OBLE flaps on.

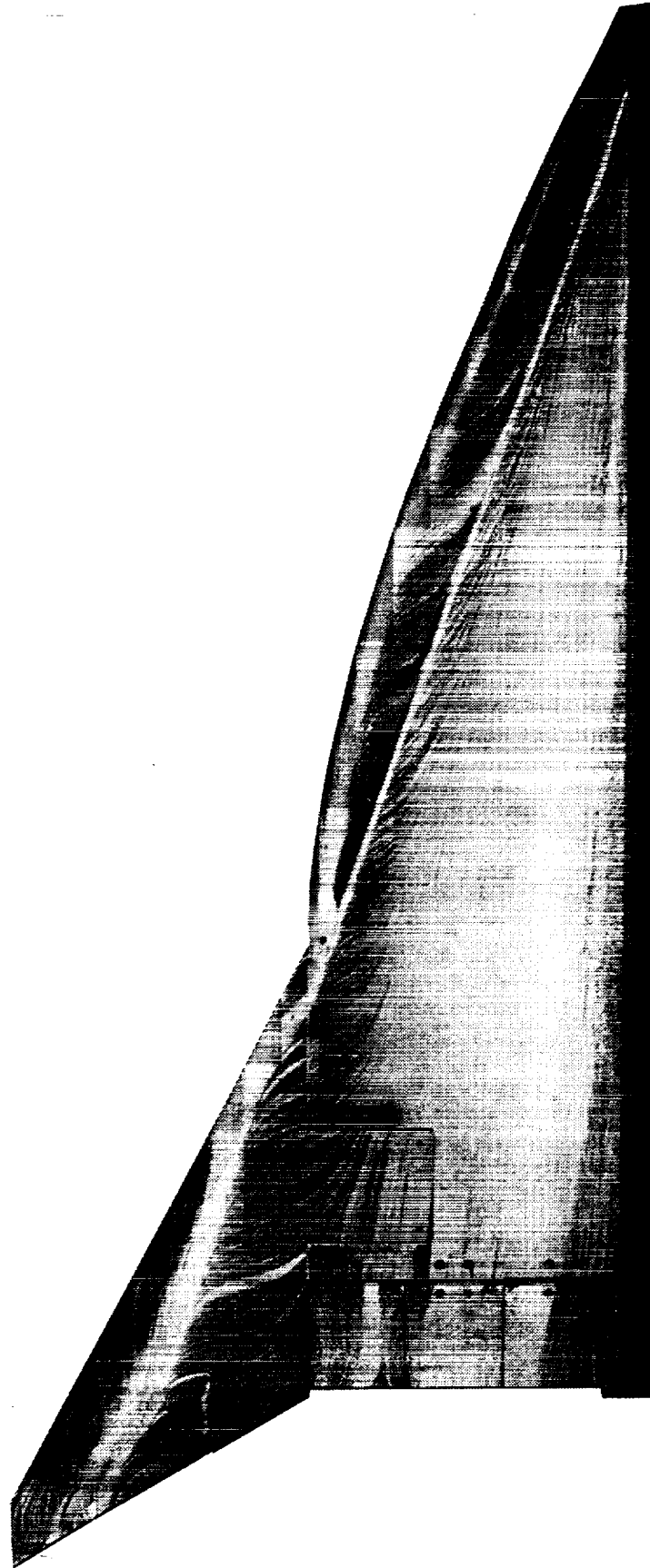


Figure A11. Planform CB 71/61 upper surface flow visualization. $q_{\infty} = 70$ psf; $\alpha = 10^\circ$; $\delta_{vf} = 30^\circ$; $\delta_{ibf} = 15^\circ$; $\delta_{obf} = 15^\circ$; and OBLE flaps off.

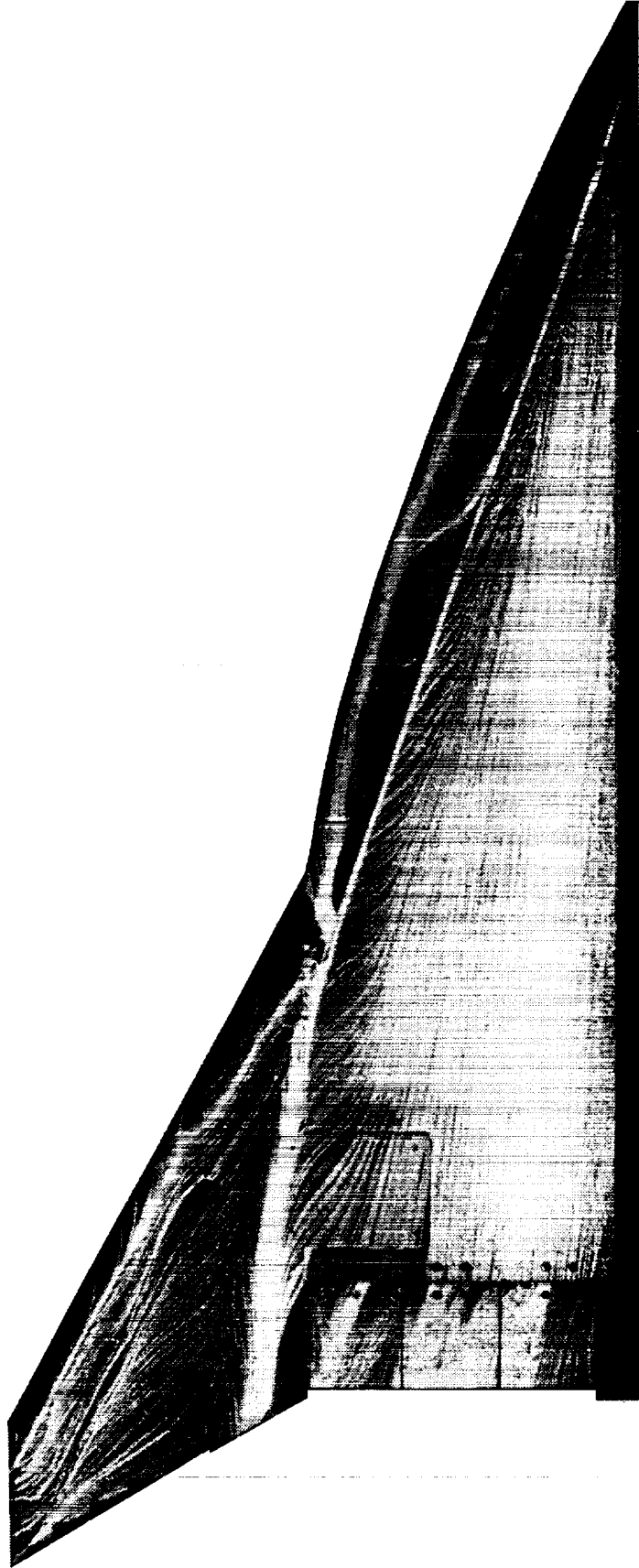
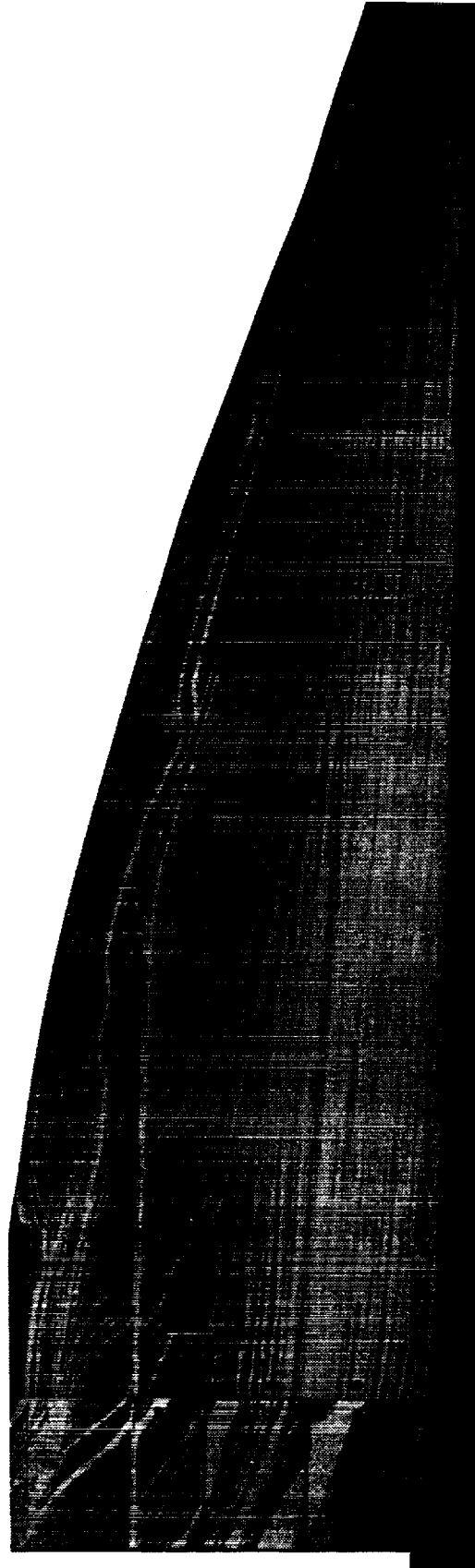
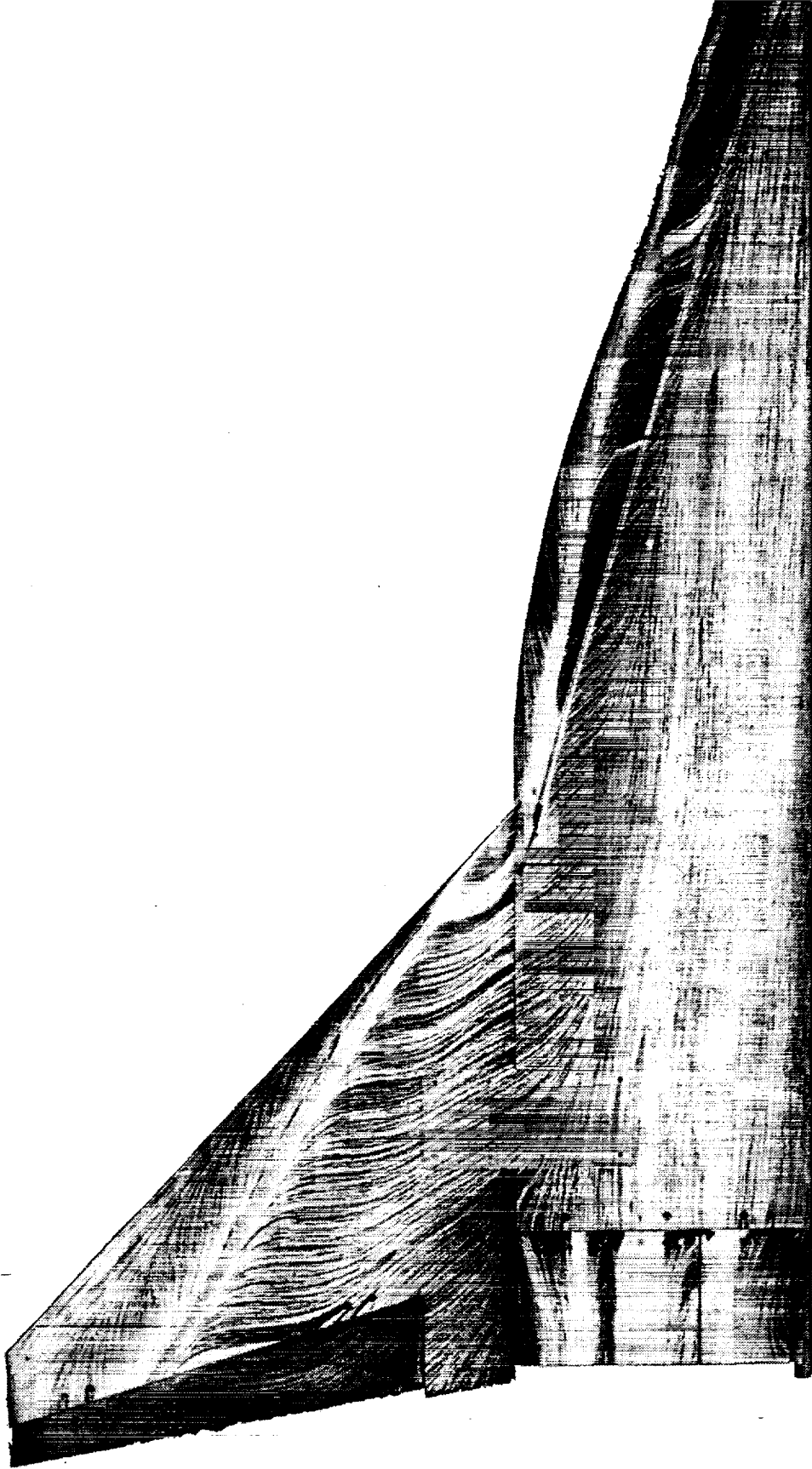


Figure A12. Planform CB 71/61 upper surface flow visualization. $q_\infty = 70$ psf; $\alpha = 10^\circ$; $\delta_{bf} = 30^\circ$; $\delta_{bf} = 15^\circ$; $\delta_{obf} = 15^\circ$; and OBLE flaps on.



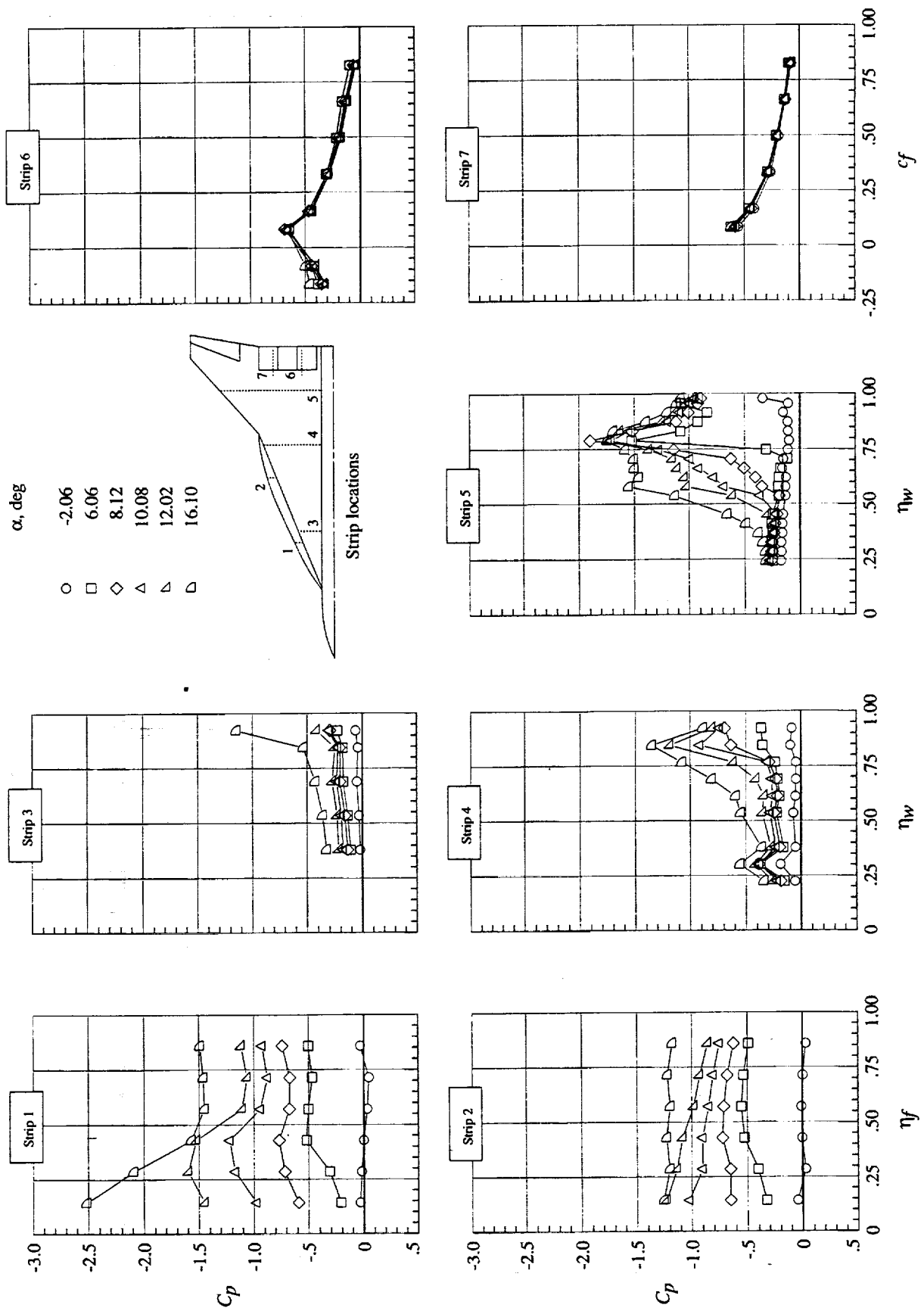
(a) Upper surface flow visualization at $\alpha = 10^\circ$.

Figure A13. Planform AR 74 flow visualization and pressure distributions. $q_\infty = 70$ psf; $\delta_{vf} = 30^\circ$; $\delta_{hf} = 15^\circ$; and OBLE flaps off.



(a) Upper surface flow visualization at $\alpha = 10^\circ$.

Figure A14. Planform AR 74/48 flow visualization and pressure distributions. $q_\infty = 70$ psf; $\delta_{vf} = 30^\circ$; $\delta_{bf} = 15^\circ$; $\delta_{obf} = 15^\circ$; and OBLE flaps off.



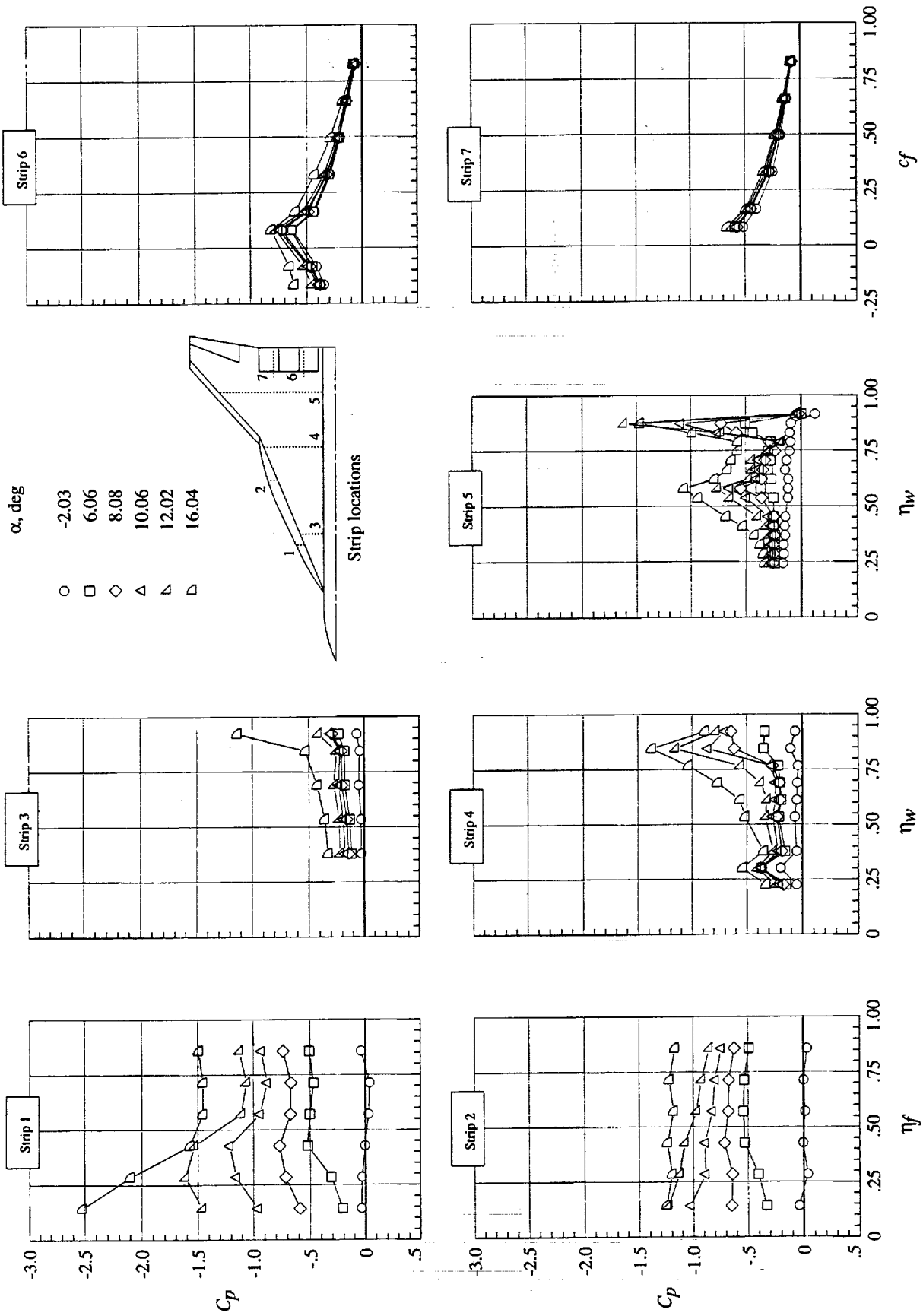
(b) Pressure distributions at various α 's.

Figure A14. Concluded.



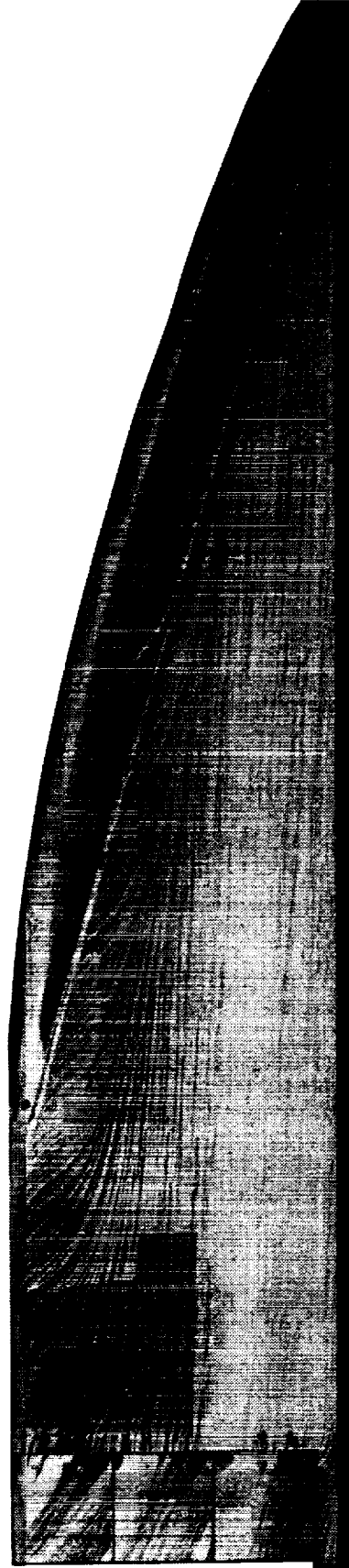
(a) Upper surface flow visualization at $\alpha = 10^\circ$.

Figure A15. Planform AR 74/48 flow visualization and pressure distributions. $q_\infty = 70$ psf; $\delta_{vf} = 30^\circ$; $\delta_{bf} = 15^\circ$; $\delta_{obf} = 15^\circ$; and OBLE flaps on.



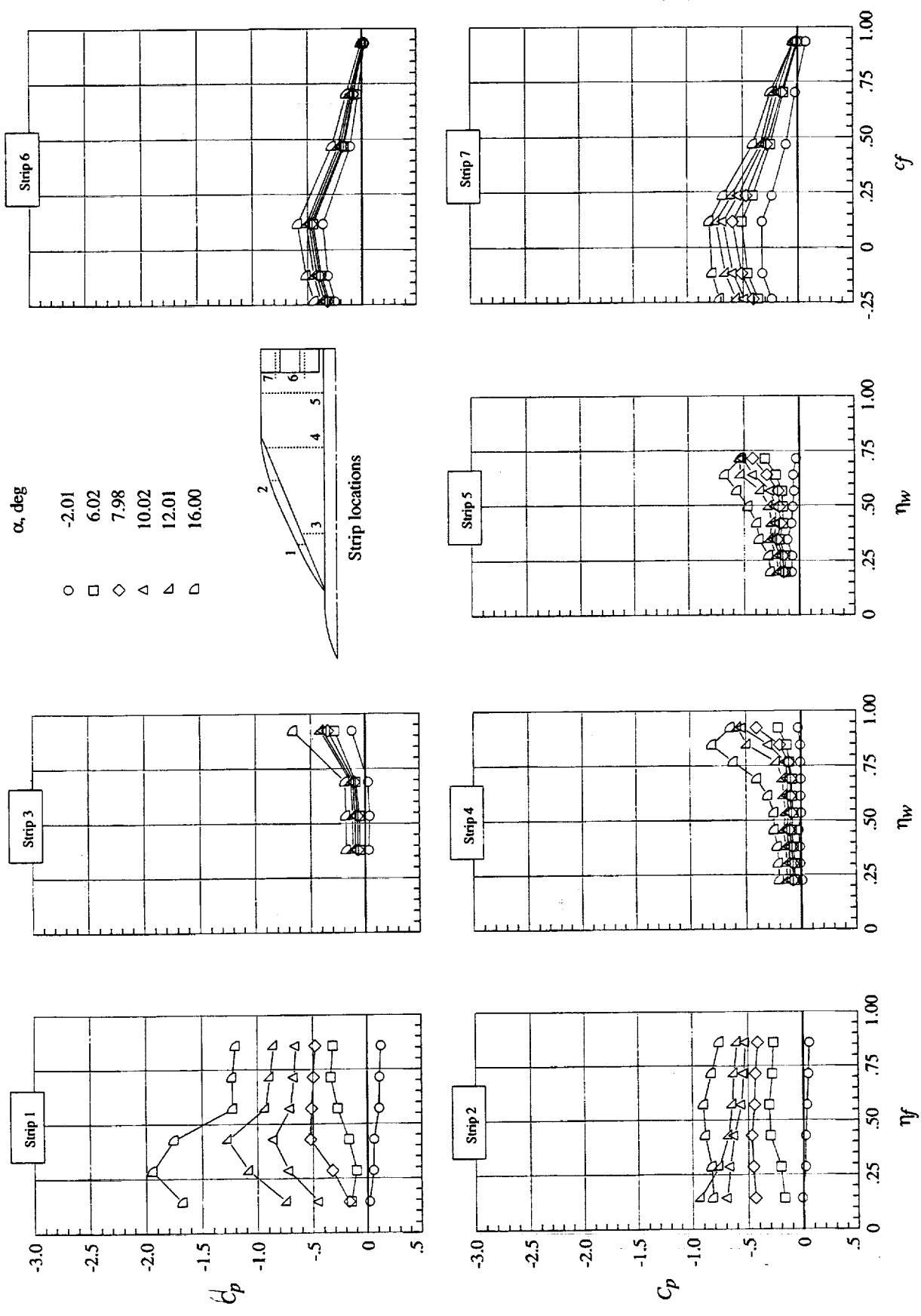
(b) Pressure distributions at various α 's.

Figure A15. Concluded.



(a) Upper surface flow visualization at $\alpha = 10^\circ$.

Figure A16. Planform CB 74 flow visualization and pressure distributions. $q_\infty = 70$ psf; $\delta_{vf} = 30^\circ$; and $\delta_{ibf} = 15^\circ$.



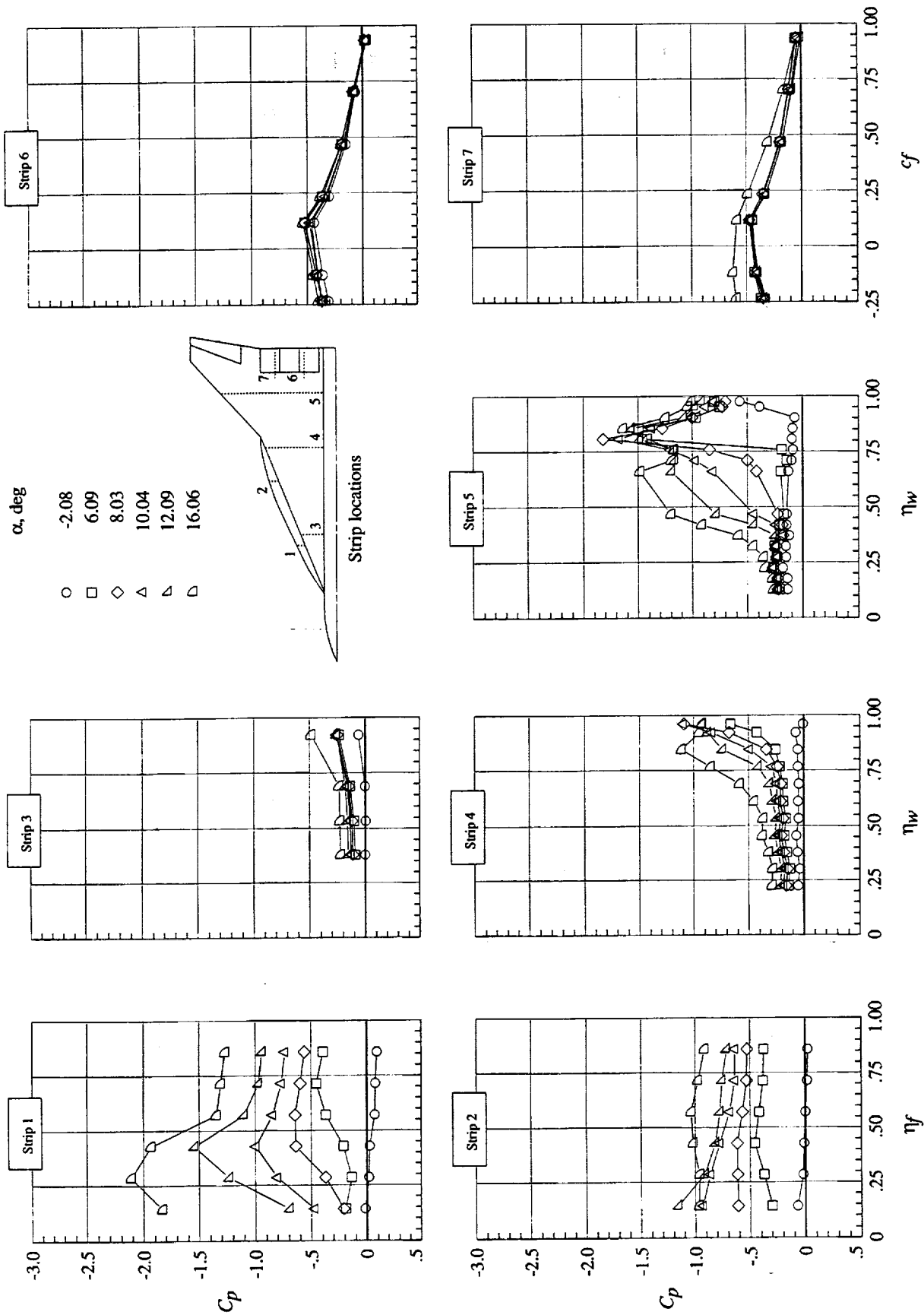
(b) Pressure distributions at various α 's.

Figure A16. Concluded.



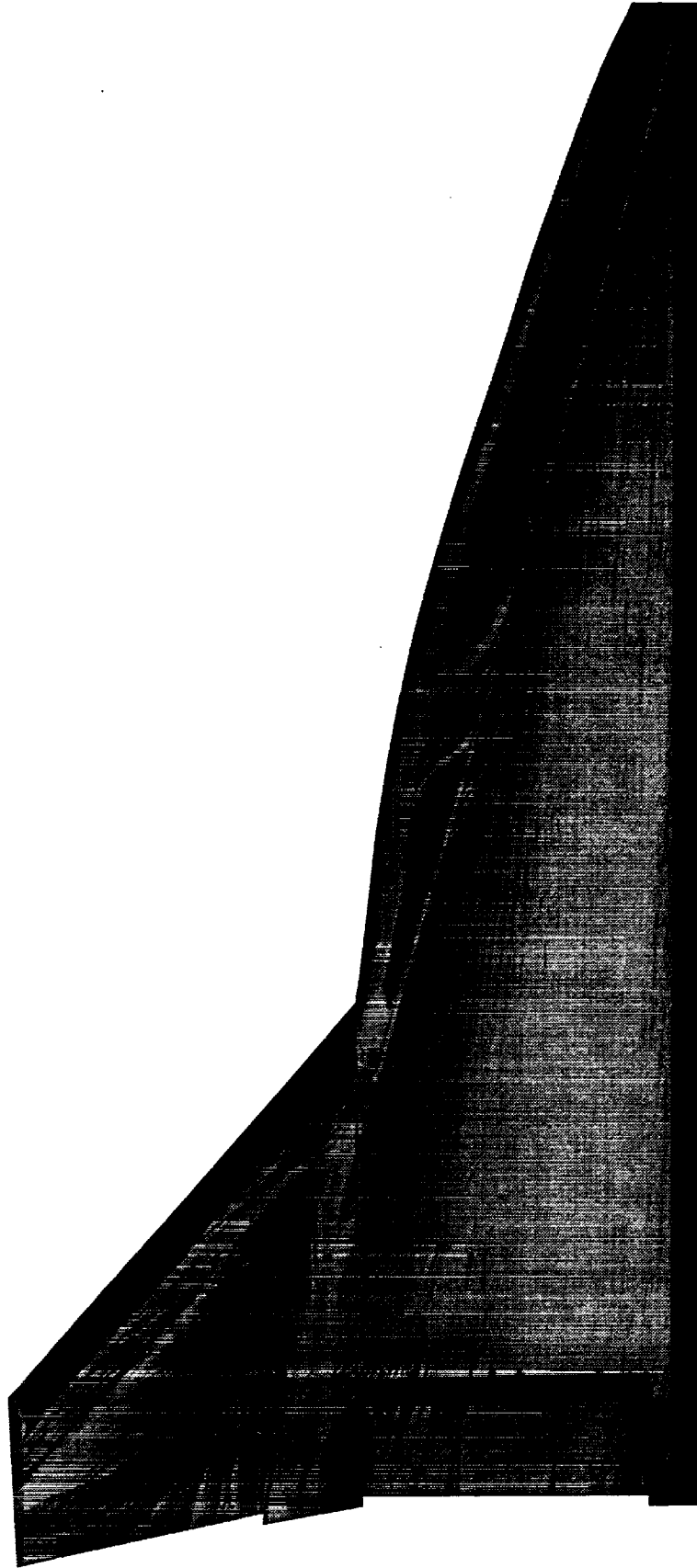
(a) Upper surface flow visualization at $\alpha = 10^\circ$.

Figure A17. Planform CB 74/48 flow visualization and pressure distributions. $q_\infty = 70$ psf; $\delta_{vt} = 30^\circ$; $\delta_{ipf} = 15^\circ$; $\delta_{obf} = 15^\circ$; and OBLE flaps off.



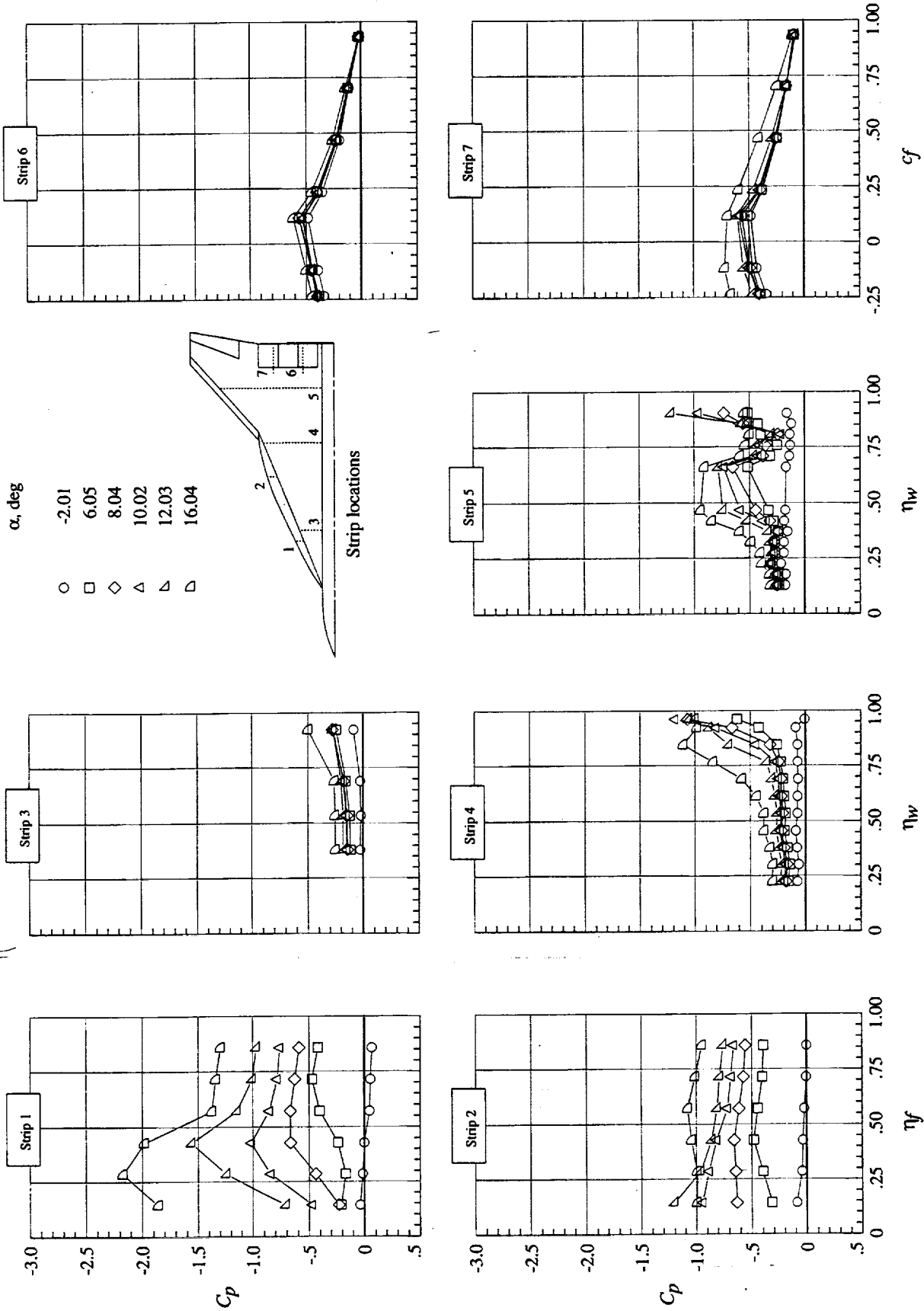
(b) Pressure distributions at various α 's.

Figure A17. Concluded.



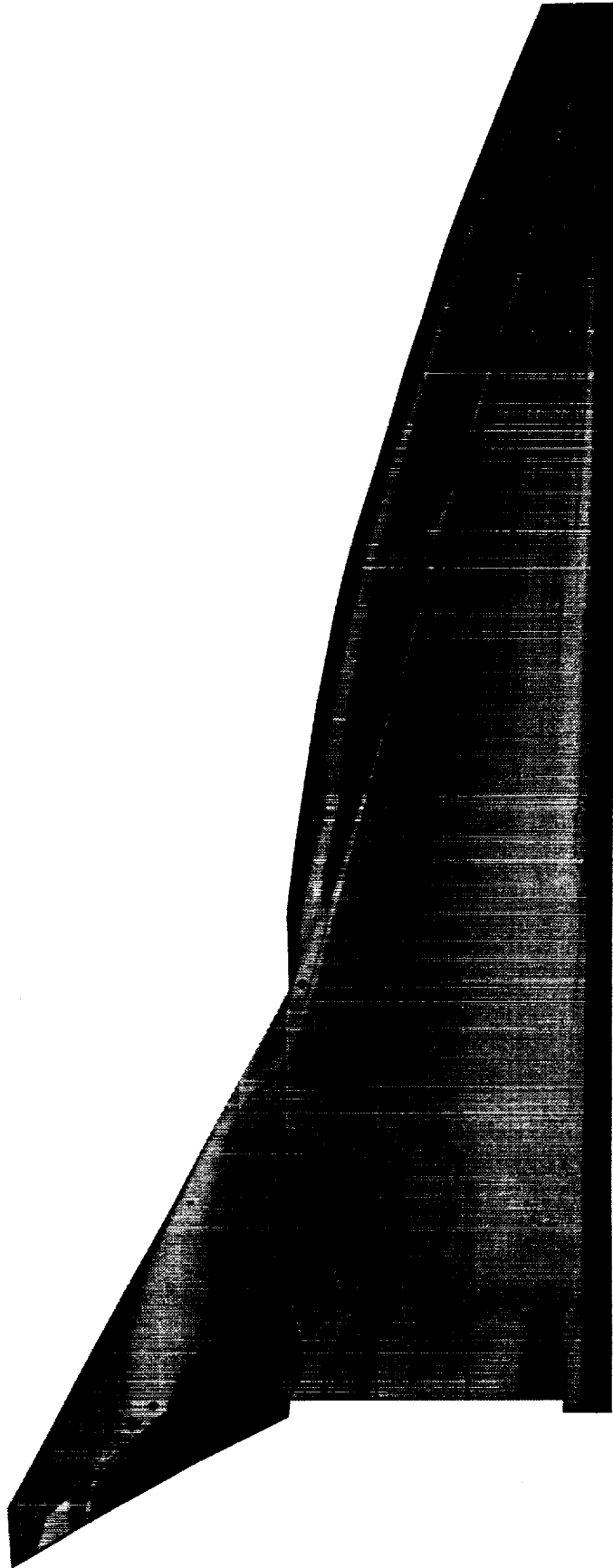
(a) Upper surface flow visualization at $\alpha = 10^\circ$.

Figure A.18. Planform CB 74/48 flow visualization and pressure distributions. $q_\infty = 70$ psf; $\delta_{vf} = 30^\circ$; $\delta_{tbf} = 15^\circ$; $\delta_{obf} = 15^\circ$; and OBLE flaps on.



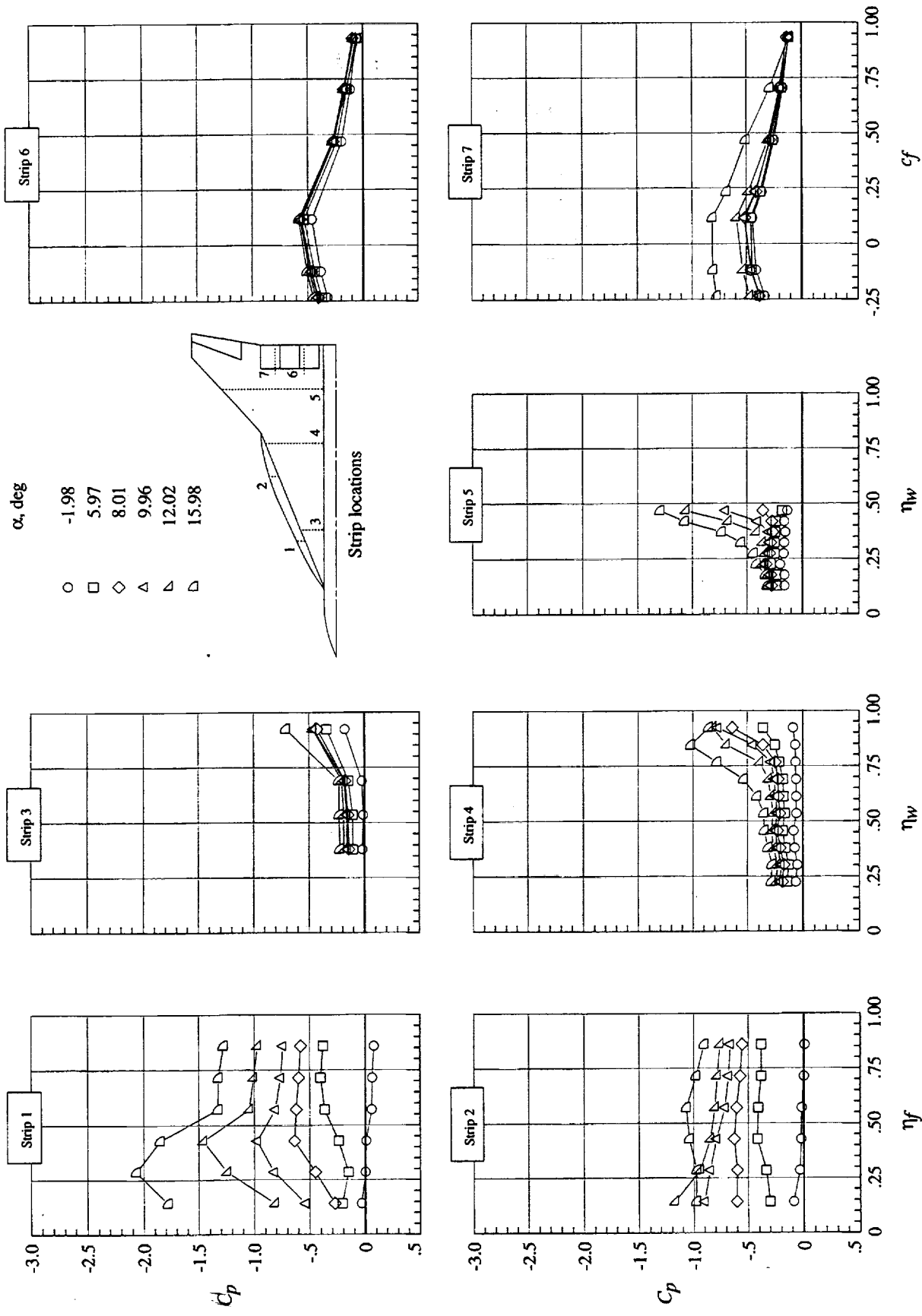
(b) Pressure distributions at various α 's.

Figure A18. Concluded.



(a) Upper surface flow visualization at $\alpha = 12^\circ$.

Figure A19. Planform CB 74/61 flow visualization and pressure distributions. $q_\infty = 70$ psf; $\delta_{vf} = 30^\circ$; $\delta_{ibf} = 15^\circ$; $\delta_{obf} = 15^\circ$; and OBLE flaps off.



(b) Pressure distributions at various α 's.

Figure A19. Concluded.

References

1. Noise Standards: Aircraft Type and Airworthiness Certification. FAA, Code of Federal Regulations, Part 36, Title 14 (Parts 1 to 59), 1993, pp. 700–772.
2. Glaab, Louis J.; Riley, Donald R.; Brandon, Jay M.; Person, Lee H., Jr.; and Glaab, Patricia C.: *Piloted Simulation Study of the Effect of High-Lift Aerodynamics on the Takeoff Noise of a Representative High-Speed Civil Transport*. NASA/TP-1999-209696, 1999.
3. Frink, Neal T.; Huffman, Jarrett K.; and Johnson, Thomas D., Jr.: *Vortex Flap Flow Reattachment Line and Subsonic Longitudinal Aerodynamic Data on 50° to 74° Delta Wings on Common Fuselage*. NASA TM-84618, 1983.
4. Rao, Dhanvada M.: *Leading Edge Vortex-Flap Experiments on a 74 Deg. Delta Wing*. NASA CR-159161, 1979.
5. Rao, Dhanvada M.: Leading-Edge 'Vortex Flaps' for Enhanced Subsonic Aerodynamics of Slender Wings. *ICAS Proceedings 1980—12th Congress of the International Council of the Aeronautical Sciences (ICAS)*, J. Singer and R. Staufenbiel, eds., 1980, pp. 554–562.
6. Marchman, J. F., III: Effectiveness of Leading-Edge Vortex Flaps on 60 and 75 Degree Delta Wings. *J. Aircr.*, vol. 18, no. 4, Apr. 1981, pp. 280–286.
7. Campbell, B. A.; Kemmerly, G. T.; Kjerstad, K. J.; and Lessard, V. R.: *Subsonic Investigation of Leading-Edge Flaps Designed for Vortex- and Attached-Flow on a High-Speed Civil Transport Configuration*. NASA/TM-1999-209701, 1999.
8. Frink, Neal T.: *Concept for Designing Vortex Flap Geometries*. NASA TP-2233, 1983.
9. Rao, Dhanvada M.; and Johnson, Thomas D., Jr.: *Subsonic Pitch-up Alleviation on a 74 Deg. Delta Wing*. NASA CR-165749, 1981.
10. Erickson, Gary E.; and Campbell, James F.: *Flow Visualization of Vortices Locked by Spanwise Blowing Over Wings Featuring a Unique Leading- and Trailing-Edge Flap System*. NASA TM X-72788, 1975.
11. Erickson, G. E.; and Campbell, J. F.: *Augmentation of Maneuver Performance by Spanwise Blowing*. TM X-73998, 1977.
12. Westesson, R. A.; and Clareus, U.: *Turbulent Lift. Comments on Some Preliminary Wind Tunnel Tests—Characteristics of Vortex on Wing Surface From Tangential Blowing on Upper Surface*. NASA-TT-F-15743 TP-74-51, 1974.
13. Lamar, John E.; and Herbert, Henry E.: *Production Version of the Extended NASA/Langley Vortex Lattice FORTRAN Computer Program, Volume I—User's Guide*. NASA TM-83303, 1982.
14. Polhamus, Edward C.: *A Concept of the Vortex Lift of Sharp-Edge Delta Wings Based on a Leading-Edge-Suction Analogy*. NASA TN D-3767, 1966.
15. Lan, C. Edward; and Chang, Jen-Fu: *Calculation of Vortex Lift Effect for Cambered Wings by the Suction Analogy*. NASA CR-3449, 1981.
16. Gentry, Garl L., Jr.; Quinto, P. Frank; Gatlin, Gregory M.; and Applin, Zachary T.: *The Langley 14- by 22-Foot Subsonic Tunnel: Description, Flow Characteristics, and Guide for Users*. NASA TP-3008, 1990.
17. Henderson, William P.: *Studies of Various Factors Affecting Drag Due to Lift at Subsonic Speeds*. NASA TN D-3584, 1966.
18. Scott, Samuel J.; Nicks, Oran W.; and Imbrie, P. K.: *Effects of Leading-Edge Devices on the Low-Speed Aerodynamic Characteristics of a Highly-Swept Arrow-Wing*. NASA CR-172531, 1985.
19. Frink, N. T.: Recent Progress Toward a Three-Dimensional Unstructured Navier-Stokes Flow Solver. AIAA-94-0061, Jan. 1994.
20. Frink, Neal T.; Parikh, Paresh; and Pirzadeh, Shahyar: A Fast Upwind Solver for the Euler Equations on Three-Dimensional Unstructured Meshes. AIAA-91-0102, Jan. 1991.
21. Parikh, Paresh; Pirzadeh, Shahyar; and Lohner, Rainald: *A Package for 3-D Unstructured Grid Generation, Finite-Element Flow Solution and Flow Field Visualization*. NASA CR-182090, 1990.
22. Pirzadeh, Shahyar: Structured Background Grids for Generation of Unstructured Grids by Advancing Front Method. AIAA-91-3233, Sept. 1991.
23. White, Frank M.: *Viscous Fluid Flow*. McGraw-Hill, Inc., 1974.
24. O'Neil, P. J.; Barnett, R. M.; and Louie, C. M.: Numerical Simulation of Leading-Edge Vortex Breakdown Using an Euler Code. AIAA-89-2189, July 1989.

Table I. Planform Reference Quantities

Planform	S, ft^2	A	\bar{c}, ft	b, ft	^a MRC, in.
68	6.134	0.828	2.961	2.253	38.867
68/48	7.887	2.381	2.511	4.333	41.764
68/61	7.450	2.161	2.587	4.025	41.529
^b AR 71	7.533	0.828	3.380	2.498	44.121
AR 71r ^c	7.196	0.706	3.473	2.253	43.561
AR 71/48	9.654	2.405	2.864	4.818	47.486
^d CB 71	6.680	0.760	3.265	2.253	42.056
CB 71/48	8.432	2.227	2.781	4.333	45.146
CB 71/61	8.041	2.015	2.866	4.025	44.847
AR 74	9.492	0.828	3.974	2.804	51.494
AR 74r	8.710	0.583	4.198	2.253	50.149
AR 74/48	12.406	2.409	3.339	5.467	55.702
CB 74	7.420	0.684	3.684	2.253	46.366
CB 74/48	9.172	2.047	3.159	4.333	49.685
CB 74/61	8.781	1.845	3.253	4.025	49.311

^aMRC—measured from nose of model to 50 percent of \bar{c} .

^bAR—constant-aspect-ratio configuration.

^cr—outer panel removed, no spanwise extension.

^dCB—LE constant break configuration.

Table II. Vortex Flap Parameters

Planform	Flap area, in ²	Design α , deg
68/48	44.40	10.7
AR 71	55.51	Not applicable
AR 71/48	50.36	10.5
CB 71/48	57.86	11.6
AR 74	91.21	Not applicable
AR 74/48	68.07	9.9
CB 74/48	79.78	11.6
CB 74/48 (inverse-tapered flap)	85.35	Not applicable

Table III. Coordinates of Test Vortex Flaps

Coordinates for planform—					
68/48		AR 71		AR 71/48	
x, in.	y, in.	x, in.	y, in.	x, in.	y, in.
0.000	0.000	0.000	0.000	0.000	0.000
1.007	.292	1.211	.245	1.211	.245
2.024	.553	2.417	.468	2.417	.468
3.047	.785	3.619	.671	3.619	.671
4.076	.988	4.819	.853	4.819	.853
5.110	1.159	6.018	1.014	6.018	1.014
6.150	1.297	7.219	1.154	7.219	1.154
7.193	1.403	8.420	1.275	8.420	1.275
8.238	1.489	9.623	1.381	9.623	1.381
9.284	1.561	10.827	1.475	10.827	1.475
10.330	1.624	12.031	1.562	12.031	1.562
11.377	1.684	13.235	1.645	13.235	1.645
12.424	1.742	14.438	1.724	14.438	1.724
13.471	1.800	15.641	1.801	15.641	1.801
14.518	1.859	16.841	1.875	16.841	1.875
15.565	1.916	18.040	1.942	18.040	1.942
16.612	1.971	19.237	2.002	19.237	2.002
17.660	2.021	20.431	2.050	20.431	2.050
18.707	2.058	21.624	2.082	21.624	2.082
19.756	2.072	22.815	2.094	22.815	2.094
20.804	2.052	24.004	2.083	24.004	2.083
21.852	1.998	25.194	2.045	25.194	2.045
22.897	1.910	26.383	1.976	26.383	1.976
23.939	1.790	27.573	1.873	27.573	1.873
24.976	1.639	28.764	1.733	28.764	1.733
26.009	1.460	29.957	1.552	29.957	1.552
27.038	1.253	31.152	1.325	31.152	1.325
28.060	1.018	32.349	1.053	32.349	1.053
29.076	.754	33.550	.735	33.550	.735
30.076	.443	34.755	.375	34.755	.375
31.027	.000	35.700	.000	35.700	.000

Table III. Continued

Coordinates for planform—					
CB 71/48		AR 74		AR 74/48	
x, in.	y, in.	x, in.	y, in.	x, in.	y, in.
0.000	0.000	0.000	0.000	0.000	0.000
1.120	.290	1.661	.727	.815	.451
2.239	.584	3.445	1.081	1.751	.739
3.360	.875	5.248	1.319	2.888	.984
4.495	1.097	7.062	1.455	4.187	1.192
5.641	1.260	8.879	1.524	5.591	1.350
6.790	1.398	10.698	1.556	7.053	1.455
7.941	1.519	12.517	1.577	8.547	1.516
9.093	1.633	14.336	1.604	10.056	1.548
10.245	1.743	16.154	1.650	11.572	1.566
11.397	1.848	17.972	1.722	13.089	1.584
12.550	1.944	19.788	1.822	14.602	1.609
13.704	2.030	21.602	1.951	16.104	1.648
14.859	2.106	23.415	2.094	17.590	1.704
16.015	2.170	25.229	2.225	19.055	1.779
17.171	2.224	27.046	2.319	20.496	1.871
18.327	2.265	28.865	2.353	21.911	1.975
19.484	2.293	30.683	2.341	23.299	2.084
20.642	2.306	32.503	2.327	24.661	2.186
21.799	2.303	34.322	2.305	25.998	2.271
22.956	2.281	36.142	2.272	27.312	2.330
24.114	2.238	37.960	2.220	28.607	2.355
25.270	2.172	39.778	2.145	29.888	2.345
26.424	2.080	41.593	2.040	31.162	2.295
27.575	1.962	43.407	1.899	32.437	2.205
28.723	1.815	45.218	1.717	33.721	2.071
29.868	1.641	47.023	1.488	35.024	1.887
31.009	1.440	48.820	1.207	36.354	1.650
32.144	1.215	50.608	.868	37.714	1.359
33.275	.964	52.384	.467	39.104	1.014
35.700	.000	54.142	.000	42.166	.000

Table III. Concluded

Coordinates for planform—			
CB 74/48		CB 74/48 (inverse-tapered flap)	
x, in.	y, in.	x, in.	y, in.
0.000	0.000	0.000	0.000
1.307	.373	-2.308	.766
2.652	.702	32.280	3.283
4.040	1.021	42.167	.000
5.443	1.311		
6.845	1.555		
8.244	1.753		
9.647	1.912		
11.055	2.043		
12.472	2.156		
13.895	2.258		
15.321	2.355		
16.747	2.453		
18.172	2.550		
19.593	2.644		
21.010	2.727		
22.423	2.788		
23.831	2.816		
25.235	2.804		
26.635	2.751		
28.032	2.660		
29.425	2.536		
30.815	2.385		
32.198	2.210		
33.574	2.009		
34.942	1.782		
36.306	1.525		
37.679	1.238		
39.070	.918		
40.478	.559		
42.166	.000		

Table IV. Six-Component Balance Load Capacities and Accuracies

Parameter	Maximum load	Load accuracy	Coefficient accuracy, ^a platform—	
			68	68/48
Normal force, lb	3000	15.00	0.0349	0.0272
Axial force, lb	250	1.25	.0029	.0023
Pitching moment, in-lb	7500	37.50	.0025	.0023

^aReflects only balance sensitivities and is based on $q_{\infty} = 70$ psf.

Table V. Planform Matrix for Vortex Flap Investigation

Planform	q_∞ , psf	δ_{vf} , deg	δ_{ibf} , deg	δ_{obf} , deg	OBLE flap	Appendix figures	Comments
68	70	Off	0	Off	Off	A1	
↓	↓	Off	15	↓	↓		
↓	↓	40	↓	↓	↓		
↓	↓	20	↓	↓	↓		
↓	↓	30	↓	↓	↓		
↓	↓	30	0	↓	↓		
68/48	70	Off	0	0	Off		
↓	↓	Off	15	15	↓		
↓	↓	40	↓	↓	↓		
↓	↓	20	↓	↓	↓		
↓	↓	30	↓	↓	↓		
↓	↓	30	↓	↓	On	A2	Vortex flap design configuration No grit
↓	10	↓	↓	↓	↓	A3	OBLE flap slotted with 0.1-in. gap
↓	20	↓	↓	↓	↓		
↓	70	↓	↓	↓	↓		
↓	110	↓	↓	↓	↓		
↓	70	↓	15	15	On	A4	Inboard TE flaps end plated
↓	↓	↓	15	↓	Snag		
↓	↓	↓	15,0,15	↓	Off		
↓	↓	↓	15,0,15	↓	↓	A5	
68/61	70	Off	0	0	Off		
↓	↓	Off	0	0	↓	A6	OBLE flap slotted with 0.1-in. gap OBLE flap slotted with 0.2-in. gap Spanwise extension added Spanwise extension added
↓	↓	30	15	15	On		
↓	↓	↓	↓	↓	↓	A6	
AR 71	70	Off	15	Off	Off		
↓	↓	30	15	Off	Off		
AR 71	70	Off	15	Off	Off	A7	Vortex flap design configuration
↓	↓	30	15	↓	↓		
AR 71r	70	Off	15	Off	Off	A8	
↓	↓	30	15	↓	↓		
↓	↓	0	0	↓	↓	A8	
AR 71/48	70	Off	15	15	Off		
↓	↓	30	↓	↓	On	A9	Vortex flap design configuration
↓	↓	30	↓	↓	↓		
CB 71	70	Off	0	Off	Off	A9	
↓	↓	Off	15	↓	↓		
↓	↓	30	15	↓	↓	A10	
CB 71/48	70	Off	0	0	Off		
↓	↓	Off	15	15	↓	A10	
↓	↓	30	↓	↓	On		
↓	↓	30	↓	↓	↓		

Table V. Concluded

Planform	q_{∞} , psf	δ_{vf} , deg	δ_{ibf} , deg	δ_{obf} , deg	OBLE flap	Appendix figures	Comments
CB 71/61	70	Off	0	0	Off		
↓	↓	Off	15	15	↓	A11	
↓	↓	30	↓	↓	On	A12	
AR 74	70	Off	15	Off	Off		Spanwise extension added
AR 74	70	30	15	Off	Off	A13	Spanwise extension added
AR 74r	70	Off	0	Off	Off		
↓	↓	Off	15	↓	↓		
AR 74/48	70	30	15	↓	↓		
↓	↓	Off	0	0	Off		
↓	↓	Off	15	15	↓	A14	Vortex flap design configuration
↓	↓	30	↓	↓	On	A15	
CB 74	70	Off	0	Off	Off		
↓	↓	Off	15	↓	↓		
CB 74/48	70	30	15	↓	↓	A16	
↓	↓	Off	0	0	Off		
↓	↓	Off	15	15	↓		
↓	↓	30	↓	↓	↓	A17	Vortex flap design configuration
↓	↓	↓	↓	↓	↓		Inverse-tapered vortex flap
CB 74/61	70	Off	0	0	On	A18	
↓	↓	↓	15	15	Off		
↓	↓	30	↓	↓	On		
↓	↓	↓	↓	↓	Off	A19	
↓	↓	↓	↓	↓	On		
↓	↓	↓	↓	↓	Off		Inverse-tapered vortex flap

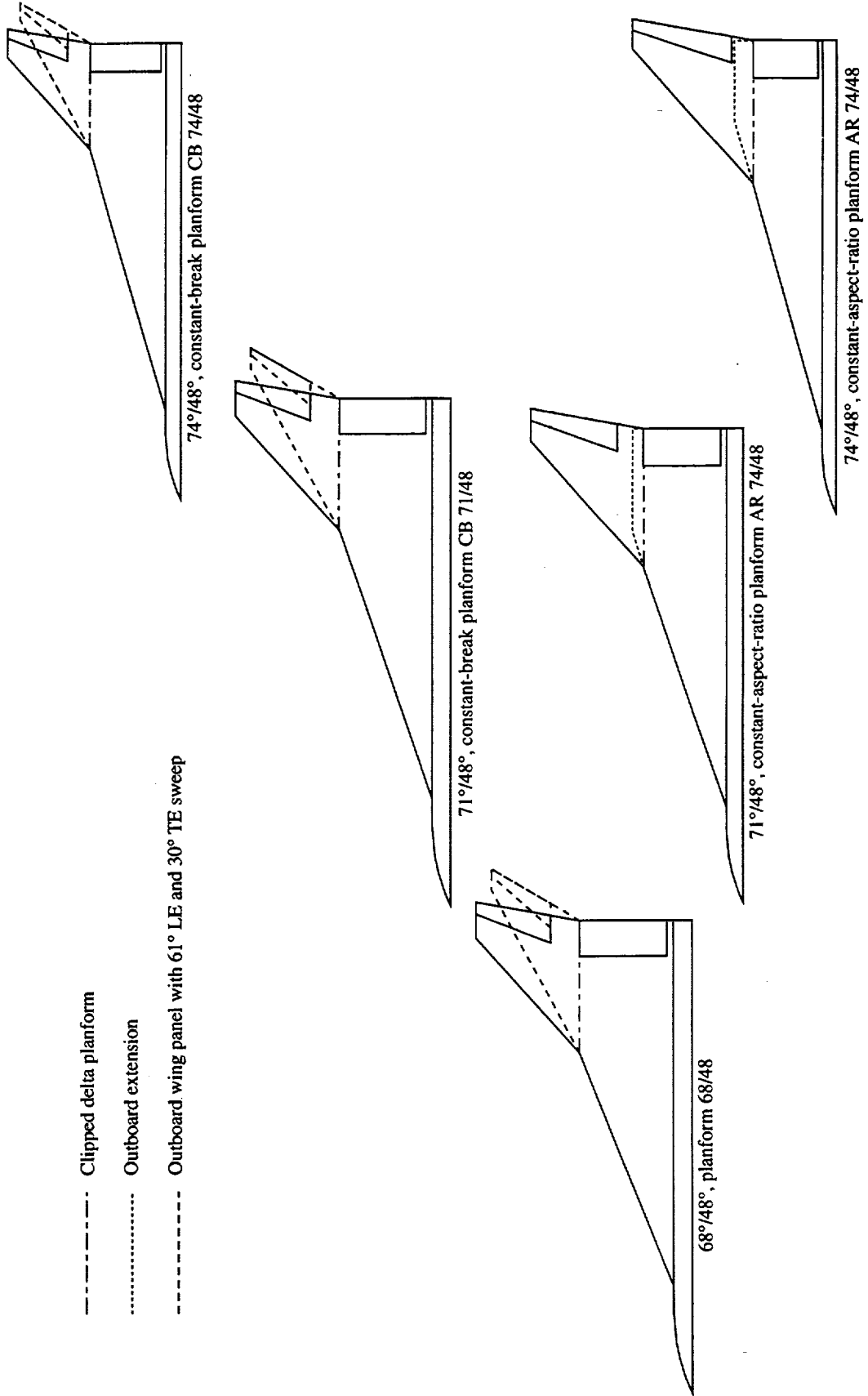


Figure 1. Test planforms.

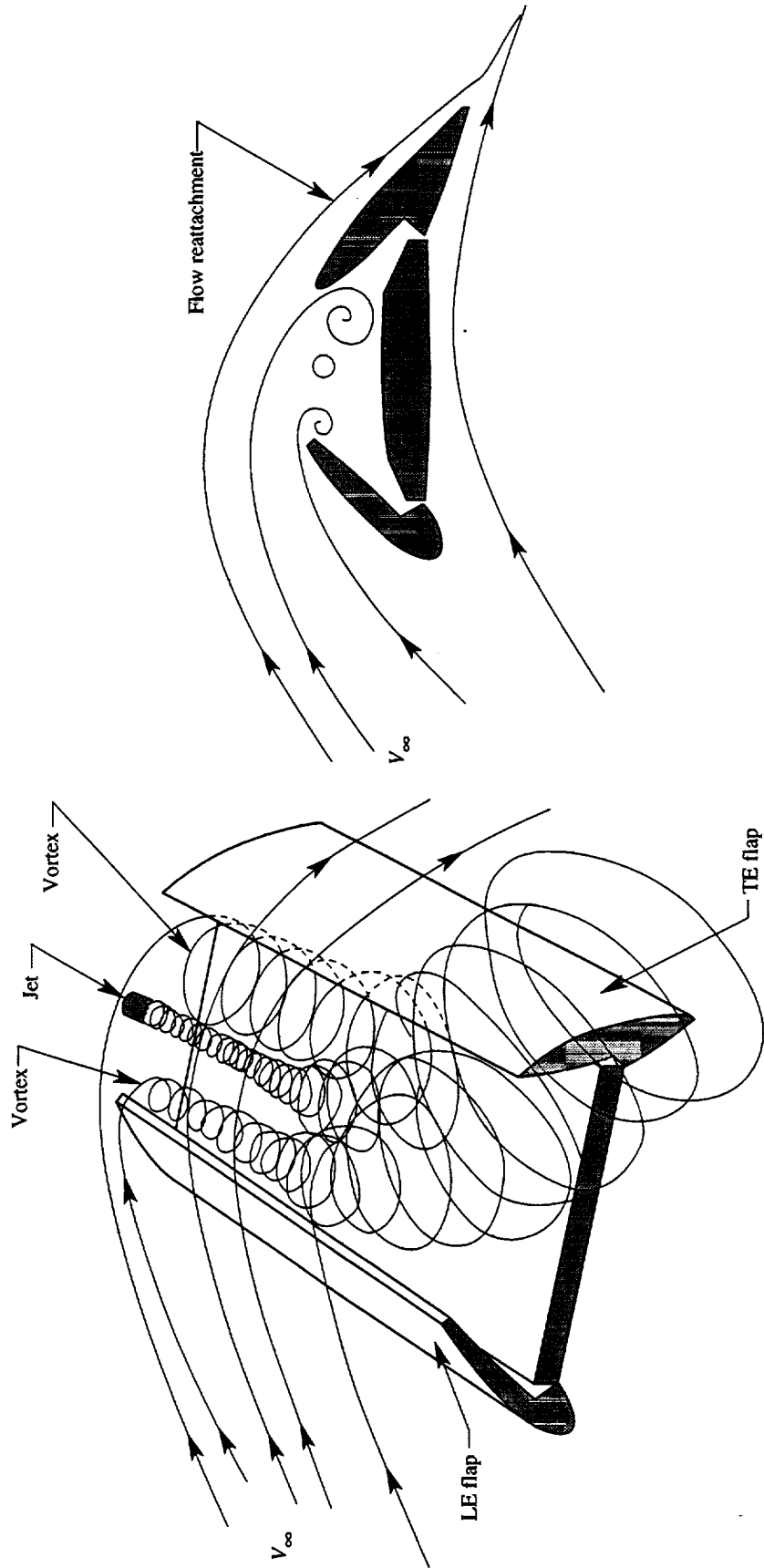
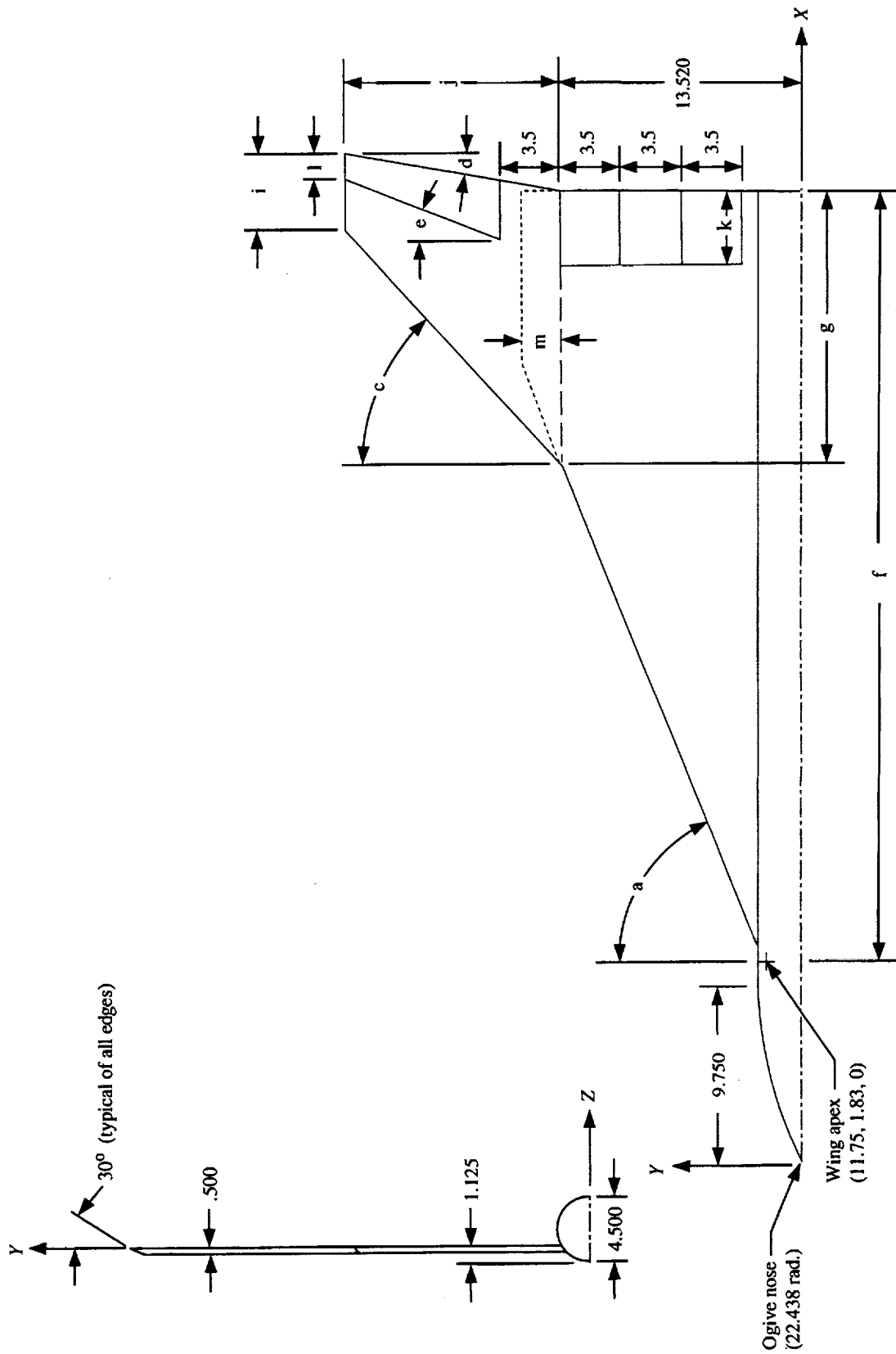


Figure 2. Flow field generated by vortex trap system installed on rectangular wing. (See ref. 9.)



(a) Constant and variable dimensions.

Figure 3. Typical test planform. All linear dimensions are in inches.

Platform	a, deg	c, deg	d, deg	e, deg	f, in.	g, in.	i, in.	j, in.	k, in.	l, in.	m, in.
68	68.0	NA ^a	NA	NA	49.403	15.940	NA	NA	4.270	NA	NA
68/48	68.0	48.0	10.0	21.1	49.403	15.940	4.281	12.480	4.270	1.390	NA
68/61	68.0	61.0	30.0	40.9	49.403	15.940	2.498	10.630	4.270	0.812	NA
AR 71	71.0	NA	NA	NA	57.955	18.690	NA	NA	5.010	NA	1.465
AR 71r	71.0	NA	NA	NA	57.955	18.690	NA	NA	5.010	NA	NA
AR 71/48	71.0	48.0	10.0	19.4	57.955	18.690	4.312	15.390	5.010	1.550	NA
CB 71	71.0	NA	NA	NA	55.204	15.940	NA	NA	4.270	NA	NA
CB 71/48	71.0	48.0	10.0	21.1	55.204	15.940	4.281	12.480	4.270	1.390	NA
CB 71/61	71.0	61.0	30.0	40.9	55.204	15.940	2.498	10.630	4.270	0.812	NA
AR 74	74.0	NA	NA	NA	69.960	22.810	NA	NA	6.050	NA	3.301
AR 74r	74.0	NA	NA	NA	69.960	22.810	NA	NA	6.050	NA	NA
AR 74/48	74.0	48.0	10.0	18.3	69.960	22.810	4.789	19.280	6.050	1.790	NA
CB 74	74.0	NA	NA	NA	63.089	15.940	NA	NA	4.270	NA	NA
CB 74/48	74.0	48.0	10.0	21.1	63.089	15.940	4.281	12.480	4.270	1.390	NA
CB 74/61	74.0	61.0	30.0	40.9	63.089	15.940	2.498	10.630	4.270	0.812	NA

^aNA = not applicable.

(b) Tabulated variable dimensions.

Figure 3. Concluded.

+ Denotes location of wing apex and local x-y origin

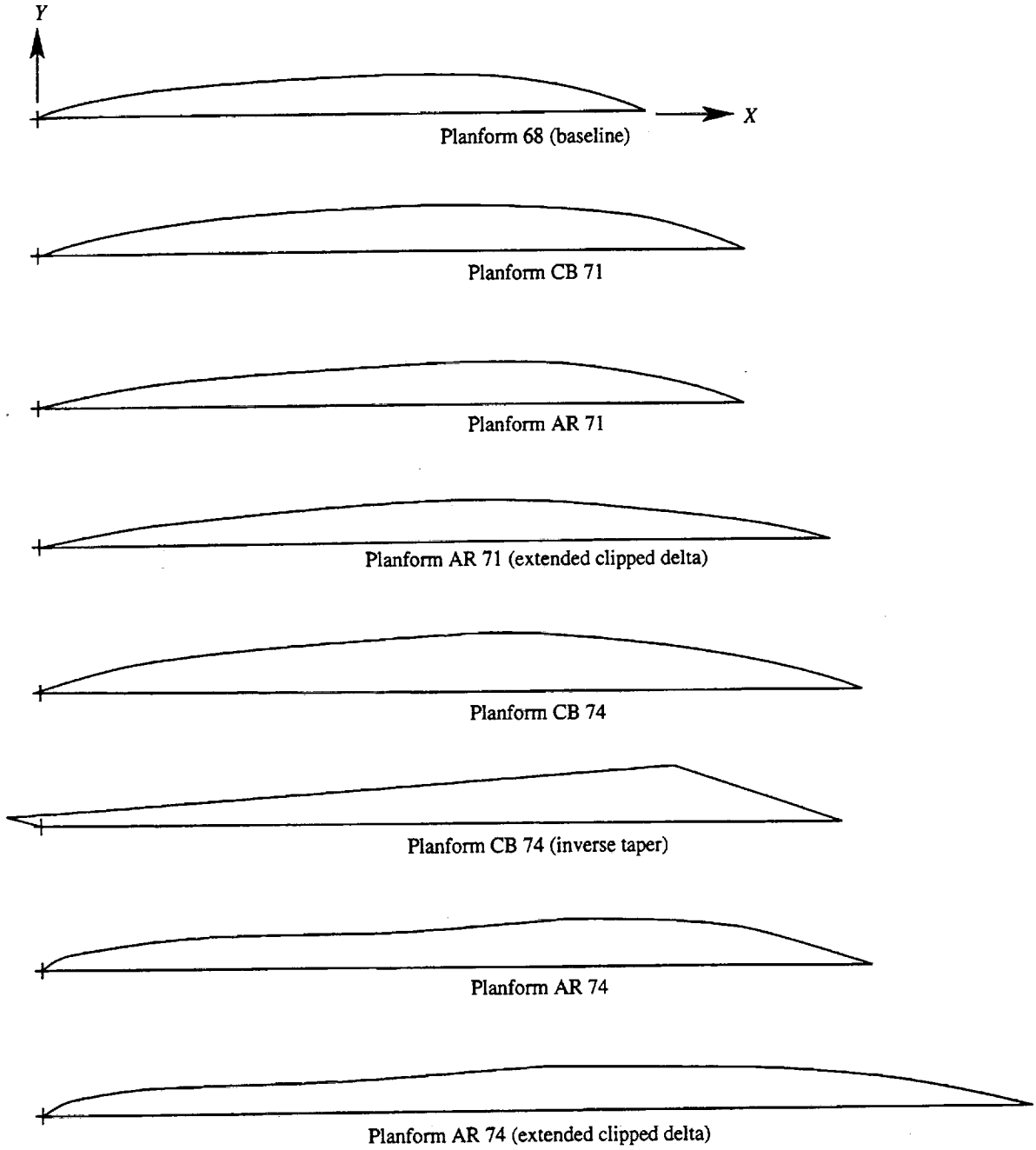
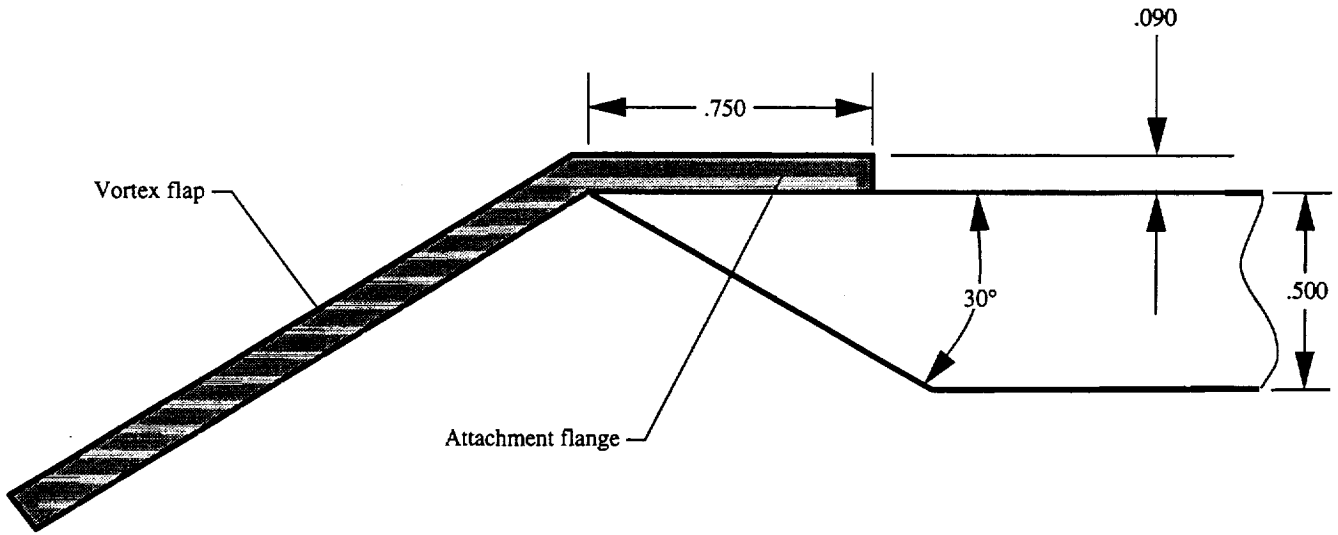
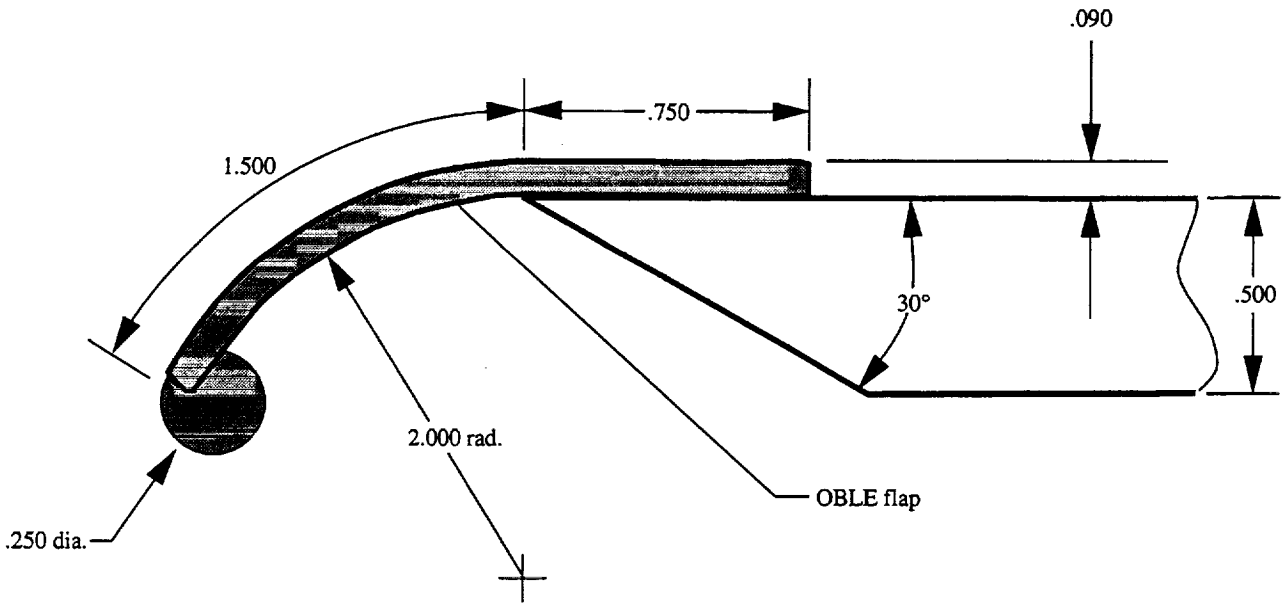


Figure 4. Vortex flaps.

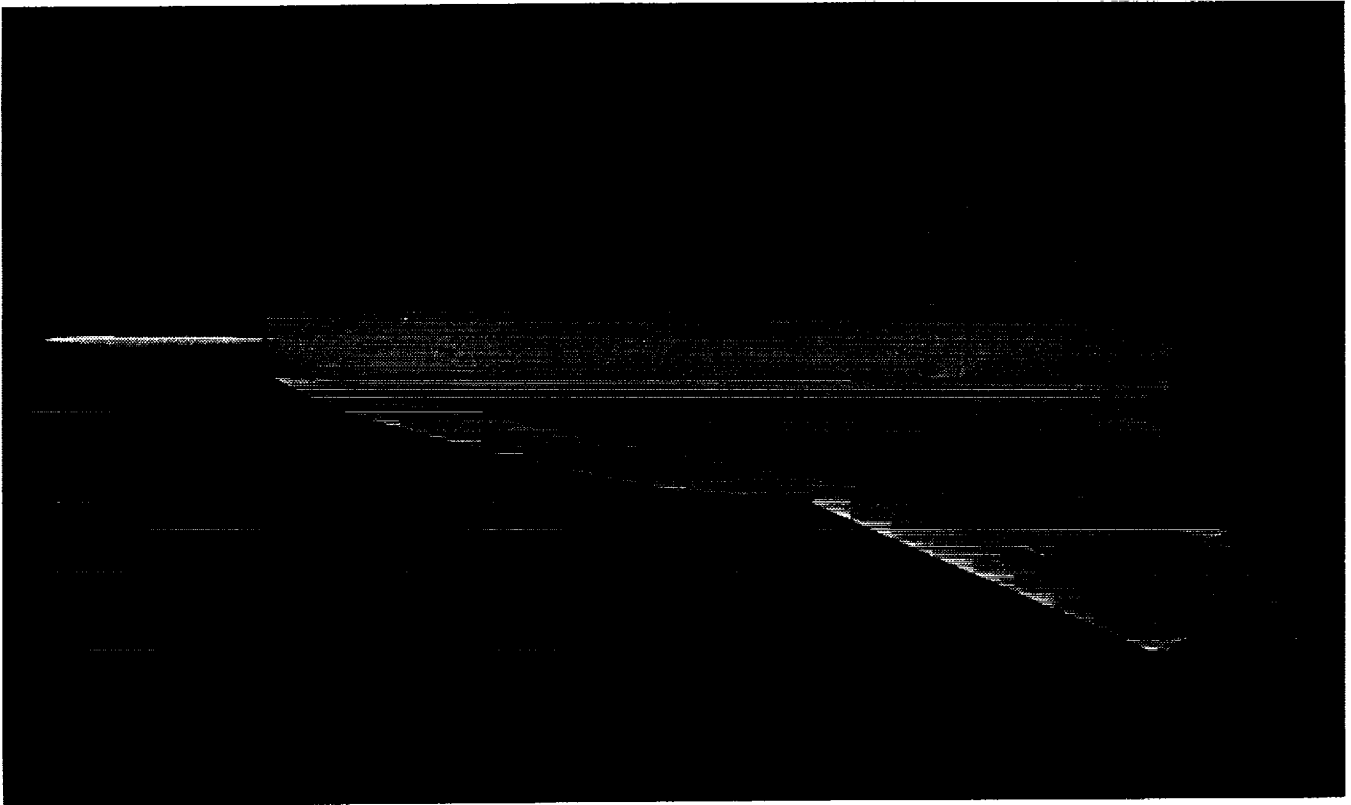


(a) Vortex flap attachment at cross section normal to leading edge.

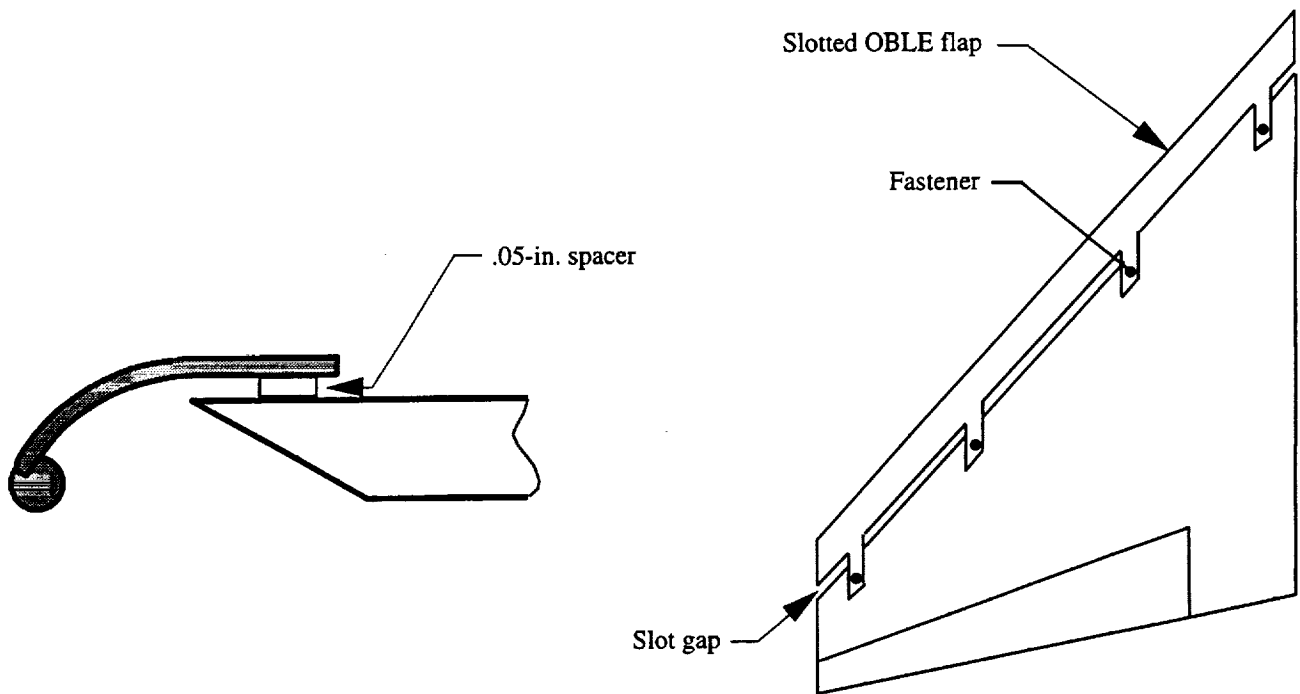


(b) OBLE flap attachment at cross section normal to leading edge.

Figure 5. Leading-edge flap attachment. All linear dimensions are in inches.

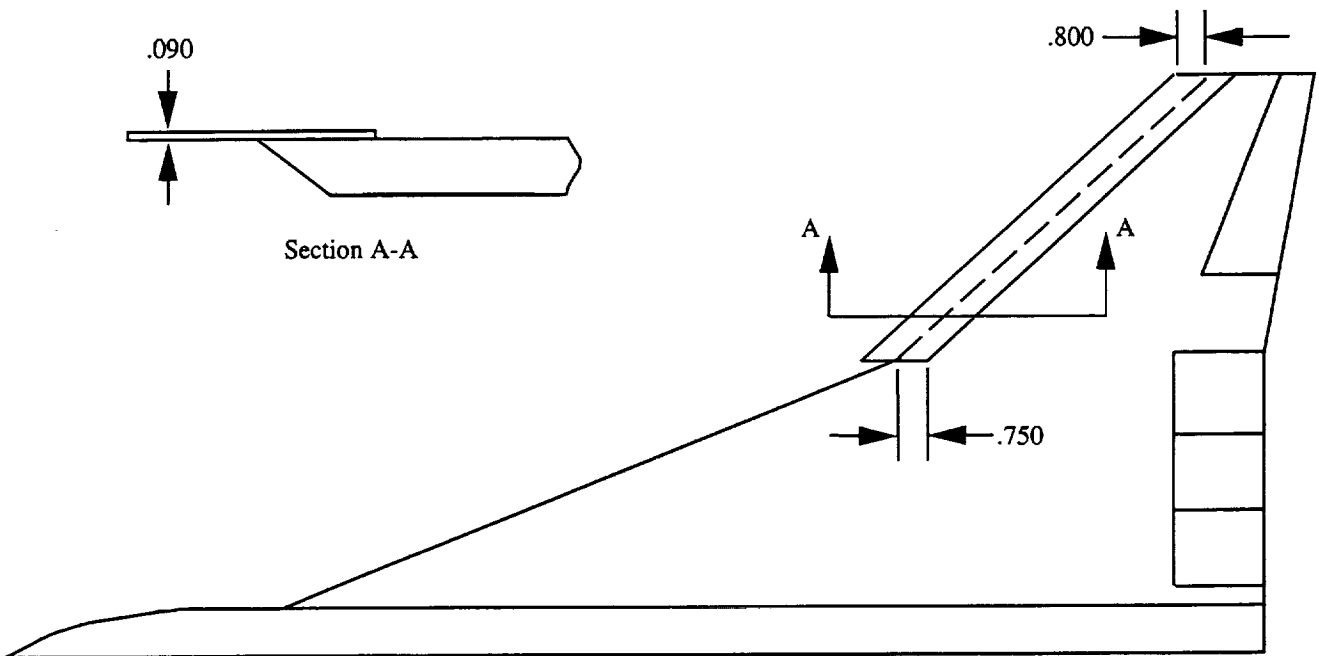


(a) Photograph of planform 68/48 with vortex and OBLE flaps.

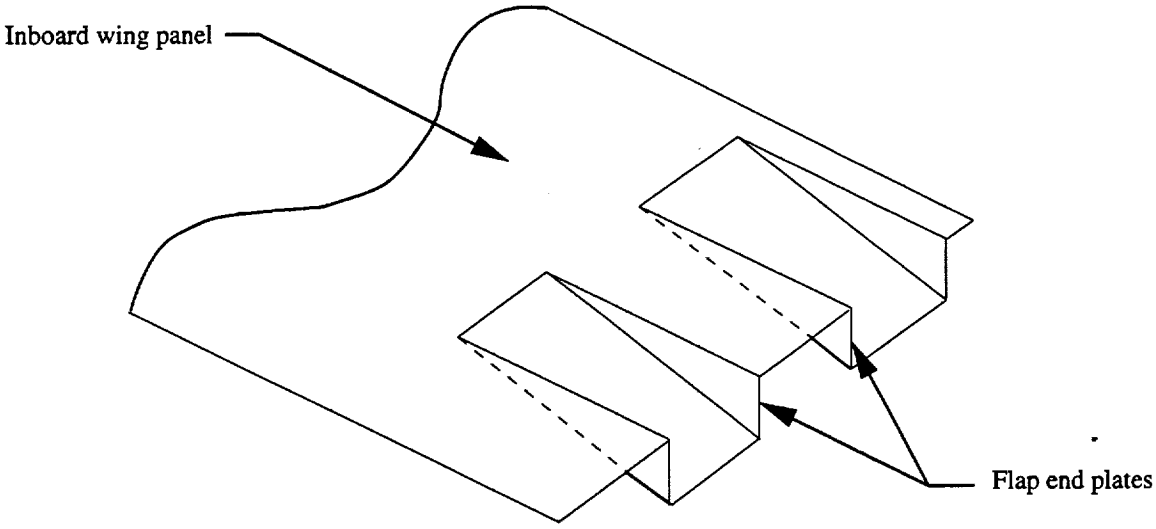


(b) Slotted OBLE flap.

Figure 6. Details of OBLE flap.



(a) OBLE snag.



(b) Inboard trailing-edge flap end plates.

Figure 7. Other devices tested. All linear dimensions are in inches.

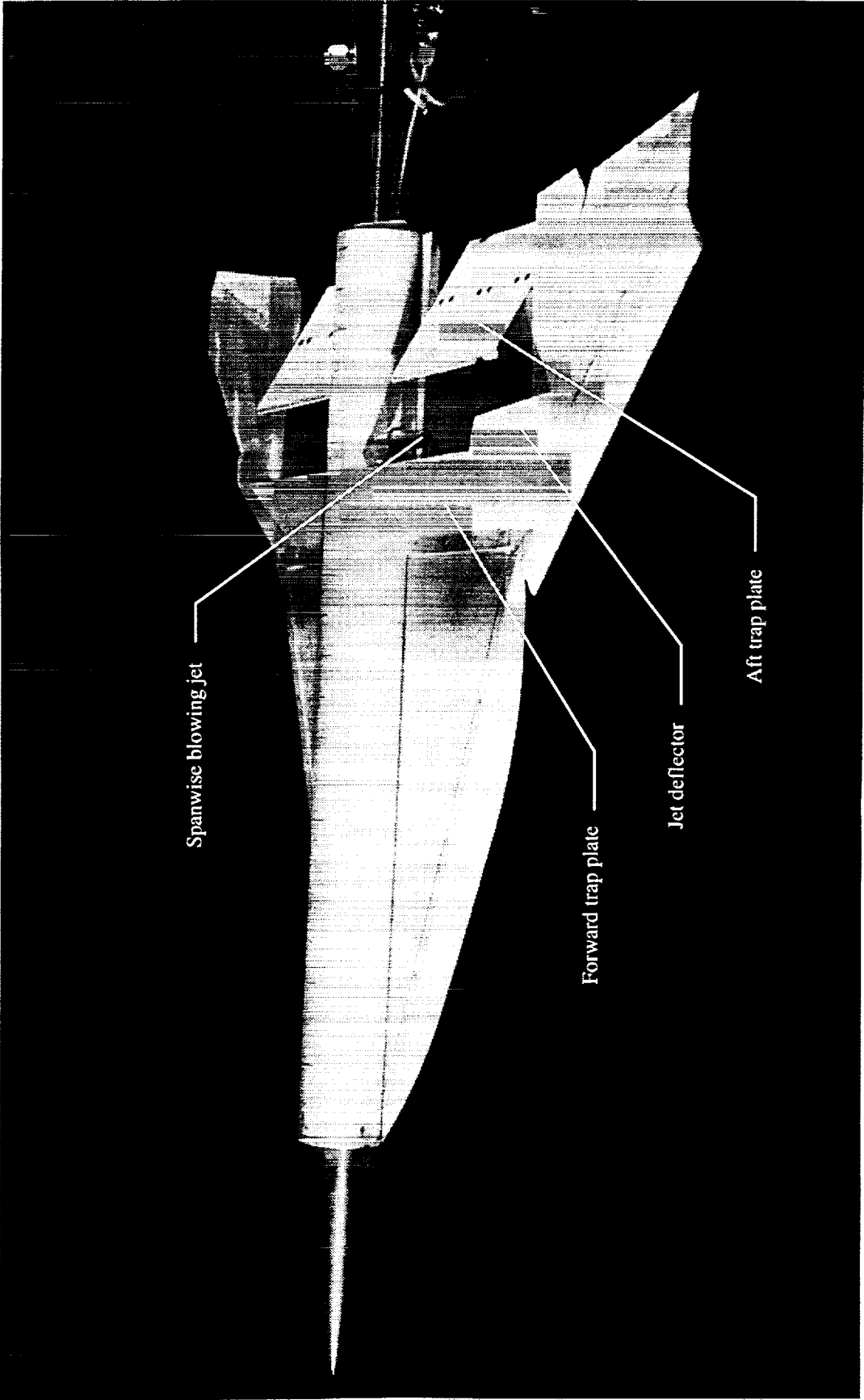


Figure 8. Photograph of inboard vortex trap system with jet deflectors installed.

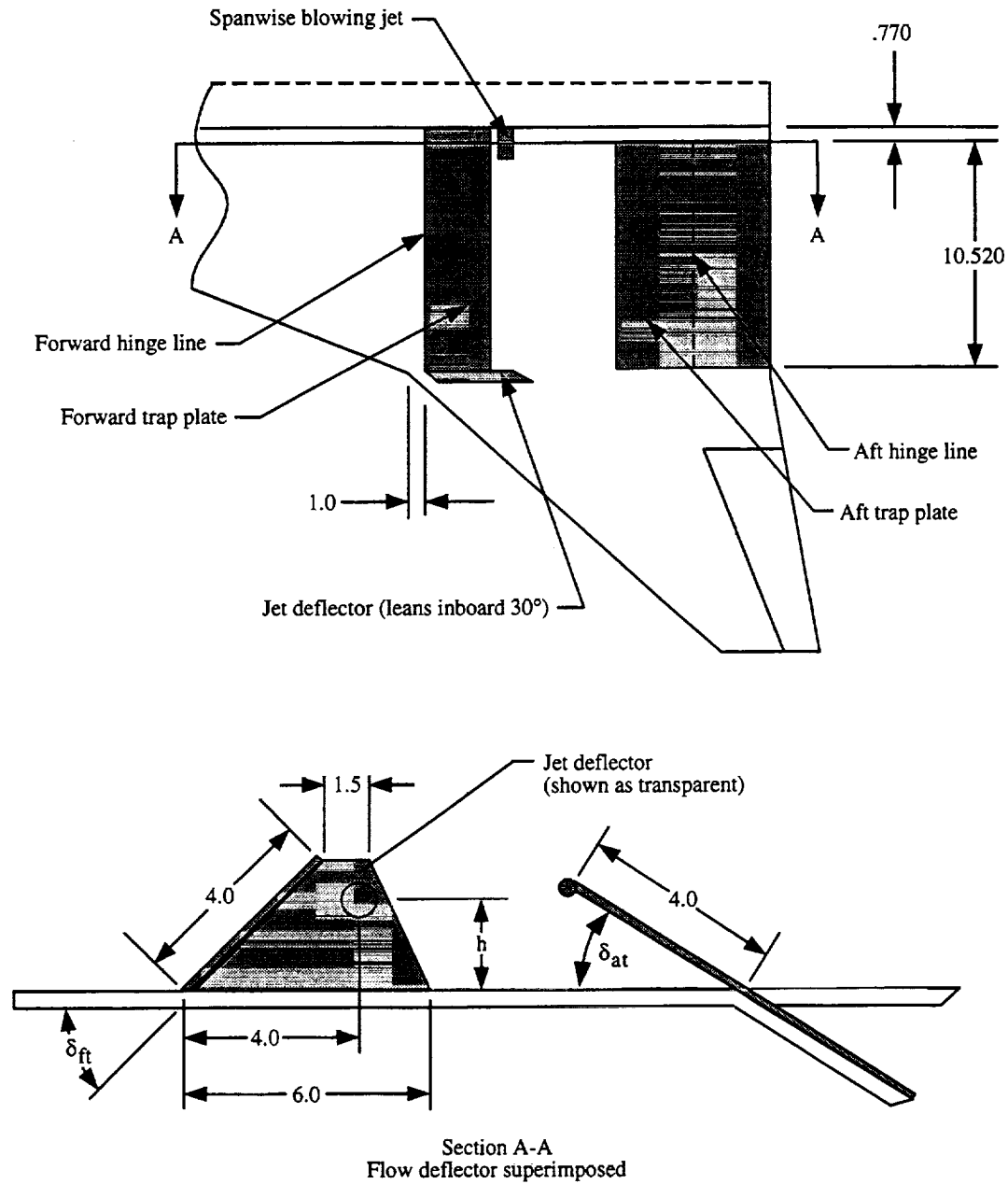


Figure 9. Inboard vortex traps. All linear dimensions are in inches.

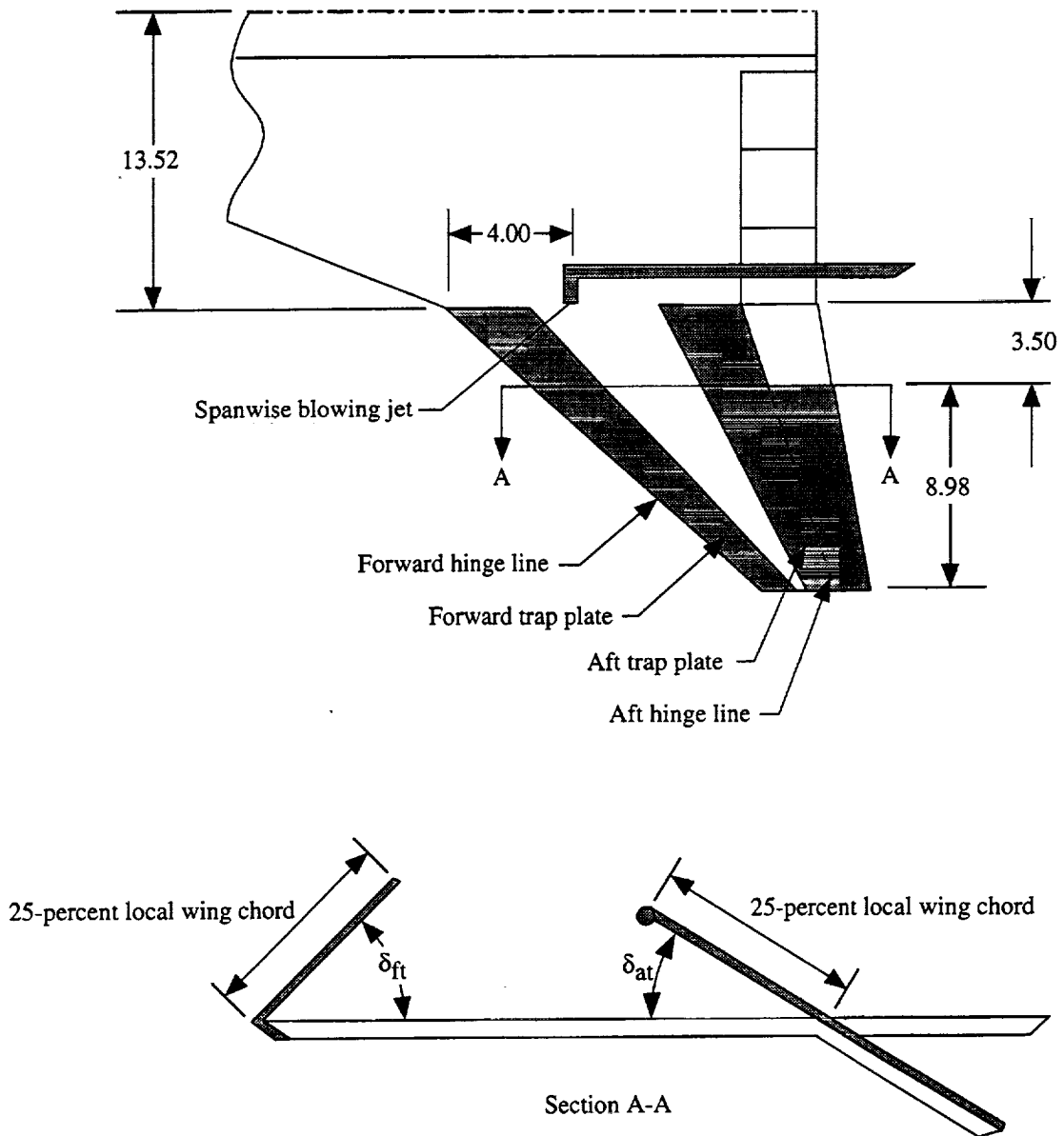


Figure 10. Outboard vortex traps. All linear dimensions are in inches.

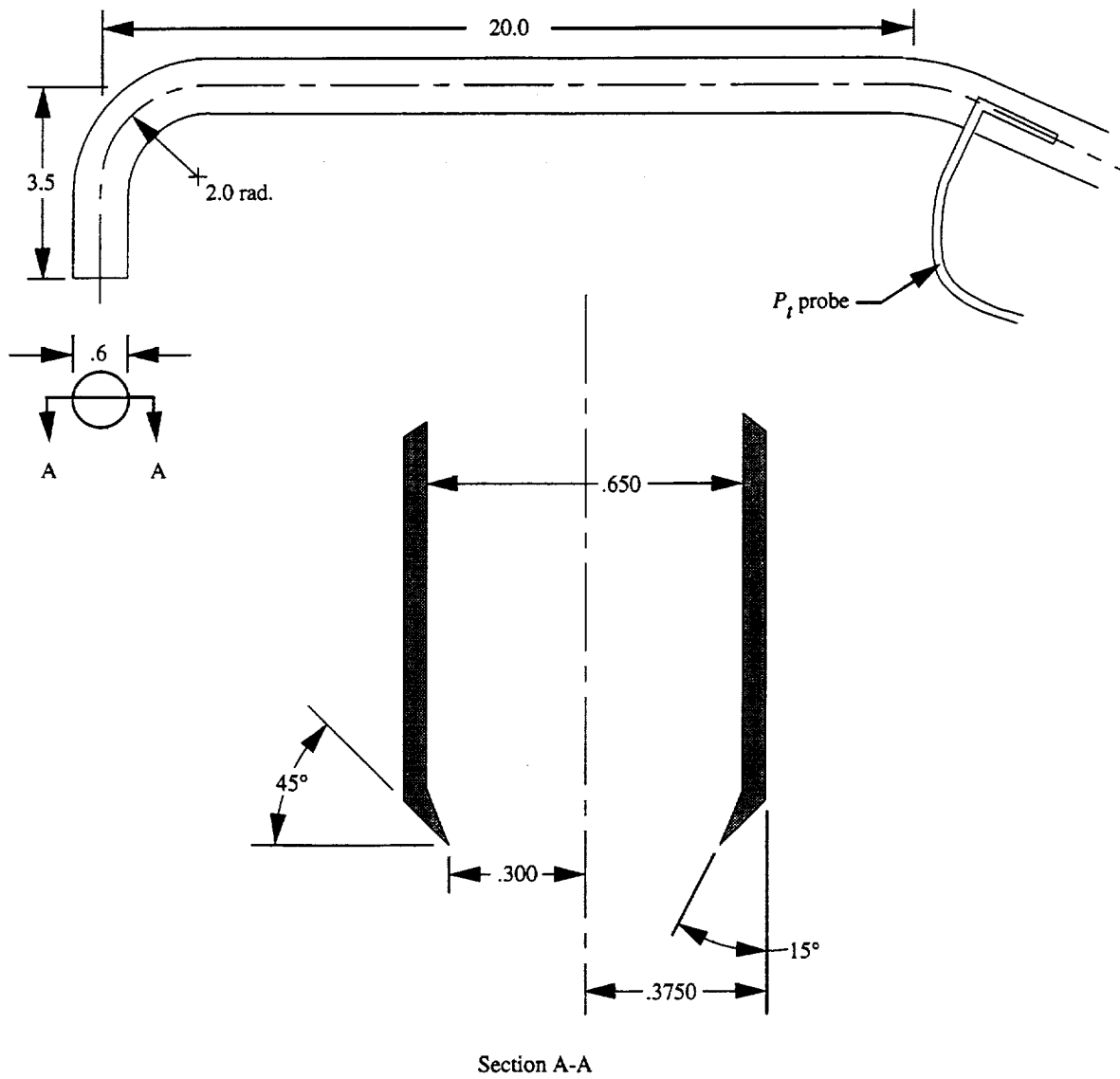


Figure 11. Air supply line and nozzle cross section. All linear dimensions are in inches.

Strip	Axis location	Planform—					
		68	68/48	AR 74	AR 74/48	CB 74	CB 74/48
1	x, in.	20.65	20.65	27.95	25.21	25.21	25.21
2	↓	32.70	32.70	50.53	42.61	42.61	42.61
3		22.95	22.95	27.95	27.95	27.95	27.95
4		38.69	38.69	50.53	50.53	50.53	50.53
5		48.66	48.66	63.93	63.93	60.50	60.50
6		y, in.	5.65	5.65	5.65	5.65	5.65
7	y, in.	10.90	10.90	10.90	10.90	10.90	10.90

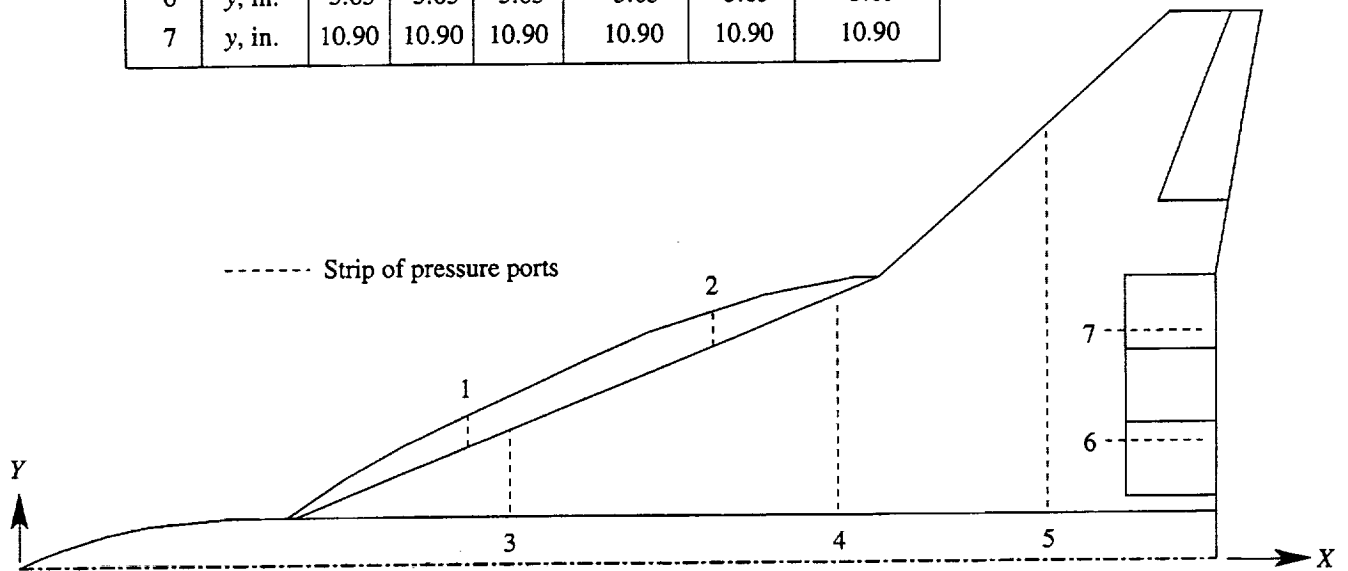


Figure 12. Upper surface pressure port strip locations at constant fuselage station (X) or buttlane (Y) for instrumented planforms.

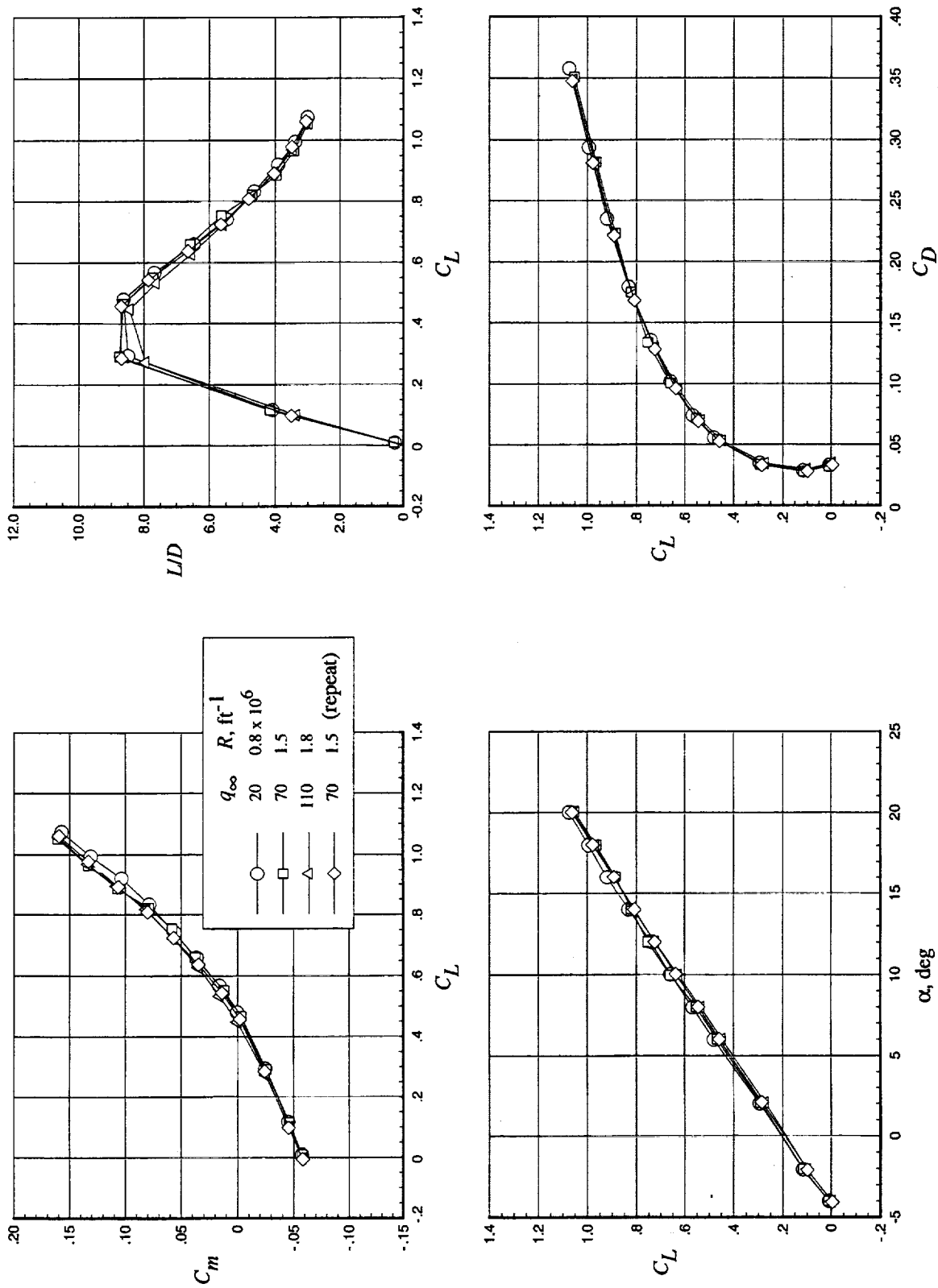
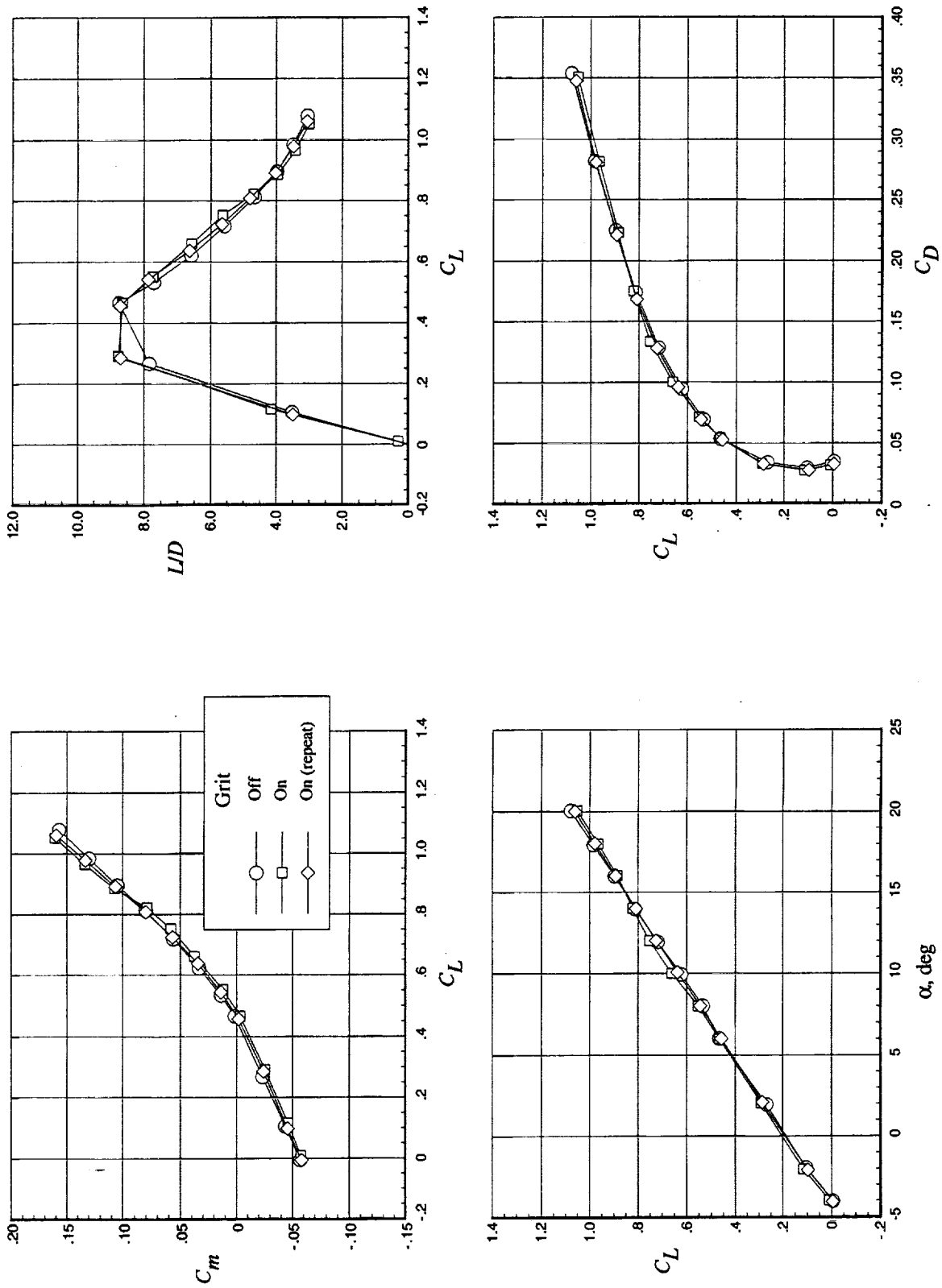
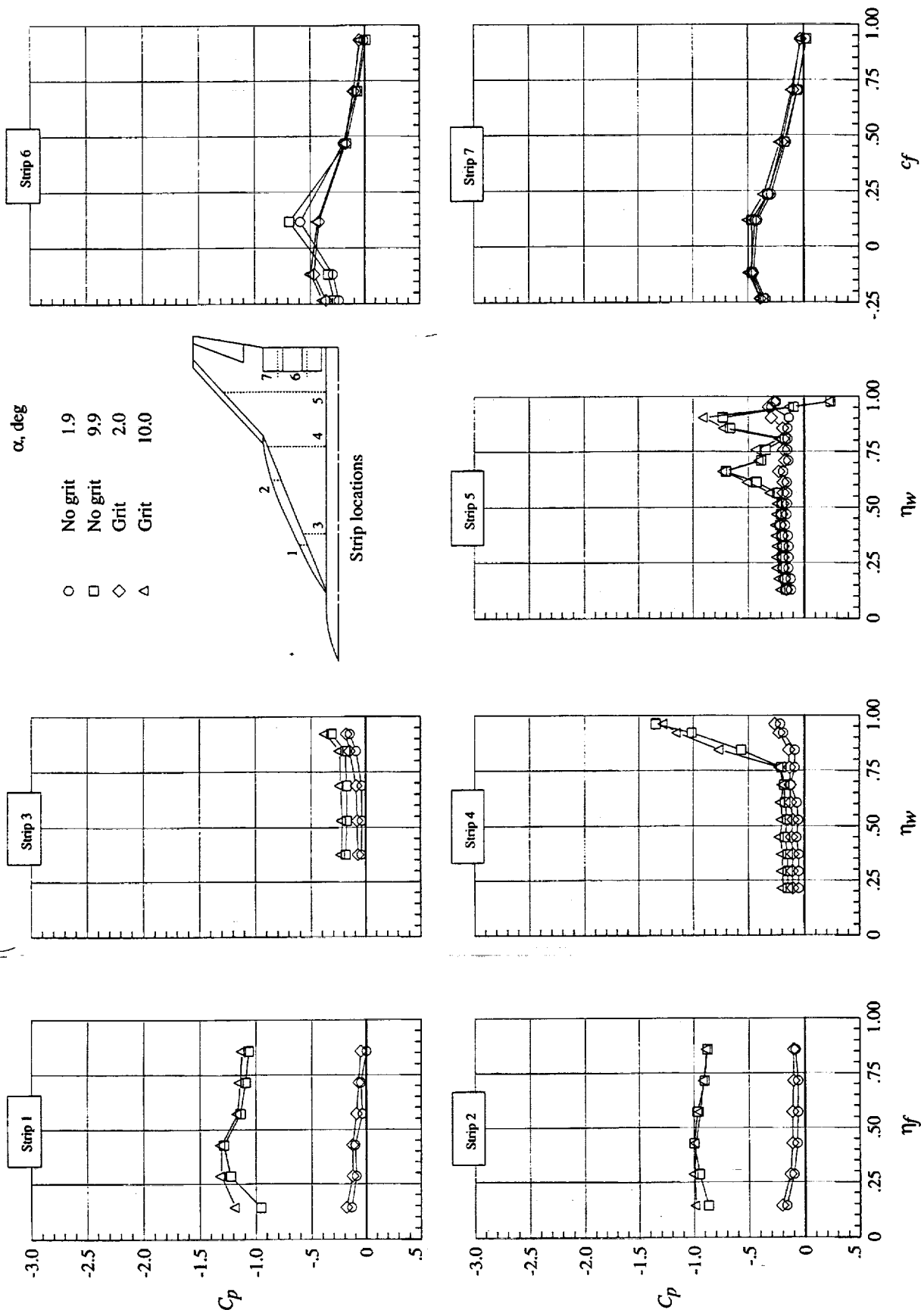


Figure 13. Effect of dynamic pressure on longitudinal aerodynamics of planform 68/48. $\delta_{vf} = 30^\circ$; $\delta_{bf} = 15^\circ$; $\delta_{obf} = 15^\circ$; and OBLE flaps on.



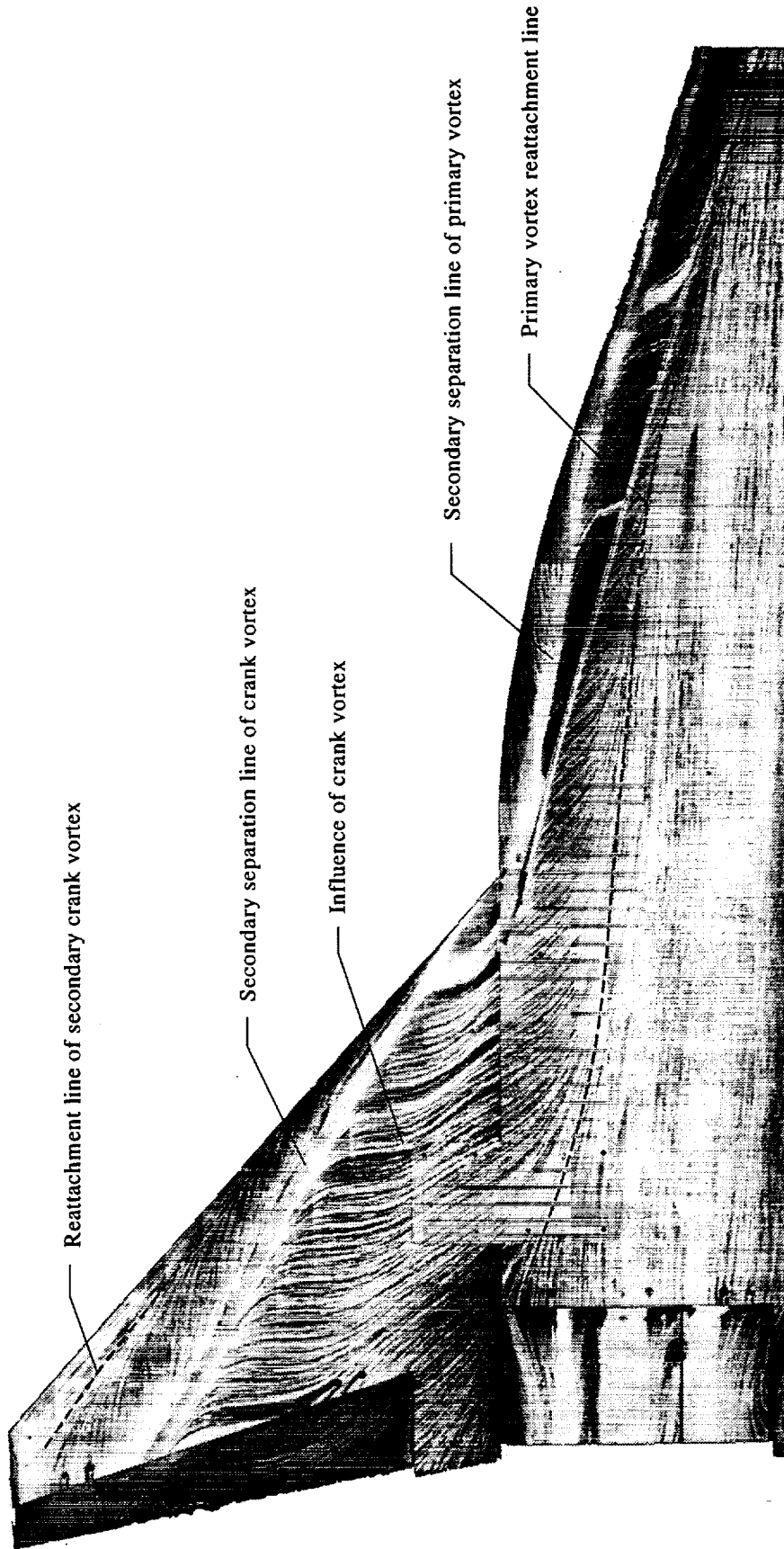
(a) Longitudinal aerodynamics.

Figure 14. Effect of grit on planform 68/48. $q_\infty = 70$ psf; $\delta_{vf} = 30^\circ$; $\delta_{bf} = 15^\circ$; $\delta_{obf} = 15^\circ$; and OBLE flaps on.



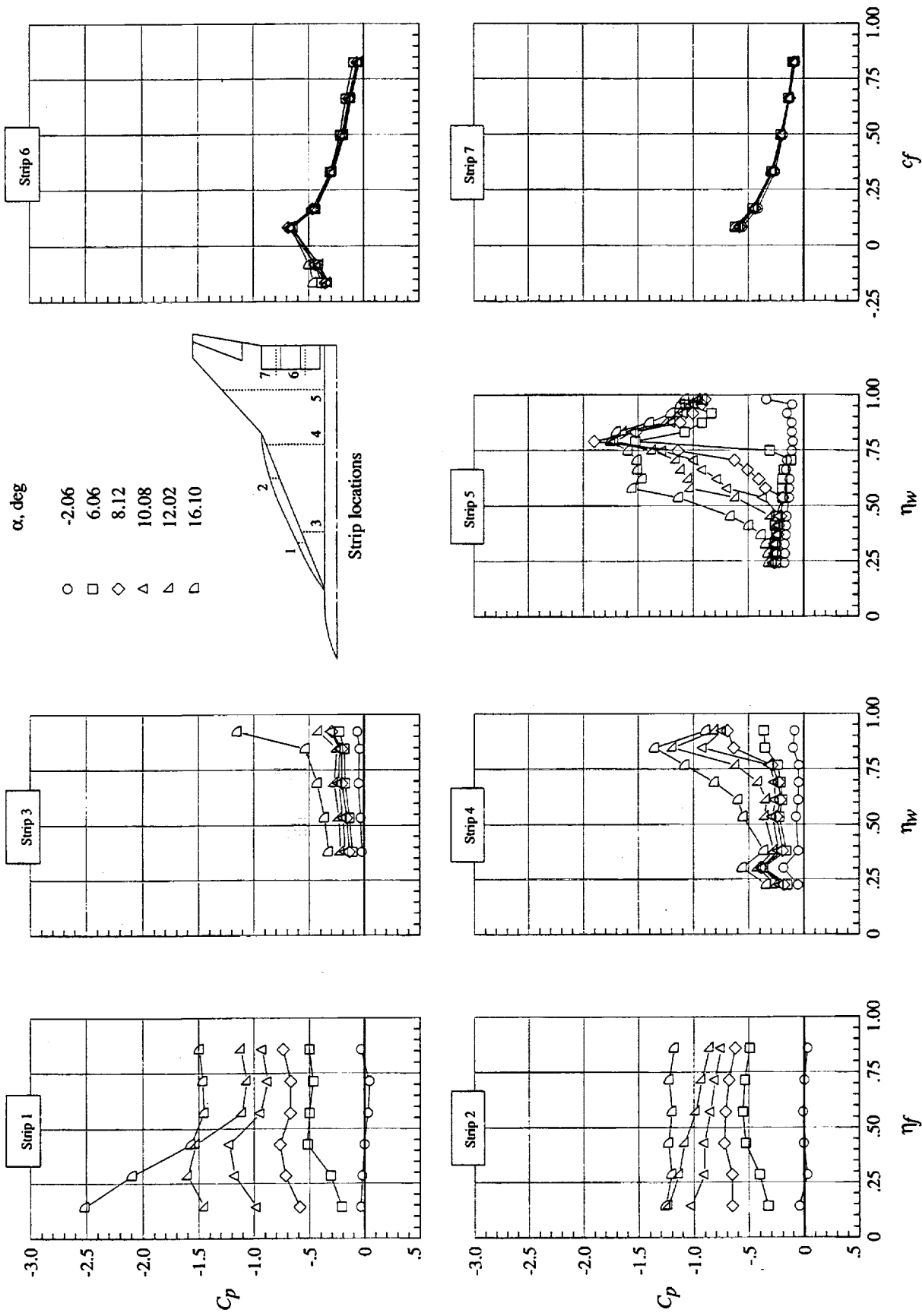
(b) Surface pressure distributions.

Figure 14. Concluded.



(a) Representative surface flow features.

Figure 15. Cranked delta planform AR 74/48. $q_{\infty} = 70$ psf; $\alpha = 10^\circ$; $\delta_{vf} = 30^\circ$; $\delta_{bf} = 15^\circ$; $\delta_{obf} = 15^\circ$; and OBLE flaps off.



(b) Representative surface pressure distributions.

Figure 15. Concluded.

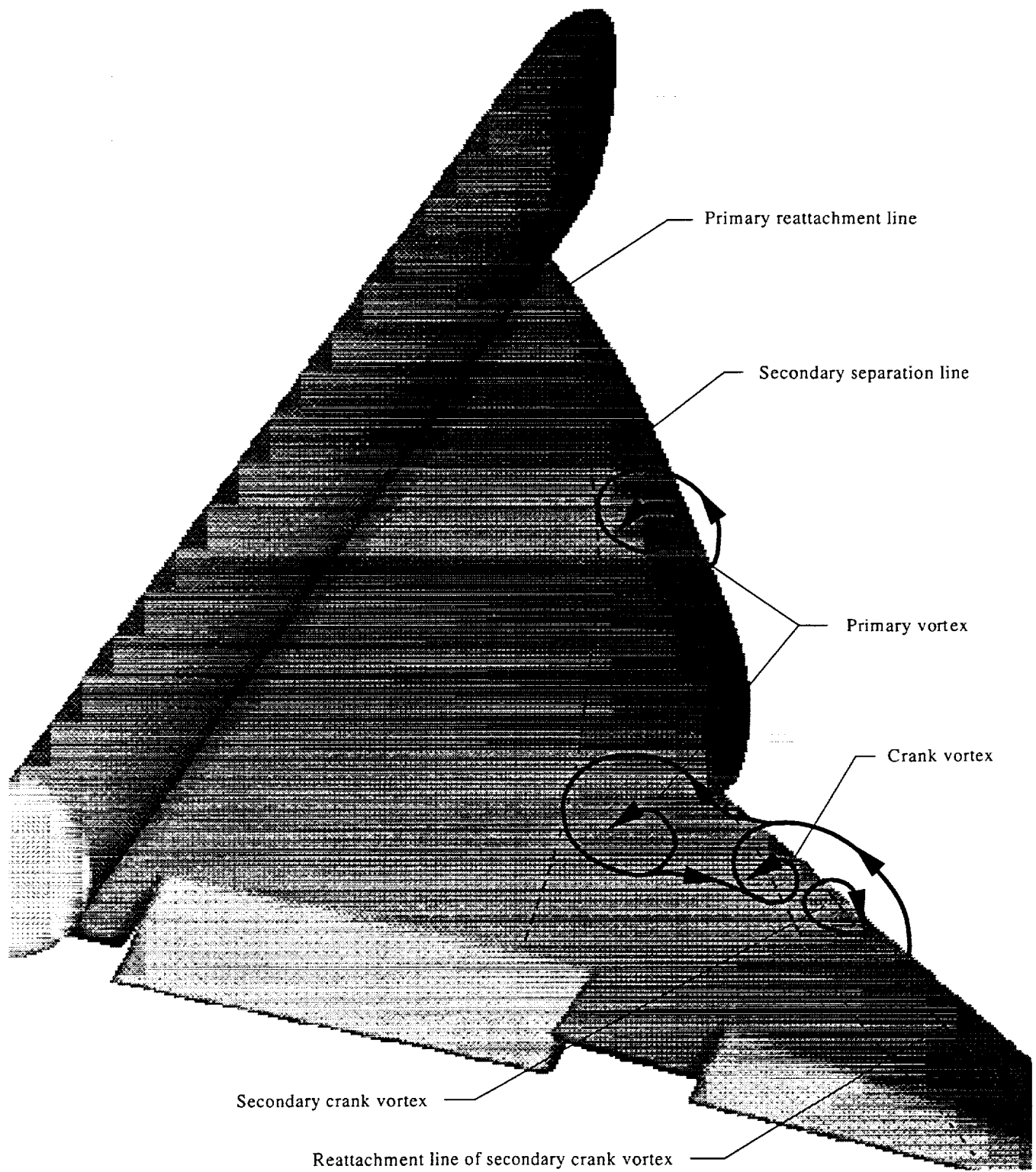
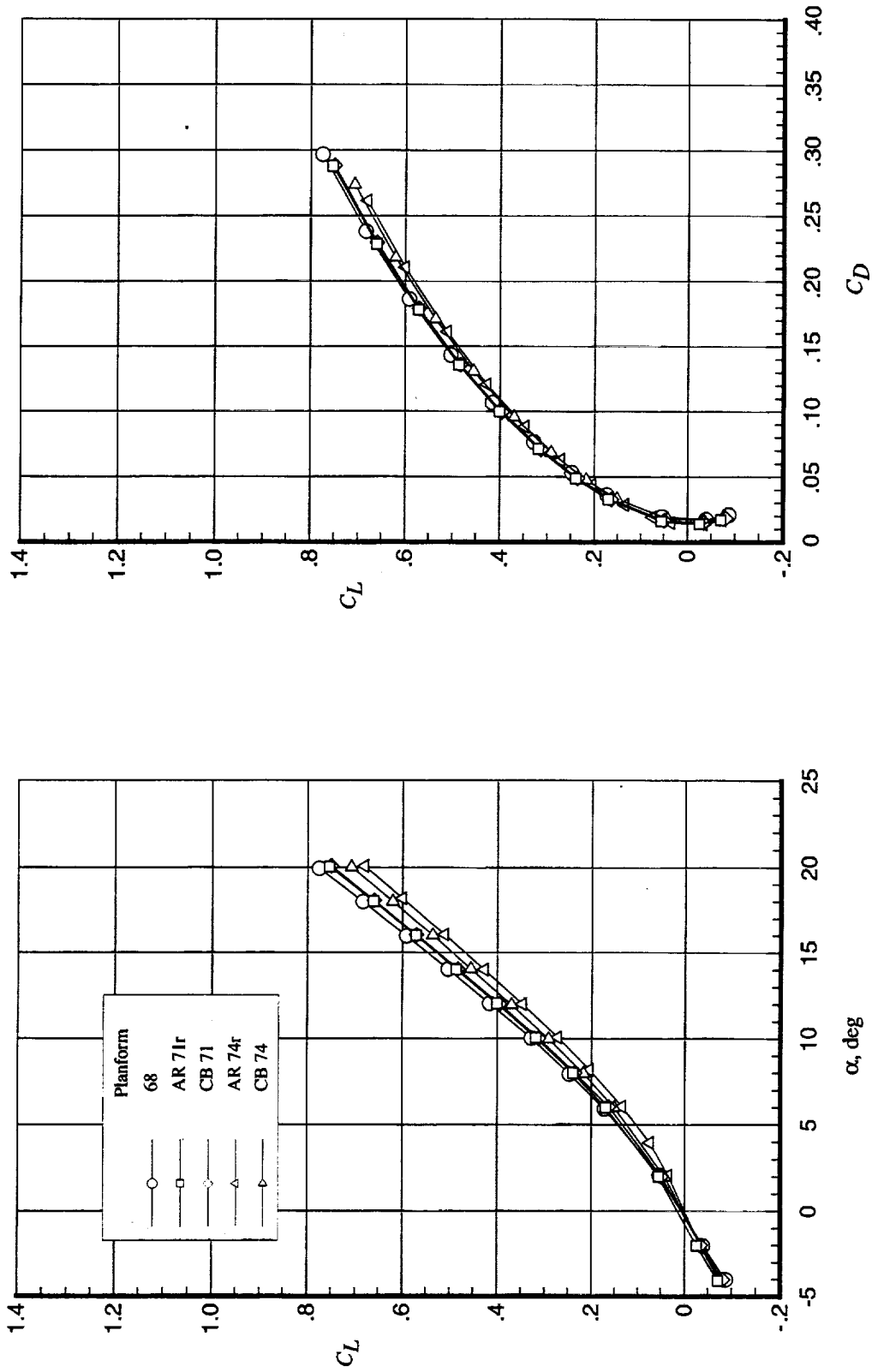
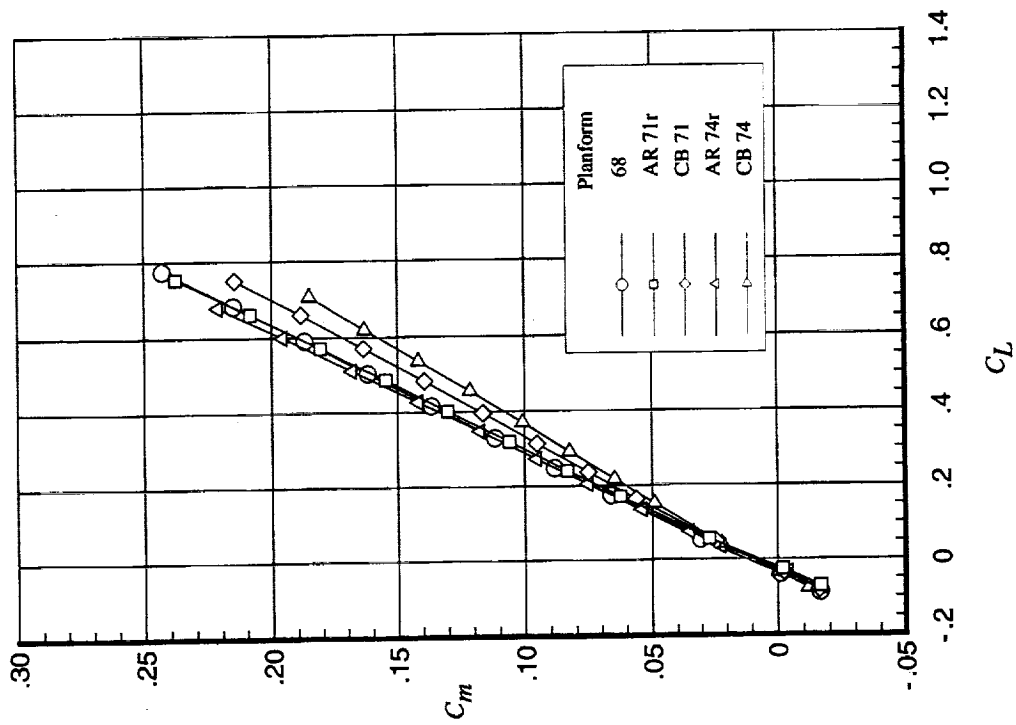
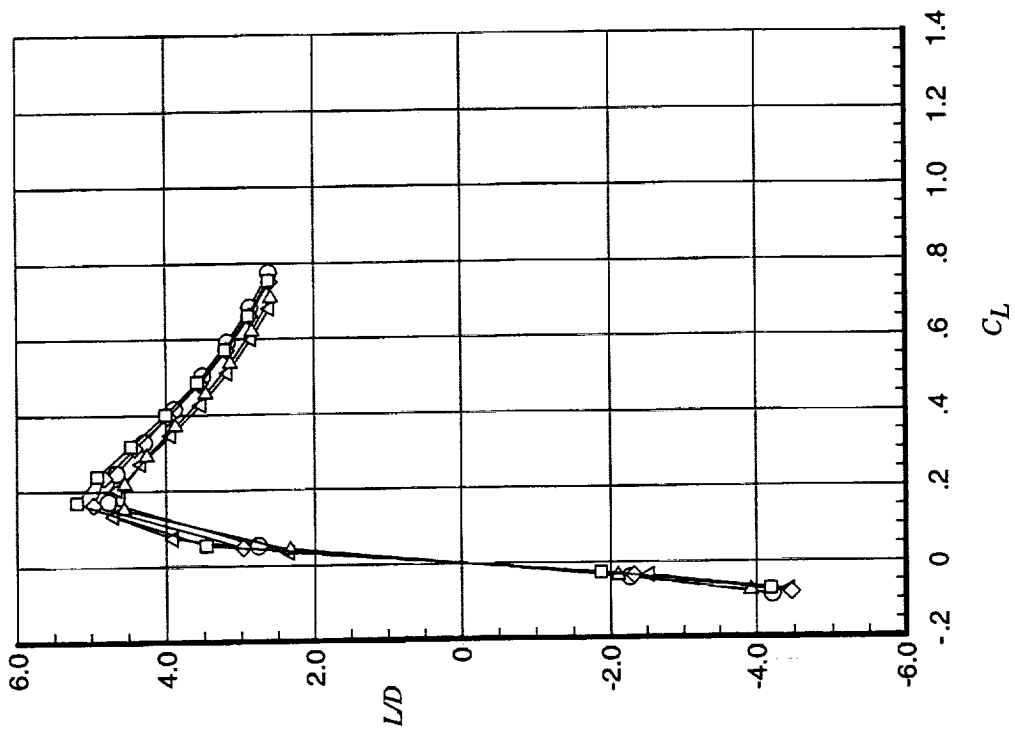


Figure 16. Vortex system on cranked delta planform with vortex and TE flaps deployed.



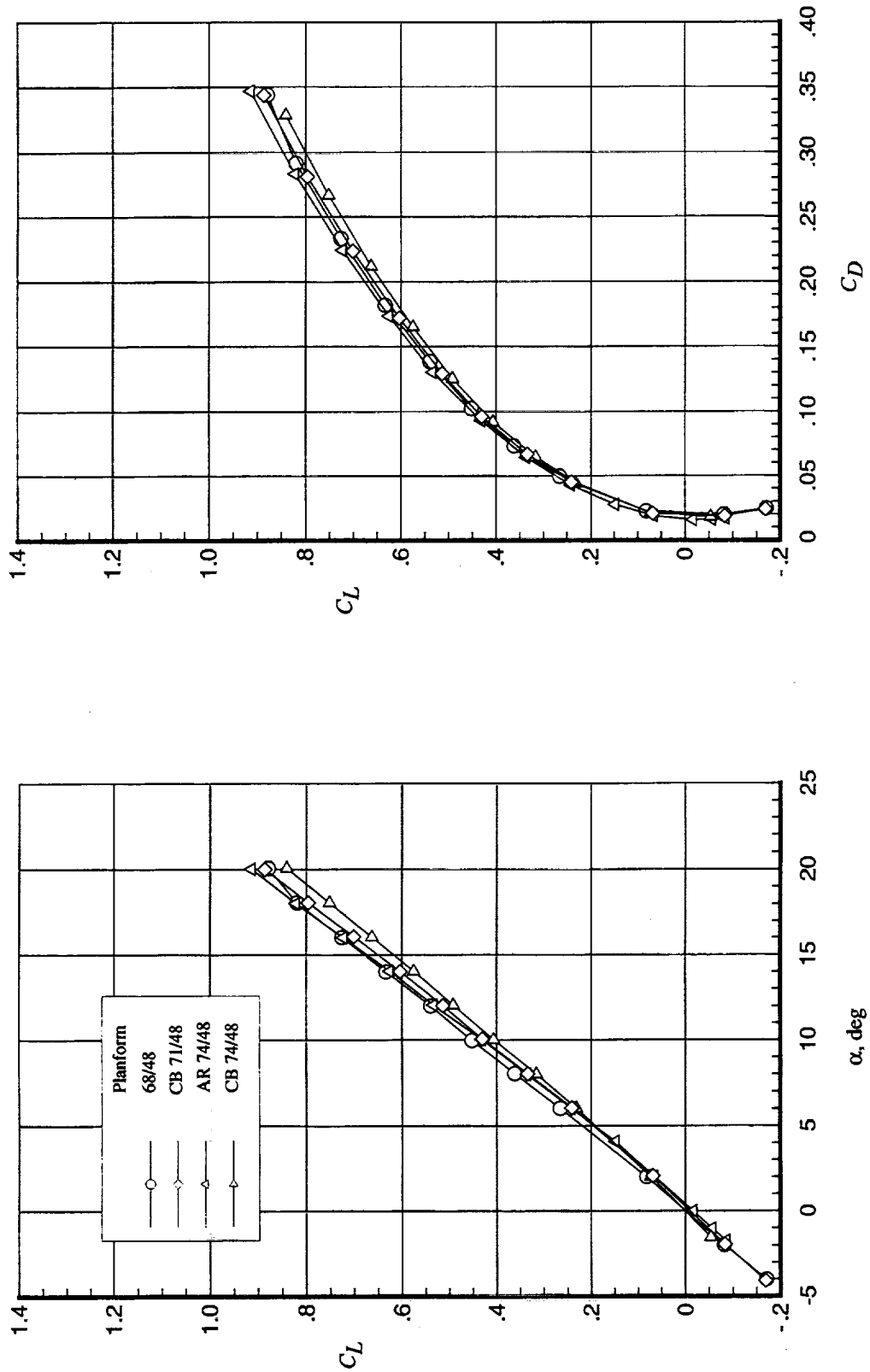
(a) Lift and drag data.

Figure 17. Longitudinal aerodynamics of clipped delta planforms in cruise configuration. $q_\infty = 70$ psf; $\delta_{vf} = \text{off}$; $\delta_{bf} = 0^\circ$; $\delta_{obf} = 0^\circ$; and OBLE flaps off.



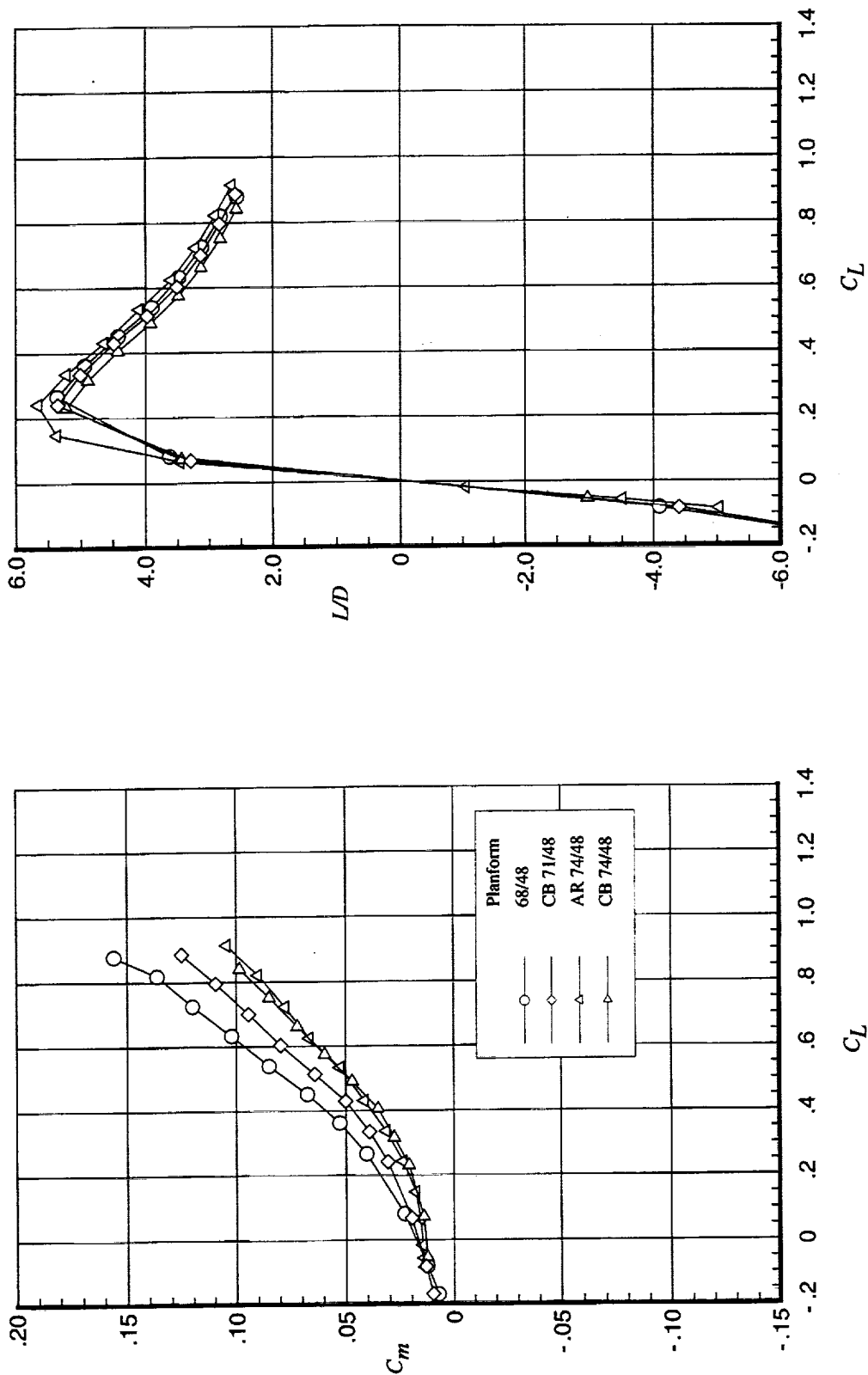
(b) Pitching-moment and LD data.

Figure 17. Concluded.



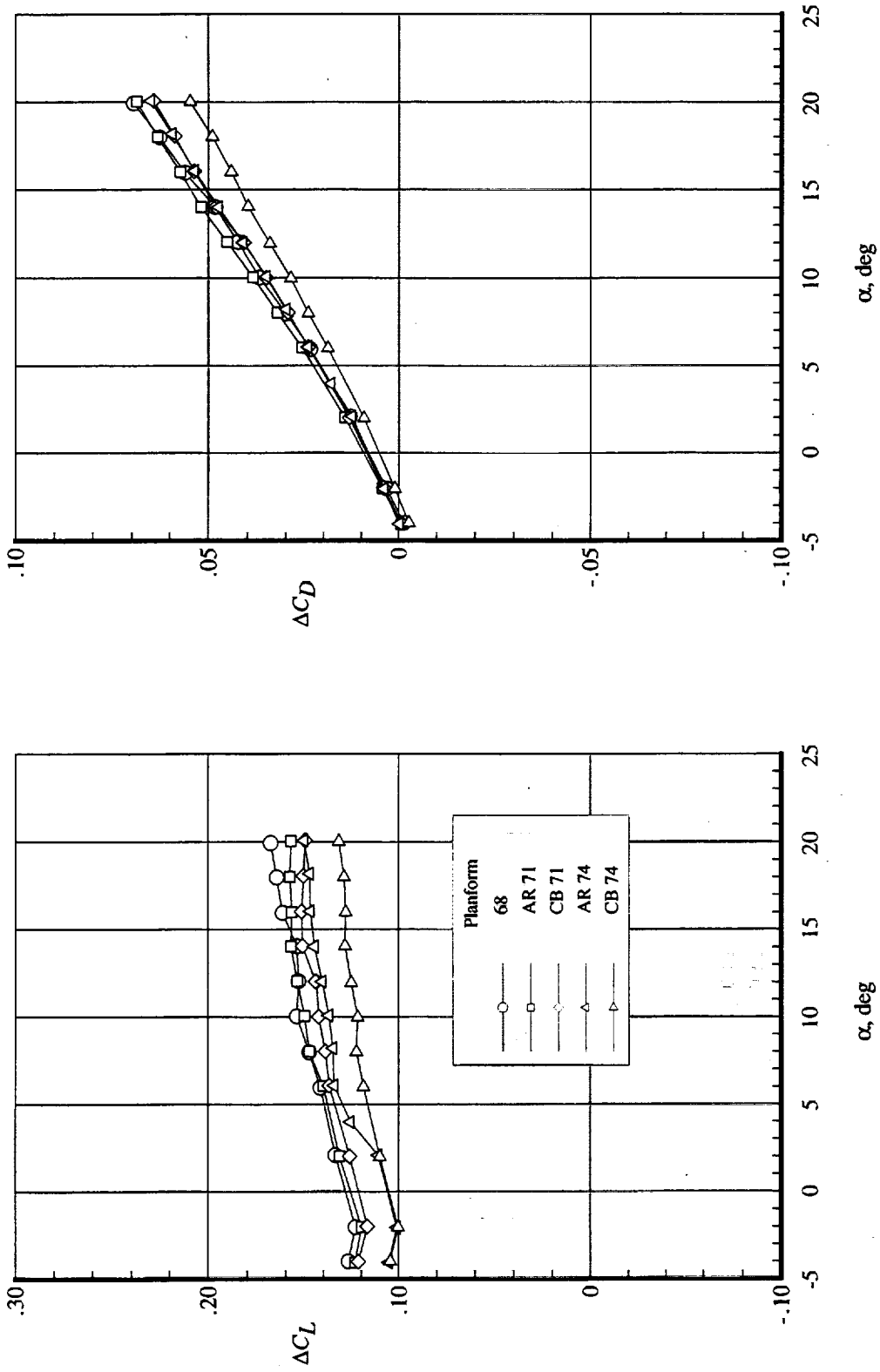
(a) Lift and drag data.

Figure 18. Longitudinal aerodynamics of cranked delta planforms in cruise configuration. $q_\infty = 70$ psf; $\delta_{bf} = 0^\circ$; $\delta_{obf} = 0^\circ$; and OBLE flaps off.



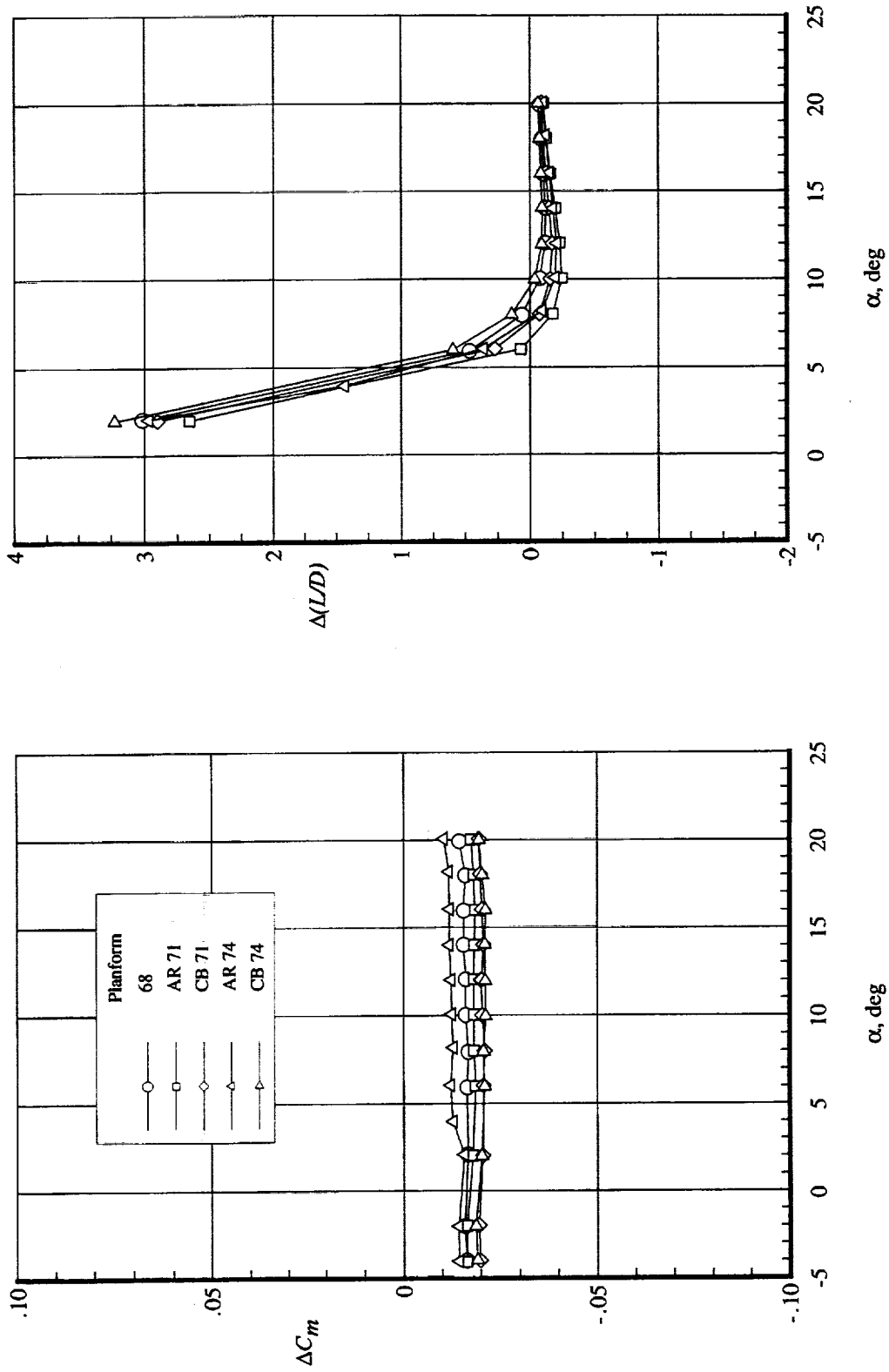
(b) Pitching-moment and LD data.

Figure 18. Concluded.



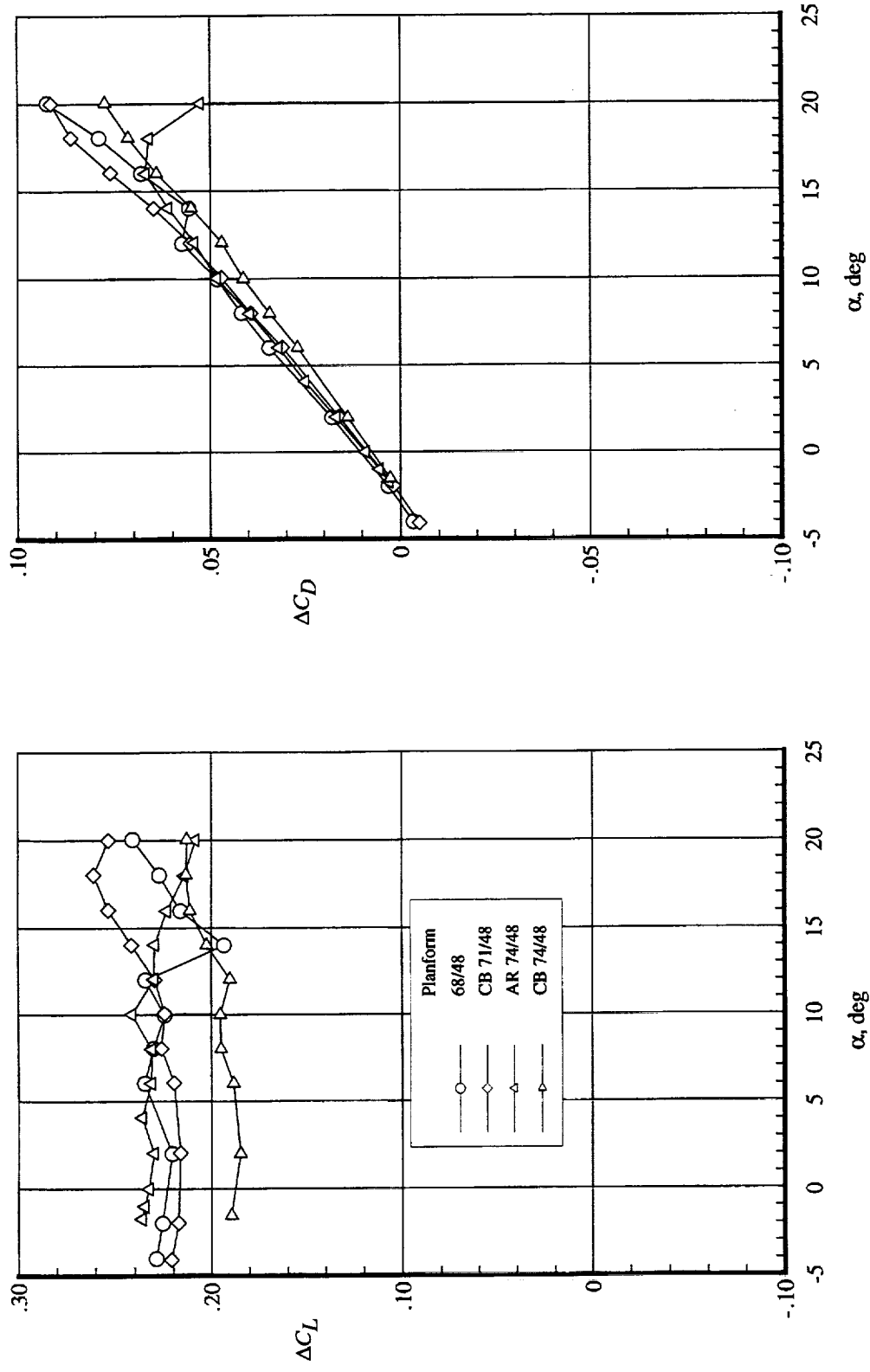
(a) Lift and drag data.

Figure 19. Trailing-edge flap effectiveness for clipped delta planforms. $q_\infty = 70$ psf; $\delta_{vf} = \text{off}$; $\delta_{hbf} = 15^\circ$; and $\Delta = \text{TE flaps} - \text{cruise}$.



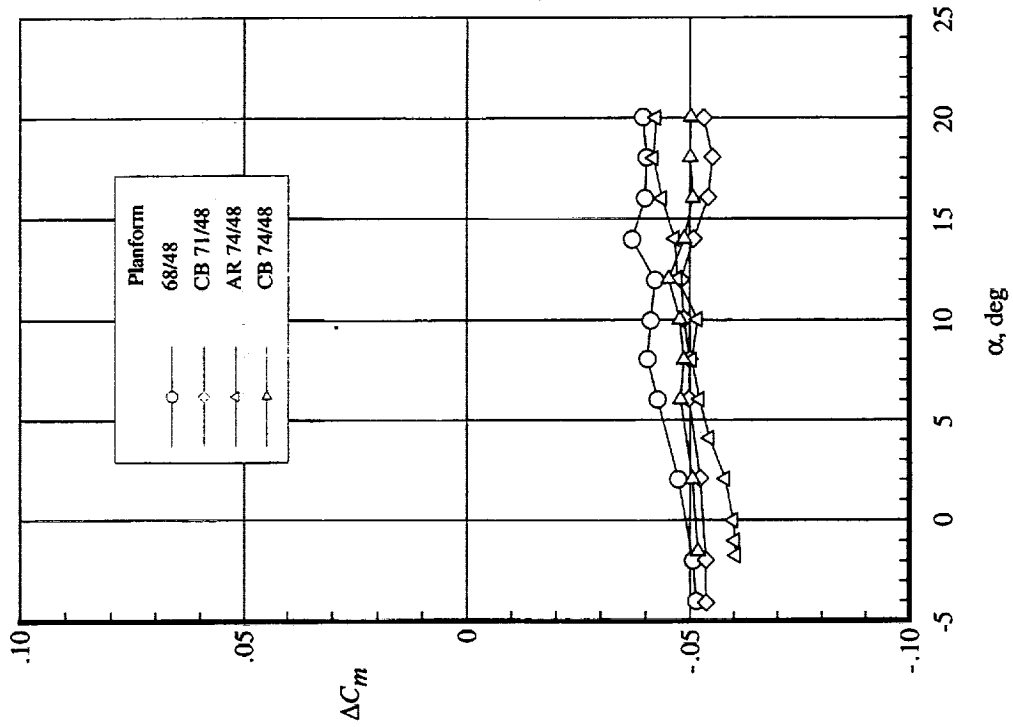
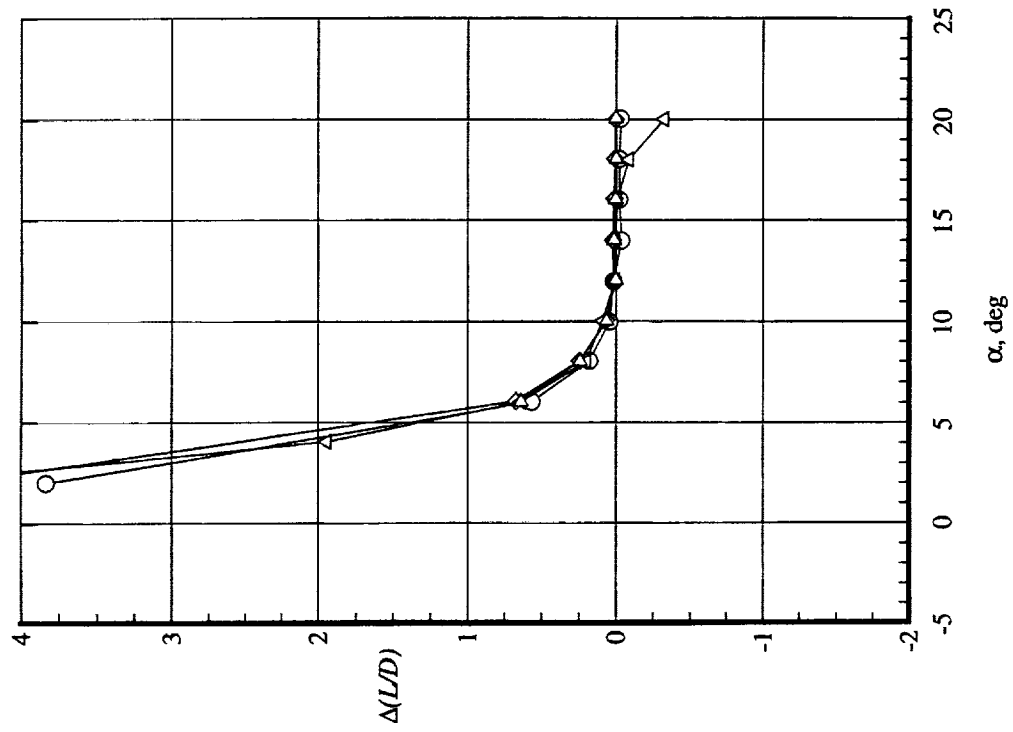
(b) Pitching-moment and L/D data.

Figure 19. Concluded.



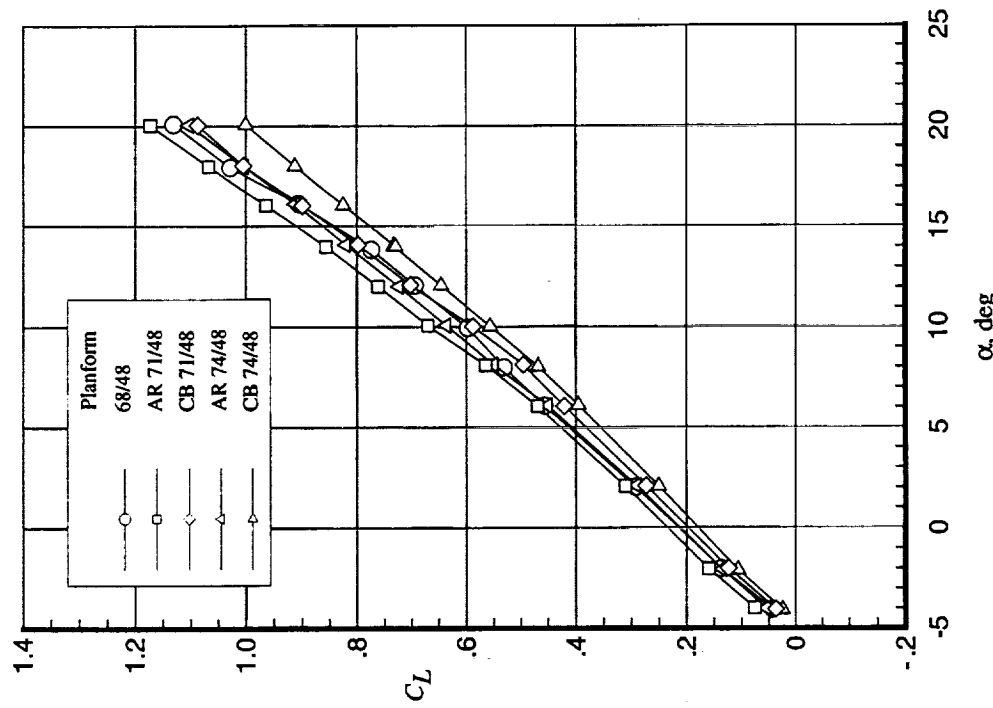
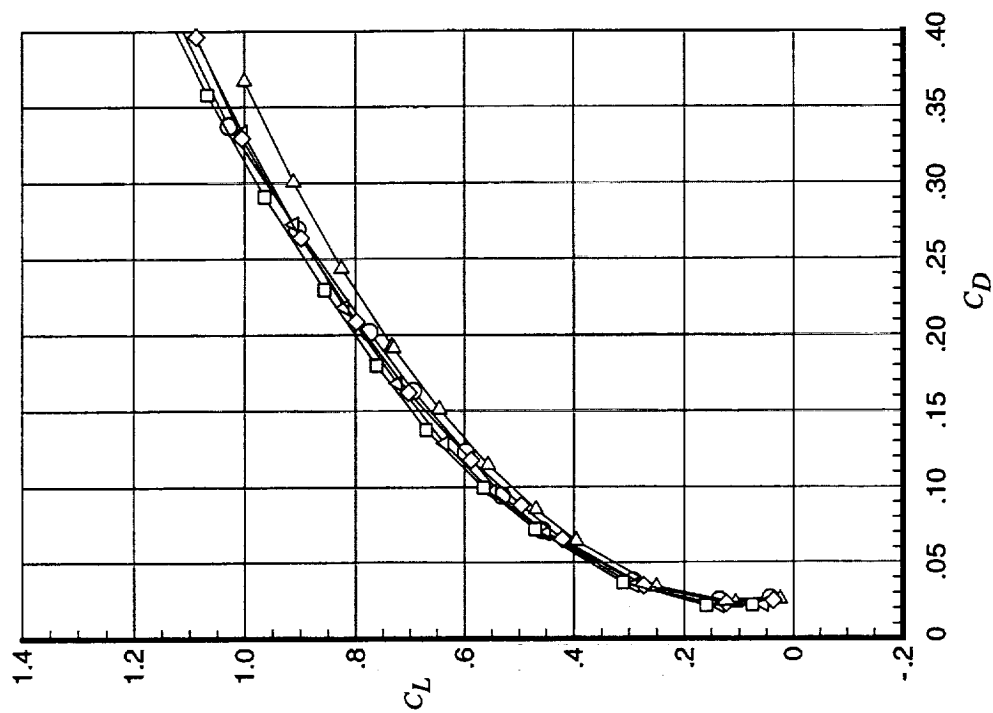
(a) Lift and drag data.

Figure 20. Trailing-edge flap effectiveness on cranked delta planforms. $q_\infty = 70$ psf; $\delta_{vf} = \text{off}$; $\delta_{hbf} = 15^\circ$; $\delta_{obf} = 15^\circ$; OBLE flaps off; and $\Delta = \text{TE flaps} - \text{cruise}$.



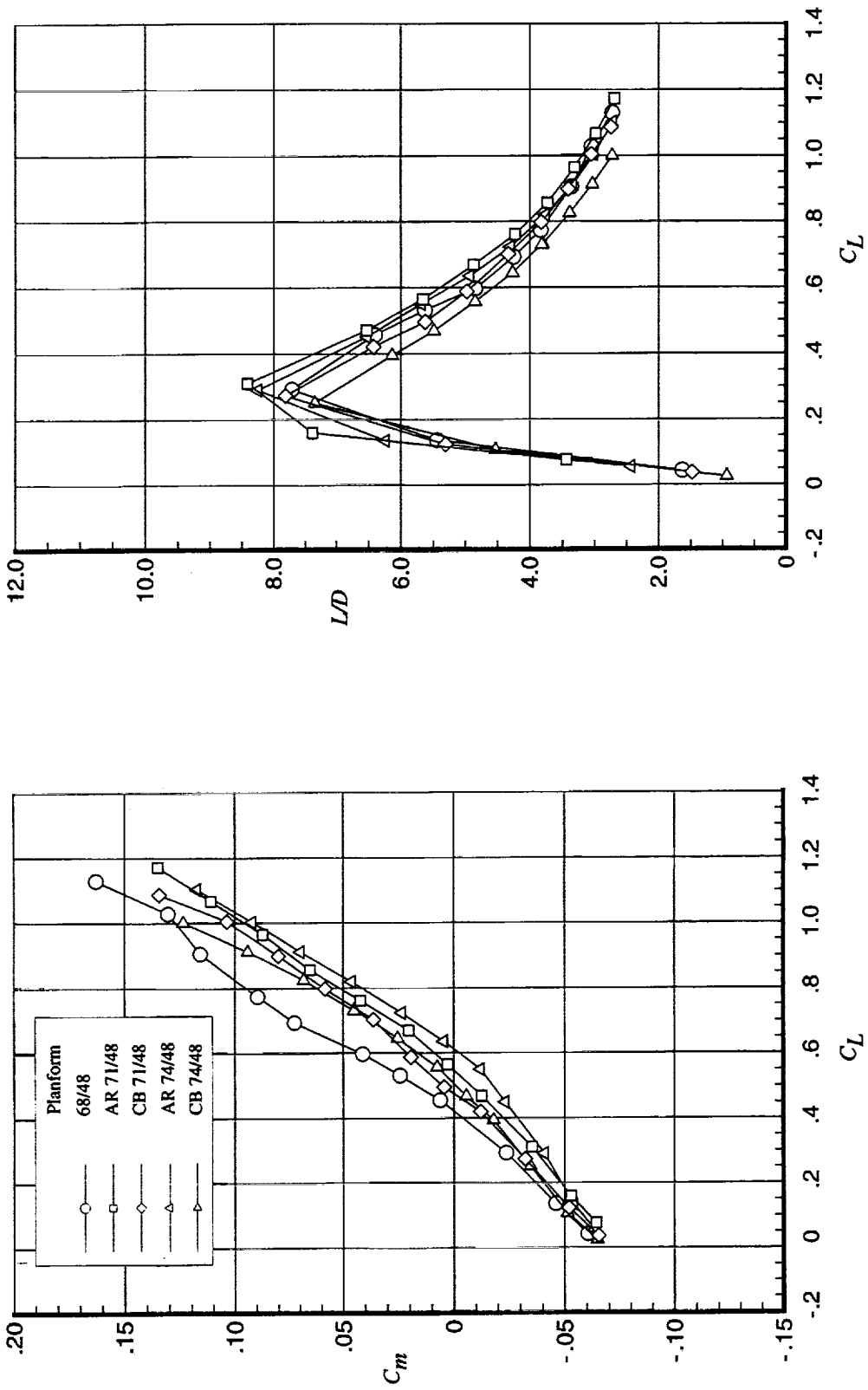
(b) Pitching-moment and L/D data.

Figure 20. Concluded.



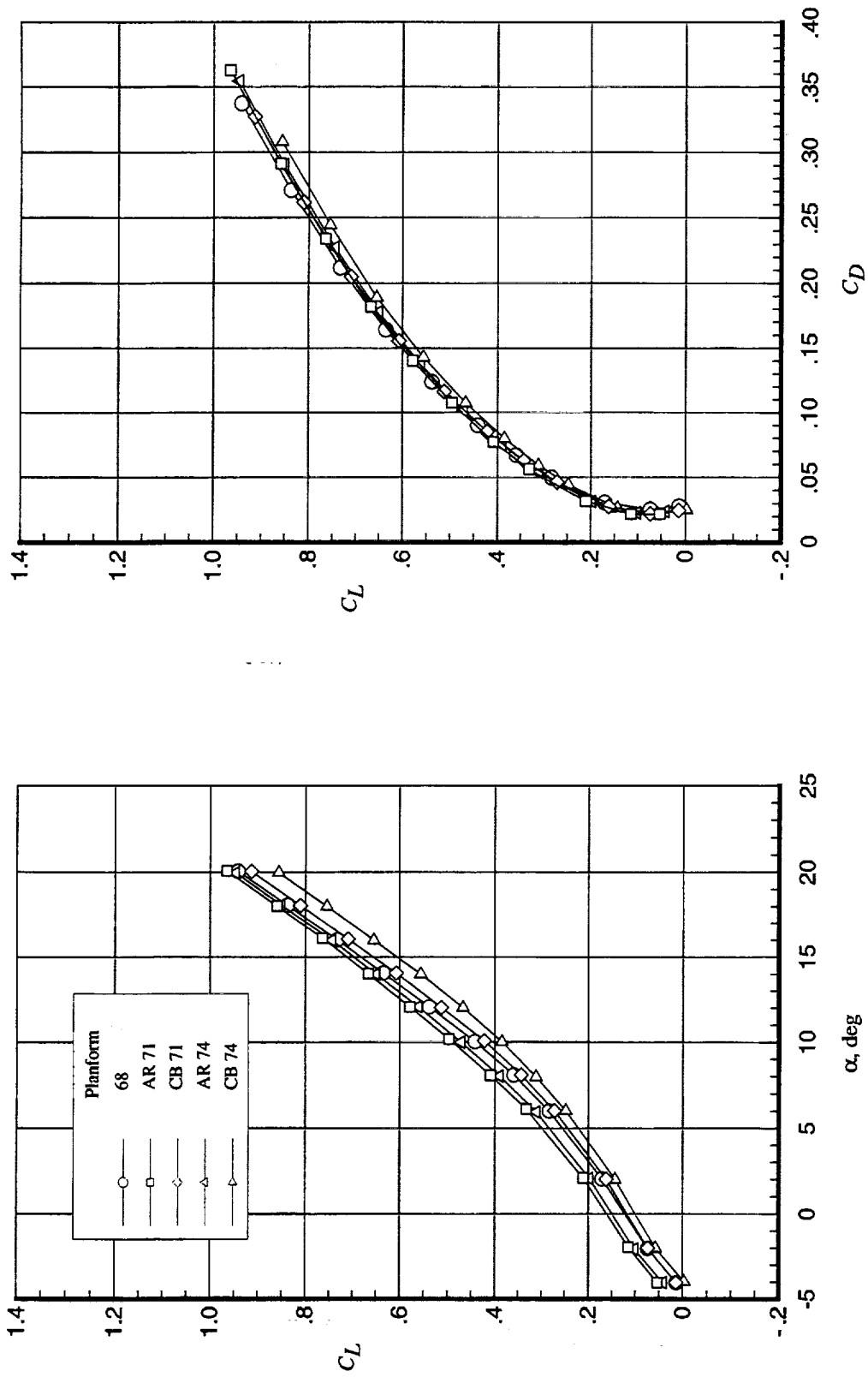
(a) Lift and drag data.

Figure 21. Longitudinal aerodynamics of cranked delta planforms in vortex flap design configuration. $q_\infty = 70$ psf; $\delta_{vf} = \text{off}$; $\delta_{ibf} = 15^\circ$; $\delta_{obf} = 15^\circ$; and OBLE flaps off.



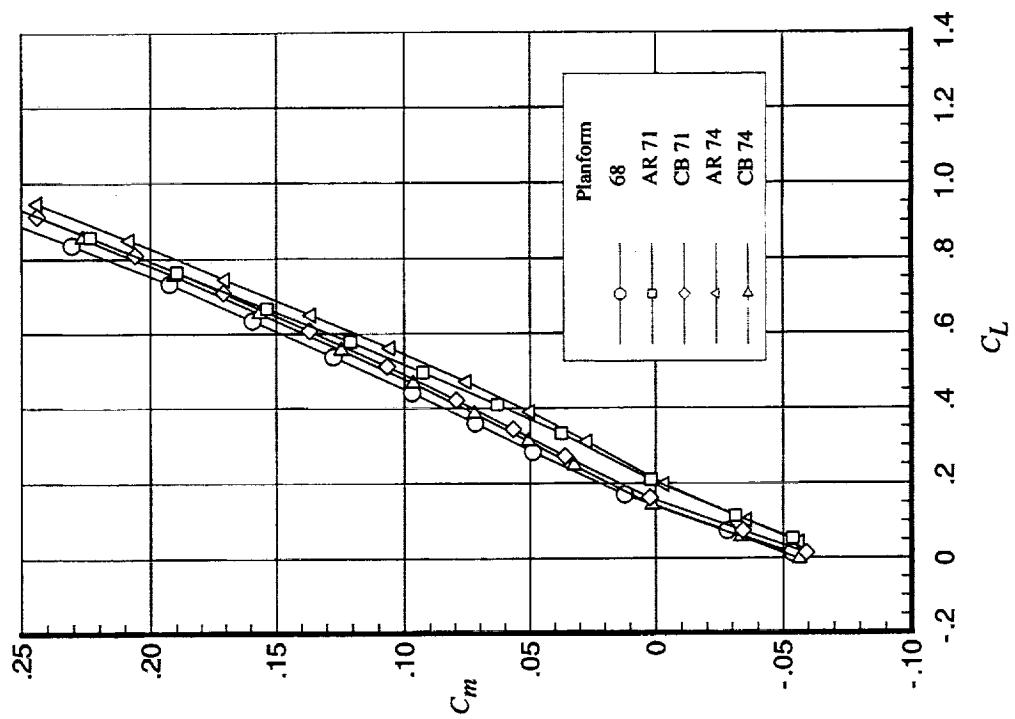
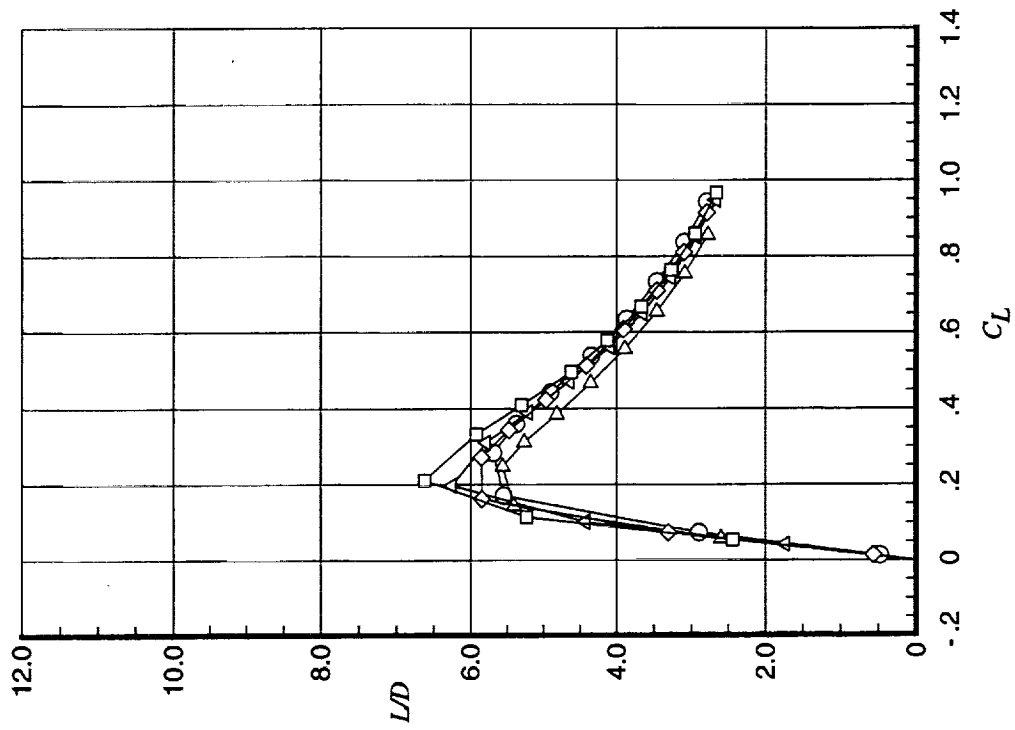
(b) Pitching-moment and L/D data.

Figure 21. Concluded.



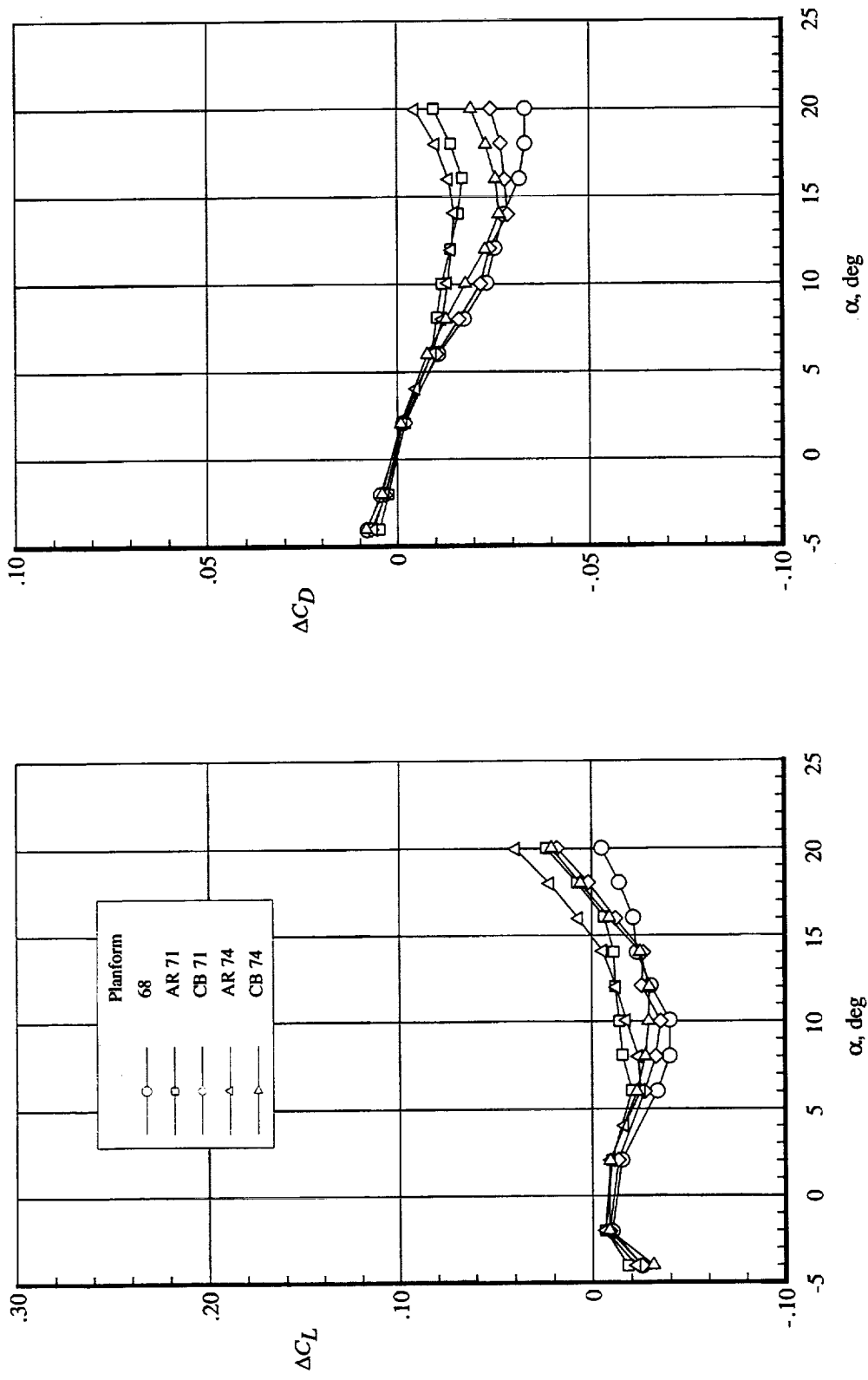
(a) Lift and drag data.

Figure 22. Longitudinal aerodynamics of clipped delta planforms in vortex flap design configuration. $q_\infty = 70$ psf; $\delta_{vf} = 30^\circ$; and $\delta_{bf} = 15^\circ$.



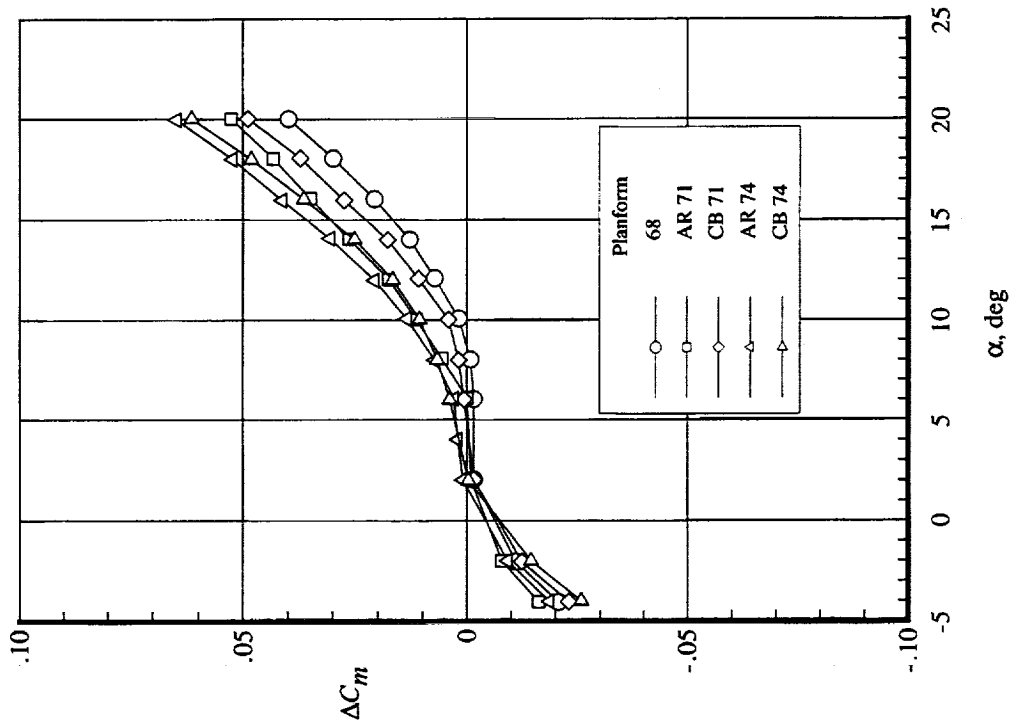
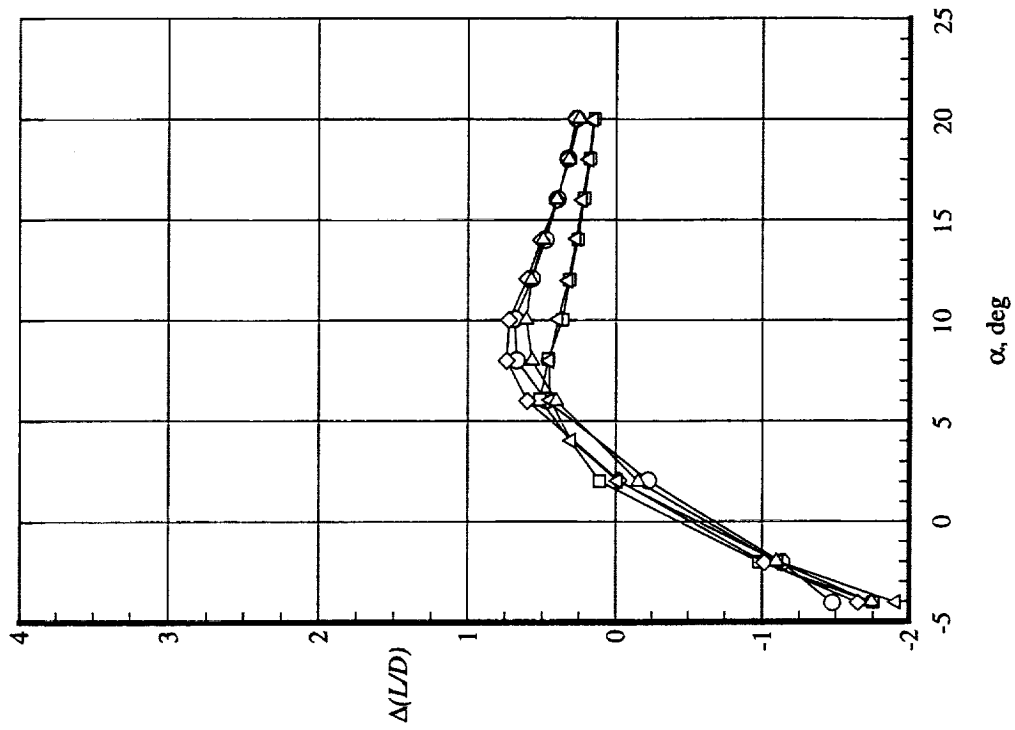
(b) Pitching-moment and LD data.

Figure 22. Concluded.



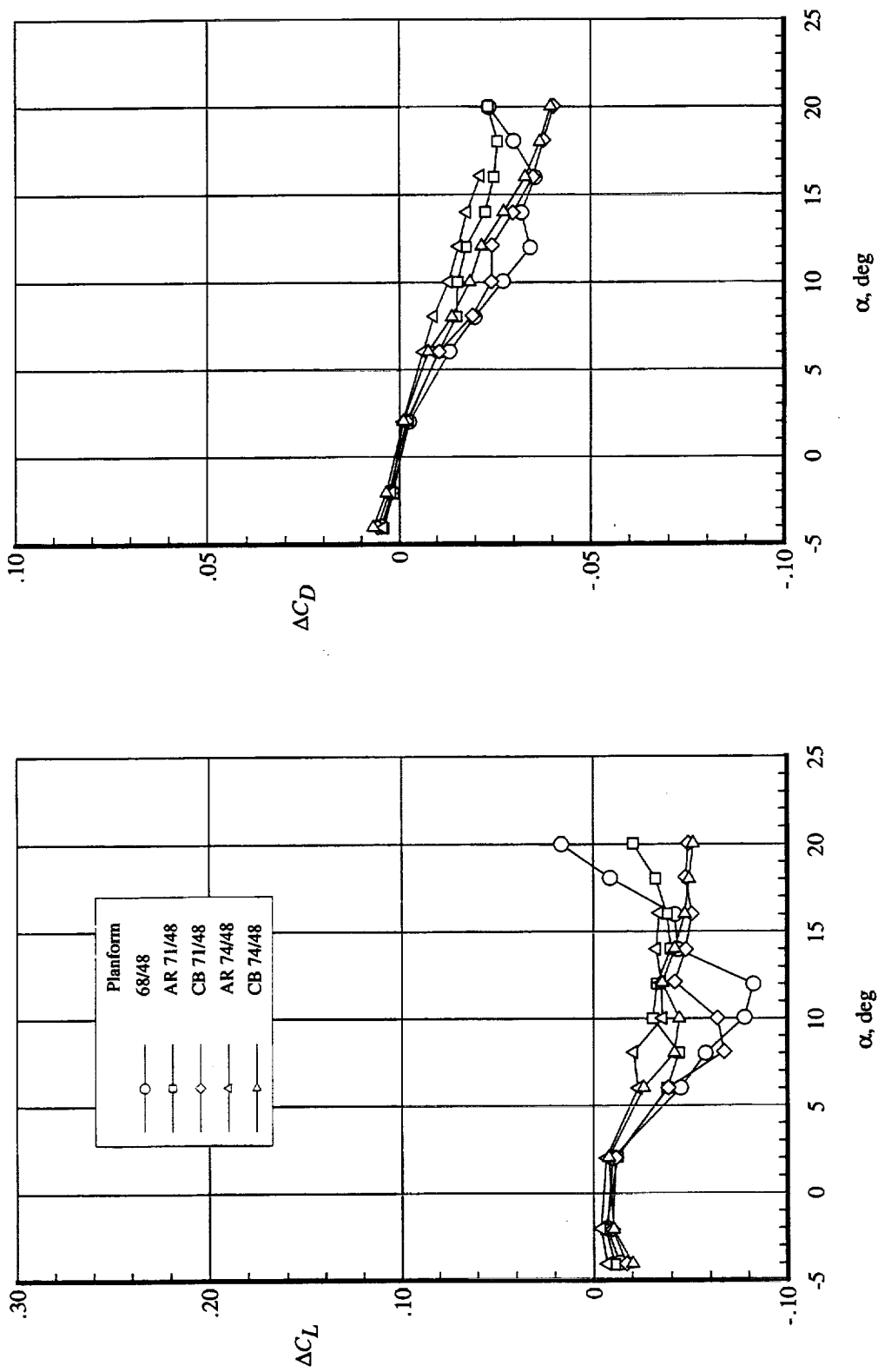
(a) Lift and drag data.

Figure 23. Vortex flap effectiveness for clipped delta planforms. $q_\infty = 70$ psf; $\delta_{vf} = 30^\circ$; $\delta_{bf} = 15^\circ$; and $\Delta =$ vortex flap on - vortex flap off.



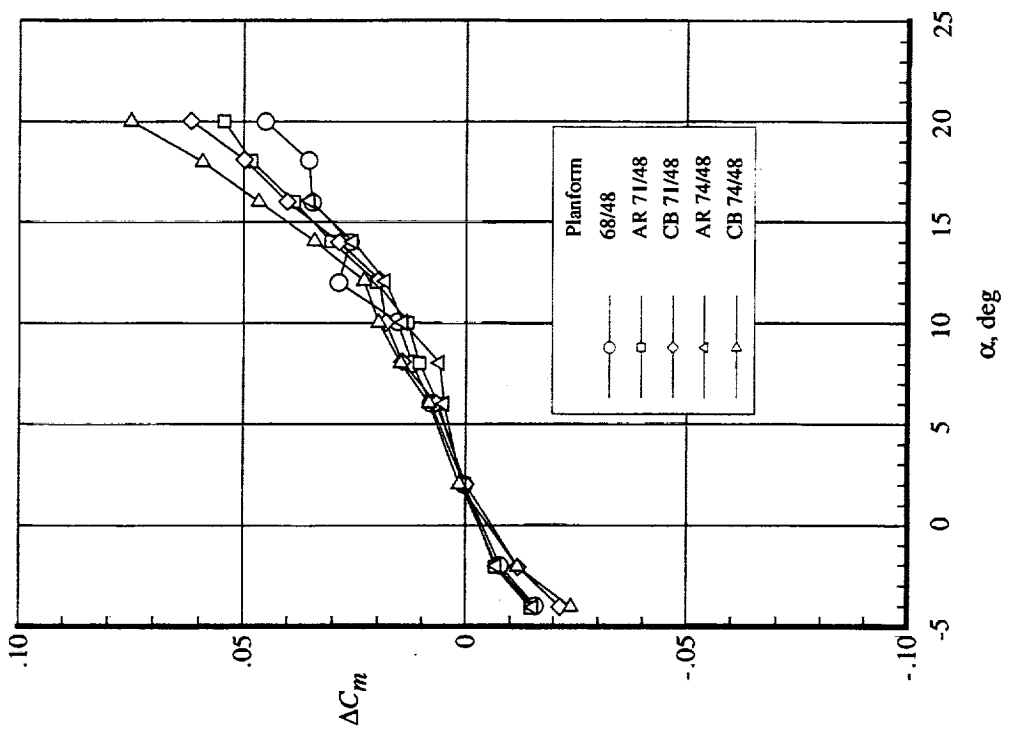
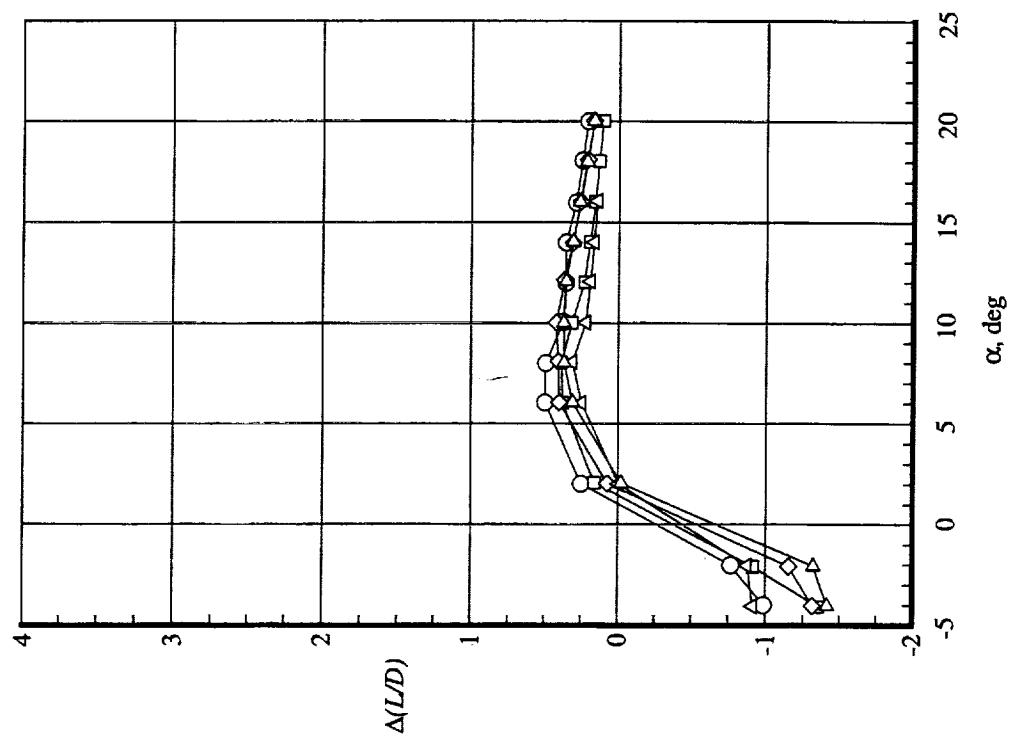
(b) Pitching-moment and L/D data.

Figure 23. Concluded.



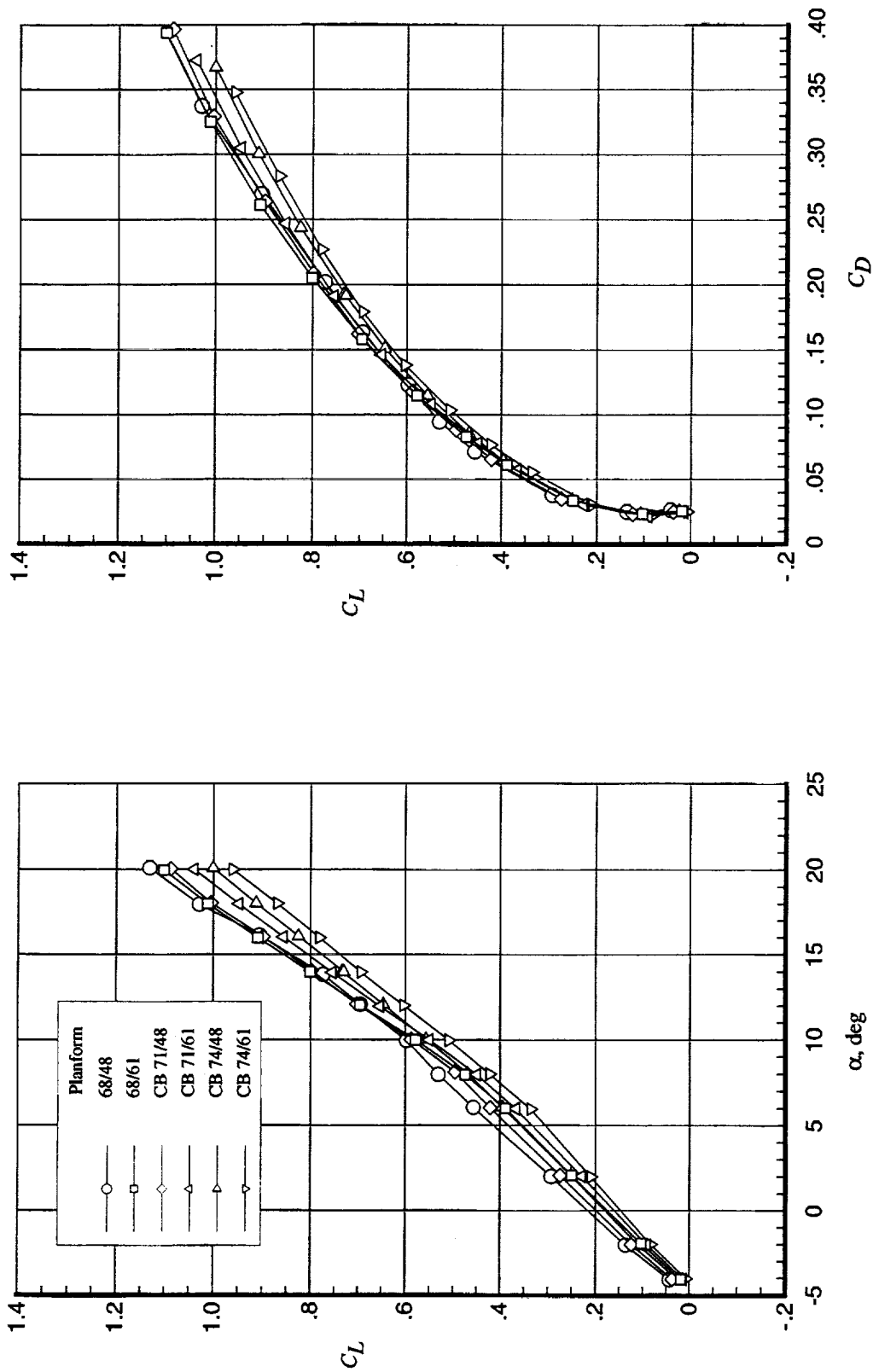
(a) Lift and drag data.

Figure 24. Vortex flap effectiveness for cranked delta planforms. $q_\infty = 70$ psf; $\delta_{vf} = 30^\circ$; $\delta_{jbf} = 15^\circ$; $\delta_{obf} = 15^\circ$; OBLE flaps off; and Δ = vortex flap on - vortex flap off.



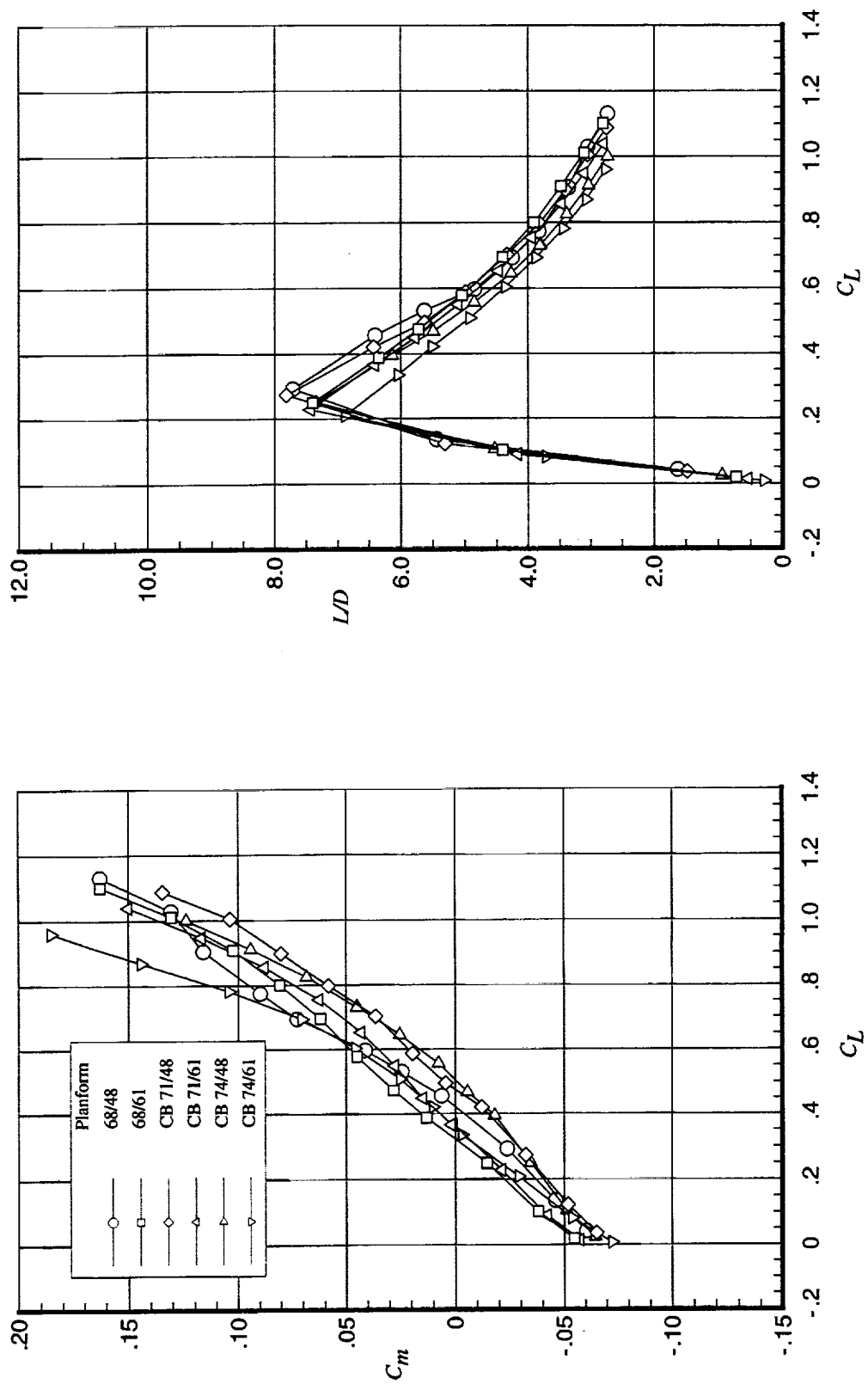
(b) Pitching-moment and L/D data.

Figure 24. Concluded.



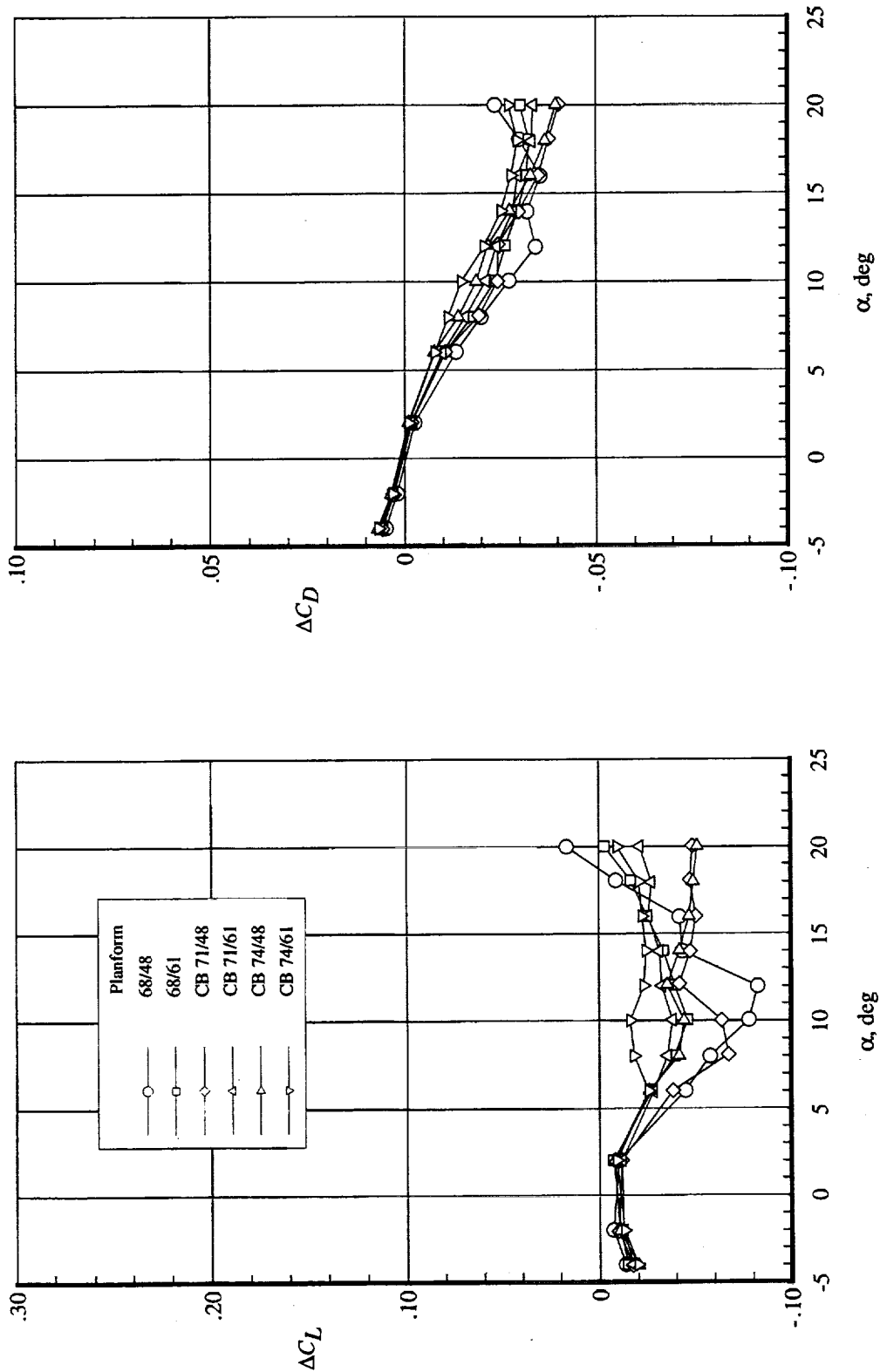
(a) Lift and drag data.

Figure 25. Effect of platform variations of outboard wing on longitudinal aerodynamics of cranked delta planforms in CB family. $q_\infty = 70$ psf; $\delta_{vf} = 30^\circ$; $\delta_{hbf} = 15^\circ$; $\delta_{obf} = 15^\circ$; and OBLE flaps off.



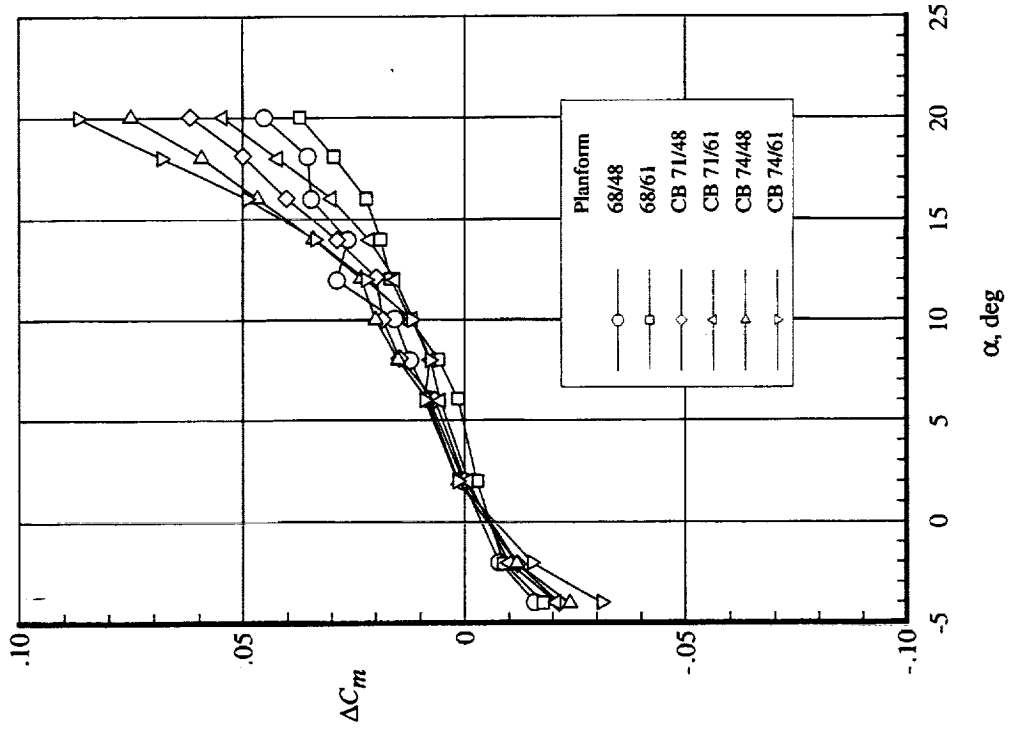
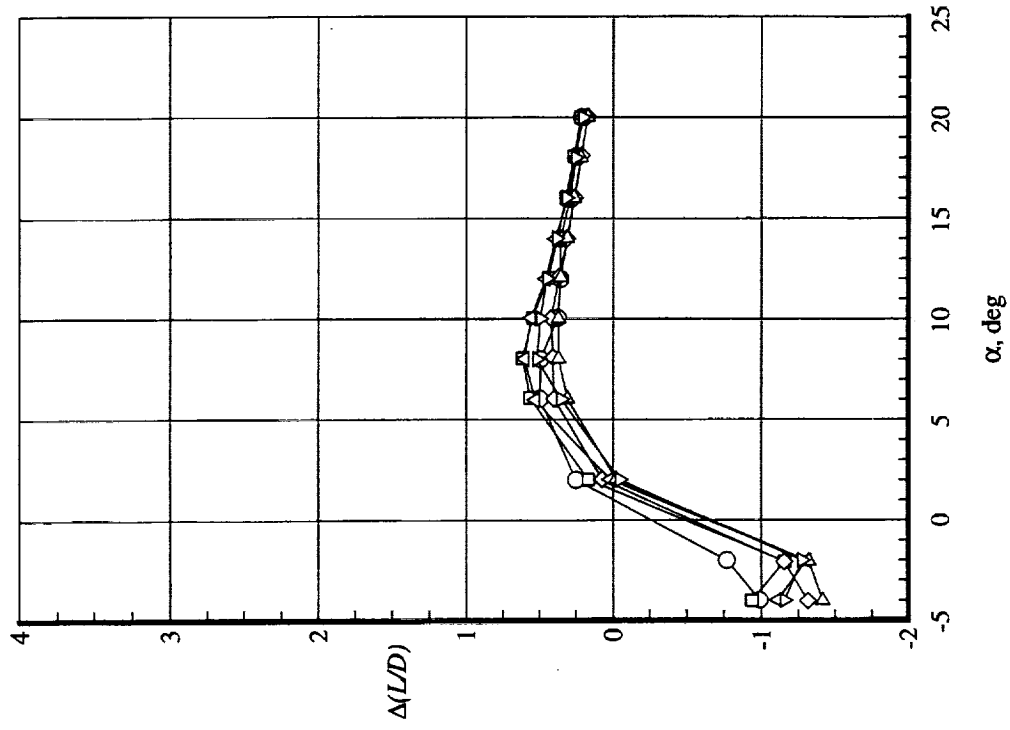
(b) Pitching-moment and L/D data.

Figure 25. Concluded.



(a) Lift and drag data.

Figure 26. Effect of platform variations of outboard wing on vortex flap performance. $q_\infty = 70$ psf; $\delta_{vf} = 30^\circ$; $\delta_{hbf} = 15^\circ$; $\delta_{obf} = 15^\circ$; OBLE flaps off; and $\Delta =$ vortex flap on - vortex flap off.



(b) Pitching-moment and *L/D* data.

Figure 26. Concluded.

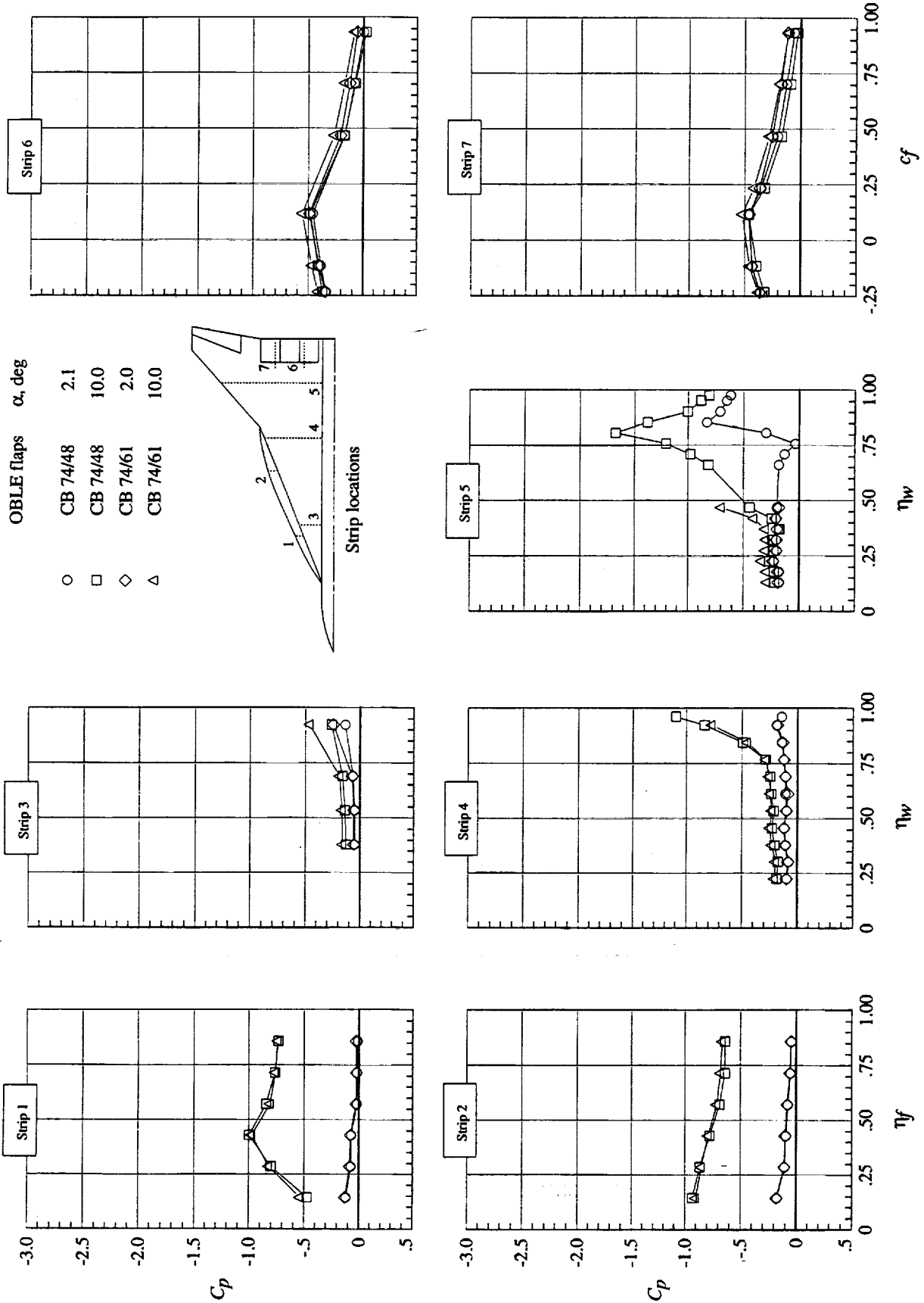
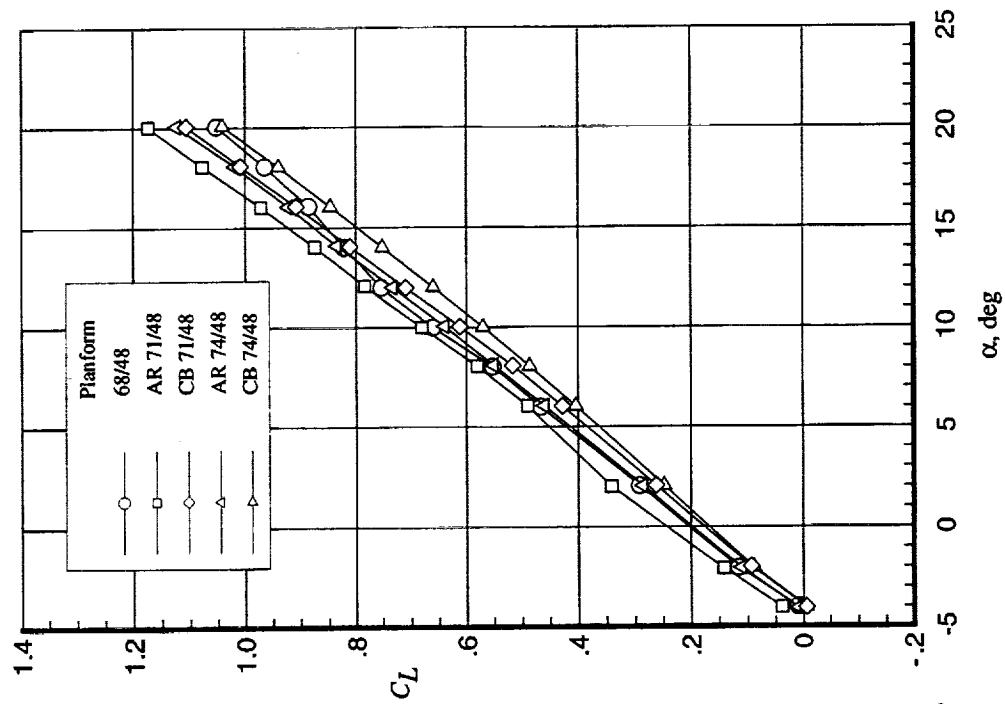
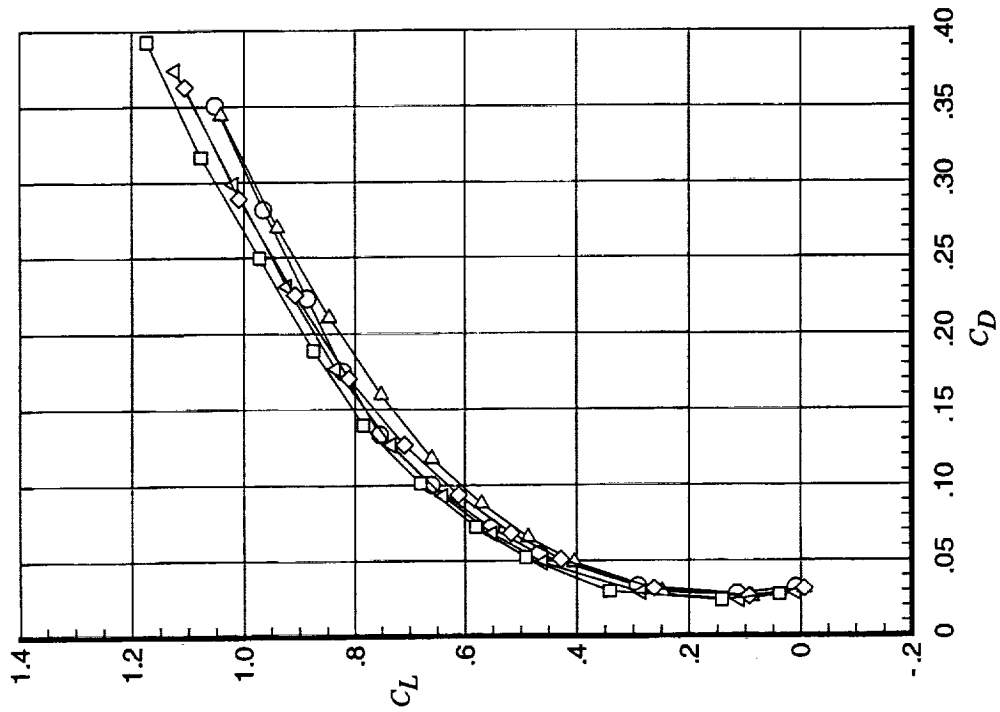
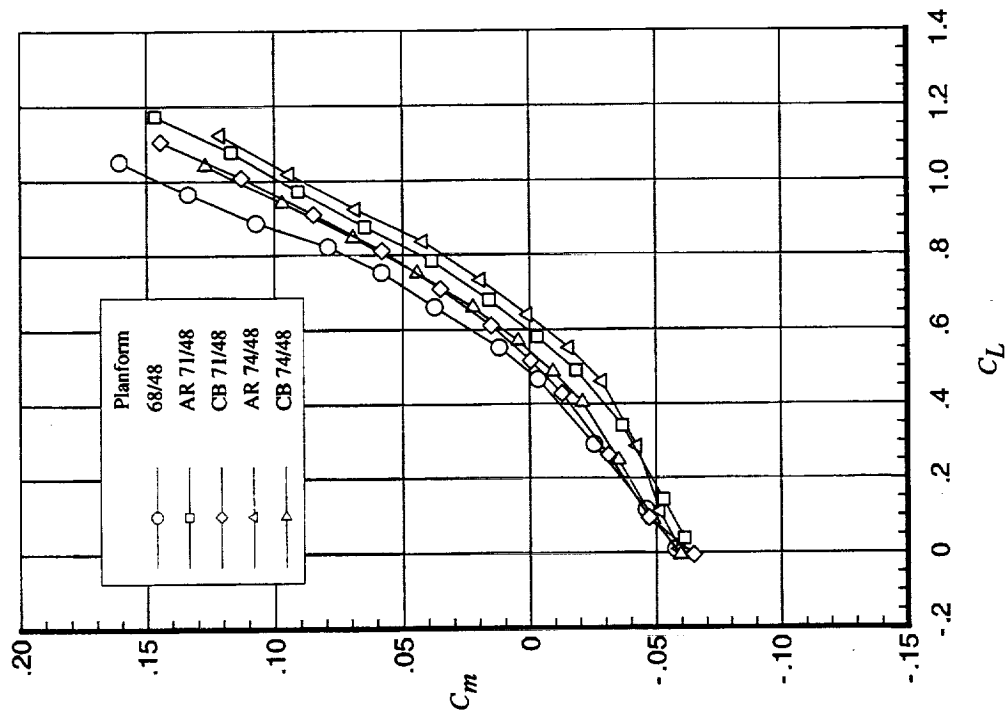
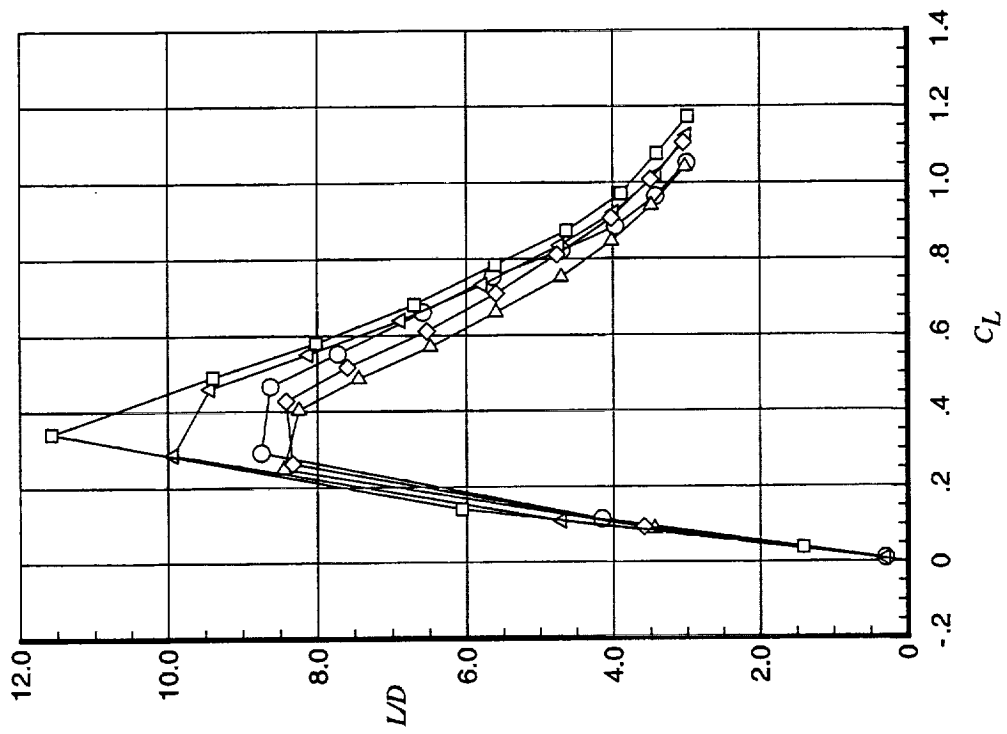


Figure 27. Planforms CB 74/48 and 74/61 surface pressure distributions. $q_\infty = 70$ psf; $\delta_{vf} = 30^\circ$; $\delta_{bf} = 15^\circ$; $\delta_{obf} = 15^\circ$; and OBLE flaps off.



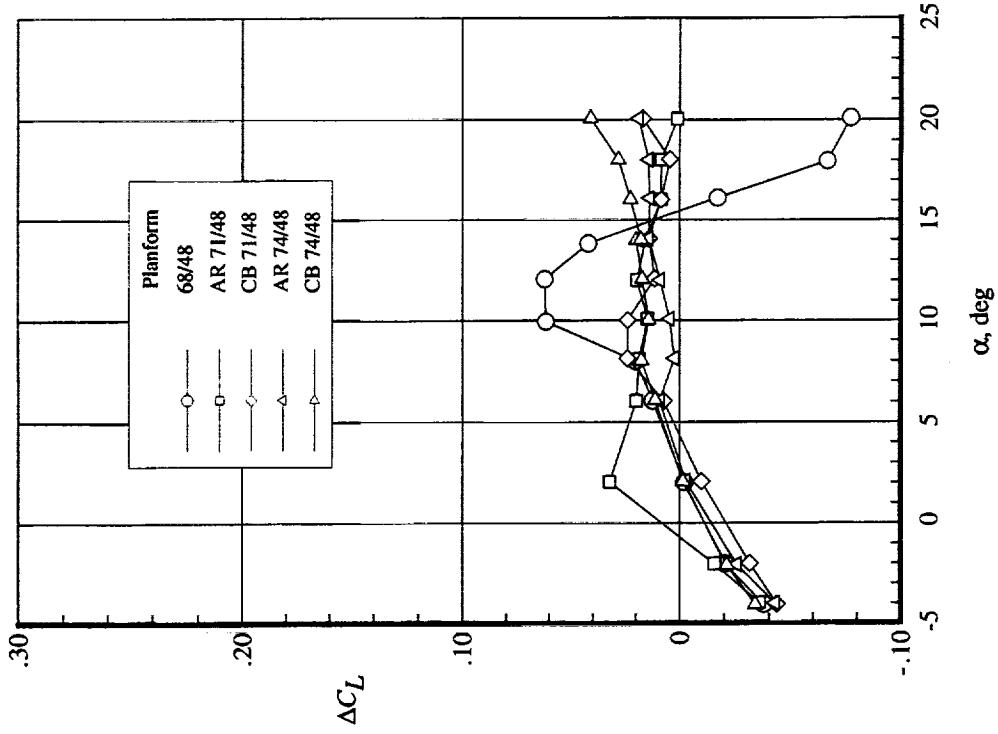
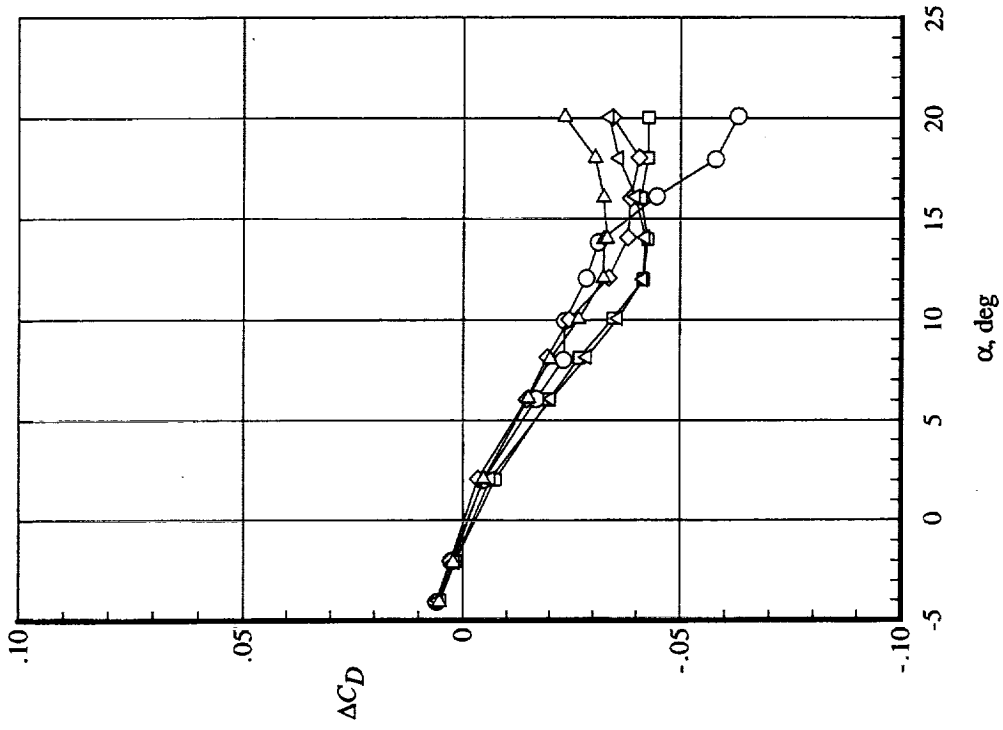
(a) Lift and drag data.

Figure 28. Longitudinal aerodynamics of cranked delta planforms with vortex and OBLE flaps. $q_\infty = 70$ psf; $\delta_{vf} = 30^\circ$; $\delta_{bf} = 15^\circ$; $\delta_{obf} = 15^\circ$; and OBLE flaps on.



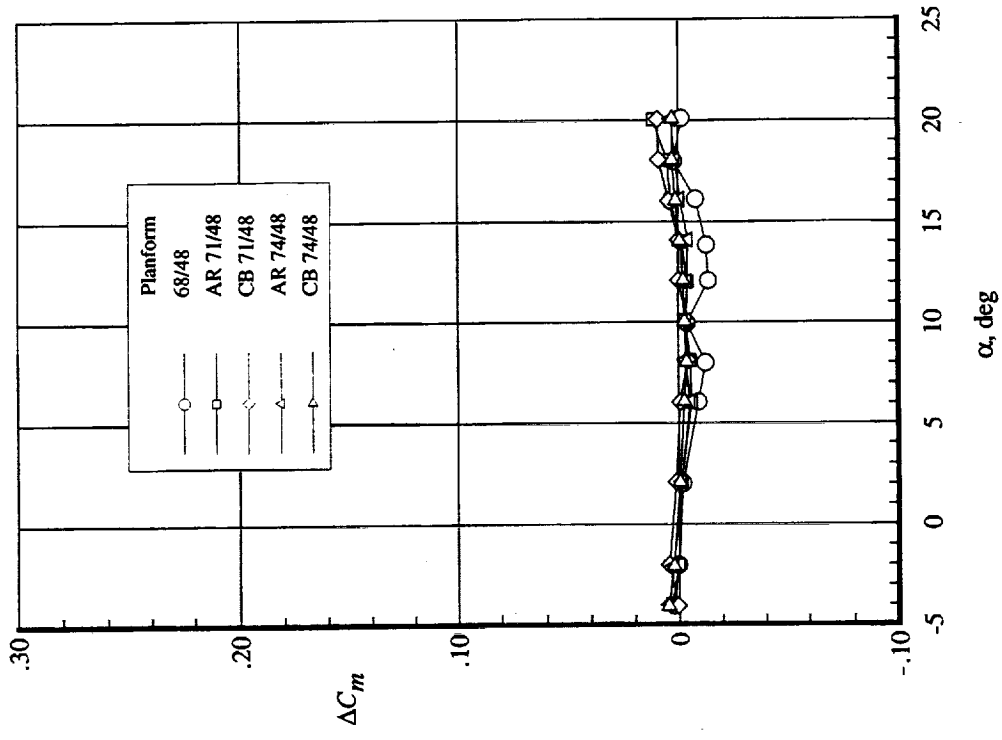
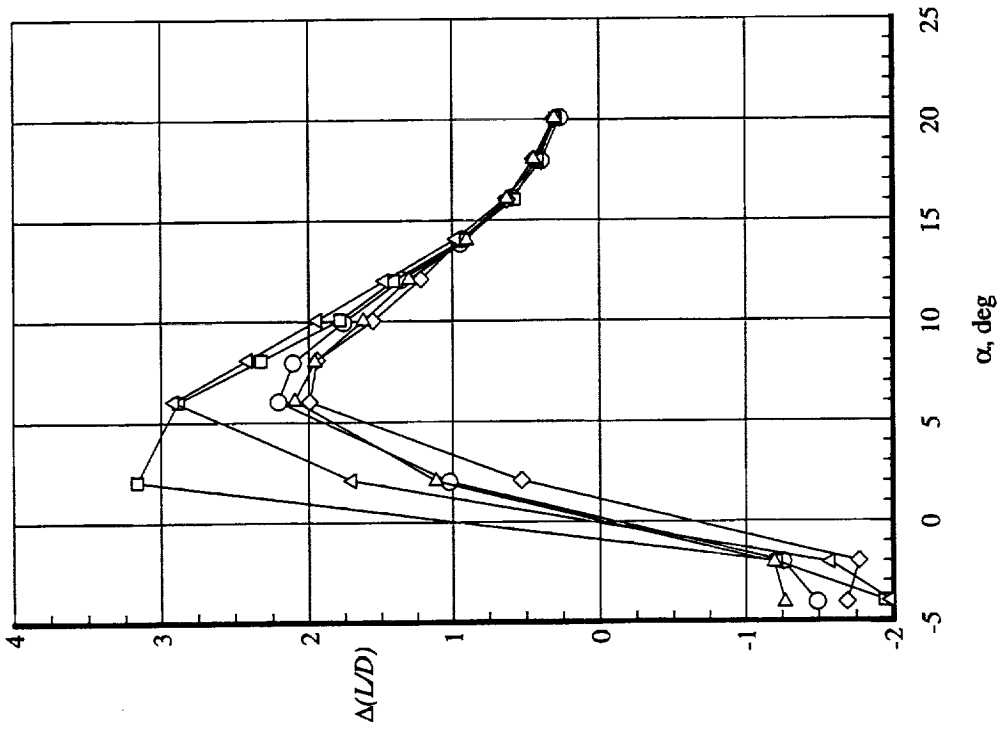
(b) Pitching-moment and L/D data.

Figure 28. Concluded.



(a) Lift and drag data.

Figure 29. Effect of OBLE flap on vortex flap performance. $q_\infty = 70$ psf; $\delta_{vf} = 30^\circ$; $\delta_{ibf} = 15^\circ$; $\delta_{obf} = 15^\circ$; and $\Delta = \text{OBLE flaps on} - \text{OBLE flaps off}$.



(b) Pitching-moment and L/D data.

Figure 29. Concluded.

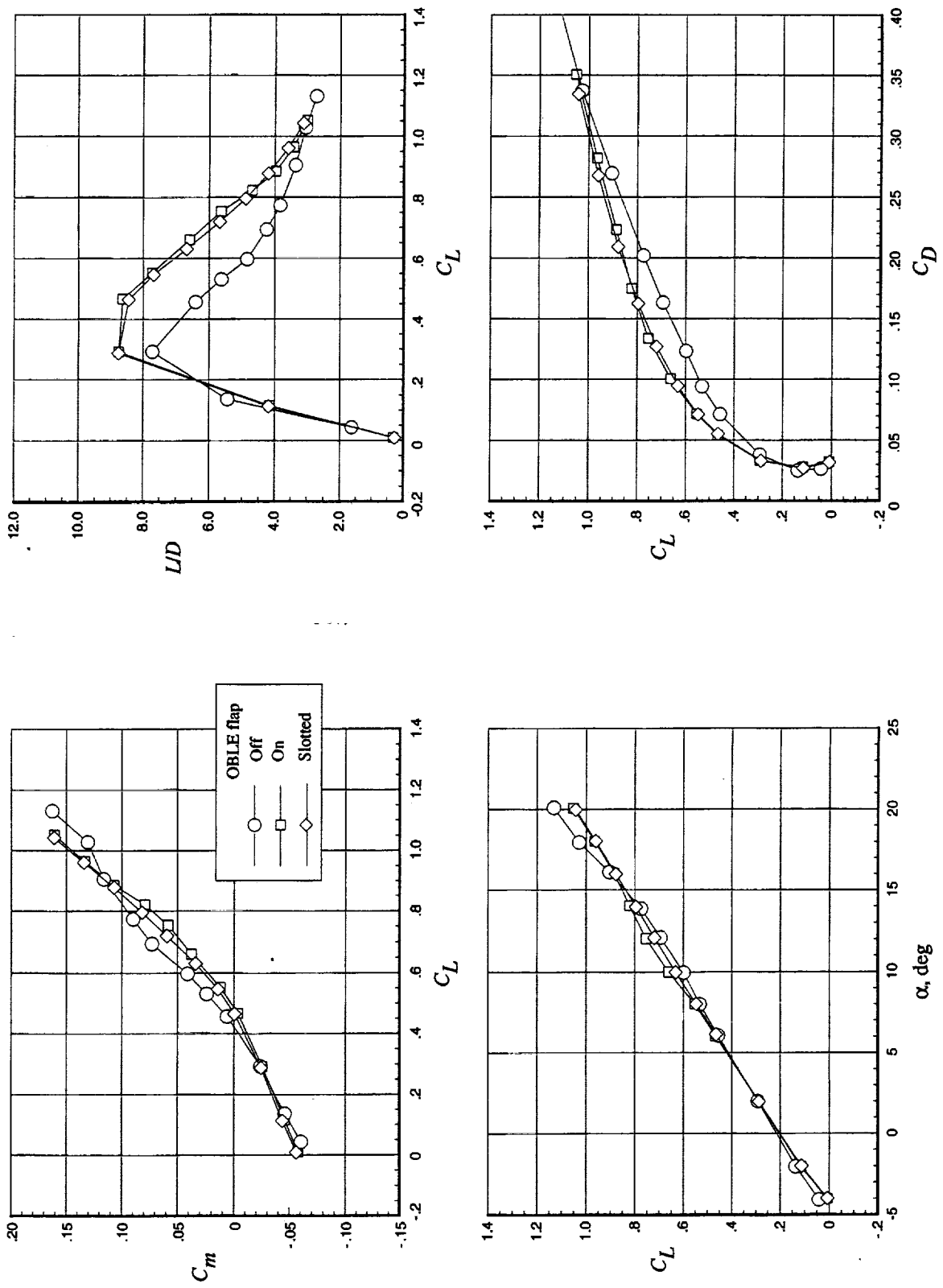


Figure 30. Effect of OBLE flaps on longitudinal aerodynamics of cranked delta planform 68/48. $q_\infty = 70$ psf; $\delta_{\text{vfl}} = 30^\circ$; $\delta_{\text{hfl}} = 15^\circ$; and $\delta_{\text{obfl}} = 15^\circ$.

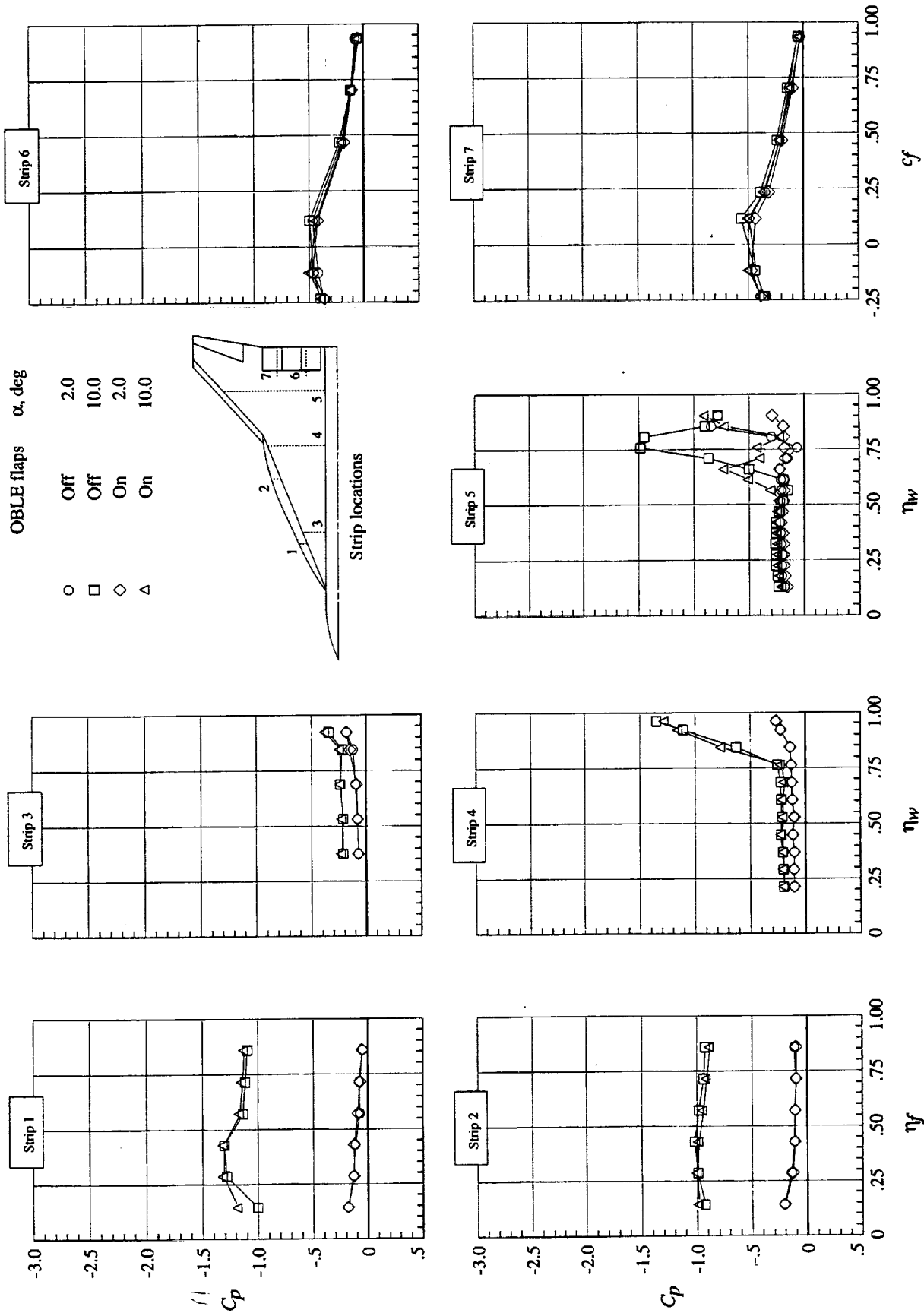
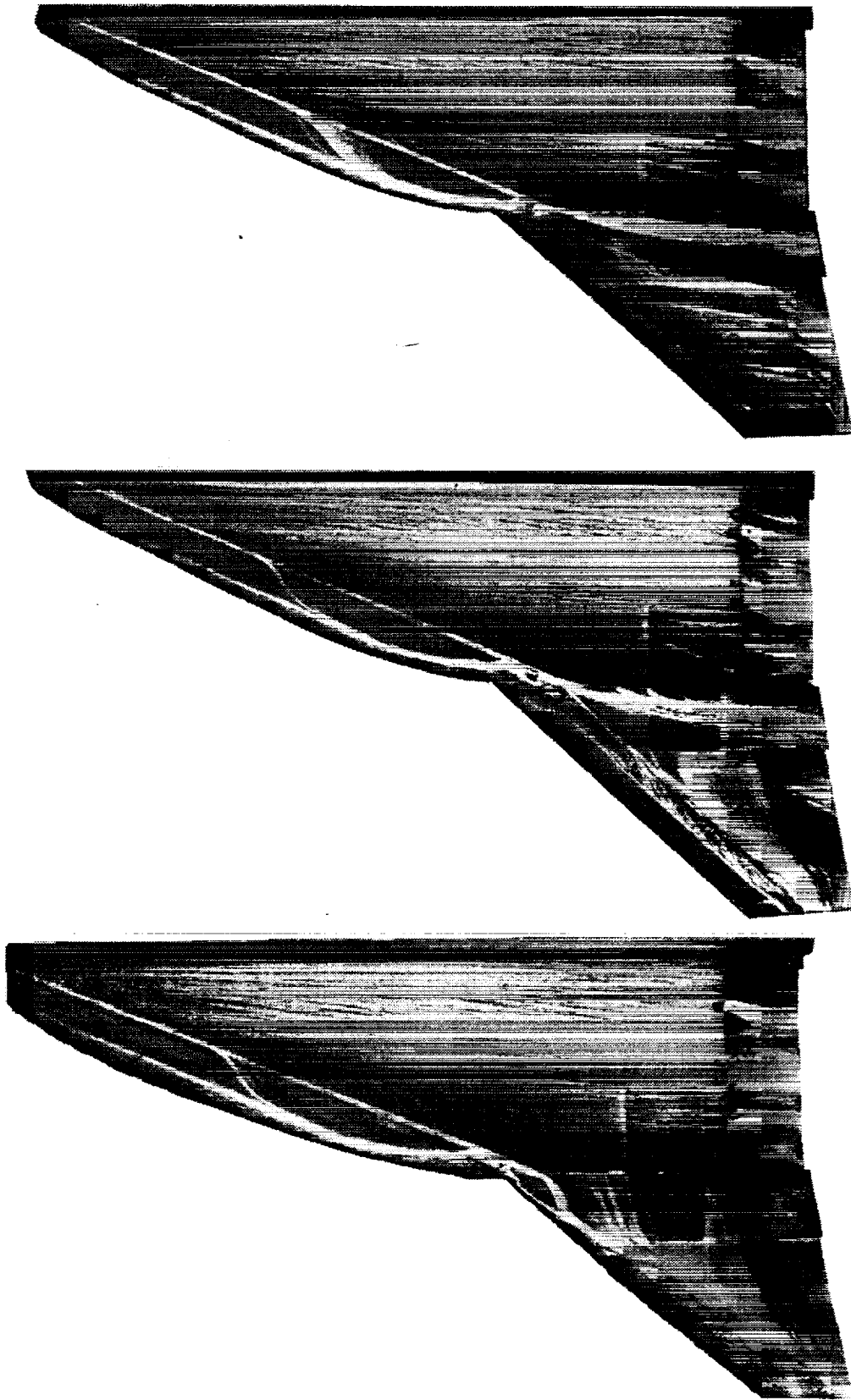


Figure 31. Effect of OBLE flaps on surface pressure distributions of planform 68/48. $q_\infty = 70$ psf; $\delta_{vf} = 30^\circ$; $\delta_{ibf} = 15^\circ$; and $\delta_{obf} = 15^\circ$.



(a) Cruise OBLE.

(b) OBLE flap.

(c) Slotted OBLE flap.

Figure 32. Surface flow fields of planform 68/48 with various outboard leading-edge configurations. $q_{\infty} = 70$ psf; $\alpha = 10^\circ$; $\delta_{vf} = 30^\circ$; $\delta_{ibf} = 15^\circ$; and $\delta_{obf} = 15^\circ$.

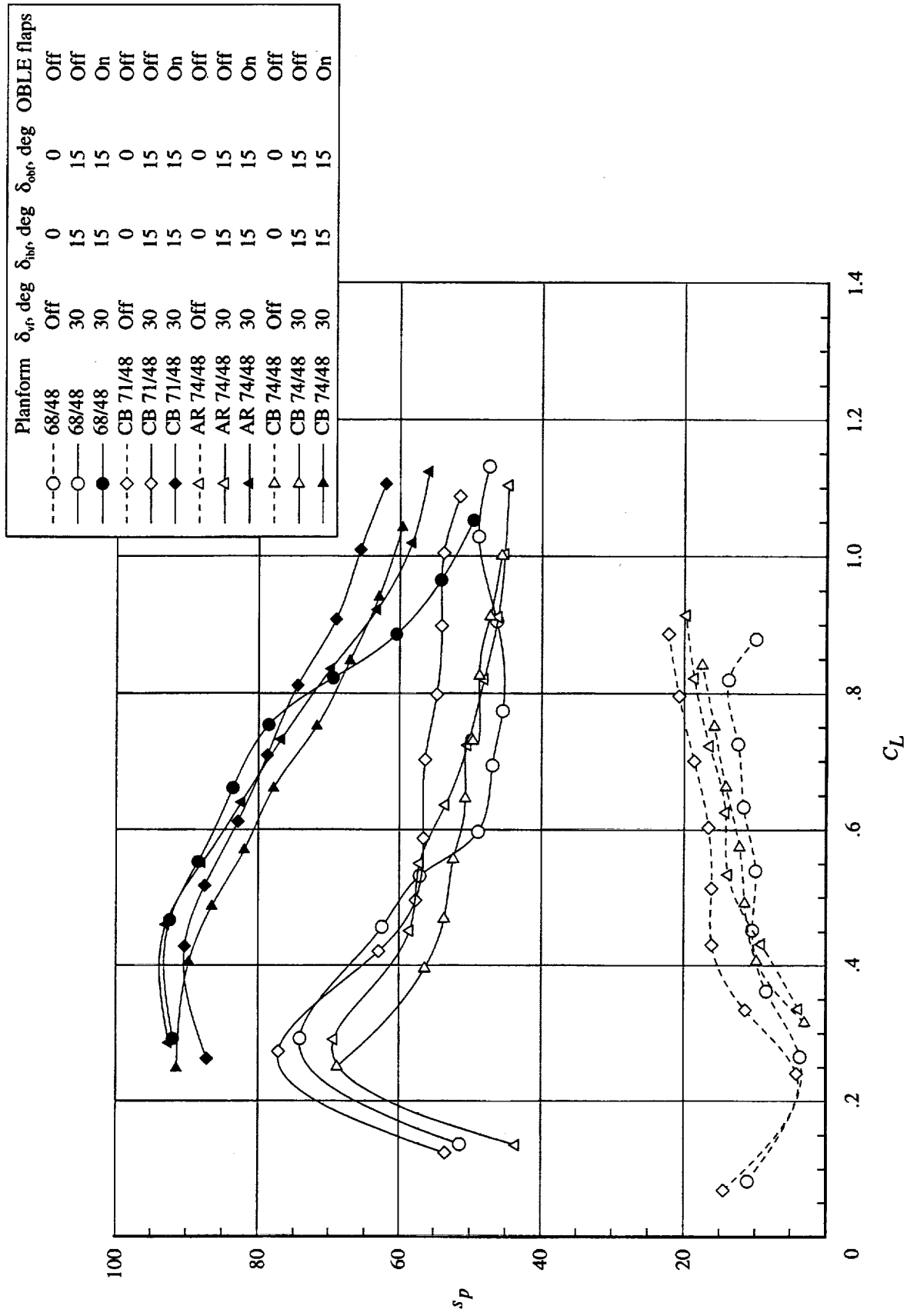
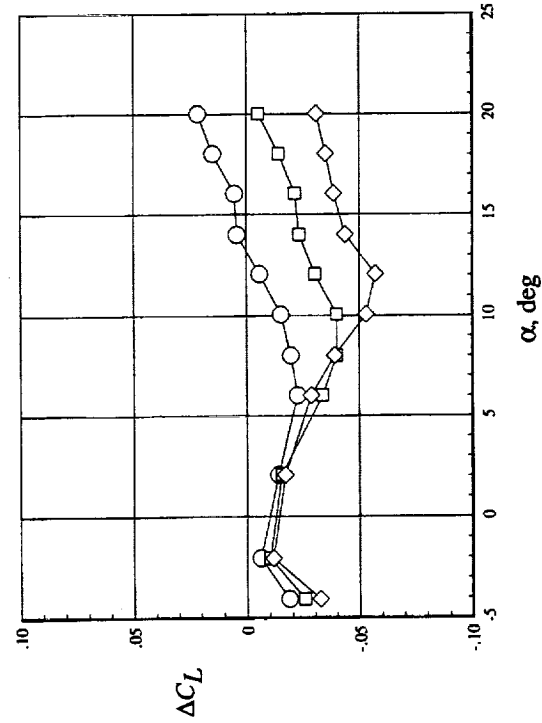
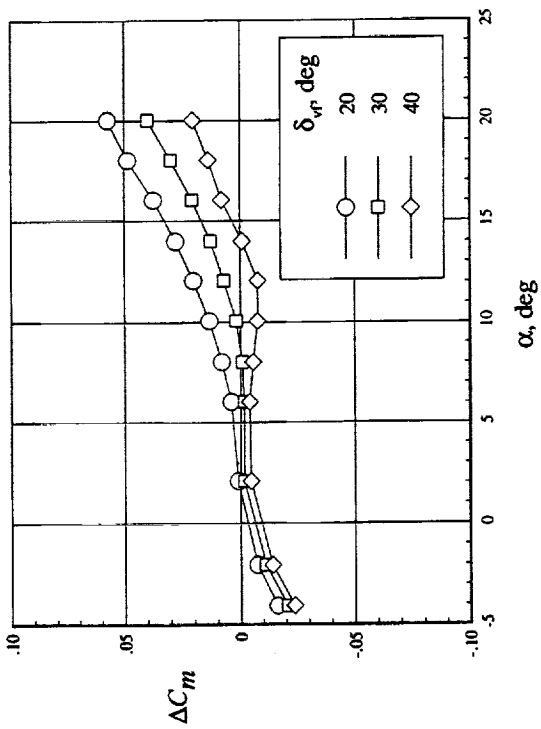
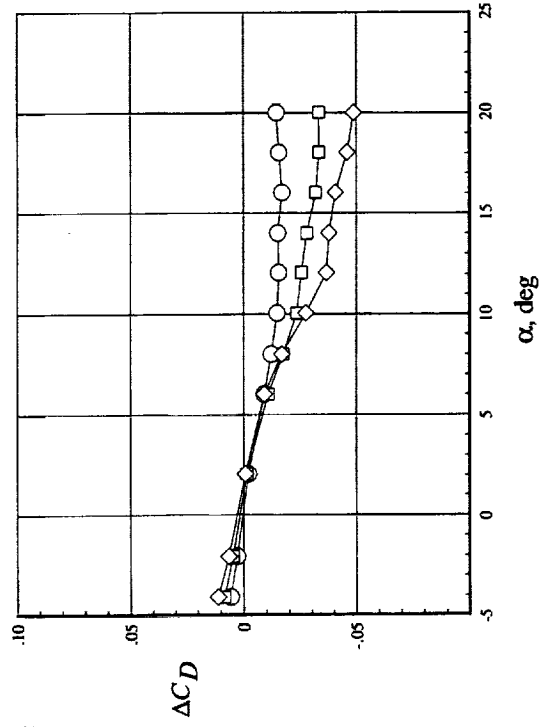
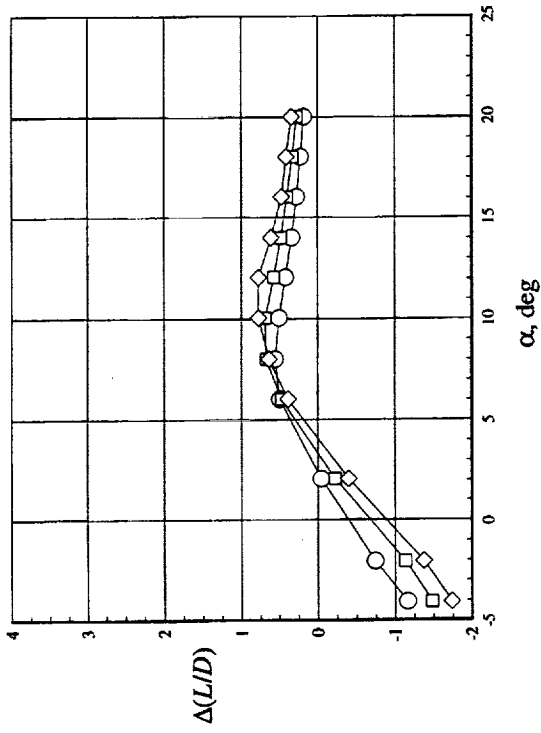
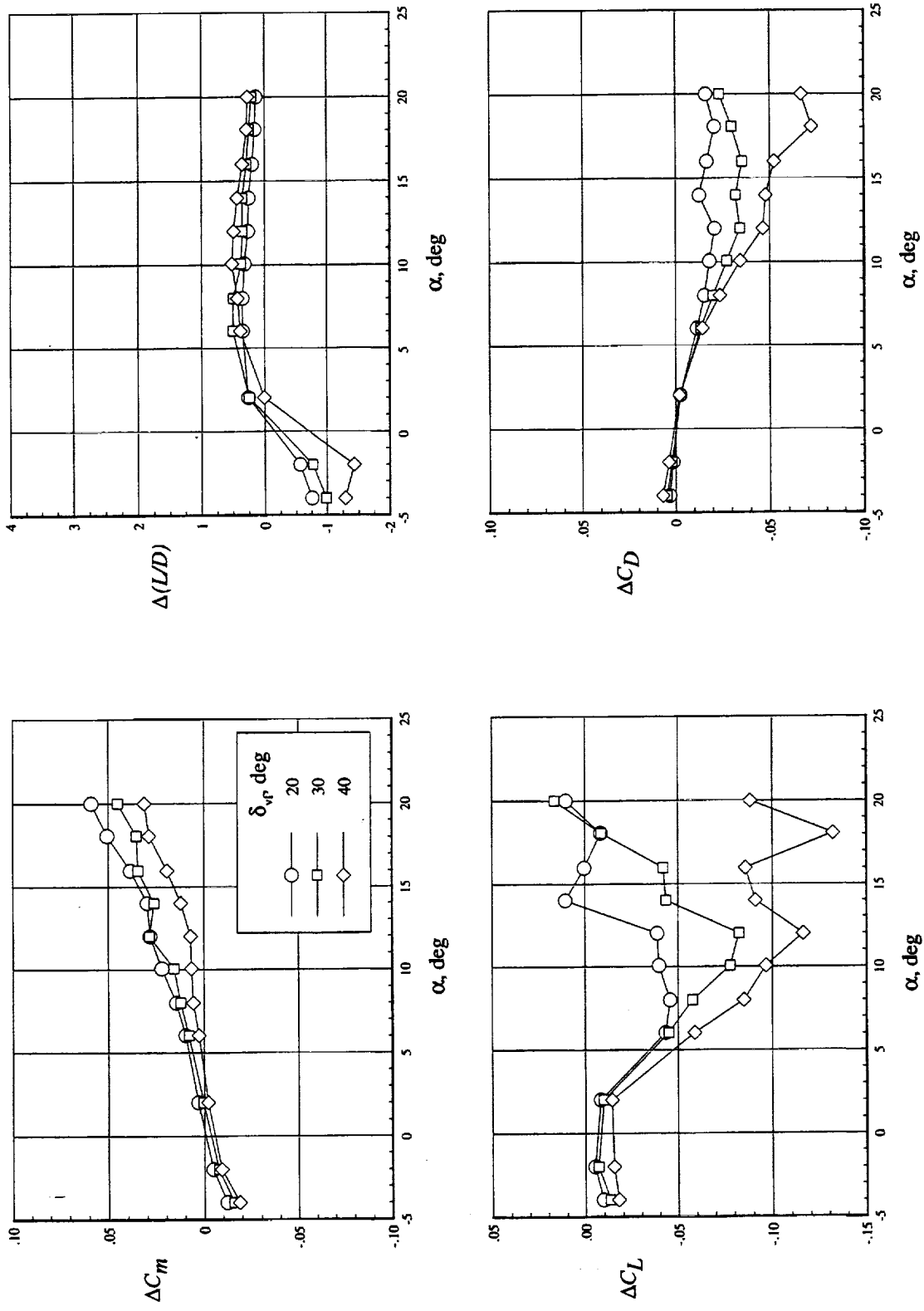


Figure 33. Planform effects on suction parameter for cruise and high-lift configurations. $q_\infty = 70$ psf.



(a) Clipped delta planform 68; $q_\infty = 70$ psf; $\delta_{\text{vf}} = 15^\circ$; and $\Delta =$ vortex flaps on - vortex flaps off.

Figure 34. Effect of vortex flap deflections on longitudinal aerodynamics.



(b) Cranked delta planform 68/48; $q_\infty = 70$ psf; $\delta_{\text{lpf}} = 15^\circ$; $\delta_{\text{obf}} = 15^\circ$; OBLE flaps off; and $\Delta =$ vortex flaps on - vortex flaps off.

Figure 34. Concluded.

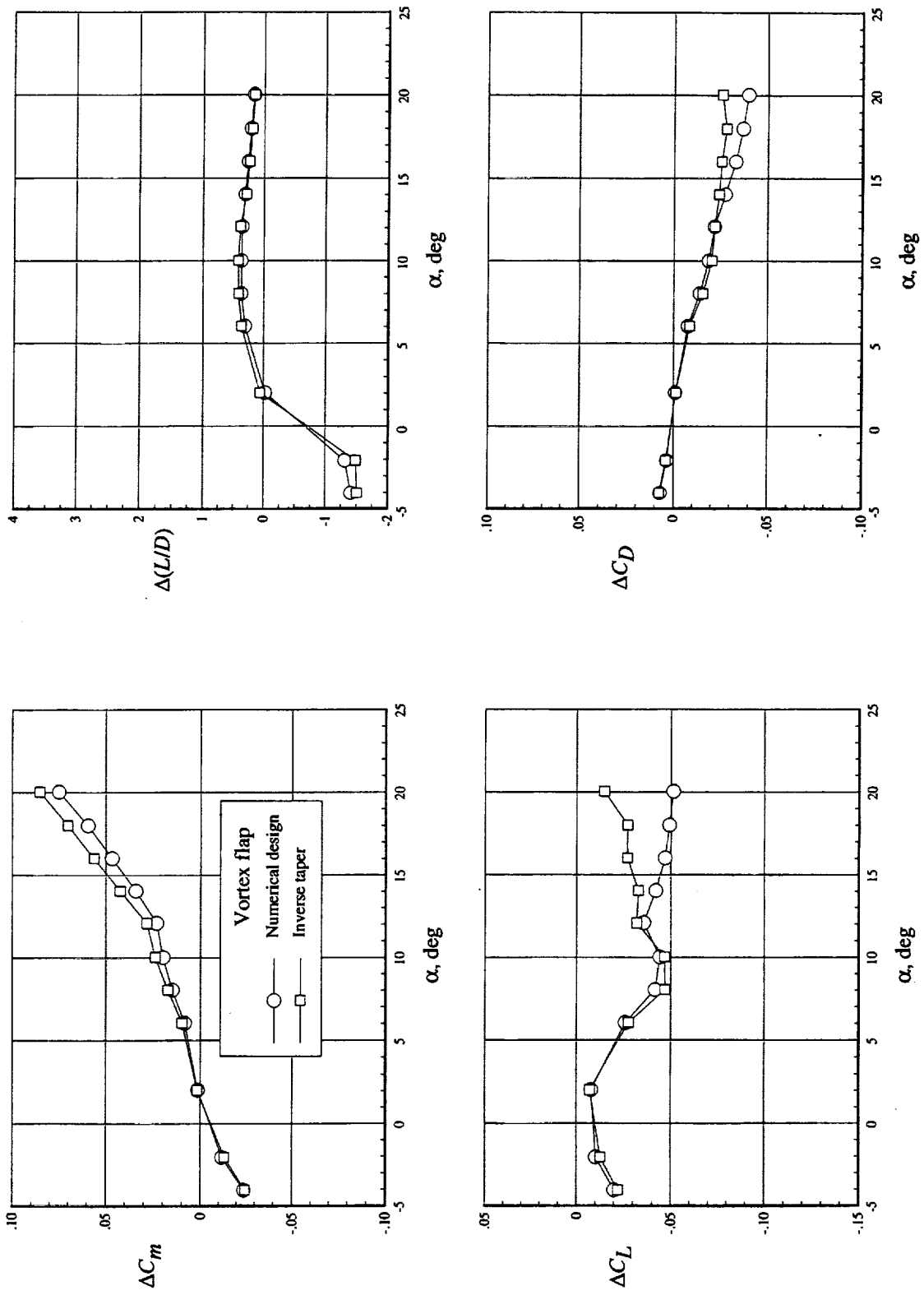


Figure 35. Effect of vortex flap design on longitudinal aerodynamics of planform CB 74/48. $q_\infty = 70$ psf; $\delta_{vf} = 30^\circ$; $\delta_{hbf} = 15^\circ$; $\delta_{obf} = 15^\circ$; OBLE flaps off; and $\Delta =$ vortex flaps on - vortex flaps off.

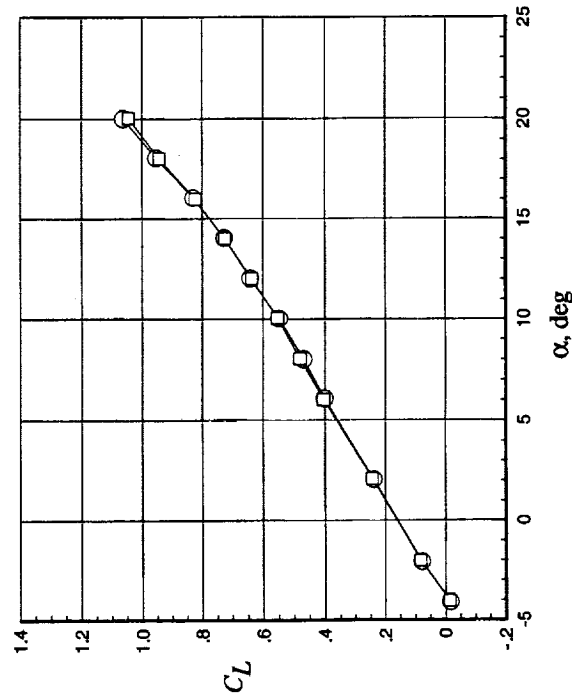
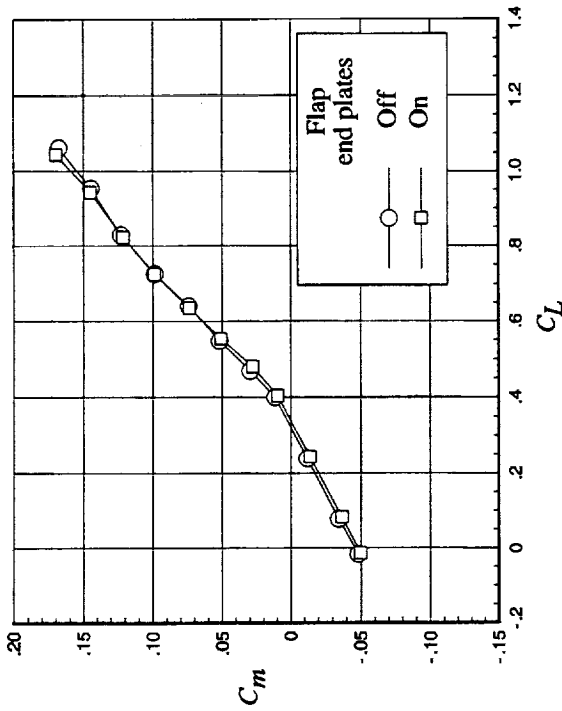
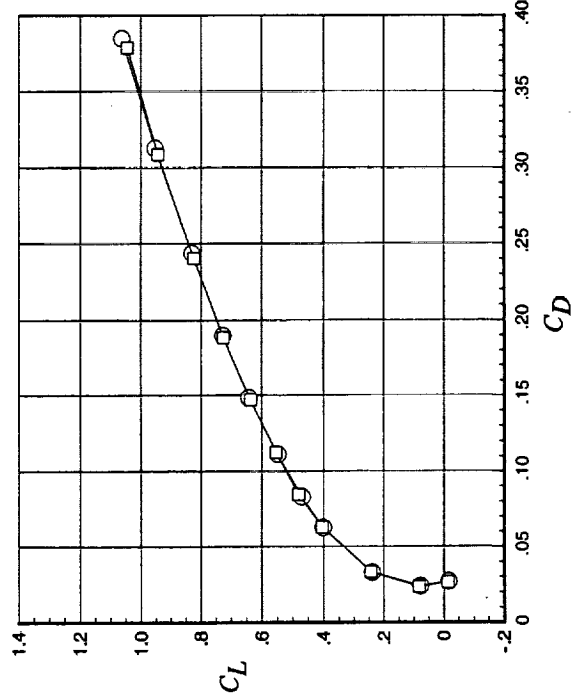
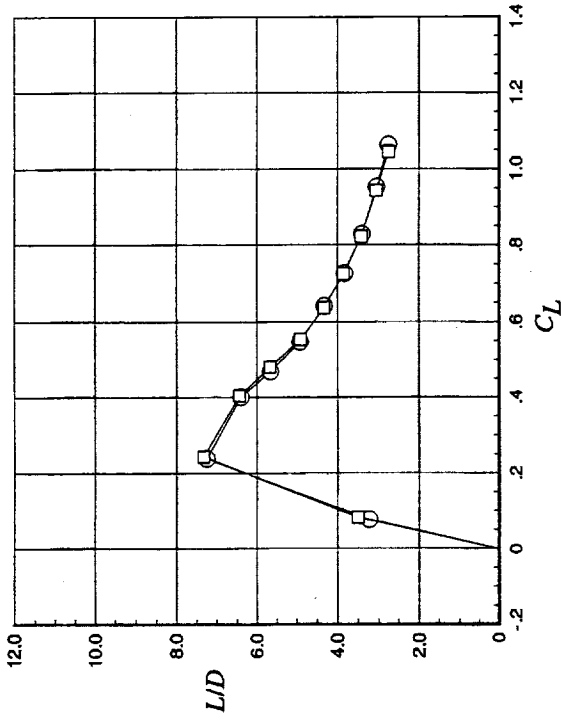


Figure 36. Effect of flap end plates on longitudinal aerodynamics of cranked delta planform 68/48. $q_\infty = 70$ psf; $\delta_{\text{tr}} = 30^\circ$; $\delta_{\text{tr}} = 15^\circ$; $\delta_{\text{obf}} = 15^\circ$; and OBLE flaps off.

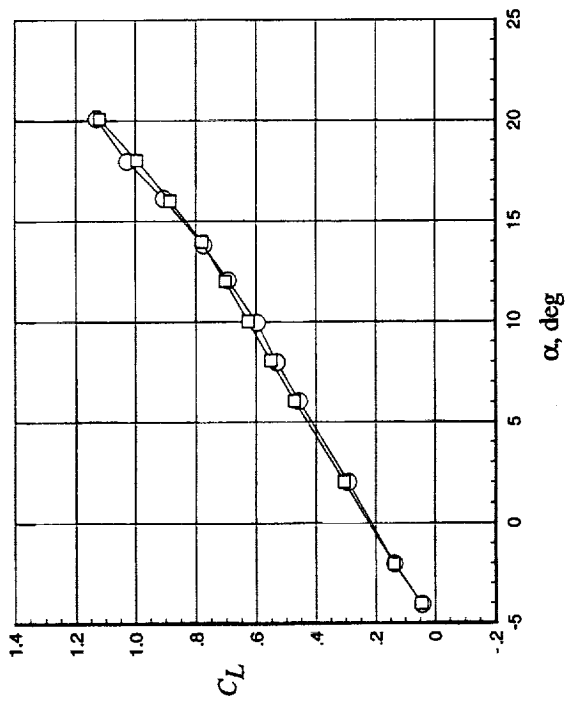
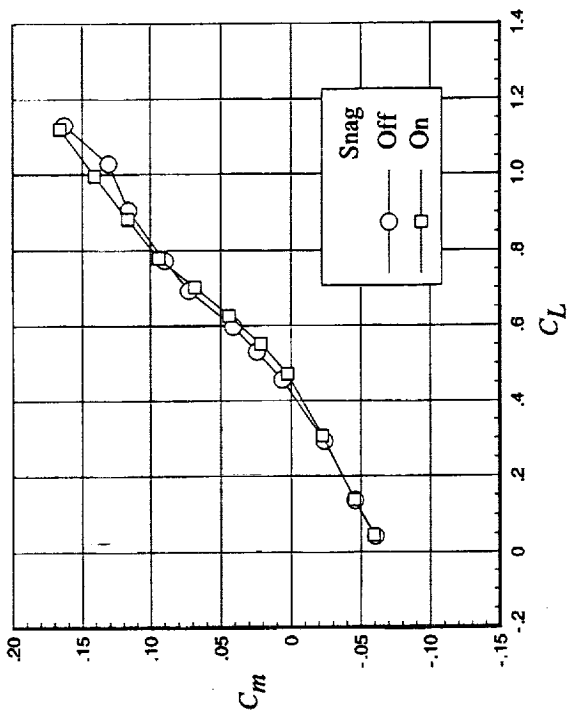
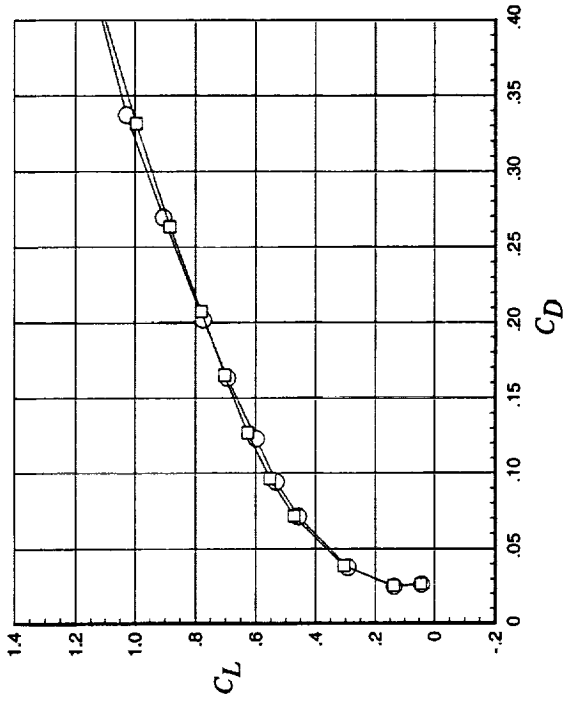
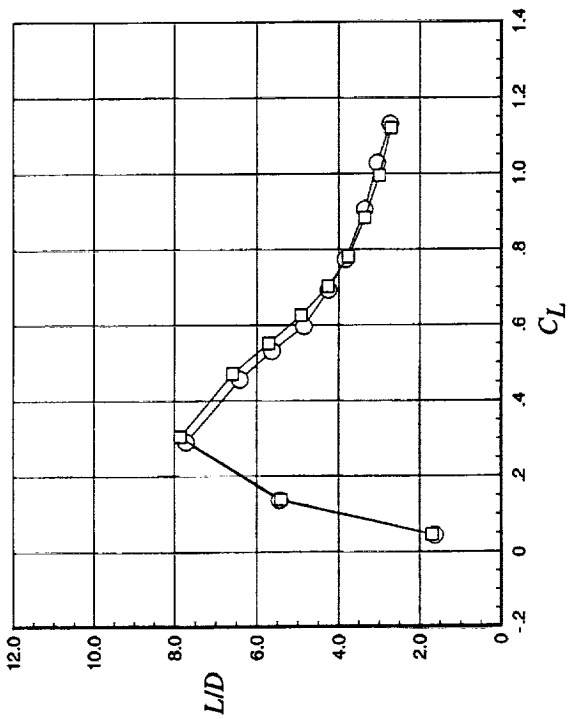


Figure 37. Effect of OBLE snag on longitudinal aerodynamics of cranked delta planform 68/48. $q_{\infty} = 70$ psf; $\delta_{vf} = 30^\circ$; $\delta_{bf} = 15^\circ$; $\delta_{obf} = 15^\circ$; and OBLE flaps off.

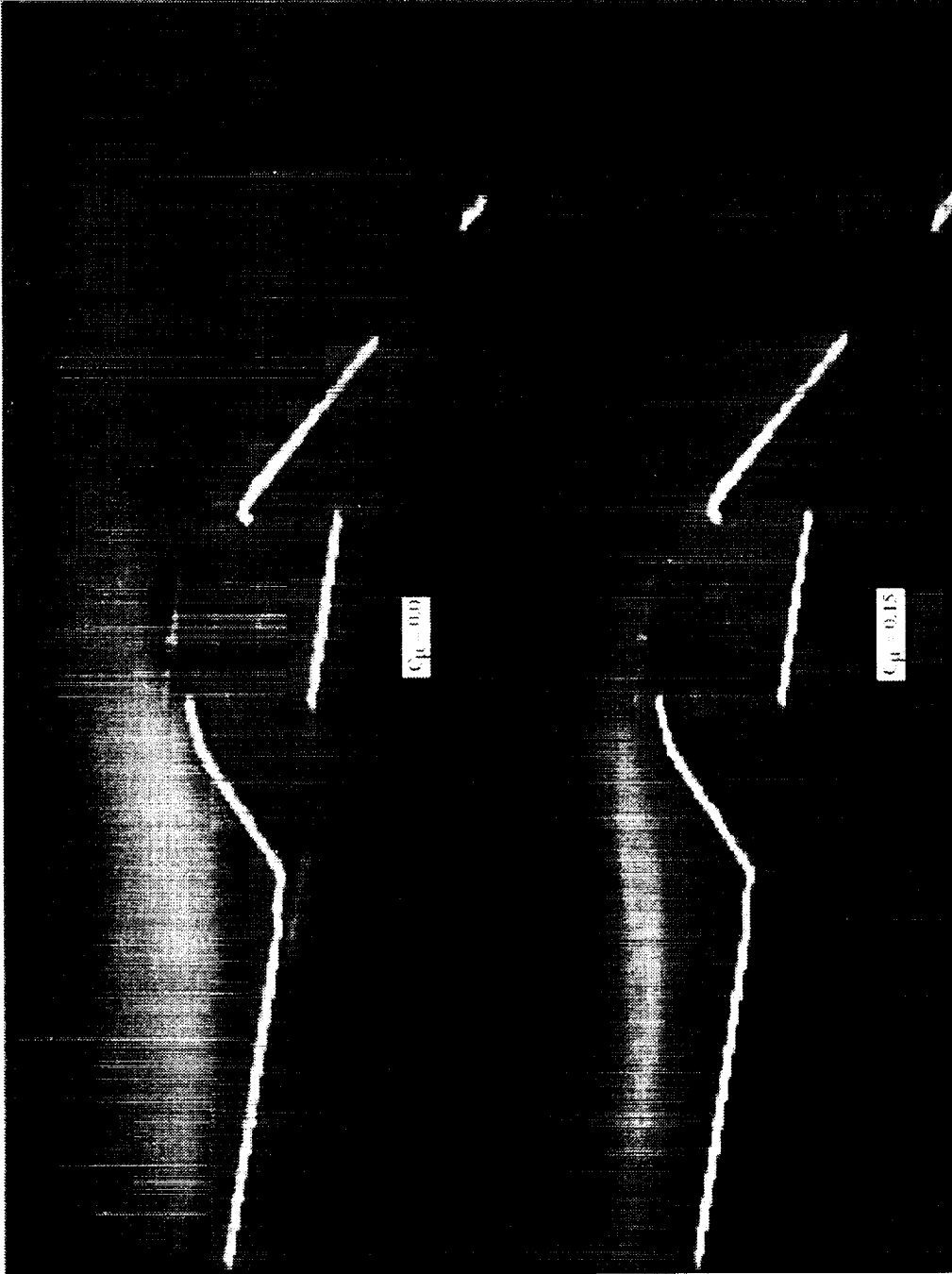


Figure 38. Off-body flow visualization of inboard vortex trap system with blowing on and off. $q_\infty = 10$ psf; $\alpha = 8^\circ$; $\delta_{vf} = 30^\circ$; $\delta_{obf} = 15^\circ$; $\delta_{ft} = 45^\circ$; $\delta_{at} = 30^\circ$; and $h = 1.5$ in.

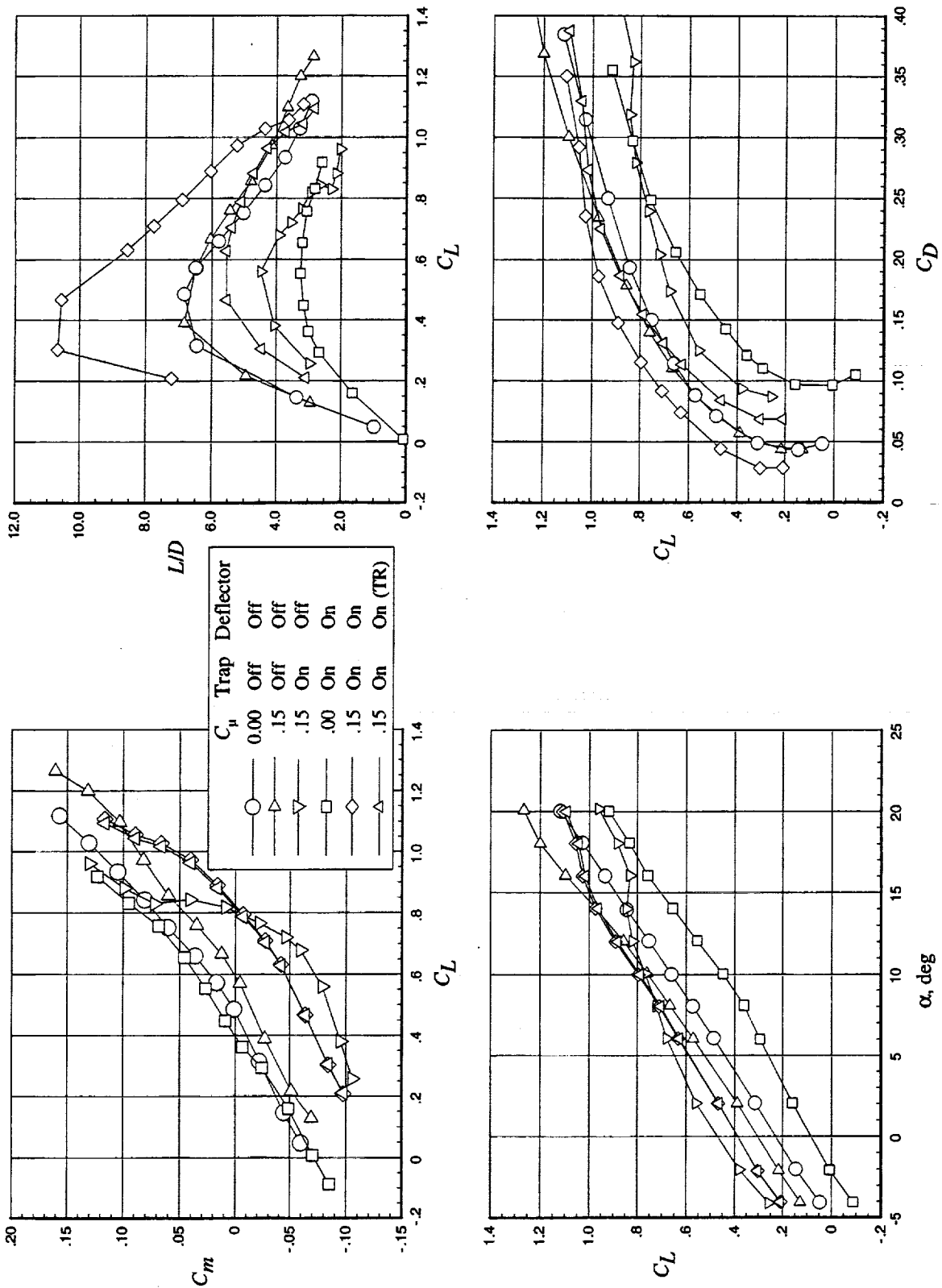
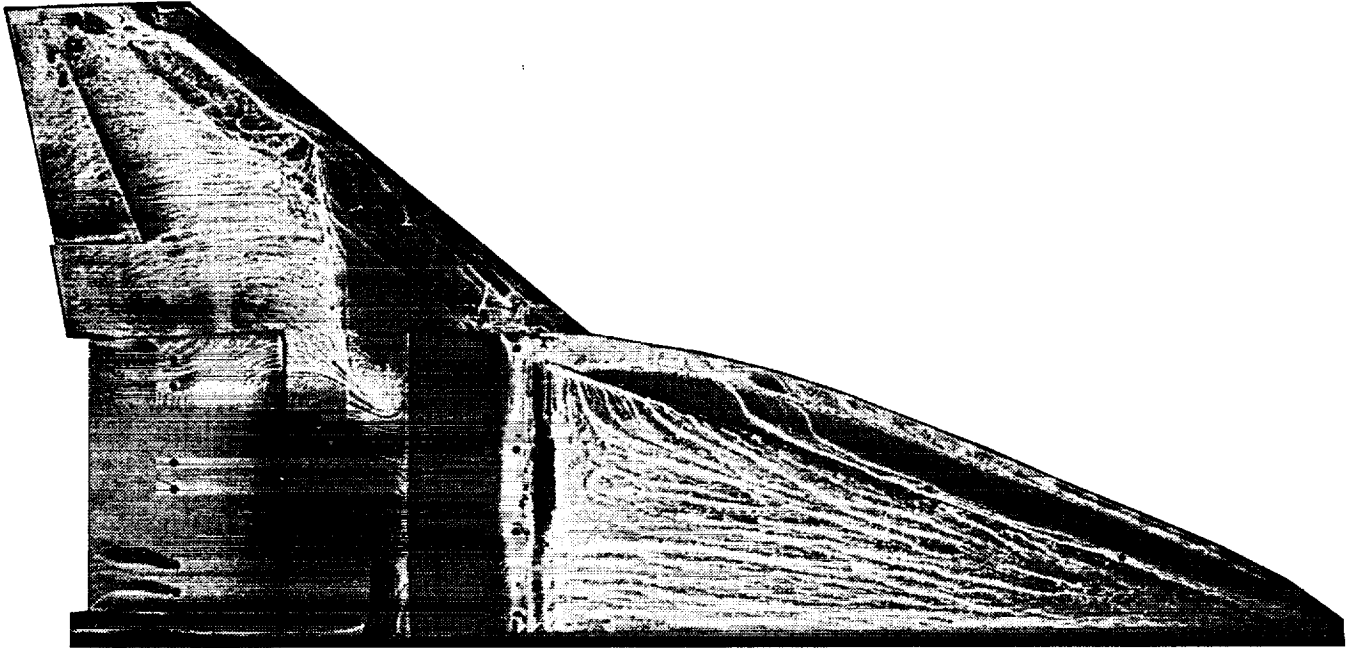
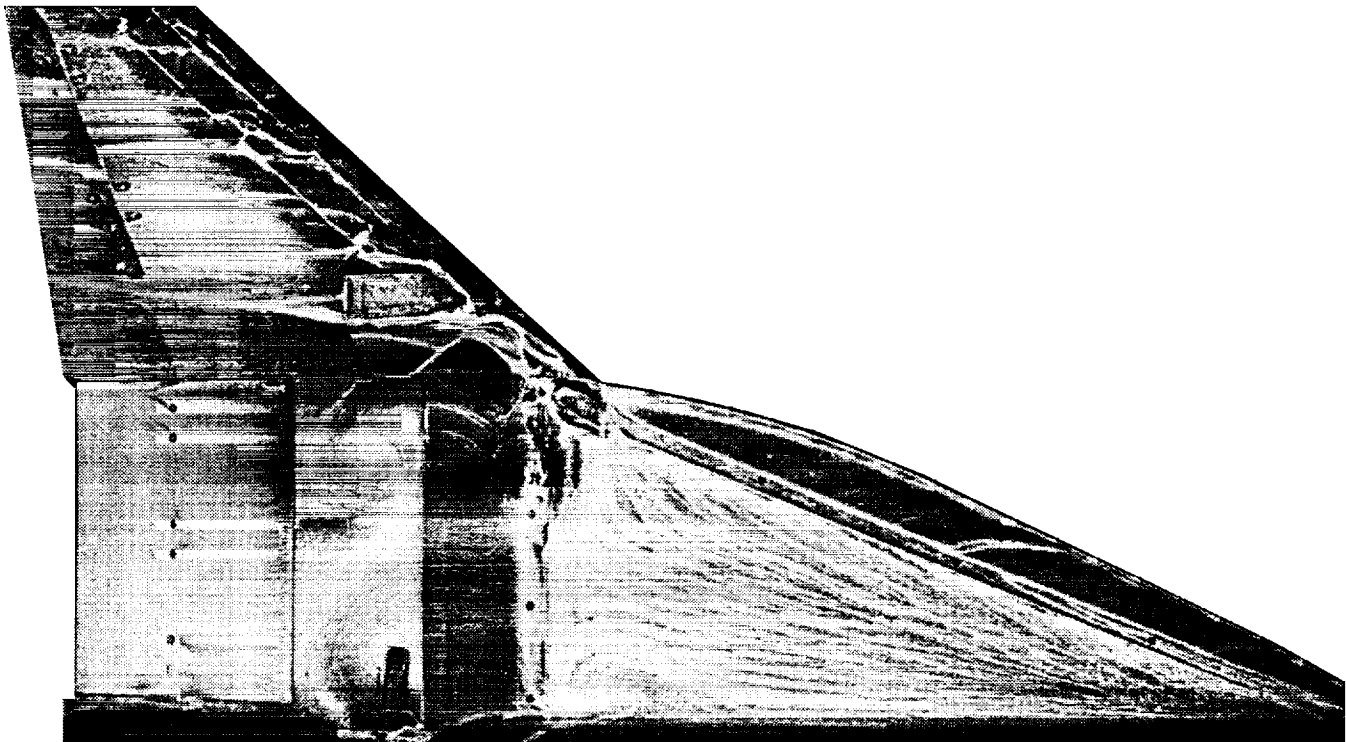


Figure 39. Buildup of inboard vortex trap system. $q_\infty = 10$ psf; $\delta_{vf} = 30^\circ$; $\delta_{obf} = 15^\circ$; $\delta_{ft} = 45^\circ$; $\delta_{at} = 30^\circ$; $h = 1.5$ in.; and OBLE flaps on.



(a) Jet deflector not installed.



(b) Jet deflector installed.

Figure 40. Surface flow field of inboard vortex trap system. $q_{\infty} = 70$ psf; $\alpha = 8^{\circ}$; $\delta_{vf} = 30^{\circ}$; $\delta_{obf} = 15^{\circ}$; $\delta_{ft} = 45^{\circ}$; $\delta_{at} = 30^{\circ}$; $C_{\mu} = 0.15$; and OBLE flaps on.

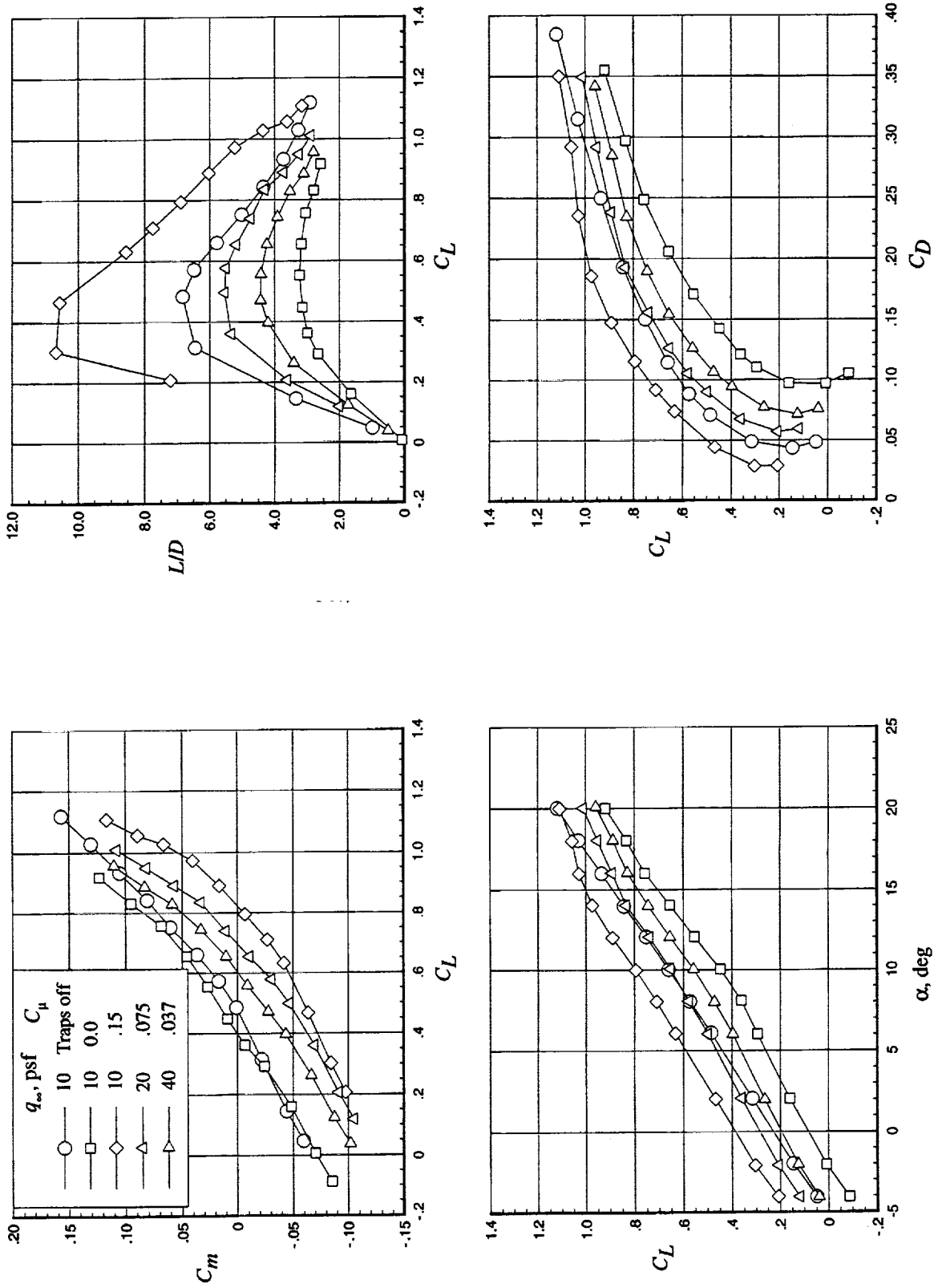


Figure 41. Effect of C_μ on inboard vortex trap system performance with jet deflectors on. $\delta_{vf} = 30^\circ$; $\delta_{obf} = 15^\circ$; $\delta_{ft} = 45^\circ$; $\delta_{at} = 30^\circ$; $h = 1.5$ in.; and OBLE flaps on.

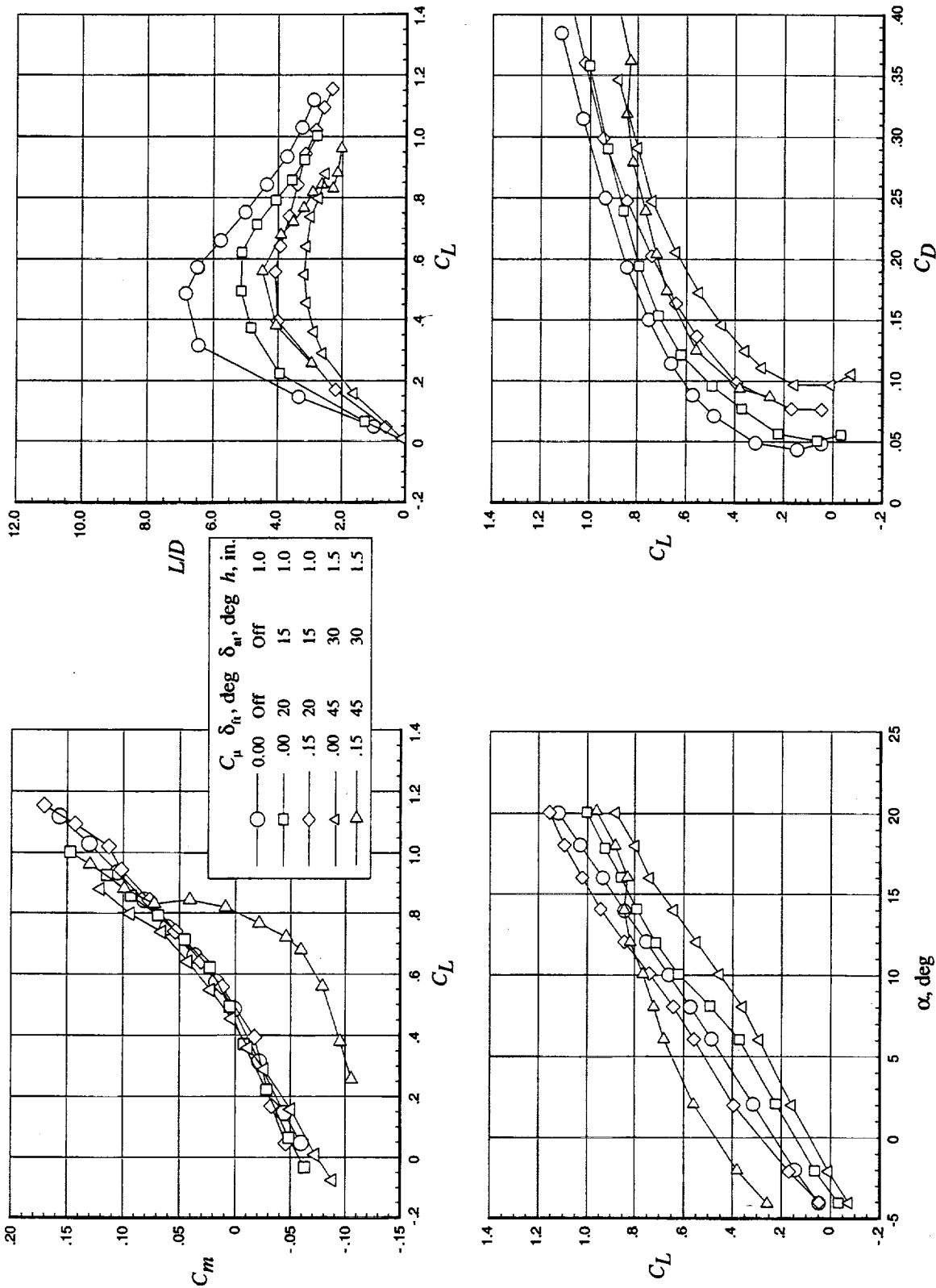


Figure 42. Effect of trap plate deflection angles on inboard vortex trap system performance. $q_{\infty} = 10$ psf; $\delta_{vf} = 30^\circ$; $\delta_{obf} = 15^\circ$; OBLE flaps on; and jet deflectors off.

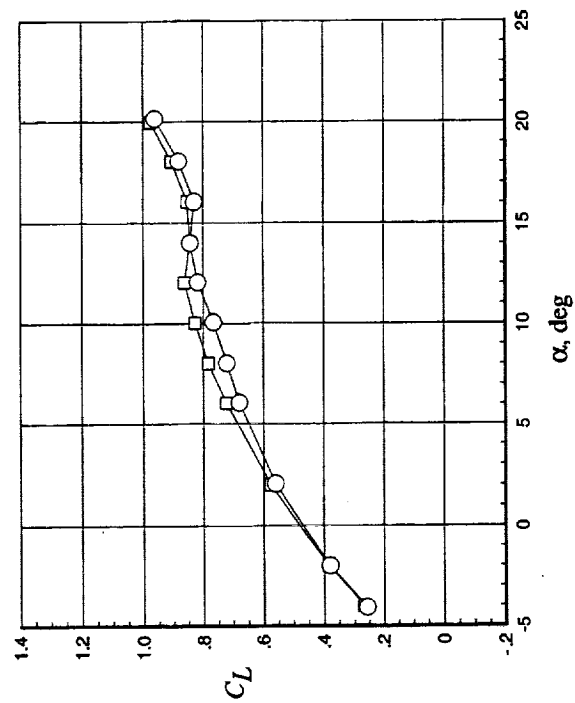
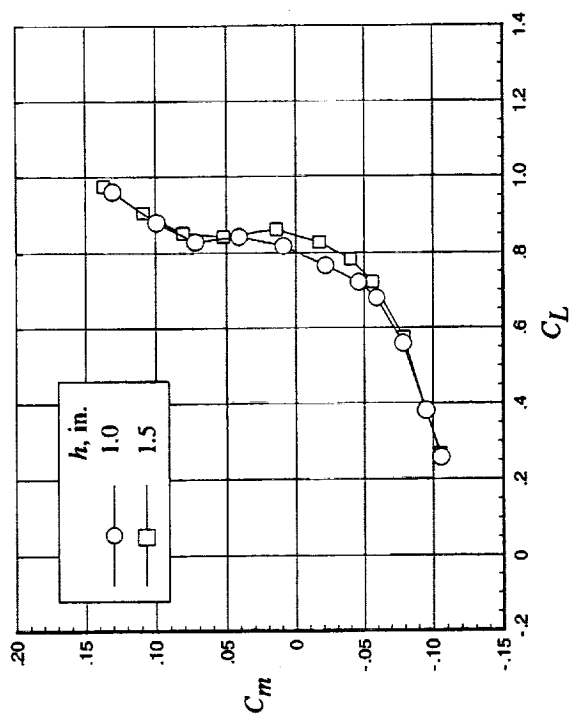
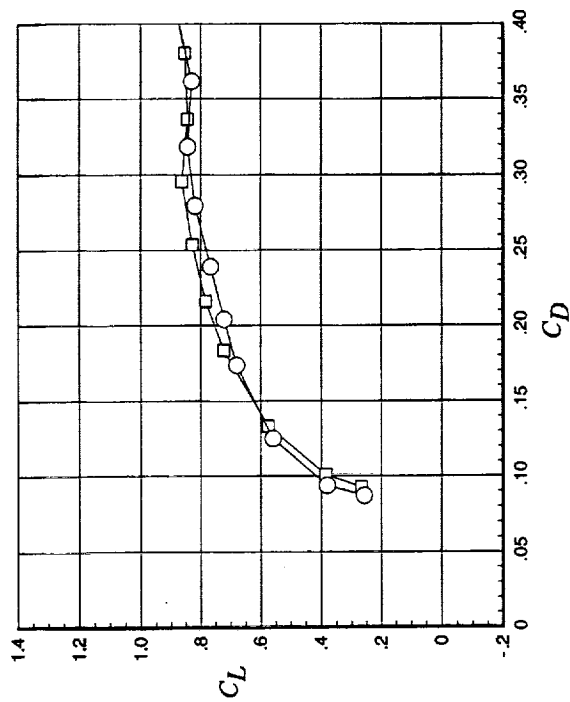
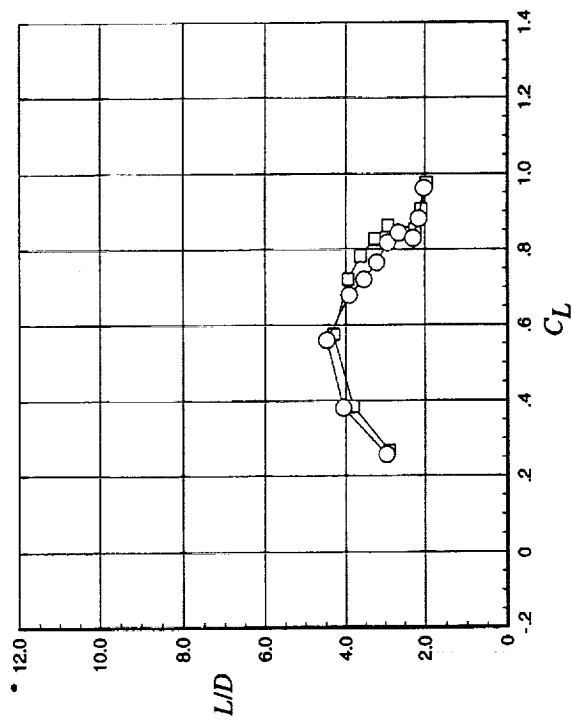


Figure 43. Effect of nozzle height on inboard vortex trap system performance. $q_{\infty} = 10$ psf; $C_{\mu} = 15$; $\delta_{vf} = 30^{\circ}$; $\delta_{obf} = 15^{\circ}$; $\delta_{fl} = 45^{\circ}$; $\delta_{at} = 30^{\circ}$; and OBLE flaps on.

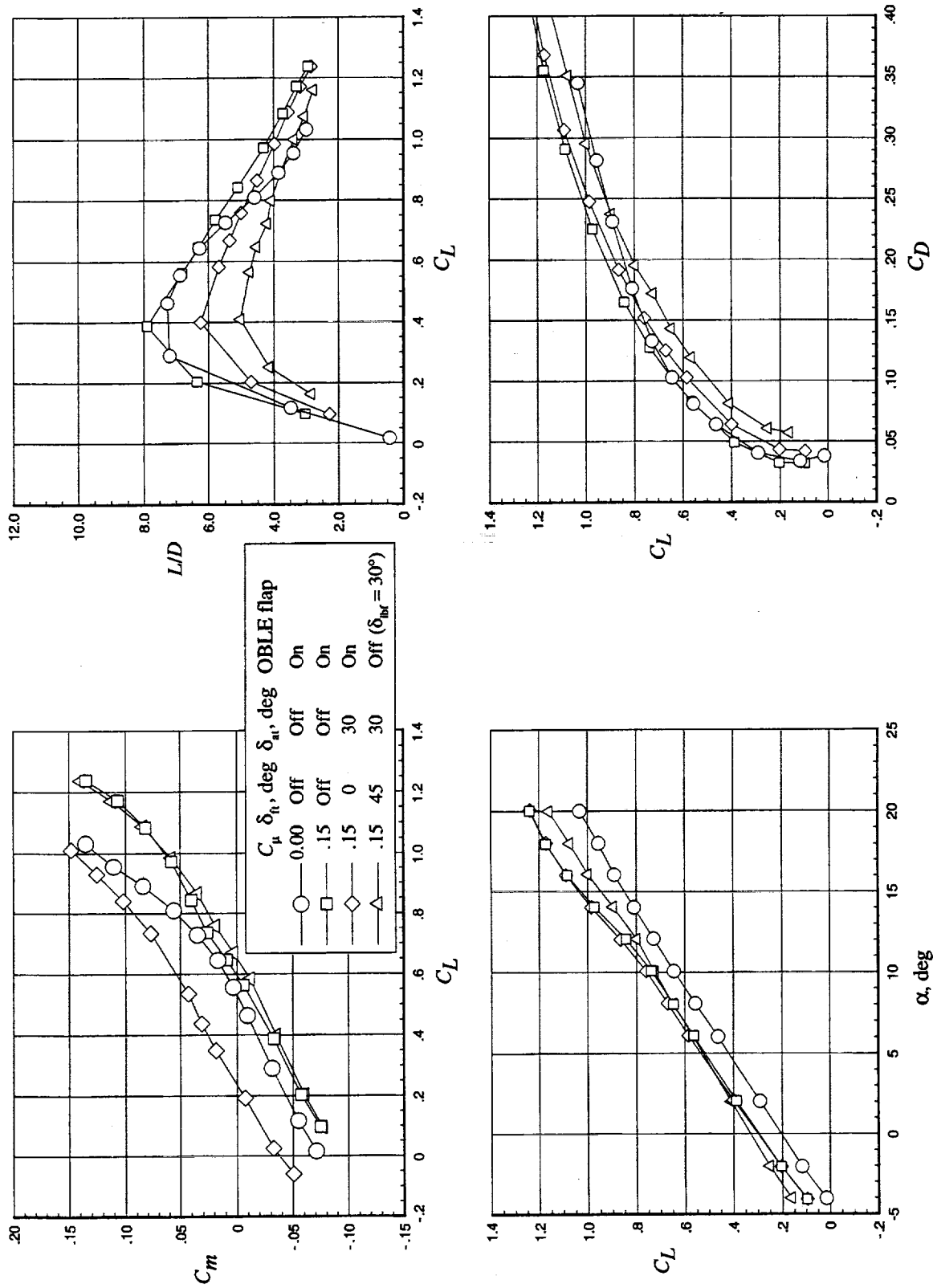


Figure 44. Buildup of outboard vortex trap system. $q_\infty = 10$ psf; $\delta_{vf} = 40^\circ$; and $\delta_{hf} = 15^\circ$.

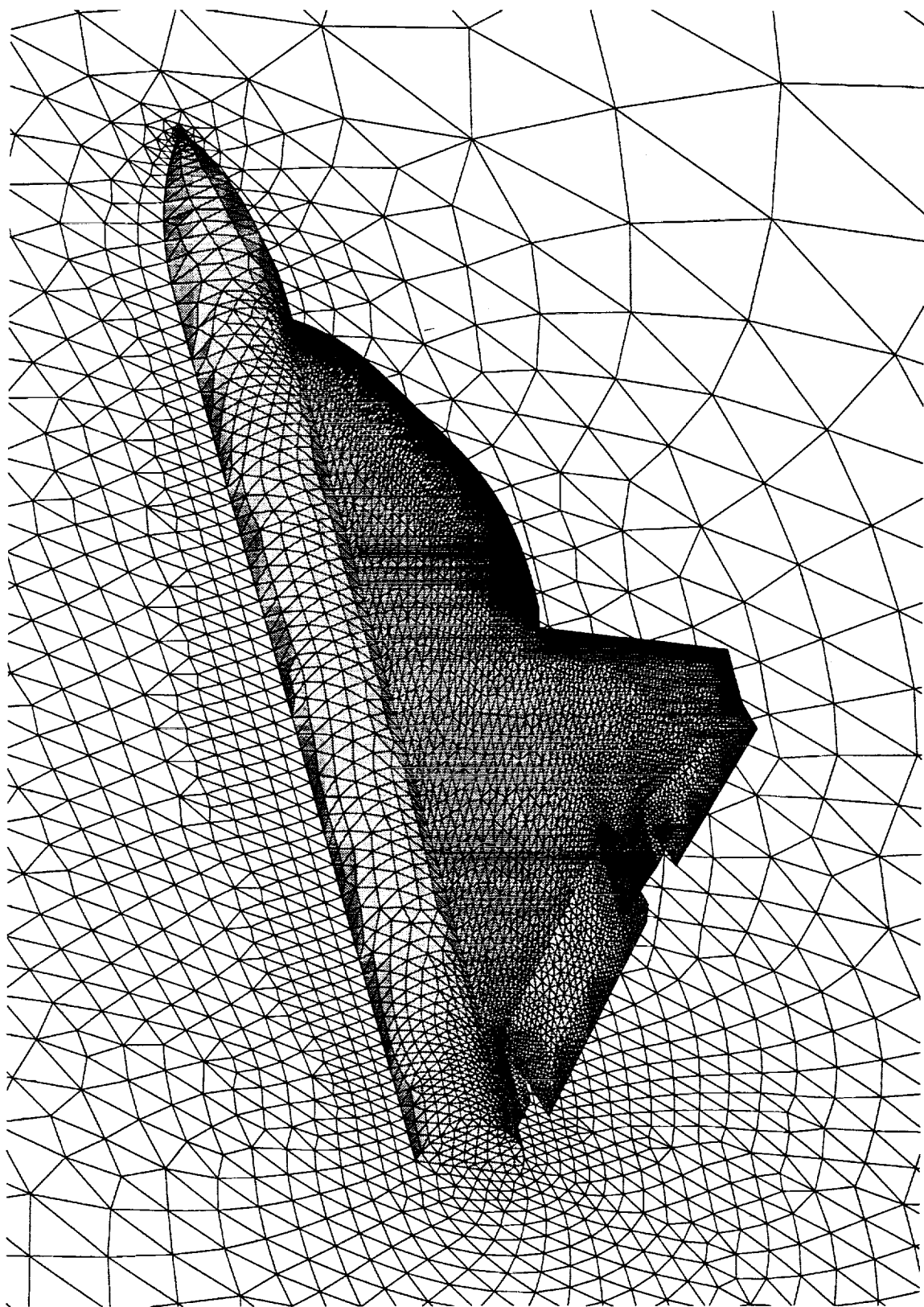


Figure 45. Surface triangulation for fine grid on planform 68/48. Mach = 0.22; $\delta_{\text{trf}} = 30^\circ$; $\delta_{\text{trf}} = 15^\circ$; $\delta_{\text{obf}} = 15^\circ$; and OBLE flaps off.

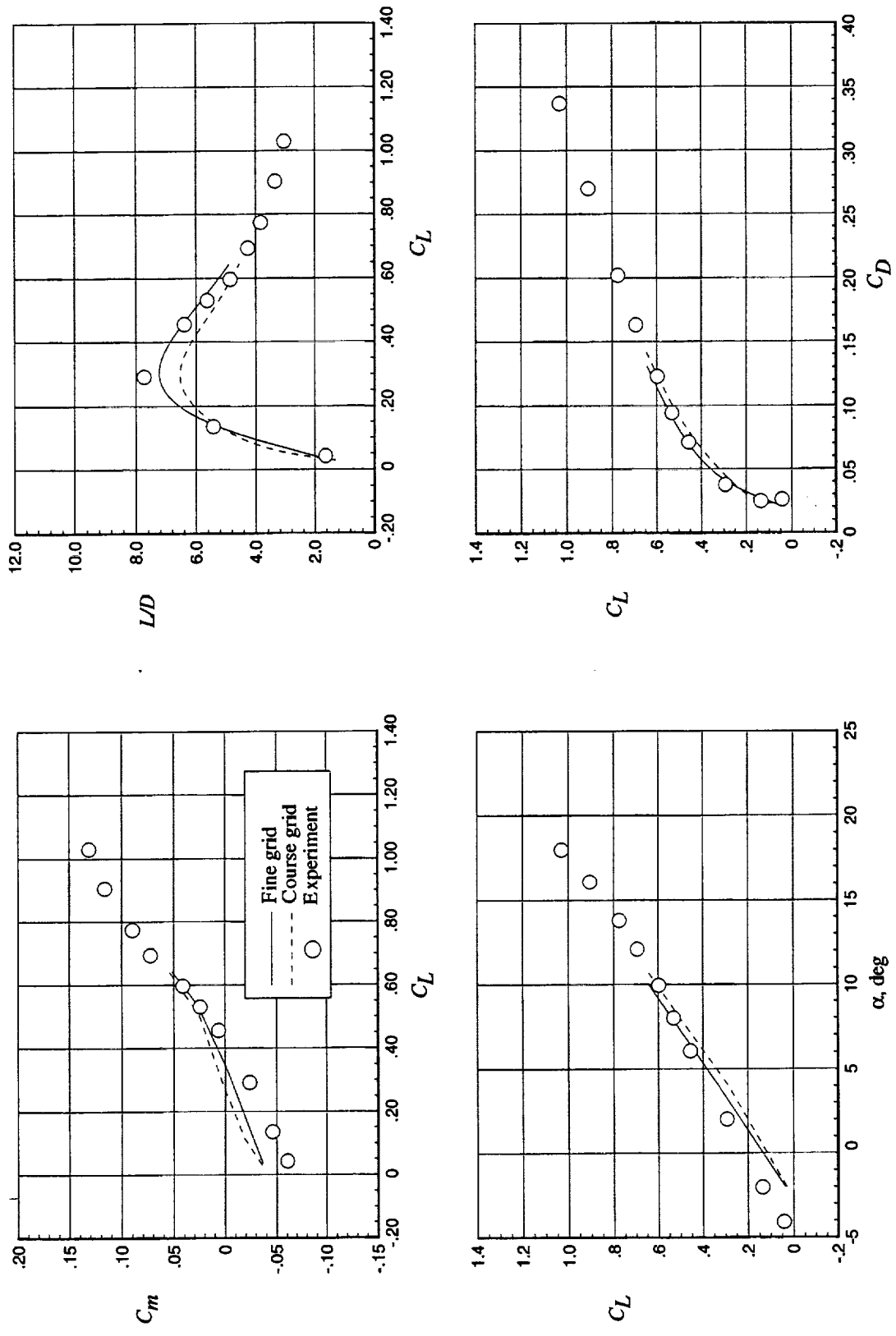


Figure 46. Longitudinal aerodynamics for planform 68/48. Mach = 0.22; $\delta_{vf} = 30^\circ$; $\delta_{tbf} = 15^\circ$; $\delta_{obf} = 15^\circ$; and OBLE flaps off.

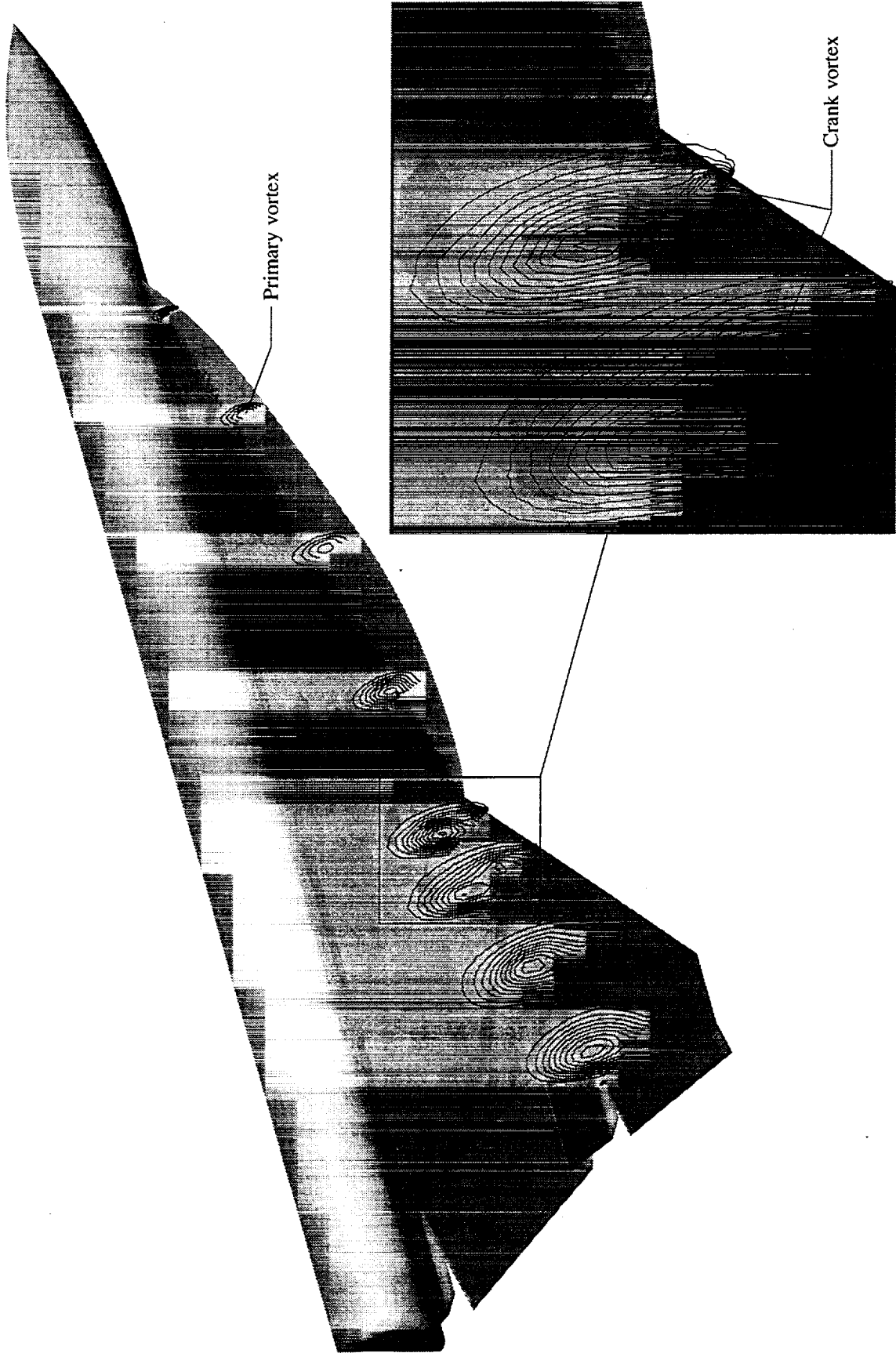


Figure 47. Off-body C_p contours predicted by USM3D on fine grid of planform 68/48. $Mach = 0.22$; $\alpha = 10^\circ$; $\delta_{vf} = 30^\circ$; $\delta_{tbf} = 15^\circ$; $\delta_{obf} = 15^\circ$; and OBLE flaps off.

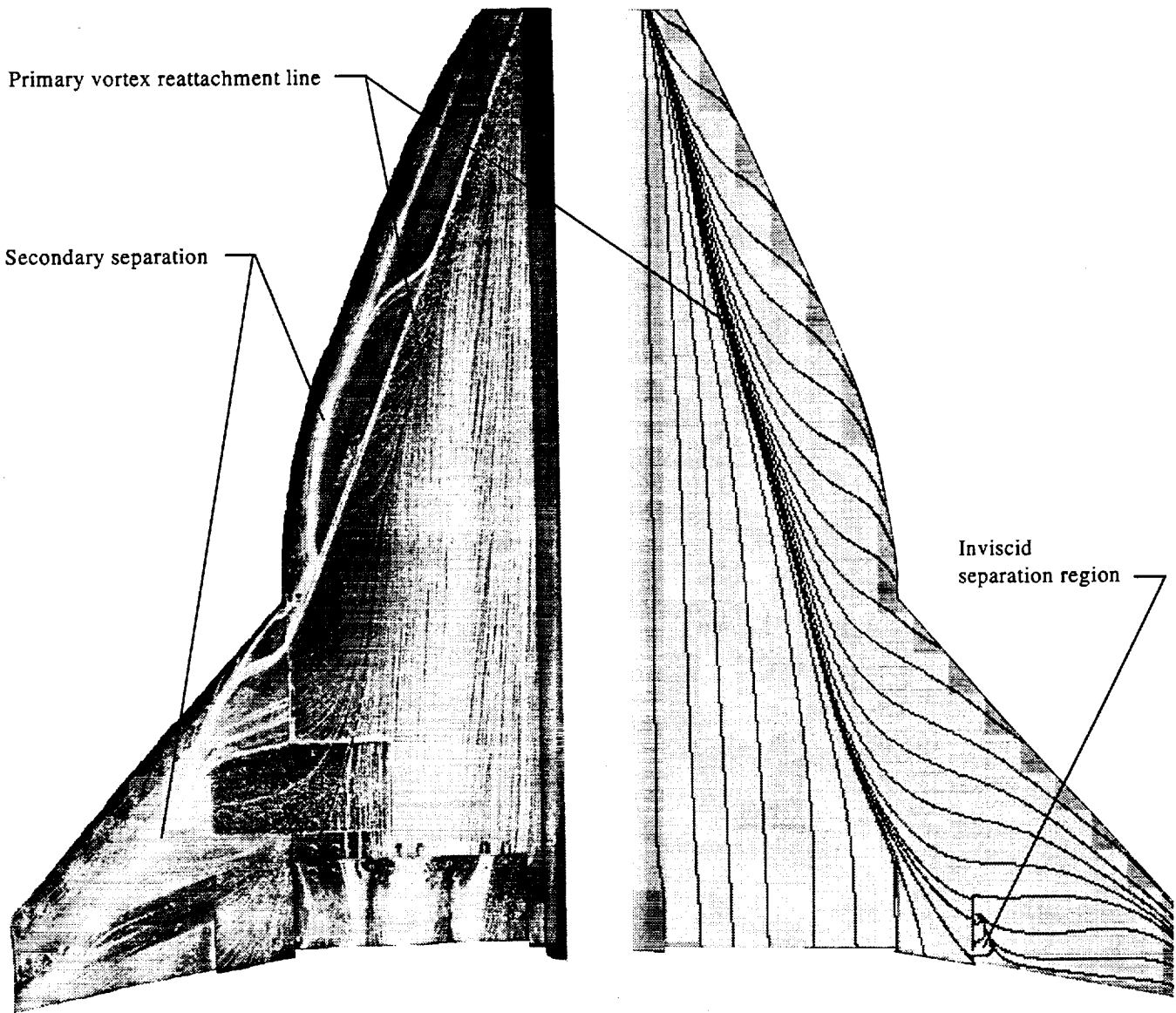


Figure 48. Surface flow field comparison of USM3D with experimental data for planform 68/48. $q_\infty = 70$ psf; $\alpha = 10^\circ$; $\delta_{vf} = 30^\circ$; $\delta_{ibf} = 15^\circ$; $\delta_{obf} = 15^\circ$; and OBLE flaps off.

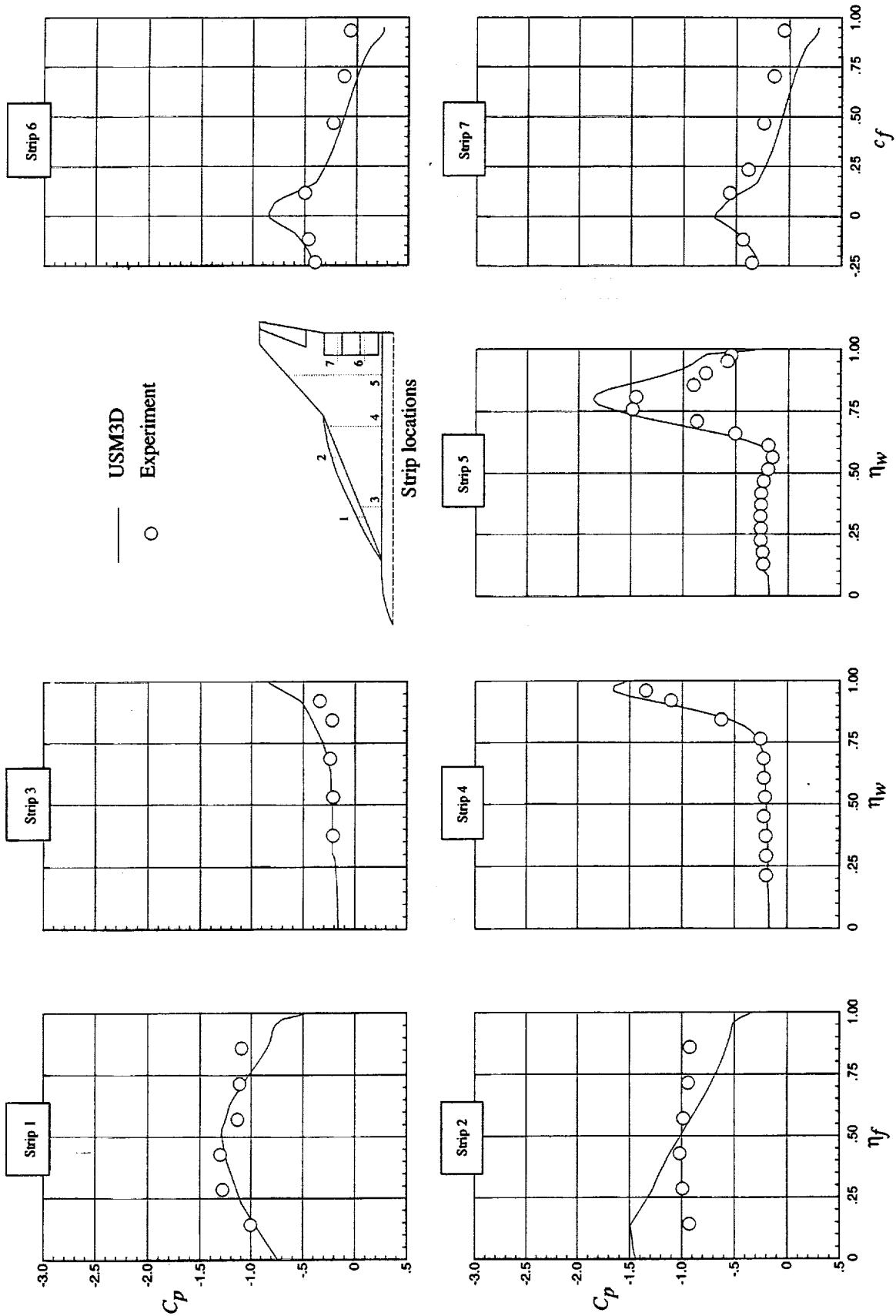
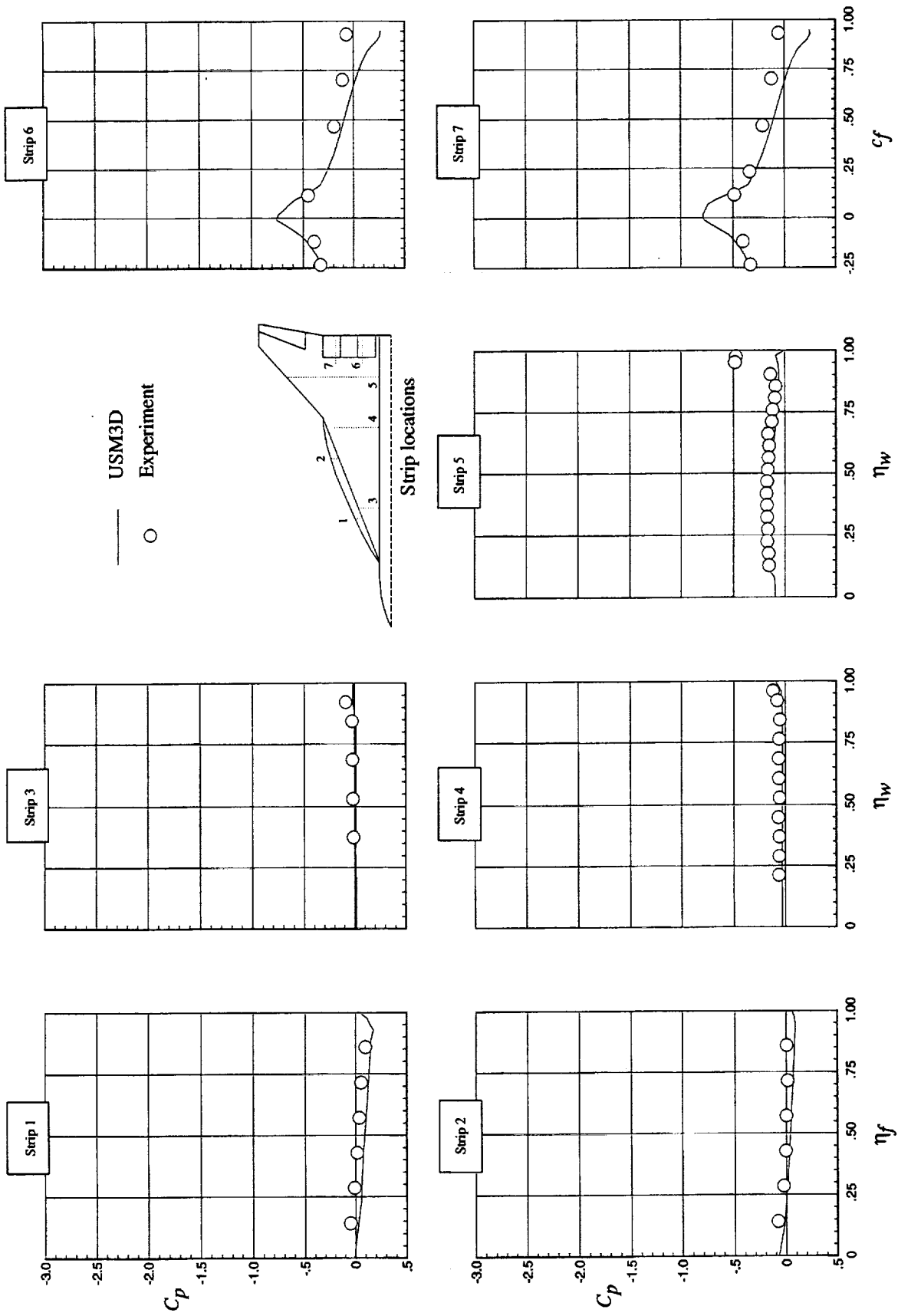
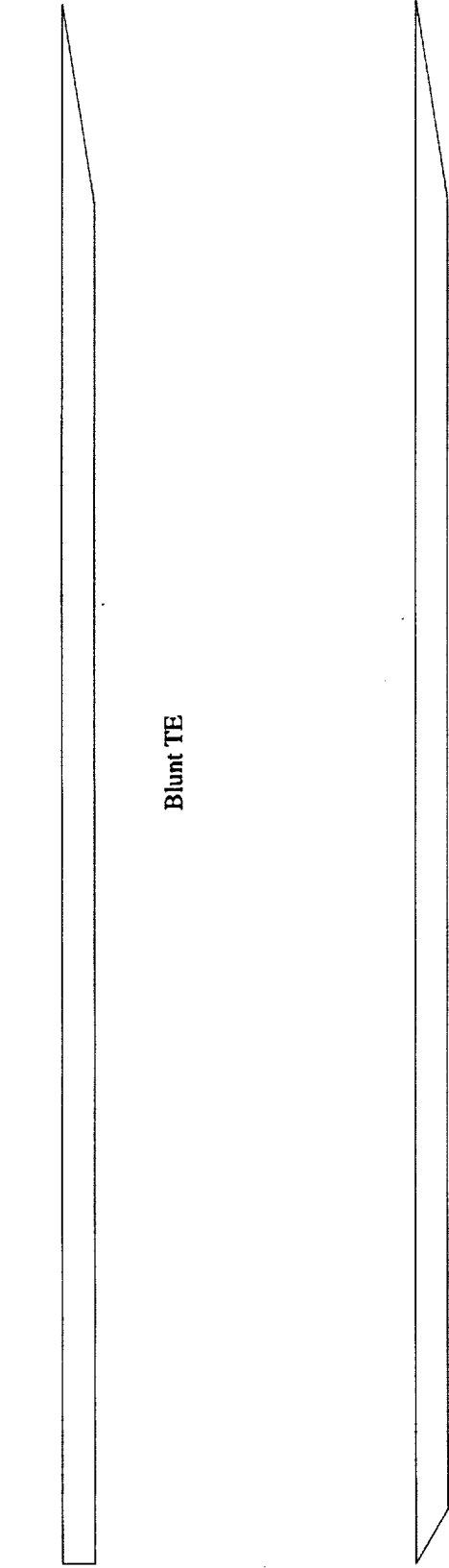


Figure 49. Upper surface C_p distributions for planform 68/48. Mach = 0.22; $\delta_{vf} = 30^\circ$; $\delta_{bf} = 15^\circ$; $\delta_{obf} = 15^\circ$; and OBLE flaps off.



(b) $\alpha = -2^\circ$.

Figure 49. Concluded.

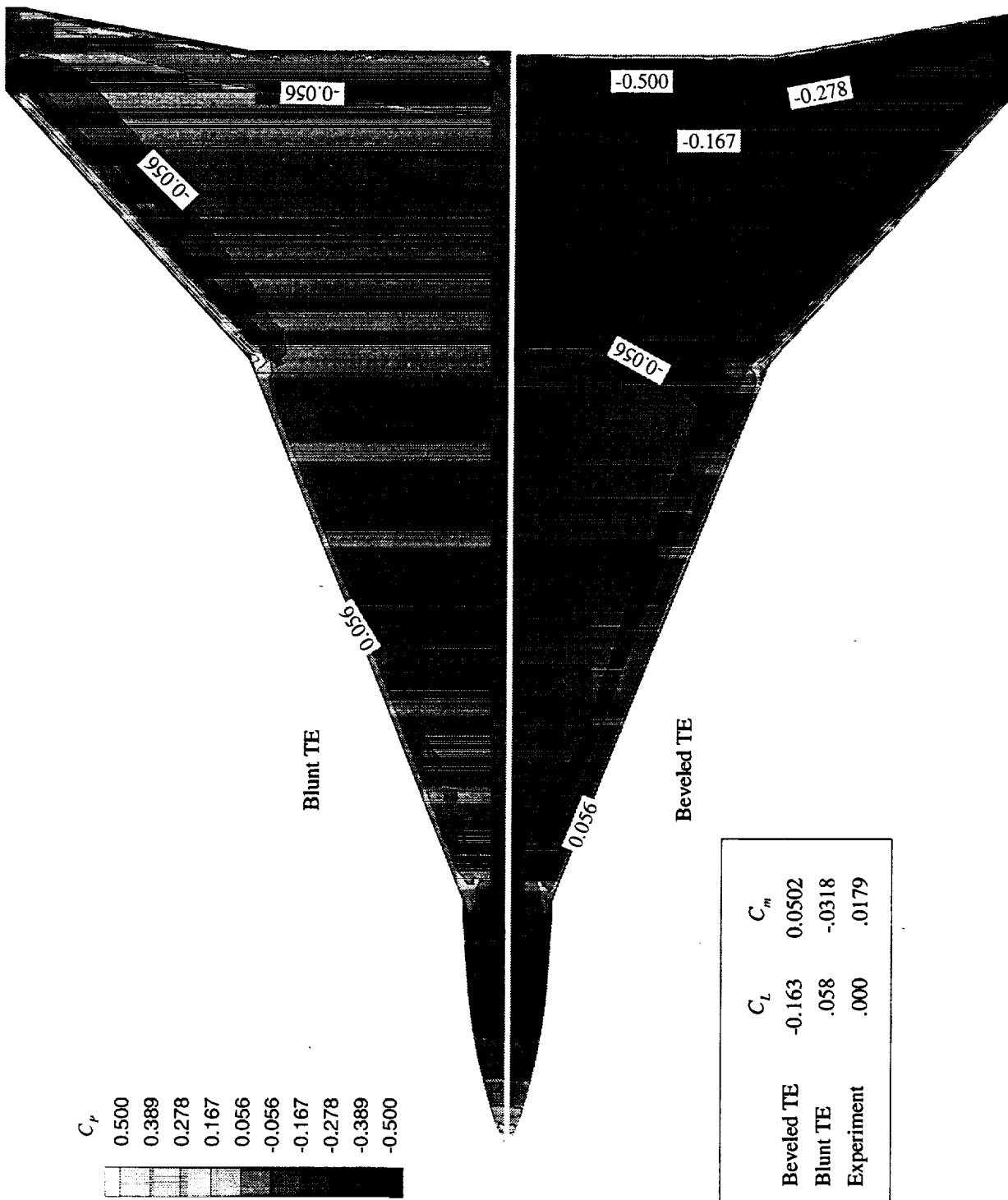


Blunt TE

Beveled TE

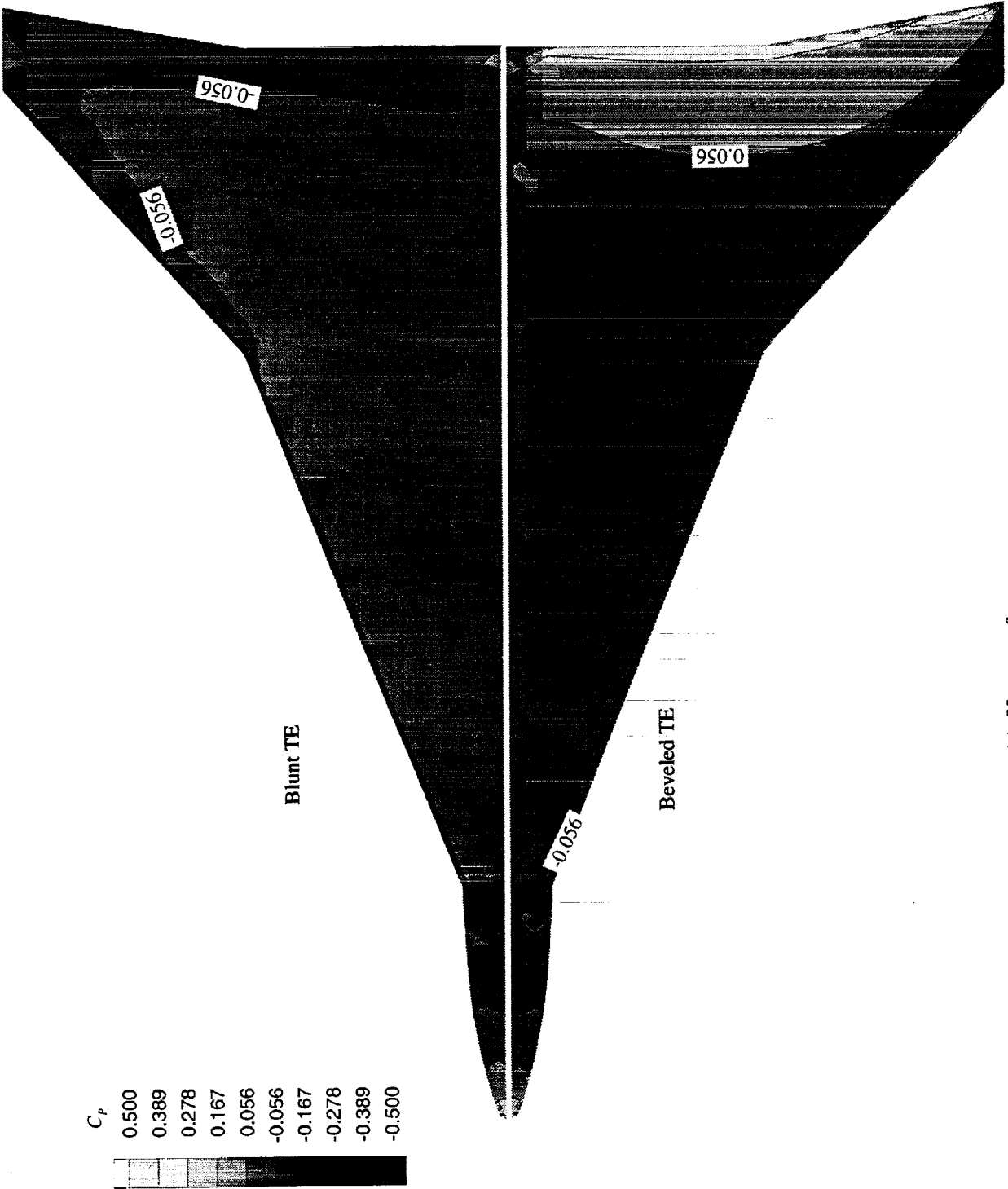
(a) Wing cross sections of two trailing-edge models ($y = 10.0$ in.).

Figure 50. Effect of trailing-edge modeling on USM3D analysis of planform 68/48 cruise configuration.



(b) Lower surface pressure contours.

Figure 50. Continued.



(c) Upper surface pressure contours.

Figure 50. Concluded.



REPORT DOCUMENTATION PAGE			Form Approved OMB No. 0704-0188	
Public reporting burden for this collection of information is estimated to average 1 hour per response, including the time for reviewing instructions, searching existing data sources, gathering and maintaining the data needed, and completing and reviewing the collection of information. Send comments regarding this burden estimate or any other aspect of this collection of information, including suggestions for reducing this burden, to Washington Headquarters Services, Directorate for Information Operations and Reports, 1215 Jefferson Davis Highway, Suite 1204, Arlington, VA 22202-4302, and to the Office of Management and Budget, Paperwork Reduction Project (0704-0188), Washington, DC 20503.				
1. AGENCY USE ONLY (Leave blank)	2. REPORT DATE December 1999	3. REPORT TYPE AND DATES COVERED Technical Publication		
4. TITLE AND SUBTITLE Investigation of Vortex Flaps and Other Flow Control Devices on Generic High-Speed Civil Transport Planforms		5. FUNDING NUMBERS WU 537-03-22-02		
6. AUTHOR(S) Kevin J. Kjerstad, Bryan A. Campbell, Brenda E. Gile, and Guy T. Kemmerly				
7. PERFORMING ORGANIZATION NAME(S) AND ADDRESS(ES) NASA Langley Research Center Hampton, VA 23681-2199		8. PERFORMING ORGANIZATION REPORT NUMBER L-17458		
9. SPONSORING/MONITORING AGENCY NAME(S) AND ADDRESS(ES) National Aeronautics and Space Administration Washington, DC 20546-0001		10. SPONSORING/MONITORING AGENCY REPORT NUMBER NASA/TP-1999-209537		
11. SUPPLEMENTARY NOTES				
12a. DISTRIBUTION/AVAILABILITY STATEMENT Unclassified-Unlimited Subject Category 02 Availability: NASA CASI (301) 621-0390		12b. DISTRIBUTION CODE Distribution: Nonstandard		
13. ABSTRACT (Maximum 200 words) <p>A parametric cranked delta planform study has been conducted in the Langley 14- by 22-Foot Subsonic Tunnel with the following objectives: (1) to evaluate the vortex flap design methodology for cranked delta wings, (2) to determine the influence of leading-edge sweep and the outboard wing on vortex flap effectiveness, (3) to evaluate novel flow control concepts, and (4) to validate unstructured grid Euler computer code predictions with modeled vortex and trailing-edge flaps. Two families of cranked delta planforms were investigated. One family had constant aspect ratio, while the other had a constant nondimensional semispan location of the leading-edge break. The inboard leading-edge sweep of the planforms was varied between 68°, 71°, and 74°, while outboard leading-edge sweep was varied between 48° and 61°. Vortex flaps for the different planforms were designed by an analytical vortex flap design method. The results indicate that the effectiveness of the vortex flaps was only slightly influenced by the variations in the parametric planforms. The unstructured grid Euler computer code was successfully used to model the configurations with vortex flaps. The vortex trap concept was successfully demonstrated.</p>				
14. SUBJECT TERMS High-Speed Civil Transport; Planform study; High lift; Vortex flaps; Vortex traps; CFD; Surface pressures; Surface flow visualization		15. NUMBER OF PAGES 126		16. PRICE CODE A06
17. SECURITY CLASSIFICATION OF REPORT Unclassified	18. SECURITY CLASSIFICATION OF THIS PAGE Unclassified	19. SECURITY CLASSIFICATION OF ABSTRACT Unclassified	20. LIMITATION OF ABSTRACT UL	